



**GeoRS**

Geopedology and Landscape Development  
Research Series

**VOLUME 13**

**Effects of historical charcoal burning  
on soil landscapes in West Connecticut,  
USA**

Alexander Bonhage

**b-tu**

Brandenburg  
University of Technology  
Cottbus - Senftenberg

**This series is edited by**

Prof. Dr. Thomas Raab

**©2023 Chair of Geopedology and Landscape Development**

Brandenburg University of Technology Cottbus – Senftenberg

Siemens-Halske-Ring 8

03046 Cottbus

Germany

**ISSN 2196 - 4122**

**[www.b-tu.de/fg-geopedologie/](http://www.b-tu.de/fg-geopedologie/)**

**<https://doi.org/10.26127/BTUOpen-6565>**

Geopedology and Landscape Development  
Research Series  
**VOLUME 13**

# **Effects of historical charcoal burning on soil landscapes in West Connecticut, USA**

Von der Fakultät Umwelt und Naturwissenschaften der Brandenburgischen Technischen Universität Cottbus – Senftenberg zur Erlangung des akademischen Grades Doktor der Naturwissenschaften genehmigte Dissertation

vorgelegt von M.Sc. Alexander Bonhage, geboren am 15. Juli 1989 in Berlin.

Gutachter: Prof. Dr. Thomas Raab

Gutachter: Prof. Dr. Jörg Völkel

Tag der mündlichen Prüfung: 17.07.2023

*The hills of little Cornwall  
Themselves are dreams.  
The mind lies down among them,  
Even by day, and snores,  
Snug in the perilous knowledge  
That nothing more inward pleasing,  
More like itself,  
Sleeps anywhere beyond them  
Even by night  
In the great land it cares two pins about,  
Possibly; not more.*

*The mind, eager for caresses,  
Lies down at its own risk in Cornwall;  
Whose hills,  
Whose cunning streams,  
Whose mazes where a thought,  
Doubling upon itself,  
Considers the way, lazily, well lost,  
Indulge it to the nick of death—  
Not quite, for where it curls it still can feel,  
Like feathers,  
Like affectionate mouse whiskers,  
The flattery, the trap.*

- Mark van Doren



## Abstract

The central theme of this thesis revolves around the impacts of historic charcoal burning on today's soils and soil landscapes in Connecticut, USA. The first chapter gives an overview of the state-of-research regarding the spatial distribution, morphology and chemical- as well as physical soil composition of so called relict charcoal hearth (RCH) landforms. RCHs can be described as unique soil microhabitats in the context of flora and fauna growth. The central research aim of the thesis is led by the question: How and to what extent does the historical charcoal industry control the distribution, development and properties of present day soils in Connecticut, USA? This thesis presents results from two field-campaigns in 2017 and 2018 where 52 RCH sites were surveyed and sampled in Litchfield County, Connecticut. The resulting dataset comprises of more than 1245 soil samples from 154 soil profiles and detailed stratigraphic and morphometrical information for all RCH sites. RCH landforms result in three distinct soils: charcoal rich horizons (Auh horizons), mineral soil horizons dividing multiple Auh horizons horizontally (Cu horizons) and buried former topsoil's (Ahb horizons) or buried mineral soil horizons (Bwb horizons). Sites on flat terrain ( $< 4^\circ$  slope) have mostly one Auh horizon, while sites on steeper terrain ( $> 4^\circ$  slope) have mostly two, sometimes up to three Auh horizons. The total volume of sites on slopes is positively correlated to the local slope, i.e. it increases with larger steepness of the terrain. Compared to reference soils, RCH soils are enriched in total soil organic carbon and especially in pyrogenic carbon. Vertical gradients of organic carbon concentrations in Auh and Cu horizons suggest an enrichment of non-pyrogenic organic matter in the topsoil and a vertical translocation of highly aromatic carbon compounds into intermediate and buried soil horizons. Furthermore, Auh horizons have a lower bulk density, a higher crystallinity ratio ( $Fe_d/Fe_t$ ) of pedogenic iron oxides and are enriched in exchangeable elements ( $Ca^{2+}$ ,  $Mg^{2+}$ ,  $Mn^{2+}$ ) as well as oxalate extractable manganese-oxides compared to reference soils. A deep-learning based automated mapping workflow called ARCHMAGE (Automated Relict Charcoal Hearth Mapping and Geospatial Exploration) was created to gain a continuous, state wide database of RCH sites locations and other relevant geospatial information. This database, in combination with calculation of site specific RCH volumes and soil carbon stocks, showed that in regions with high RCH site densities, significant additions to local soil organic and especially pyrogenic carbon stocks are present. This effect is scale dependent, with a larger effect size on county scale and below ( $\leq 1:650,000$ ).

## Zusammenfassung

The central theme of this thesis revolves around the impacts of historic charcoal burning on today's soils and soil landscapes in Connecticut, USA. The first chapter gives an overview of the state-of-research regarding the spatial distribution, morphology and chemical- as well as physical soil composition of so called relict charcoal hearth (RCH) landforms. RCHs can be described as unique soil microhabitats in the context of flora and fauna growth. The central research aim of the thesis is led by the question: How and to what extent does the historical charcoal industry control the distribution, development and properties of present day soils in Connecticut, USA? This thesis presents results from two field-campaigns in 2017 and 2018 where 52 RCH sites were surveyed and sampled in Litchfield County, Connecticut. The resulting dataset comprises of more than 1245 soil samples from 154 soil profiles and detailed stratigraphic and morphometrical information for all RCH sites. RCH landforms result in three distinct soils: charcoal rich horizons (Auh horizons), mineral soil horizons dividing multiple Auh horizons horizontally (Cu horizons) and buried former topsoil's (Ahb horizons) or buried mineral soil horizons (Bwb horizons). Sites on flat terrain ( $< 4^\circ$  slope) have mostly one Auh horizon, while sites on steeper terrain ( $> 4^\circ$  slope) have mostly two, sometimes up to three Auh horizons. The total volume of sites on slopes is positively correlated to the local slope, i.e. it increases with larger steepness of the terrain. Compared to reference soils, RCH soils are enriched in total soil organic carbon and especially in pyrogenic carbon. Vertical gradients of organic carbon concentrations in Auh and Cu horizons suggest an enrichment of non-pyrogenic organic matter in the topsoil and a vertical translocation of highly aromatic carbon compounds into intermediate and buried soil horizons. Furthermore, Auh horizons have a lower bulk density, a higher crystallinity ratio ( $Fe_d/Fe_t$ ) of pedogenic iron oxides and are enriched in exchangeable elements ( $Ca^{2+}$ ,  $Mg^{2+}$ ,  $Mn^{2+}$ ) as well as oxalate extractable manganese-oxides compared to reference soils. A deep-learning based automated mapping workflow called ARCHMAGE (Automated Relict Charcoal Hearth Mapping and Geospatial Exploration) was created to gain a continuous, state wide database of RCH sites locations and other relevant geospatial information. This database, in combination with calculation of site specific RCH volumes and soil carbon stocks, showed that in regions with high RCH site densities, significant additions to local soil organic and especially pyrogenic carbon stocks are present. This effect is scale dependent, with a larger effect size on county scale and below ( $\leq 1:650,000$ ).



## Acknowledgements

I want to thank Thomas Raab for giving me the opportunity to work on this dissertation under his supervision, for always being available to discuss challenges and problems and for enabling me to present my work on many international conferences. Furthermore, I'd like to thank Jörg Völkel for being a co-examiner of this thesis. For financial support I thank the German Research Foundation (DFG) and the BTU Cottbus-Senftenberg.

I thank Florian Hirsch for countless, sometimes transcontinental fieldtrips and discussions, teaching me a great deal about pedology, geomorphology and scientific working. Anna Schneider, who, with her scientific excellence and writing, will always be a role model for me. My eternal gratitude goes to Alexandra Raab, for without her constant encouragement, honest critique and care, I would not be where I am today. 10 years flew by just like that.

Of course, I thank the complete Geopedology team at BTU for making this the best possible place to work at and also the many students who tirelessly helped me over the years preparing the flood of samples we shipped from the US. Furthermore, I'd like to thank William Ouimet from the University of Connecticut for being our local guide and for many helpful discussions. Last but not least, I would like to thank Michael Seidel, who introduced me to the scientific method and proved to me that a University can be a fun place to work at.



# Table of Content

<b>Zusammenfassung</b>	<b>I</b>
<b>Table of Content</b>	<b>IV</b>
<b>List of figures</b>	<b>VII</b>
<b>List of tables</b>	<b>XII</b>
<b>I. Thesis structure</b>	<b>XVI</b>
<b>II. Author contributions to the chapters</b>	<b>XVII</b>
<b>1. Introduction</b>	<b>1</b>
1.1. RCH landform morphology and soil classification . . . . .	2
1.2. Mapping RCH sites . . . . .	5
1.3. RCH soil properties . . . . .	7
1.4. Soil organic matter and pyrogenic carbon in RCH soil . . . . .	10
1.5. RCHs as microhabitat . . . . .	11
<b>2. Hypotheses and aims</b>	<b>13</b>
<b>3. Overview of studies</b>	<b>15</b>
<b>4. Study area</b>	<b>17</b>
<b>5. Characteristics of small anthropogenic landforms resulting from historical charcoal production in western Connecticut, USA</b>	<b>20</b>
5.1. Abstract . . . . .	20
5.2. Aims . . . . .	21



5.3. Study area . . . . .	21
5.4. Field measurements and laboratory analysis . . . . .	23
5.5. Results . . . . .	25
5.6. Synthesis and discussion . . . . .	32
5.7. Summary and Conclusion . . . . .	37
5.8. Acknowledgements . . . . .	38

**6. Vertical SOC distribution and aromatic carbon in centuries old charcoal-rich Technosols 39**

6.1. Abstract . . . . .	39
6.2. Aims . . . . .	40
6.3. Methodology . . . . .	41
6.4. Results . . . . .	42
6.5. Discussion . . . . .	48
6.6. Conclusions . . . . .	53
6.7. Acknowledgements . . . . .	53

**7. Automated large-scale mapping and analysis of relict charcoal hearths in Connecticut (USA) using a Deep Learning YOLOv4 framework 55**

7.1. Abstract . . . . .	55
7.2. Introduction . . . . .	56
7.3. Research areas and LiDAR data . . . . .	59
7.4. Methodology . . . . .	61
7.5. Results . . . . .	70
7.6. Discussion . . . . .	77
7.7. Conclusion . . . . .	79
7.8. Acknowledgements . . . . .	80

**8. From site to state - Quantifying multi-scale legacy effects of historic land-forms from charcoal production on soils in Connecticut, USA 81**

8.1. Abstract . . . . .	81
8.2. Aims . . . . .	82
8.3. Methods . . . . .	83
8.4. Results and Discussion . . . . .	85
8.5. Conclusions and Outlook . . . . .	96
8.6. Acknowledgements . . . . .	98



<b>9. Synthesis</b>	<b>99</b>
<b>10. Outlook</b>	<b>105</b>
<b>11. References</b>	<b>107</b>
<b>Anhang</b>	<b>128</b>

# List of Figures

1.1.	A – B) Uncovered charcoal hearth wood stack and covered hearth in use (pictures: S. Vane & F. Hirsch). C – D) After the pyrolysis is complete, the hearth is harvested carefully (pictures: A. Bonhage). The pictures have been taken 2018 and 2022 in Brandenburg, Germany and show reconstructions of the historic charcoal hearth operation process. . . . .	2
1.2.	A) Schematic overview of a flatland RCH in the lignite mining area Jänschwalde, Brandenburg; B) Archaeological work on an RCH after removing the topsoil, showing the charcoal filled ditch surrounding the site (Pictures: Raab et al. 2015, modified). . . . .	3
1.3.	A) Schematic view of a slope RCH construction (Raab et al. 2017). B) Field-view of a slope RCH site as seen in Massachusetts (Picture: A. Bonhage). . . . .	3
1.4.	A) Schematic of soil stratigraphy for RCH sites on slope (modified from Bonhage et al. 2022), B) Multi-layered RCH soil for sites on slopes, C) Single-layered RCH soil for sites on flatland, D) Thick Auh horizon burying a well-developed Podzol in southern Poland (Pictures: A. Bonhage). . . . .	4
1.5.	Flatland RCH sites in Brandenburg, Germany as seen on a hillshade DEM (Bonhage et al. 2021). . . . .	5
1.6.	Location of studies dealing with mapping RCH sites (as of December 2022). Background map: ESRI. . . . .	6
2.1.	Outline of the thesis structure. . . . .	14
4.1.	Elevation map of Connecticut showing the general location of the main study area within the Salisbury Iron District and the Appalachian Mountains. Elevation data: NASA Shuttle Radar Topography Mission (SRTM) (2013). . . . .	18

- 4.2. Elevation map of Connecticut showing the general location of the main study area within the Salisbury Iron District and the Appalachian Mountains. Elevation data: NASA Shuttle Radar Topography Mission (SRTM) (2013). . . . . 18
- 4.3. Elevation map of Connecticut showing the general location of the main study area within the Salisbury Iron District and the Appalachian Mountains. Elevation data: NASA Shuttle Radar Topography Mission (SRTM) (2013). . . . . 19
- 5.1. Location of the transects “Wickwire” and “Hollenbeck” depicted on a 1 m LiDAR DEM. Red signatures mark the position of analysed RCHs. Site coordinates are provided in Annex A.2. LiDAR data courtesy of the Connecticut Department of Energy and Environmental Protection (CTECO, <http://www.cteco.uconn.edu/>). . . . . 22
- 5.2. Schematic of the two prevailing RCH types found in the study area, the position of sampling pits and the extent of the platforms diameter measurements: A) RCHs on slopes > 4°, with multiple technogenic layers; B) Example data and pit photos for RCH (no. 39), a high slope RCH; C) RCHs on slopes of < 4° with a single technogenic layer; D) Example data and pit photos for RCH (no. 46), a low slope RCH. . . . . 24
- 5.3. A) Relationship between slope and downslope change in Auh-layer thickness ( $\Delta T$ ) for individual RCH sites; Right) Relationship between slope and class 2 RCH diameter . . . . . 28
- 5.4. Overview of Wickwire RCH site locations and summary of soil stratigraphy data. The map shows 1.5 m contour lines. . . . . 29
- 5.5. Overview of Hollenbeck RCH site locations and summary of soil stratigraphy data. The map shows 1.5 m contour lines. . . . . 30
- 5.6. Box and whisker plots comparing average soil horizon thickness and variation at the four positions of a RCH site (1: RCH upslope end; 2: center of the RCH; 3: RCH downslope end; 4: reference forest soil). . . . . 31
- 5.7. Box and whisker plots comparing soil horizon bulk density and its variation at the four positions of a RCH site (1: RCH upslope end; 2: center of the RCH; 3: RCH downslope end; 4: reference forest soil). . . . . 32
- 5.8. Model for class 1 and 2 RCH architecture with generalized layers and average bulk densities for each soil layer. . . . . 35

# VIII

- 6.1. Diffuse reflectance spectra of BPCAquant RCH soils (Auh, Cu Horizons) and non-RCH soils (Ahb, Bwb, Ah, Bw Horizons). The black line shows the averaged spectra. Close ups of the aliphatic CH absorption wavenumber region exclusively show spectra of soil samples taken from the top 10 cm of a soil profile. . . . . 44
- 6.2. A) Principal component analysis (PCA) score- and B) loading plots for untreated BPCA<sub>quant</sub> soil sample spectra. RCH soil: Auh & Cu horizons; non-RCH soil: Ahb, Bwb, Ah, Bw and C horizons. . . . . 44
- 6.3. PLSR BPCA-C prediction model evaluation using cross-validation for RCH soil (Auh & Cu horizons) and non-RCH soil (Ahb, Bwb, Ah, Bw, C horizons) BPACquant spectra. . . . . 45
- 6.4. PLSR regression coefficient for RCH soil spectra in the BPCAquant dataset 46
- 6.5. Total carbon (TOC), predicted BPCA-derived carbon (BPCA-C) and calculated black carbon (BC) concentrations for RCH soils and non-RCH soil horizons . . . . . 46
- 6.6. Vertical distribution of total carbon and BC carbon concentrations in RCH soil horizons. P values from Mann–Whitney U testing are given as a measure for evidence of systematic differences between sampling increments (P > 0.10 not shown). . . . . 48
  
- 7.1. Excerpts of LiDAR data, visualized with Simple Local Relief Model (Hesse, 2010), showing examples of relict charcoal hearths in the Netherlands (left), Connecticut, USA (center), and Germany (right). . . . . 56
- 7.2. The research areas on an elevation map of Connecticut, USA. . . . . 59
- 7.3. Simplified representation of the ARCHMAGE workflow. . . . . 61
- 7.4. Excerpt of LiDAR data, visualized with Simple Local Relief Model (Hesse, 2010), showing the outline of a RCH (black), the ground truth (green), and the predicted bounding box (blue). . . . . 67
- 7.5. Excerpt of LiDAR data, in (scale 1:2000), visualized with Simple Local Relief Model (Hesse, 2010), showing a RCH in (blue outline) and an interpolation error in (red outline). . . . . 71
- 7.6. Boxplot graph showing the difference (in fractions) between the automatically and manually determined area of 25 RCHs. . . . . 74
- 7.7. Excerpts of LiDAR data, in scale 1:2000, visualized with Simple Local Relief Model (Hesse, 2010), showing the three predicted RCH locations in blue outline. . . . . 74

- 7.8. Overview of the distribution of RCHs (per sq. km) in the state of Connecticut, based on prior research by Anderson (2019; top) and current research (bottom). The top figure shows the presence (orange) or absence (lilac) of RCHs. The bottom figure shows the numbers of RCHs per sq. km (in shades of orange) or absence (lilac). Note that cells with less than 3 RCHs are omitted. The Training area is shown in black, the Test areas in blue. The red outline shows the newly discovered concentration of RCHs near West Stafford. . . . . 75
- 7.9. Excerpt of LiDAR data, visualized with Simple Local Relief Model (Hesse, 2010), showing part of the newly discovered cluster of RCHs in Shenipsit State Forest near West Stafford. . . . . 76
- 8.1. Concentrations of sequentially extracted pedogenic oxides (pyro – pyrophosphate, oxa – oxalate, dit – dithionite) in RCH soil (Auh, Cu), buried soil (Ahb, Bwb) and reference soil (Ah, Bw, C). . . . . 88
- 8.2. A) RCH site density in the state of Connecticut. Site locations are taken from Verschoof-van der Vaart et al. (2022). DEM data, State- and County boundary polygons are taken from the Connecticut Department of Energy and Environmental Protection (CTECO, <http://www.cteco.uconn.edu/>), Coordinate system WKID: 6434.; B) Map of Getis-Gi\* Clusters for RCH sites areas. Hot Spots indicate significant spatial clusters of larger sites; Cold Spots indicate significant spatial clusters of smaller sites. C) Map of the state-wide Terrain Ruggedness Index (TRI). . . . . 90
- 8.3. State-wide A) Terrain Ruggedness Index (TRI) cell values for each class (1 level, 10 extremely rugged) compared to RCH site occurrence, B) Topographic Position Index (TPI) cell values for each class compared to RCH site occurrence. . . . . 91
- 8.4. A) RCH site Getis-Gi\* cluster along the Housatonic River in Litchfield County, Connecticut. B) Detail view of RCH locations related to slope positions and boundary of the Miles Wildlife Sanctuary site aggregation example. Site locations are taken from Verschoof van-der Vaart et al. (2022). DEM data, State- and County boundary polygons are taken from the Connecticut Department of Energy and Environmental Protection (CTECO, <http://www.cteco.uconn.edu/>). . . . . 93
- 8.5. Soil unit polygons from the Gridded Soil Survey Geographic Database (gS-SURGO, Soil Survey staff 2022) with added total organic carbon stocks from RCHs compared to forest soil stocks (0 – 100 cm depth) . . . . . 95



8.6. Synthesis of A) site specific RCH soil properties. Percentages are in relation to reference forest topsoil properties; Large scale legacy effects on soil organic carbon and soil pyrogenic carbon stocks on a B) landscape, C) County and D) State scale. . . . . 97

A1. Soil texture for RCH sites no. 28, 29, 30, 32, 33 (averaged per site) and their respective reference forest soil profiles (USDA texture triangle) . . . . . 131

A2. Site Stratigraphy. The following morphometric and stratigraphic information regarding the 52 RCH sites sampled in Litchfield County has not been published with Chapter 5, but is included in this thesis for completeness. The soil horizons classification varies slightly compared to chapter 5. . . . 132

A28. MIR spectra of dried benzenecarboxylic acid (BPCA) residue showing absorptions for aromatic C=C ( $\leq 1481\text{ cm}^{-1}$ ), carboxyl C=O ( $1668\text{ cm}^{-1}$ ) as well as a broad OH absorption band ( $3500\text{ cm}^{-1}$ ). Additionally, shown are possible structures of BPCA (reproduced from Brodowski et al. 2005). . . . 158

A29. Hierarchical cluster analysis of 20 exemplary BPCAcal soil sample spectra and their total organic carbon concentration (TOC). . . . . 158

# List of Tables

1.1. Overview of studies discussing RCH soil chemical properties. Acknowledged where studies that list element concentrations in tables or appendixes. Properties where averaged whenever necessary. For brevity, if multiple sites from different location where discussed, then only the first one listed is included here. Numbers in parentheses are reference soil values. (Raab et al. 2022). . . . .	8
1.2. Overview of the commonly applied total organic carbon (TOC) and pyrogenic carbon (PyC) quantification methods used on pre/early industrial relict charcoal hearth (RCH) soils. . . . .	11
4.1. Natural setting and main properties of the studied soils (data from Bonhage et al. 2022, Raab et al. 2017, Hirsch et al. 2018). Soil type classification according to US Soil Taxonomy (Soil Survey staff, 2014) and World Reference Base for Soil Resources (IUSS Working Group World Reference Base, WRB, 2014). The soil acidity (pH) in CaCl <sub>2</sub> is given as a range and average. (Bonhage et al. 2022, modified). . . . .	19
5.1. Wickwire RCH sites properties and the derived generalized classification of sites based on the difference ( $\Delta T$ ) in thickness of technogenic Auh layers between the up- (pos. 1) and downslope position (pos. 3) of a site (class 1: $\Delta T < 50\%$ , class 2: $\Delta T > 50\%$ ). $Dp$ and $Do$ give the diameter of a site measured parallel and orthogonal to the slope. . . . .	26



- 5.2. Hollenbeck RCH sites properties and the derived generalized classification of sites based on the difference ( $\Delta T$ ) in thickness of technogenic Auh layers between the up- (pos. 1) and downslope position (pos. 3) of a site (class 1:  $\Delta T < 50\%$ , class 2:  $\Delta T > 50\%$ ).  $D_p$  and  $D_o$  give the diameter of a site measured parallel and orthogonal to the slope. . . . . 27
- 5.3. Parameters for the model of idealized RCH sites suitable for calculating geometry, pedostratigraphical thicknesses and stocks of elements . . . . . 34
- 6.1. Total concentrations of nitrogen (TN), organic carbon (TOC), BPCA-derived carbon (BPCA-C) and black carbon (BC) grouped by soil horizon (mean  $\pm$  standard deviation) for BPCAquant samples. Soil acidity (pH) is given as a range and average. The ratio gives the BC to TOC ratio. . . . . 43
- 6.2. Concentrations of measured nitrogen (TN), carbon (TOC), predicted BPCA-derived carbon (BPCA-C) and calculated black carbon (BC) concentrations grouped by soil horizon (mean  $\pm$  standard deviation) for all samples. The ratio gives the BPCA-C and BC to TOC ratio. . . . . 47
- 6.3. Average total organic carbon (TOC) and pyrogenic/highly aromatic carbon (PyC) concentrations for relict charcoal hearth (RCH) topsoil in temperate forests. The ratio gives the PyC /Charcoal-derived C to TOC ratio. . . . . 50
- 7.1. Overview of the research areas and the number and density of manually mapped relict charcoal hearts. . . . . 60
- 7.2. The number of subtiles per research area, resulting from the dataset generation. . . . . 62
- 7.3. Overview of the general (hyper)parameters for the YOLOv4 framework (before specific modifications) used in this research. . . . . 64
- 7.4. Overview of the different versions of the YOLOv4 framework used in this research. . . . . 65
- 7.5. The performance (Recall, Precision, F1) of the different versions of the YOLOv4 framework on the validation, and test datasets. Notice the difference in confidence threshold between the different datasets. . . . . 70
- 7.6. The original and recalculated performance (Recall, Precision, F1) of the different versions of the YOLOv4 framework on the test datasets. Notice the difference in confidence threshold between test area 1 and 2. . . . . 72

- 8.1. Averaged total organic carbon (TOC), pyrogenic carbon (PyC) and pH values for RCH (Auh, Cu), reference (Ah, Bw, C) and buried soil horizons (Ahb, Bwb) (data taken from Bonhage et al. 2022) . . . . . 86
- 8.2. Cation exchange capacity (CEC in cmolc kg<sup>-1</sup>) and exchangeable cations (in cmolc kg<sup>-1</sup>) for reference (Ah, Bw, C), technogenic (Auh, Cu) and buried soil horizons (Ahb, Bwb). BS (%) and Al (%) give the base- and aluminium saturation . . . . . 87
- 8.3. Total element concentrations of recovered macroscopic charcoal pieces from two RCH sites . . . . . 89
- 8.4. Measured and calculated morphometrics and mass for relict charcoal hearth sites in the state of Connecticut (average ± one standard deviation). . . 92
- 8.5. Calculated average (± one standard deviation) and total stocks of total organic carbon (TOC) and pyrogenic carbon (PyC) for RCH soils in Connecticut . . . . . 94
- 8.6. Calculated SOC and PyC stocks for forested areas compared to carbon stored in Connecticut's RCH soils . . . . . 94
- 8.7. Comparison of morphometrics and SOC stocks from RCHs and historical terrace/lynchet systems. . . . . 96
  
- A1. Physical and chemical soil properties for a representative RCH site and corresponding reference forest soil. . . . . 129
- A2. Descriptive statistics of all measured soil horizons thickness for every position on the RCH sites and for reference forest soil profiles. Only Bwb- and Bw-horizons where the subsequent C-horizon was visible are included (SDW = Standard deviation, CV= Coefficient of variation). . . . . 129
- A3. Coefficient matrix of Mann-Whitney-U test results comparing bulk density for soil horizons ( / p > 0.05 (not significant), \* p ≤ 0.05 , \*\* p ≤ 0.01, \*\*\* p ≤ 0.001) . . . . . 130
- A4. Descriptive statistics of soil horizons bulk densities for every position on the RCH sites and for reference forest soil profiles. . . . . 130
- A5. List of measured (C, N) and predicted (BPCA) soil properties for volumetric samples. . . . . 159
- A6. Calibration dataset of measured BPCA-C values for the chemometric BPCA-C prediction. . . . . 173
- A7. Soil acidity (pH in CaCl<sub>2</sub>) for studied soil samples. . . . . 175

- A8. Average element concentrations by sequential extraction in RCH and reference soils. T - total, P – pyrophosphate extractable, Ox – oxalate extractable, D – Dithionite extractable . . . . . 177
- A9. Effective cation exchange capacity (CEC) and exchangeable cations for RCH soils . . . . . 178
- A10. Effective cation exchange capacity (CEC) and exchangeable cations for Reference soils . . . . . 180
- A11. Total element concentrations for RCH soils . . . . . 182
- A12. Total element concentrations for reference soils . . . . . 185
- A13. Pedogenic (hydr)oxide concentrations in RCH soils . . . . . 187
- A14. Pedogenic (hydr)oxide concentrations in reference soils . . . . . 189

# I Thesis structure

This is a cumulative thesis essentially based on three published studies (chapters 5, 6, 7) and one study currently submitted to a journal (chapter 8, as of January 2023). All studies are (or will be) available “open-access”, meaning they fall under the Creative Commons Attribution Licence, which permits use, distribution and reproduction in any medium, provided the original work is cited properly. All rights to this thesis belong to the author (AB).

Changes have been made to chapter 5 - 8 to avoid repetition and for the structural integrity of the thesis. This affects the introductory sections of these four chapters, which have been summarized as a stand-alone chapter at the beginning of the thesis with some extensions and updates to the original text. Furthermore, sections regarding the study area have been cut wherever possible to reduce or remove redundancy. Nonetheless, some repetitions could not be avoided, as to keep the integrity of each study intact. Instead of section specific reference lists, there is a summary of all references at the end of the thesis. The soil horizon classification for the first study (chapter 5) differs slightly from the others, where intermediate (int) Auh horizons have been reclassified to Cu horizons.

For the framework of this thesis, four chapters have been added at the beginning (chapter 1 – 4). Parts of these chapters have been taken and adapted from publications written or co-written by the author (AB). Two chapters at the end (chapter 9, 10) consist of previously unpublished text.

## II Author contributions to the chapters

**1. Introduction:** 1.1 Text partly taken from Raab et al. (2022), written by AB; 1.2 Text partly taken from Raab et al. (2022), written by AB, text partly taken from Bonhage et al. (2020); 1.3 Text partly taken from Raab et al. (2022), written by AB; 1.4 Text partly taken from Bonhage et al. (2022).

**2. Hypotheses and Aims:** Original text written by AB.

**3. Publication overview:** Original text written by AB.

**4. Study area:** Original text written by AB.

**5. Characteristics of small anthropogenic landforms resulting from historical charcoal production in western Connecticut, USA.** AB – data analysis, conception of the study, writing first draft; TR, FH – conception of the study, manuscript editing; AS, AR, WI – manuscript editing.

**6. Vertical SOC distribution and aromatic carbon in centuries old charcoal-rich Technosols.** AB – data analysis, conception of the study, writing first draft, TR – conception of the study, manuscript editing; AS, AR, TF – manuscript editing; SR – data analysis and visualisation; WO, FH – conception of the study.

**7. Automated large-scale mapping and analysis of relict charcoal hearths in Connecticut (USA) using a Deep Learning YOLOv4 framework.** WV – conception of the study, data analysis, writing first draft; AB - conception of the study, data analysis, manuscript editing; AS, WO, TR – manuscript editing.

**8. From site to state - Quantifying multi-scale legacy effects of historic landforms from charcoal production on soils in Connecticut, USA.** AB – data analysis, conception of the study, writing first draft, TR – conception of the study, manuscript editing, AS, AR, WO, JV – manuscript editing, SR – data analysis.

**9. Synthesis:** Original text written by AB.

**10. Outlook:** Original text written by AB.

# 1 Introduction

In recent years, the body of scientific literature dealing with anthropogenic landforms resulting from historic charcoal production is steadily growing. This historic craft dates back to pre- and early industrial times and produced charcoal as fuel for local industries like iron furnaces, tar kilns and glass manufacturers. Only the advent of more efficient sources of fuel, like coal, caused a stop to this large scale use of woodlands. These landforms are mostly called relict charcoal hearths (RCHs), sometimes also charcoal kilns, charcoal platform remains, charcoal piles or, in North Eastern America, charcoal pits (which is misleading in terms of the landforms morphology). A charcoal hearth was built by so called colliers and is an unhitched structure made from stacked wood that would be covered with grass sods, twigs, leaves and reused soil from the hearths platform. Charcoal was created by slow pyrolysis, a process that could take up to several weeks to complete (Fig. 1A-B). The hearth was then harvested by raking out the charcoal (Fig. 1C-D), all the while care had to be taken for the pieces to not reignite. In the end, leftover charcoal pieces in various sizes (large pieces to fine dust) remained on the site, intermixed with the residual cover material of the hearth.

The remains of the hearths platform and cover material is the origin of the landforms we find today, forming small, circular (or nearly circular) elevations throughout the landscape with soils heavily enriched in charcoal. This enrichment is one of the most distinct properties of RCH landforms, resulting in unique soil properties influencing local flora and fauna. The following subsections will give an overview of the current state-of-knowledge regarding different RCH types, the spatial distribution of RCH sites and their soil properties.



**Abbildung 1.1.** A – B) Uncovered charcoal hearth wood stack and covered hearth in use (pictures: S. Vane & F. Hirsch). C – D) After the pyrolysis is complete, the hearth is harvested carefully (pictures: A. Bonhage). The pictures have been taken 2018 and 2022 in Brandenburg, Germany and show reconstructions of the historic charcoal hearth operation process.

## 1.1 RCH landform morphology and soil classification

On flatland, the colliers prepared the RCH platform by clearing a section of forest floor to make an even surface. The charcoal burning resulted in leftover cover material that formed a button-shaped elevation of up to multiple decimeters thickness. This elevation is usually surrounded by a shallow ditch or multiple pits (Fig. 1.2A). The negative and positive relief features result in a relatively strong contrast that makes them visible in the field, however, understory vegetation and disturbances by forestry activities sometimes obstruct this view (Raab et al., 2015; Risbøl et al., 2013). The ditch (Fig. 1.2B) was most likely constructed as a protective measure against the spreading of fires and as a source of substrate to cover the hearth (Hirsch et al. 2020).

Flatland RCH sites are single-layered, with the charcoal substrate layer having an average thickness of around 20 cm (Bonhage et al. 2020a), although this can vary locally. Sites on slopes (e.g. in the Harz and Appalachian Mountains) form a similar relief contrast, as



the colliers had to create artificial breaks in a slope to make an even surface for the RCHs construction. Sites on slopes are often multilayered, meaning they feature multiple charcoal rich substrate layers with dividing mineral substrate layers.



**Abbildung 1.2.** A) Schematic overview of a flatland RCH in the lignite mining area Jänschwalde, Brandenburg; B) Archaeological work on an RCH after removing the topsoil, showing the charcoal filled ditch surrounding the site (Pictures: Raab et al. 2015, modified).

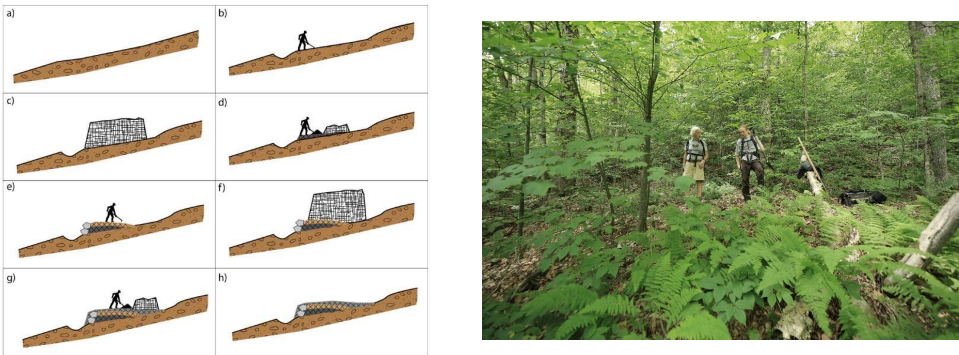


**Abbildung 1.3.** A) Schematic view of a slope RCH construction (Raab et al. 2017). B) Field-view of a slope RCH site as seen in Massachusetts (Picture: A. Bonhage).

This results most likely from efforts to repair and enlarge the original platform and is therefore indicative of multiple usages of a site. Sites on flatland and on slopes are by far the most common types of RCHs described worldwide. Other construction types like charcoal pits or rectangular hearths are either too old to be detected anymore or very rarely observed. A comprehensive overview of various RCH types is given by Hirsch et al. (2020).

Soils on RCH landforms can be classified as Spolic Technosols, i.e. they have 20 % volume (weighted average) of anthropogenic artifacts (charcoal) in the upper 100 cm from the soil

surface (IUSS working group WRB, 2014) (Fig. 1.4A). The soil horizon directly originating from the hearths operation, with the largest amount of charcoal and soil organic carbon is the Auh horizon (FAO 2006). Flatland sites consist of one Auh-horizon, while sites on slopes often have multiple (mostly two, up to three) (Fig. 1.4B-C). The intermediate mineral soil horizon between Auh-horizons is classified as Cu-horizons. But, this classification should be seen as a placeholder, since the origin of the mineral substrate has not been determined conclusively yet and is likely a mixture of topsoil and mineral soil horizons. Soils underneath RCH soil layers and horizons are classified as buried soils, with mostly B-horizons (Bwb) being affected. Buried topsoil Ah horizons (Ahb) are sometimes observed, however the preparation of the RCH platforms by the colliers most likely destroyed or truncated this horizon significantly. Sometimes RCH soils bury Podzols (Fig. 1.4D).

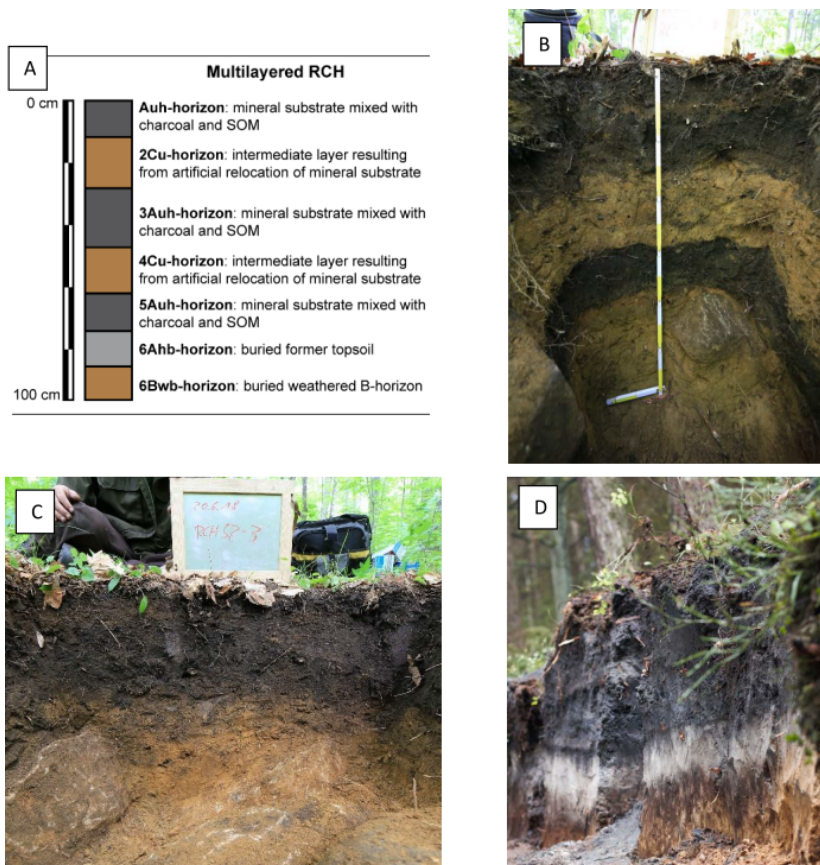


**Abbildung 1.4.** A) Schematic of soil stratigraphy for RCH sites on slope (modified from Bonhage et al. 2022), B) Multi-layered RCH soil for sites on slopes, C) Single-layered RCH soil for sites on flatland, D) Thick Auh horizon burying a well-developed Podzol in southern Poland (Pictures: A. Bonhage).

## 1.2 Mapping RCH sites

Before the widespread availability of high-resolution digital elevation models (DEMs) based on airborne LiDAR data, RCHs were field-mapped during ground surveys on comparably small areas (e.g., Bond, 2007; Bonhôte et al., 2002; Ludemann, 2003; von Kortzfleisch, 2008; Young et al., 1996). Arguably the first (organized) larger scale RCH site detection happened in Lower Lusatia, Brandenburg (Germany), where archaeological work in the forefront of the lignite mining operations uncovered a large RCH site field that fueled a local historic ironwork in the vicinity (Rösler et al. 2012). To this date, more than 1400 RCHs (pers. communication) have been uncovered and archaeologically described in this area (Raab et al. 2017). The negative-positive elevation contrasts make RCHs ideal candidates for digital mapping techniques based on high-resolution LiDAR-derived DEMs (Fig. 1.5), much like, e.g., burial mounds in the field of archaeology.

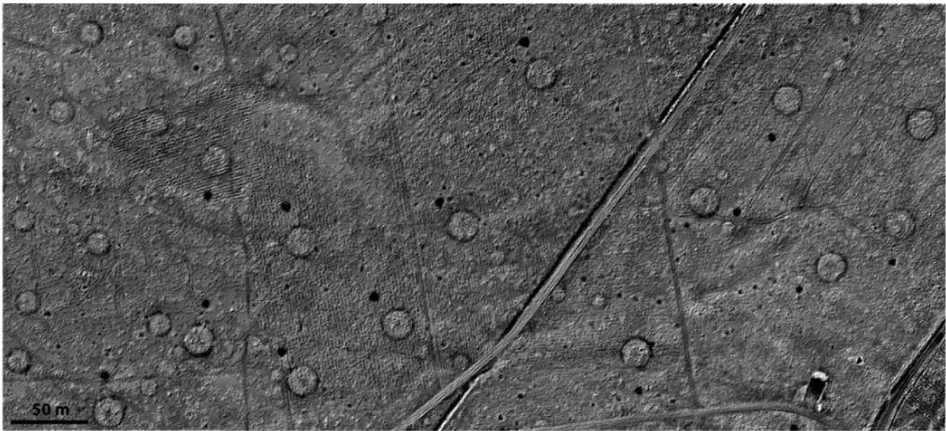


**Abbildung 1.5.** Flatland RCH sites in Brandenburg, Germany as seen on a hillshade DEM (Bonhage et al. 2021).

The earliest approaches mapped sites manually using a variety of DEM-derived relief visualizations, such as local relief models and hillshade maps (e.g., Deforce et al., 2013; Hesse, 2010; Raab et al., 2015; Risbøl et al., 2013). With increasing LiDAR data coverage, mapping efforts have expanded to even larger areas, culminating in several studies that cover hundreds to thousands of square kilometers, resulting in databases of ten to hundreds of thousand RCH sites (Rutkiewicz et al., 2019; Schneider et al., 2020a). An overview of the world-wide location of RCH mapping studies is given in Fig. 1.6 and Raab et al. 2022.



**Abbildung 1.6.** Location of studies dealing with mapping RCH sites (as of December 2022). Background map: ESRI.

It is clear now that RCHs are a widespread landscape feature of central European and northeastern U.S. forests, so widespread that the task of manually mapping them digitally becomes inefficient. The first semi-automated mapping approach on a larger scale by Schneider et al. (2014) used a template matching approach in a GIS environment. Withanara et al. (2018) applied Geographic Object-Based Image Analysis (GEOBIA) for sloped areas in Connecticut to extract RCH features from DEMs. In recent years, machine learning based object detection has become increasingly popular and efficient for geoarchaeological and archaeological research (Opitz and Herrmann, 2018). Thereby, datasets with manually digitized and labelled sites are used to train convoluted neural network (CNN)-based object detectors for site locations and segmentation (e.g., Bonhage et al., 2021; Trier et al., 2021; Verschoof-van der Vaart et al., 2020; Verschoof-van der Vaart & Lambers, 2019; Kazimi et al., 2019).

Although the reported mapping accuracies of recent studies are impressive, there is an inherent error associated with site detection on DEMs. It has been shown that there can be large disparities between field- and DEM-based manually mapped sites for an area. For example, Bonhage et al. (2020a) reported that >50 % of the actual RCH sites for an area in the North German lowlands were not detected by humans. This error associated with LiDAR point densities and human factors is then of course transferred to CNN-based models via the training data. Nonetheless, the major advantage of machine learning-assisted map-

ping is the ability to scan large areas relatively quickly and systematically (Verschoof-van der Vaart et al., 2020), with the potential for the complete workflow to be realized using freely available open source software and LiDAR data (Carter, 2019). Current advances in machine learning-based remote sensing techniques therefore greatly facilitate the detection of the full-scale legacy effect that historic charcoal burning has on today's soil landscapes, and it can be expected that RCH site databases will grow considerably in the near future. As has been recently shown by Suh et al. (2022) and Verschoof-van der Vaart et al. (2022, this thesis), this is a very promising approach for site detections over large areas.

### 1.3 RCH soil properties

Mikan and Abrams (1995) and Young et al. (1996), working in the North Central Appalachians of Pennsylvania, noted that RCH soils had unique soil chemistry patterns that could affect the chemistry of some woody plant species and even inhibit their growth. Since then, several studies have focused specifically on the soil chemical properties of RCH soils (Tab. 1.1). The ubiquitously observed differences from reference soils are increases in total organic carbon (TOC), black/pyrogenic carbon (BC) and exchangeable element concentrations. These differences are spatially distinct within hearths but are also detectable along gradients away from hearths (Donovan et al., 2021). The main controlling factor of these changes is the content of macro- and microscopic charcoal pieces that are intermixed with the mineral substrate. Soil organic carbon contents of RCH sites will be discussed more detailed in section 1.3.

Although varying natural settings and sampling schemes make a direct comparison between the studies listed in Table 1.1 difficult, general trends regarding differences between RCH and reference soil chemistries can be derived. Overall, there is little change in soil acidity (pH), with an average difference of 0.11 ( $\pm$  0.38) pH units. TOC contents are on average 188 % ( $\pm$  280 %) higher, while in some cases, the difference can be up to approximately 1000 % (Hart et al., 2008; Mastrolonardo et al., 2018). The usual procedure in soil analysis to disregard soil particles  $>2$  mm can result in underestimation of TOC contents in RCH soils, as large charcoal fragments will not be accounted for (Bonhage et al., 2020a; Mastrolonardo et al., 2018). When buried A-horizons below the RCH soils are preserved, they can show slightly reduced TOC contents compared with those of the A horizons of surrounding forest soils (Hirsch et al., 2018b). This reduction can be attributed to the ceased input of organic material along with proceeding mineralization of organic matter in the buried horizons and with the combustion of organic matter during hearth operation.

**Table 1.1.** Overview of studies discussing RCH soil chemical properties. Acknowledged where studies that list element concentrations in tables or appendixes. Properties were averaged whenever necessary. For brevity, if multiple sites from different location where discussed, then only the first one listed is included here. Numbers in parentheses are reference soil values. (Raab et al. 2022).

Study	Location	Depth cm	pH	TOC	TN g kg <sup>-1</sup>	BC	CEC cmolc kg <sup>-1</sup>
Abdelrahman et al. 2018	South Germany	0-5	4.9 (5.1)	144 (69)	5.7 (4.26)	39.9 (5.4)	
Bonhage et al. 2020b	Connecticut, USA	0-21	3.5-4.3 (41)				
Buras et al. 2020	North-East Germany	n.a.	3.2-3.9 (3.6-4.1)	46.7 (11.0)	7.0 (0.4)		0.49-0.77 (0.46)
Burgeon et al. 2020	Belgium	0-30	7.0 (7.1)	26.0 (14.0)	23.0 (14.0)		
Carrarie et al. 2016	Central Italy	0-15	6.1 (5.9)	105.0 (56.5)	5.0 (4.2)		
Donovan et al. 2021	Connecticut, USA	0-20	4.6 (4.9)	227.6 (154.6)	3.5 (3.3)		
Eriksson & Lundin 2021	Sweden	0-15	5.0 (4.7)				
Hardy et al. 2016	Belgium	0-25	5.0 (3.8)	41.1 (42.9)			9.6 (13.3)
Hardy et al. 2017	Belgium	0-25	5.7 (5.8)	34.5 (17.9)	2.4 (1.8)	13.5 (0.9)	16.6 (10.7)
Hardy & Dufey 2017	Belgium (Forest sites)	0-30		106.1 (50.4)		82.3 (n.a.)	
Hardy & Dufey 2017	Belgium (Cropland sites)	0-25		35.6 (17.5)		13.9 (n.a.)	
Hardy et al. 2019	Belgium (Forest sites)	0-59	3.4 (3.1)	85.7 (72.5)		53.8 (1.2)	28.1 (18.4) pot
Hardy et al. 2019	Belgium (Cropland sites)	0-25	6.2 (6.3)	30.3 (13.9)		13.4 (1.1)	16.0 (10.6) pot
Hart et al. (2008)	Tennessee, USA	0-5	4.9 (5.1)	61.6 (5.14)			14.66 (8.12) n.a.
Heitkötter & Marschner	South Germany	0-10	3.8 (3.9)	97.9 (65.9)	5.6 (5.4)		8.51 (6.9) eff
Hirsch et al. 2018a	Connecticut, USA	0-16	4.2 (3.7)	86.6 (71.1)	2.2 (6.0)		
Hirsch et al. 2018b	North-East Germany	0-5	3.5 (3.6)	28.8 (10.9)	0.7 (0.1)		
Jabin et al. 2006	Eifel, Germany	0-10	4.4 (3.7)	284.0 (171.1)	8.7 (8.5)		
Kerré et al. 2016	Belgium (Cropland sites)	0-23	6.2 (6.4)	35.0 (20.0)		22.2 (7.6)	16.0 (13.0)
Lasota et al. 2022	Poland			46.6 (21.9)	1.4 (1.3)		
Mastrodonardo et al. 2019	Belgium (Forest sites)	0-20	3.5 (3.5)	161.7 (31.5)		113.9 (3.1)	51.6 (25.5)
Mastrodonardo et al. 2018	Central Italy	0-22		119.5 (11.5)		47.4 (0.4)	
Mikan & Abrams 1995		0-10		257.0 (132.0)			
Pollet et al. 2022	Belgium (Forest sites)	0-10	3.7 (3.7)	103.0 (88.0)	6.4 (6.2)		7.73 (8.38) pot

The determination of BC (or PyC) concentrations is prone to methodological uncertainties, as different laboratory procedures usually target a different, more or less small, fraction of the black carbon spectrum, and thus far, there has been no standard protocol established. On average, RCH soils have an increase in BC concentrations of approximately 3300 % ( $\pm$  3700 %). The increased charcoal/BC contents result in + 37 % ( $\pm$  37 %) higher cation exchange capacities on average, caused by the negative surface charges of charcoal (Mastrolonardo et al., 2018). This effect can be increased by charcoal degradation processes, resulting in higher levels of surface hydroxyl functional groups (Hardy, 2017). Differences in available cation concentrations are discussed in the studies in detail, but notably, there are lower concentrations of available phosphorous reported in some RCH soils (e.g., Donovan et al., 2021; Hardy et al., 2016).

To date, information regarding soil mineralogical changes in RCH soils is rare. Hirsch et al. (2018b) noted that the vertical heat flow of a burning RCH affects only the topmost centimeters of the buried soils. The layer immediately below the RCH substrate is influenced by thermally induced transformation of iron (hydr-)oxides, apparent in the reddish color of the buried substrate which is sometimes observed. This heating influence on buried minerals enables RCH sites to be dated using the optical stimulated luminescence (OSL) technique (Karimi Moayed et al., 2020). Powell et al. (2012) and Dupin et al. (2019) discuss the increase in buried soil magnetic properties caused by hearth operation, which makes RCH sites potentially detectable by geophysical prospecting techniques.

In terms of soil physical properties, multiple studies show that RCH soils feature lower bulk densities (Raab et al. 2022), with higher coarse pore volumes being reported for some sites (Schneider et al. 2018a). This can have effects on water retention and water infiltration rates and patterns (Schneider et al. 2018a, Schneider et al. 2020b) that not necessarily result in better plant available water contents. Long term monitoring of water contents and soil temperature has shown that RCH soils are moister during wet climate conditions, that they dry faster during dry periods and that they show increased variability of topsoil temperatures and lower temperature variability in deeper soil horizons (Schneider et al. 2020b, Schneider et al. 2019). Also, RCHs have been shown to alter surface hydrology of slopes, where they can act as moisture sinks, with areas below the RCHs being drier than the surroundings (Bayuzick et al. 2022a).

## 1.4 Soil organic matter and pyrogenic carbon in RCH soil

Pyrogenic carbon (PyC) is a broadly defined term that refers to a degradation continuum ranging from lightly charred, relatively easily degradable, to highly condensed aromatic and recalcitrant carbon compounds (Bird et al. 2015), albeit this thesis will refer to the later part of the definition when mentioning PyC. Ongoing discussions point out the difficulty in applying PyC quantification methods to soil samples and interpreting their results, with various studies reporting variability in PyC concentrations of up to orders of magnitude for the same soil samples when applying different methodologies (e.g., Kerré et al. 2016, Hammes et al. 2007, Kurth et al. 2006, Schmidt et al. 2001). RCH soil have the potential to be used as a model system for studying the long-term effects of pyrogenic carbon/biochar additions to soils (Burgeon et al. 2020, Borchard et al. 2014, Criscuoli et al. 2014).

The obvious primary driver for RCH soil's chemical and physical properties is their large content of charcoal and it remains unclear if or to what extent non-PyC dynamics in RCH soils are affected by this. For similar charcoal-rich soils, some studies describe a positive correlation between PyC measured from a variety of methods and total organic carbon (TOC) concentration (Zimmerman & Mitra 2017, Reisser et al. 2016). In biochar-rich soils, the effect is mainly attributed to a persistent negative priming effect of PyC on soil organic carbon (SOC), i.e., an enhanced carbon storage caused by the sorption of organic matter on charcoal surfaces that decreases the SOM mineralisation rate (Tilston et al. 2016, Sing and Cowie 2014, Zimmerman et al. 2011, Kasozi et al. 2010). Furthermore, a “self-humification” effect of aged charcoal in soils has been described by some authors (Ascough et al. 2020, Ascough et al. 2011, Cohen-Ofri et al. 2006). Thereby, it can be assumed that the charcoal-influenced carbon pool can be quite dynamic in RCH soils. And indeed, a positive correlation between TOC and PyC concentrations has been described for RCH soils more than 60 years old (Abdelrahman et al. 2018, Borchard et al. 2014) and RCH soils older than 150 years currently under agricultural use (Kerré et al. 2017, Hernandez-Soriano et al. 2016), as have been weathering signs of RCH charcoal (Hardy et al. 2019). Research on RCH soil properties thus far mostly does not differentiate between fractions of the soil organic carbon spectrum, with more than half of the studies listed in Table 1.2 solely reporting total carbon or soil organic matter concentrations. The remaining studies mainly use wet chemical digestion methods that rely on the oxidization of nonpyrogenic SOM, resulting in a poorly defined end product, or thermogravimetric methods that directly measure CO<sub>2</sub> outputs at charcoal-specific oxidization temperatures to determine PyC concentrations in soils. The vertical distribution of carbon fractions in RCHs has been poorly studied so far,



despite being of potential interest to understand pedogenic processes in charcoal rich soils and to identify translocation of aromatic carbon, a subject of ongoing research on biochar-amended and wildfire-affected soils (Bellè et al. 2021, Braun et al. 2020, Hobbey 2019, Abney & Berhe 2018).

**Table 1.2.** Overview of the commonly applied total organic carbon (TOC) and pyrogenic carbon (PyC) quantification methods used on pre/early industrial relict charcoal hearth (RCH) soils.

Study	Methodology (and specific source if relevant)	Targeted SOC fractions
Buras et al. 2020, Hirsch et al. 2018b, Carrari et al. 2018, Heitkötter & Marschner 2015, Criscuoli et al. 2014, Dehkordi et al. 2020, Young et al. 1996	Dry combustion total element analysis	TOC
Hirsch et al. 2018a	Dry combustion total element analysis	PyC = RCH-Ctotal - nonRCH-Ctotal
Donovan et al. 2021, Tolksdorf et al. 2020, Bonhage et al. 2020a, Schneider et al. 2020, Schneider et al. 2019, Schneider et al. 2018a, Mikan & Abrams 1995	Loss on ignition (550°C)	TOC
Mastrolonardo et al. 2018	Weak nitric acid digestion (Kurth et al. 2006)	Non-oxidizable SOM
Mastrolonardo et al. 2019, Hardy & Dufey 2017	Walkley-Black digestion (Walkley 1974)	Non-oxidizable SOM
Kerré et al. 2016	Acid dichromate oxidation (Lim & Cachier 1996)	Non-oxidizable SOM
Kerré et al. 2016	Chemo-thermal oxidation (CTO-285) (Gustafsson et al. 2001, modified)	Non-oxidizable SOM
Burgeon et al. 2020, Hardy et al. 2019, Hardy et al. 2017, Hardy & Dufey 2017, Kerré et al. 2016	Differential scanning calorimetry (DSC) (Leifeld 2007)	Charcoal
Hernandez-Soriano et al. 2016	Isotope ratio mass spectrometer	Charcoal derived $\delta$ 13C Isotopes
Bonhage et al. 2022, Abdelrahman et al. 2018, Borchard et al. 2014	Benzene polycarboxylic acid method (BPCA) (Brodowski et al. 2005)	Condensed highly aromatic carbon compounds

## 1.5 RCHs as microhabitat

The properties of RCH soil have the potential to change the local soil habitat conditions, so much so that they are described as unique soil microhabitats (Bayuzick et al. 2022b, Carrari et al. 2016). This discussion started in the mid-1990s by Mikan and Abrams (1995) and Young et al. (1996), who reported primarily negative to neutral effects on tree growth on RCHs. Recent studies report neutral (Mastrolonardo et al. 2019) to negative (Buras et al. 2020, Carrari et al. 2018) effects on tree growth but positive effects on understory vegetation growth (Carrari et al. 2017). Some studies focus on soil meso- and microfaunal communities in RCH soils and report neutral effects overall and higher abundances of specific nematode communities in affected soils and litter (Gießelmann et al. 2019). Signifi-

cant changes in soil microbiological and fungal composition have been described for RCH soils compared to reference soils (Lasota et al. 2021, Hardy et al. 2019, Garcia-Barreda et al. 2017). A recent study on RCH sites in the Czech Republic noted changes in RCH soil biochemistry compared to reference soils and generally favourable conditions for soil microbiota and plant root abundance, calling RCHs “microhabitat hotspots” (Kučera et al. 2023).

## 2 Hypotheses and aims

This thesis hypotheses and aims were conceived in 2017 at the start of the DFG funded research project titled: Effects of historical charcoal burning on soil landscapes in West Connecticut, USA. At this point in time, RCHs have been mapped and described in the North-Eastern United States, but only on a local, site specific scale. However, it was indicated that the historic charcoaling industry has led to widespread anthropogenic changes to soils, and therefore potentially influenced the soil landscape evolution. The research aim of this thesis is to broaden our knowledge about the so called “legacy effects” of historic charcoal burning on multiple scales. A graphical outline of the thesis structure is given in Fig. 2.1. The main hypotheses of the thesis are:

**(H) Historical charcoal burning notably affects the distribution, development and properties of recent soils in Connecticut.**

- **(H1) The architecture of RCHs results in three distinct soils in the study area: Technosols, buried soils and natural (reference) soils.**
- **(H2) Topsoil properties of RCH soils vary significantly in their chemical and physical properties compared to natural (reference) soils.**

The hypotheses result in the primary research question, further subdivided into two secondary questions.

**(Q) How and to what extent does the historic charcoaling industry control the distribution, development and properties of present day soils in Connecticut?**

- **(Q1) Can we prove the distribution of soils as stated in H1 in our study area?**
  - 1.1 What is the average depth and the typical soil horizon sequence found on RCH soils and natural (reference) soils?

- 1.2 Does the topographic position control the distribution and morphometrical parameters of RCH soils?
- **(Q2) Can we prove „legacy effects” of charcoal burning on soil properties?**
  - 2.1 How are carbon concentrations and carbon quality controlled by the legacies of charcoal burning?
  - 2.2 Is there an effect of charcoal burning on soil physical properties?
  - 2.3 Is there a change in element concentrations beside organic and pyrogenic carbon?
  - 2.4 How can we quantify legacy effects on a site-specific scale and on a soil-landscape scale?

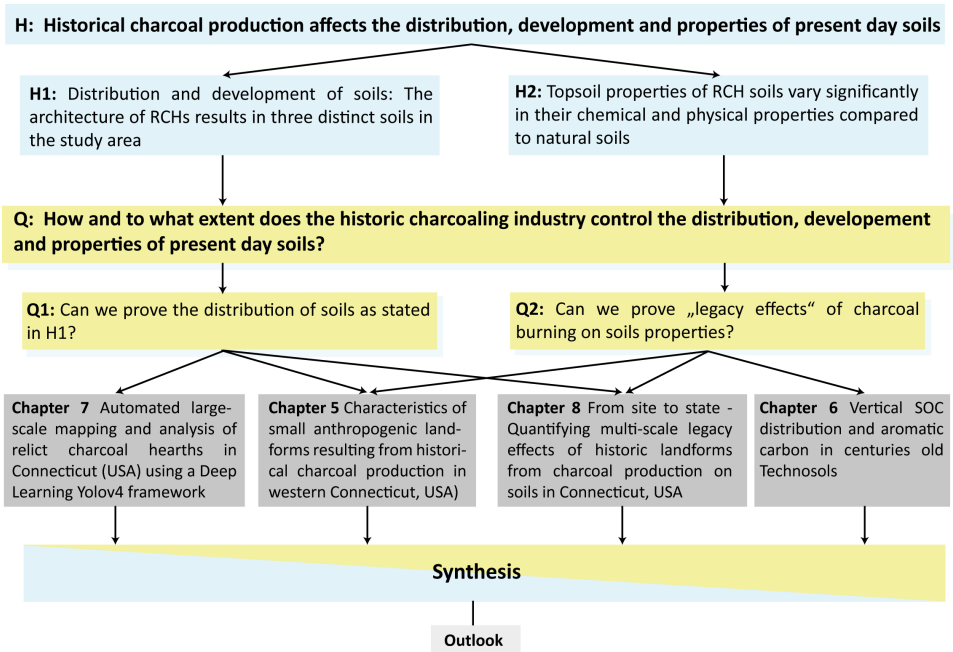


**Abbildung 2.1.** Outline of the thesis structure.

## 3 Overview of studies

The first study (chapter 5): “**Characteristics of small anthropogenic landforms resulting from historical charcoal production in western Connecticut, USA**” (Bonhage et al. 2020) examines the morphology and stratigraphy of 52 RCH sites in Litchfield County (NW Connecticut) in detail. The research presented here is the outcome of two extensive field campaigns (2017 & 2018) in which the sites were measured in terms of their morphometric characteristics and sampled using a high resolution vertical sampling scheme. The outcome is a model that enables the calculation of RCH site volumes using a geometrical abstraction of the sites morphology, average thicknesses and bulk densities of RCH soil horizons while taking into account slope dependent variations of stratigraphy and soil horizons thickness. This chapter addresses **Q1.1, Q1.2** and **Q2.2**.

The second study (chapter 6): “**Vertical SOC distribution and aromatic carbon in centuries old charcoal-rich Technosols**” (Bonhage et al. 2022) examines the RCH soils carbon contents in detail. Using a chemometric approach with FTIR-DRIFT soil spectra and elemental analysis, total organic and pyrogenic carbon contents are predicted for the complete soil sample dataset (n = 1245) of the 52 RCH sites. The results show that RCH soils are enriched in TOC and PyC and that there are vertical concentration gradients on the soil horizons. Furthermore, there is a translocation of highly aromatic carbon into intermediate Cu-horizons and buried subsoils, potentially resulting from ongoing charcoal degradation processes and self-humification of aged charcoal in RCH soils that release soluble aromatic acids. This chapter addresses **Q2.1** in detail.

The third study (chapter 7): “**Automated large-scale mapping and analysis of relict charcoal hearths in Connecticut (USA) using a Deep Learning YOLOv4 framework**” (Verschoof- van der Vaart et al. 2022) details a workflow to map RCH sites on DEMs using a state-of-the art machine learning-based object detector and how to describe some key

morphometric parameters (site area, local slope) automatically. We outline how to modify the framework to enhance prediction results for smaller sites and how to reduce false positive prediction caused by bad DEM data quality. The result is a continuous state-wide RCH site database for Connecticut. This chapter addresses **Q2.4** peripherally. Although a state-wide mapping was not originally planned for this thesis, it allows for the overall results to be more significant in scale.

The fourth study (chapter 8): “**From site to state - Quantifying multi-scale legacy effects of historic landforms from charcoal production on soils in Connecticut, USA**” (Bonhage et al. submitted) combines the results of all three previous studies. We expand the available soil property database for our soil sample set by determining exchangeable cation and pedogenic oxide concentrations. Using the state-wide RCH site database in combination with the model to calculate RCH site volumes and carbon concentrations from the fifth and sixth chapter, we gain a comprehensive overview of legacy effects on a larger than site-specific scale. The results show that RCH sites are enriched in certain exchangeable elements (Ca, Mg, Mn) and have an increased state of weathering. The legacy effect on landscapes are increases in local SOC and PyC stocks. This is shown to be a scale dependent effect; the larger the scale of observation, the higher the additions become. The aggregated pattern of RCH site distribution revealed by the state-wide mapping also means that these additions are only significant locally, in areas with high RCH site densities. This chapter addresses **Q1.2, Q2.1, Q2.3** and **Q2.4**.

## 4 Study area

North-western Connecticut became a hotspot for pre/early industrial iron industries for multiple reasons, as described by Gordon (2001). It had the advantage of large deposits of Limonite, offering higher quality bog iron ore that fuelled New England's forges at that point. It also had enough forest land suitable to produce the large amount of fuel (charcoal) needed to run the forges. The early New England settlers used every opportunity to convert suitable land into agriculture, making uphill forests with steep hills predestined for charcoal production. Although there have been earlier attempts, the iron making industry consolidated around the mid-18th century in the so called Salisbury Iron Making District, comprised of 16 townships (Fig. 4.1, red outline). Ironmaking in this district lasted almost 200 years, and ended in 1923, caused by drying up markets. More than 20 blast furnaces (Fig. 4.2) produced iron during that time.

The main study area is located in Litchfield County (Fig. 4.3). The area is part of the Appalachian Highlands, with glacial sediments dominated by till from the Wisconsin glaciation (Stone et al. 2005). The main properties of the study area and its soils are given in Table 4.1. Generally, the vegetation in the area is a mixed forest dominated by Oak, Maple and Birch. State wide, Connecticut is 59 % forested, with 72 % of forests being Oak/Hickory (Hochholzer et al. 2010). The soil sampling site is part of the Housatonic Highlands Massif, with bedrock containing granitic gneiss and amphibolite (Gates 1964). Soils in the area are usually Cambisols (IUSS working group WRB 2022).

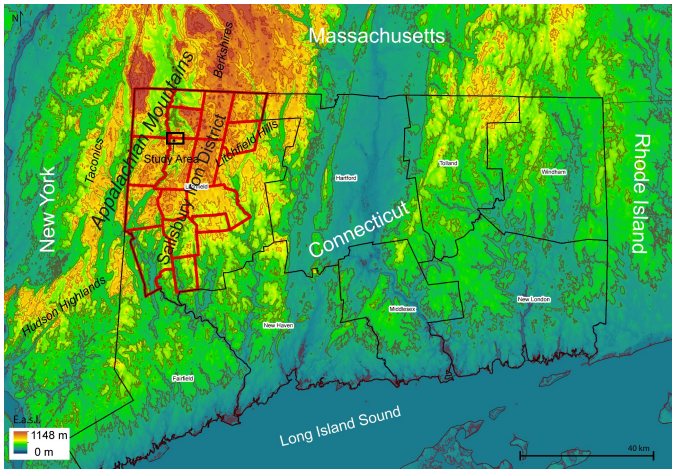


**Abbildung 4.1.** Elevation map of Connecticut showing the general location of the main study area within the Salisbury Iron District and the Appalachian Mountains. Elevation data: NASA Shuttle Radar Topography Mission (SRTM) (2013).



**Abbildung 4.2.** Elevation map of Connecticut showing the general location of the main study area within the Salisbury Iron District and the Appalachian Mountains. Elevation data: NASA Shuttle Radar Topography Mission (SRTM) (2013).



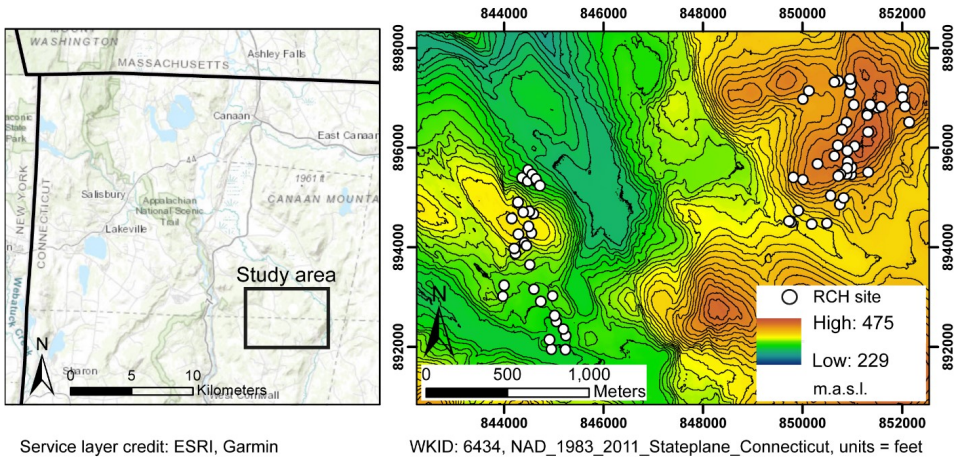


**Abbildung 4.3.** Elevation map of Connecticut showing the general location of the main study area within the Salisbury Iron District and the Appalachian Mountains. Elevation data: NASA Shuttle Radar Topography Mission (SRTM) (2013).

**Tabelle 4.1.** Natural setting and main properties of the studied soils (data from Bonhage et al. 2022, Raab et al. 2017, Hirsch et al. 2018). Soil type classification according to US Soil Taxonomy (Soil Survey staff, 2014) and World Reference Base for Soil Resources (IUSS Working Group World Reference Base, WRB, 2014). The soil acidity (pH) in CaCl<sub>2</sub> is given as a range and average. (Bonhage et al. 2022, modified).

<b>Climate</b>	Temperate
<b>Mean annual temperature</b>	8.3 °C#
<b>Mean annual precipitation</b>	1350 mm#
<b>Vegetation</b>	Mixed forest (Maple, Oak, Birch, Aspen, White Pine)
<b>Reference soils</b>	
Type	Typic Dystrudets (US Soil Taxonomy)/Cambisols (WRB)
Soil acidity (pH) topsoil	3.6–4.7 (4.1)
Average TOC content topsoil	50 g kg <sup>-1</sup>
Soil texture	Sandy loam
Munsell colour	10 YR 4/2 (dark greyish brown) – 7.5 YR 3.5 (strong brown)
<b>RCH topsoils</b>	
Type	Anthropic Udorthents (US Soil Taxonomy)/Spolic Technosols (WRB)
Soil acidity (pH) topsoil	3.5–4.8 (4.2)
Average TOC content topsoil	89 g kg <sup>-1</sup>
Munsell colour topsoil	10YR 2.5/1 (Black)
Period of charcoaling activity	AD 1760–1900

#based on monthly (1981–2010) normals, station Hartford. <https://www.usclimatedata.com>

# 5 Characteristics of small anthropogenic landforms resulting from historical charcoal production in western Connecticut, USA

This chapter is published as: Bonhage, A., Hirsch, F., Raab, T., Schneider, A., Raab, A., & Ouimet, W. (2020): Characteristics of small anthropogenic landforms resulting from historical charcoal production in western Connecticut, USA. *CATENA*, 195, 104896. <https://doi.org/10.1016/j.catena.2020.104896>. The Annex contains additional, previously unpublished material regarding site morphometrics and stratigraphy.

## 5.1 Abstract

Relict charcoal hearths (RCHs) are anthropogenic geomorphic features with an average diameter of 12 m found in many forests of Central Europe and in the eastern USA wherever pre-industrial iron production took place or other industries demanded the production of charcoal. To expand the knowledge about their geoarchaeological significance and their legacy effect on soil properties and forest ecosystems, we propose a method for a generalized description of soil stratigraphy on RCHs. We studied 154 soil profiles at 52 RCH sites alongside two 1 km transects in Litchfield County, Connecticut, USA. The sites can be classified based on the slope inclination, with sites on  $< 4^\circ$  mostly having a single-layered stratigraphy and an elevated circular shape, while sites on slopes  $> 4^\circ$  mostly are built as levelled and multilayered platforms. The latter have two or more charcoal rich technogenic Auh-layers separated by intermediate Auh-layers mostly consisting of mineral substrate. Based on average layer thicknesses and their dependence on the sites slope inclinations, we propose a model with two idealized RCH shapes with slope controlled properties that allow

for an easy computation of site diameters and elemental stocks. With ongoing advances in remote sensing of RCH sites, our proposed model can help to further understand the effects of historic land use on a landscape scale.

## 5.2 Aims

In their 2017 study, Raab et al. analyzed stratigraphic properties of 18 RCH sites on multiple locations in Litchfield County, Connecticut, USA, and concluded that local forest soils are heavily influenced by historical charcoal burning and that the building technique of RCHs is comparable to sites in Europe. However, the small number of sites described in the Raab et al. study did not allow for generalizable soil sequences on RCHs with differing specifications such as size and topographic position (local slope). In this study, we analyze the variation of RCH soil stratigraphy and layer geometry on two separate, coherent topographic transects with regularly spaced RCHs that cover a wide range of topographical positions in terms of their slope inclination. We examine the pedostratigraphy of 153 soil profiles at 52 RCHs and their correlation with the topographical position to develop a RCH classification based on slope inclination. We also analyze variation of bulk density as a proxy for physical soil properties. We want to create a model consisting of generalized shapes of RCHs and soil stratigraphy that could potentially help in the upscaling of site specific physical and chemical soil properties to a regional or landscape scale. This would allow for fully assessing the legacy effects of historical charcoal production on today's soil landscapes and forest ecosystems.

## 5.3 Study area

The study area is located approximately 7 kilometers north-east of the town West Cornwall in Litchfield County, Connecticut, USA (Fig. 5.1). The area is part of the Appalachian Highlands with glacial sediments dominated by tills from the Wisconsin glaciation (Stone et al. 2005). The main morphological units are till-mantled hillslopes with narrow floodplains from the Housatonic River (Stone et al. 2005, Raab et al. 2017). The vegetation consists of maple, oak, birch and aspen forest (Raab et al. 2017). The climate is temperate with an annual mean temperature of 8.2 °C and a mean annual precipitation of 1164 mm. Soils are classified as Typic Dystrudepts (US Soil Taxonomy) or Cambisols (IUSS Working Group WRB 2014) developed on fine sand dominated sandy loam, with an acidity that ranges from very strong to strongly acidic (pH 3.3 – 4.2, CaCl<sub>2</sub>) (Hirsch et al. 2018a, Raab et al. 2017). Soils on RCHs are Anthropic Udorthents (US Soil Taxonomy) or Spolic Technosols (Humic) (IUSS Working Group WRB 2014) (Hirsch et al. 2018a). RCHs in the area often have a

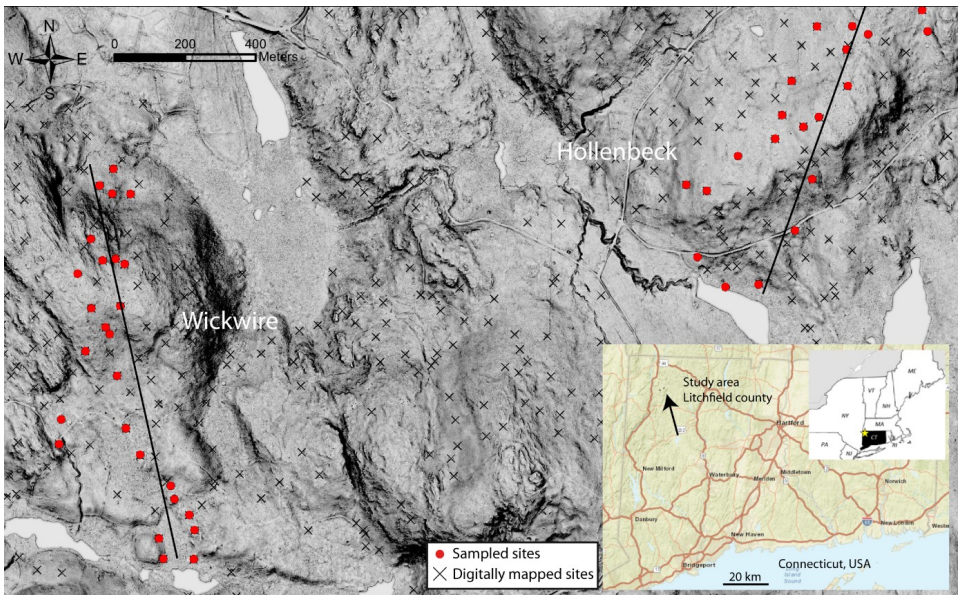


**Abbildung 5.1.** Location of the transects “Wickwire” and “Hollenbeck” depicted on a 1 m LiDAR DEM. Red signatures mark the position of analysed RCHs. Site coordinates are provided in Annex A.2. LiDAR data courtesy of the Connecticut Department of Energy and Environmental Protection (CTECO, <http://www.cteco.uconn.edu/>).

multi-layered stratigraphy with charcoal rich Auh-layers and intermediate layers consisting of relocated mineral substrate (hereinafter referred to as intermediate Auh-layers). These intermediate layers are most likely not the result of in situ pedogenic processes or of erosive slopewash, but rather have their origin in the purposeful relocation of adjacent mineral substrate to enlarge or to renew the platform for further hearth operations (Raab et al. 2017, Hirsch et al. 2018a).

Besides RCHs there are further signs of historic anthropogenic activity in the study area, such as building foundations, old roads and stone walls, the latter are related to agricultural land use activities beginning in the early 18th century (Johnson & Ouimet 2014). Although no direct dating of RCHs is available, they can be indirectly dated by proxy of the blast furnaces operating in the area, which would mean they were most likely built between 1750 and 1850 (Raab et al. 2017). During this time period the area was deforested, as shown by historical documents (Raab et al. 2017). There is no evidence for other deforestations after this time period.

## 5.4 Field measurements and laboratory analysis

We surveyed RCH sites adjacent to two topographic transects, approximately 2 km apart, on a total area of 0.7 km<sup>2</sup> (Fig. 5.1). The transects were chosen in areas with the same surface geology and vegetation and to cover the characteristic topographic units with slopes of varying inclination and relatively flat areas in plateau or floodplain positions. Each transect consists of surficial geology characterized as thin glacial till mapped at 1:125,000 scale. RCH sites to be surveyed were chosen on a LiDAR DEM prior to field work based on their proximity to the idealized lines of the two transects. In total, 52 RCH sites were measured for their stratigraphy, diameter and surrounding slope inclination. To account for possible small scale variations in soil layer thickness, soil profiles were described for three 1 x 1 m soil pits for each RCH site. The location of the soil pits was determined according to the survey pattern shown in Figure 5.2 to enable the reconstruction of the complete RCHs stratigraphy orthogonally to the slope. Position 1 is located at the upslope end, position 2 in the middle and position 3 at the downslope end of each RCH site. In case of a very flat relief at a site, we used the general slope of the landscape to determine position 1 and 2. One reference forest soil profile was dug for each site in a downslope position and a distance within 10-15 m from the site (Position 4). Soil profiles were usually dug to a depth that reaches the C-horizon, except when this was impossible because of large amount of rocks. The Auh-layers were completely measured in any case. The diameter of each site was measured orthogonally and parallel to the slope. The transects are named after nearby street designations. In the eastern end of the study area, the transect “Hollenbeck”, has a length of 920 m and an altitude ranging from 381 m to 440 m a.s.l. The western transect, “Wickwire”, has a length of 1100 m and an altitude ranging from 316 m to 375 m a.s.l. We analysed 26 RCH sites adjacent to each transect (Fig. 5.1). The site specific slope inclination for each RCH was measured trigonometrically using adjacent elevations from a 1 m LiDAR DEM (horizontal accuracy  $\pm 1$  m, vertical accuracy 0.138 – 0.170 m, CTECO 2017) taken parallel to the upslope-downslope orientation of the soil pits.

All soil profiles were sampled volumetrically in 5 cm vertical spacing's with 250 ml steel cylinders and additionally in 10 cm steps as bulk samples. The bulk density was calculated based on 40 °C dry weight of the volumetric samples. Grain-size distribution of representative soil profiles was analysed by wet sieving and fractionation according to the Soil Survey Investigation Report No. 42 method 3A1a1a (Soil Survey Staff, 2014). Soil pH was measured in 0.01 M CaCl<sub>2</sub>. Descriptive and comparative statistics were done using ArcGIS 10.4.1 (ESRI) and SPSS 25 (IBM). For descriptive statistics of soil horizon thicknesses and bulk

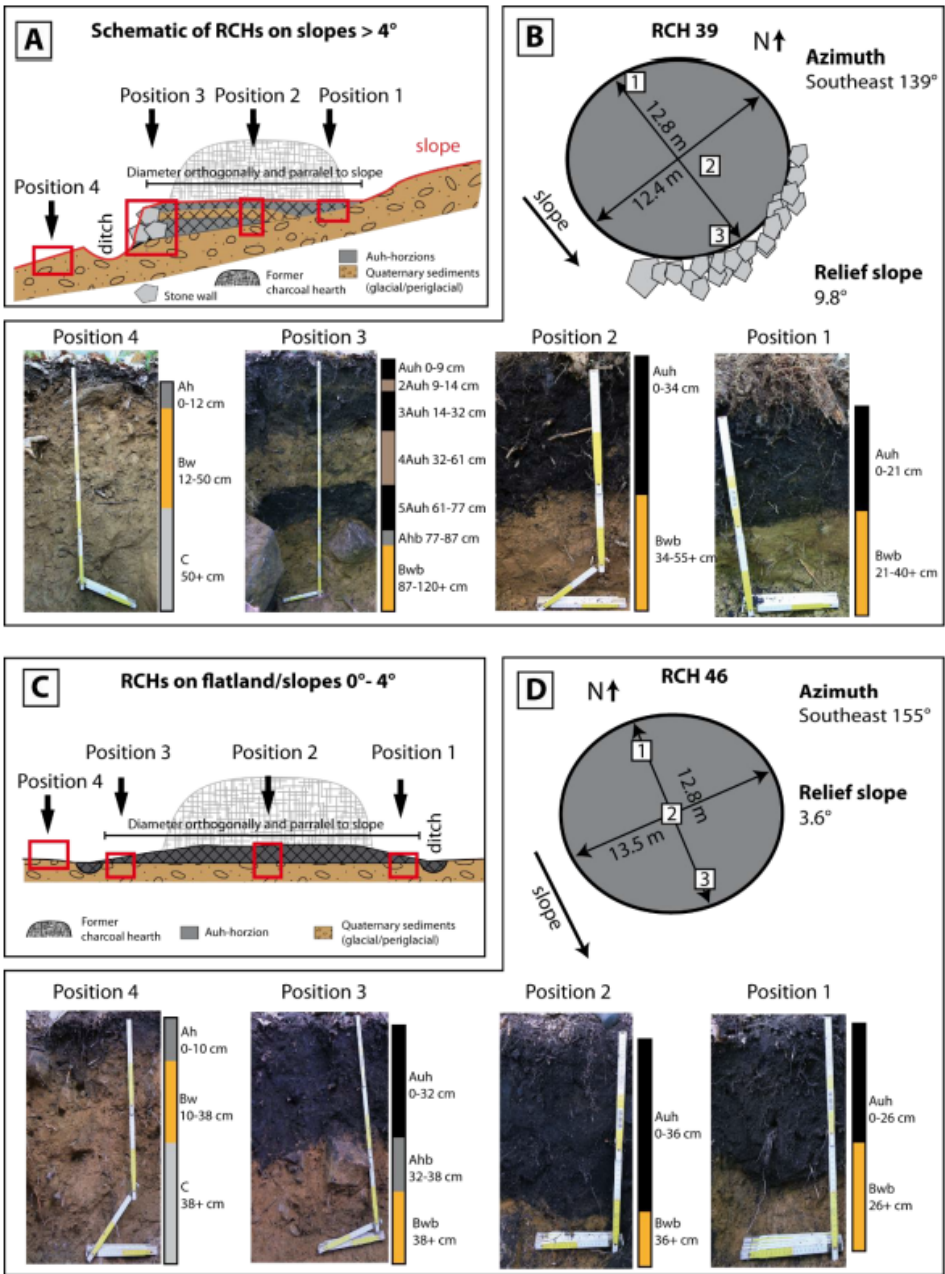


**Abbildung 5.2.** Schematic of the two prevailing RCH types found in the study area, the position of sampling pits and the extent of the platforms diameter measurements: A) RCHs on slopes > 4°, with multiple technogenic layers; B) Example data and pit photos for RCH (no. 39), a high slope RCH; C) RCHs on slopes of < 4° with a single technogenic layer; D) Example data and pit photos for RCH (no. 46), a low slope RCH.

densities, any observation 1.5 times the interquartile range from Q1 and Q3 respectively, was treated as an outlier and was not included in further calculations. Significant differences between samples were determined using Mann-Whitney-U tests. LiDAR derived DEM visualizations were created using the Relief Visualization toolbox 2.2.1 and the Visualization for Archaeological Topography (VAT) method (Kokalj & Somrak 2019).

## 5.5 Results

### 5.5.1 RCH classification and size

There are two typical architectural types of RCHs in the study area that are previously described for locations in Central Europe and the Eastern United States: RCHs on slopes and RCHs on flatland. RCHs on slopes consist of a levelled, slightly oval platform built into the slope, often framed by a stone wall at the downslope end. At most sites, they feature multiple charcoal rich Auh-layers with an increasing thickness towards the downslope end of the platform. RCHs on flatland are round, circular elevations of multiple decimeters, usually consisting of one charcoal rich Auh-layer whose thickness does not vary substantially for different positions on the site. For a detailed description of the genesis and historical background of these two typical architectural types we refer to Hirsch et al. (2020), Hirsch et al. (2018a) and Raab et al. (2017). Most common in our study area are RCH platforms on slopes ( $n = 34$ ) and circular RCHs surrounded by a ditch on flatter terrain ( $n = 15$ ). However, the ditches of the circular RCHs are not as pronounced and filled with charcoal as reported in other studies, therefore subsequent analysis will omit them from generalizations. Wickwire has 7 flat- and 19 platform RCHs on slopes while Hollenbeck has 8 flat- and 15 slope RCHs (Tab. 5.1 & 5.2).

Soil physical and chemical properties of a representative site (Annex Tab. A2) are in accordance with results from former studies in this area. The soils are predominantly sandy loams dominated by coarse-fine sand (Annex Fig. A.1). Figure 5.2 illustrates characteristic stratigraphy of both RCH types, showing the typical visual difference between both types, i.e. the occurrence or absence of charcoal rich- and intermediate Auh strata, mostly in position 2 and 3 of a site. However, this visual difference is not always present. We analyzed one multilayered RCH on flat terrain with an intermediate Auh-layer and eleven RCHs on steeper slopes with only one discernible Auh-layer. A definitive decision for classification was consequently based on a clear increase in summarized Auh- and intermediate Auh-layer thickness between the first and the third profile position of a site. This ratio is given

**Table 5.1.** Wickwire RCH sites properties and the derived generalized classification of sites based on the difference ( $\Delta T$ ) in thickness of technogenic Auh layers between the up- (pos. 1) and downslope position (pos. 3) of a site (class 1:  $\Delta T < 50\%$ , class 2:  $\Delta T > 50\%$ ).  $D_p$  and  $D_o$  give the diameter of a site measured parallel and orthogonal to the slope.

RCH no.	Slope [°]	$D_p$ [m]	$D_o$ [m]	Diameter Average [m]	Total Auh thickness pos. 1 [cm]	Total Auh thickness pos. 3 [cm]	$\Delta T$ [%]	RCH class
39	9.1	12.4	12.8	12.6	21	77	267	2
40	11.2	8.4	9.8	9.1	10	38	280	2
41	6.9	9.5	11.3	10.4	18	42	133	2
42	8.2	11.6	10.8	11.2	24	43	79	2
43	7.8	10.0	10.0	10.0	23	78	239	2
44	11.9	9.2	8.3	8.8	11	44	300	2
45	10.0	10.4	9.3	9.9	25	54	116	2
46	4.7	13.5	12.8	13.2	26	32	23	1
47	0.9	15.4	13.8	14.6	31	60	93	2
48	7.1	9.8	10.1	10.0	23	50	117	2
49	9.7	10.7	10.0	10.4	23	55	139	2
50	11.5	10.5	8.3	11.7	25	84	236	2
51	4.5	15.0	12.9	14.0	23	61	165	2
52	1.6	13.2	13.5	13.4	27	27	0	1
53	3.1	11.6	10.7	11.2	34	36	6	1
54	1.3	10.9	9.4	10.2	22	9	-59	1
55	4.0	12.8	11.3	12.1	24	55	129	2
56	6.9	11.3	11.3	11.3	10	62	520	2
57	6.6	12.6	12.1	12.4	20	70	250	2
58	11.3	11.5	11.0	11.3	18	50	178	2
59	6.6	9.5	13.3	11.4	18	60	233	2
60	5.3	9.9	9.7	9.8	15	63	320	2
61	3.5	8.4	8.4	8.4	5	5	0	1
62	10.4	10.6	10.4	10.5	18	60	233	2
63	2.1	12.1	11.1	11.6	24	33	37	1
64	6.4	11.8	13.8	12.8	27	30	11	1

as percentage value ( $\Delta T$ ) in tables 5.1 and 5.2, with positive values showing an increase in Auh-layer thickness in the downslope direction, and negative values showing a decrease.

We set the threshold value for classifying sites to be  $\Delta T < \text{or} > 50\%$  (Fig. 5.3), as this puts most sites with a low or negative  $\Delta T$  value that are not multilayered in a separate class from multilayered sites with a high  $\Delta T$  value. RCHs with  $\Delta T < 50\%$  are located on significantly ( $p < 0.001$ ) more level terrain than RCHs with  $\Delta T > 50\%$ , with an average ( $\pm 1$  standard deviation) inclination of  $2.8 \pm 1.6^\circ$  against  $7.0 \pm 3.0^\circ$ , respectively. Therefore, we attribute sites with  $\Delta T < 50\%$  to generally be on slopes  $< 4^\circ$  and sites with  $\Delta T > 50\%$  to generally be on slopes  $> 4^\circ$ . For the sake of brevity, the first group will be labeled as class 1 RCHs and the latter as class 2 RCHs henceforth. The site diameters were measured slope parallel ( $D_p$ ) and slope orthogonal ( $D_o$ ). Class 1 RCHs have an average  $D_p$  of  $11.6 \pm 1.3$  m and a  $D_o$  of  $11.4 \pm 1.6$  m. Class 2 RCHs have an average  $D_p$  of  $11.4 \pm 1.6$  m and a  $D_o$  of  $11.1 \pm 1.4$  m.



**Table 5.2.** Hollenbeck RCH sites properties and the derived generalized classification of sites based on the difference ( $\Delta T$ ) in thickness of technogenic Auh layers between the up- (pos. 1) and downslope position (pos. 3) of a site (class 1:  $\Delta T < 50\%$ , class 2:  $\Delta T > 50\%$ ).  $D_p$  and  $D_o$  give the diameter of a site measured parallel and orthogonal to the slope.

RCH no.	Slope [°]	$D_p$ [m]	$D_o$ [m]	Diameter Average [m]	Total Auh thickness pos. 1 [cm]	Total Auh thickness pos. 3 [cm]	$\Delta T$ [%]	RCH class
28	11.1	13.0	11.6	12.3	13	83	538	2
29	3.0	12.0	12.6	12.3	17	30	76	2
30	4.7	12.2	12.4	12.3	21	54	157	2
31	8.5	11.9	10.8	11.4	19	87	358	2
32	7.1	9.5	10.2	9.9	15	50	233	2
33	10.6	8.8	8.9	8.9	19	43	126	2
34	2.8	12.4	11.8	12.1	20	20	0	1
35	2.1	11.5	10.8	11.2	-	-	-	-
36	2.0	11.8	12.2	12.0	25	31	24	1
37	3.0	11.7	11.4	11.6	29	36	24	1
38	2.3	9.8	8.9	9.4	-	-	-	-
65	6.0	11.9	10.9	11.2	40	54	35	-
66	4.2	11.6	10.8	11.8	16	52	225	2
67	6.0	11.8	11.7	12.3	25	53	112	2
68	7.4	13.0	11.6	13.3	19	70	268	2
69	3.2	13.4	13.2	11.4	21	11	-48	1
70	1.5	11.6	11.2	11.1	24	44	83	2
71	5.6	11.2	11.0	12.2	16	45	181	2
72	4.6	11.5	12.8	12.6	30	54	80	2
73	0.6	12.3	12.8	11.9	35	23	-34	1
74	1.5	12.0	11.8	12.8	26	40	54	2
75	6.4	13.1	12.5	11.4	20	64	220	2
76	4.4	12.9	9.8	11.5	20	57	185	2
77	2.7	11.2	11.8	12.3	20	10	-50	1
78	0.3	11.9	12.6	9.4	26	16	-38	1
79	5.2	9.6	9.1	12.3	26	37	42	1

Both classes of RCHs therefore showcase a slight ovality, with the longer axis in the slope parallel direction. However, the difference between  $D_p$  and  $D_o$  is not statistically significant. Therefore, we subsequently assume a circular shape for RCHs on slopes, consisting of the averaged  $D_o$  and  $D_p$  of each site.

A uniquely located site is RCH no. 38, which was surveyed in a bankside position next to a pond in the south of Hollenbeck. Due to groundwater influence we could only create a pit at position 2 in the middle of the platform on this site, therefore it could not be classified. Beside slope- and flat RCHs, we found one slope platform RCH surrounded by a ridge (no. 65) in the north of Hollenbeck as described by Hirsch et al. (2020) and Tolksdorf et al. (2020). RCH no. 35 could not be classified due to lacking a profile at the first position.

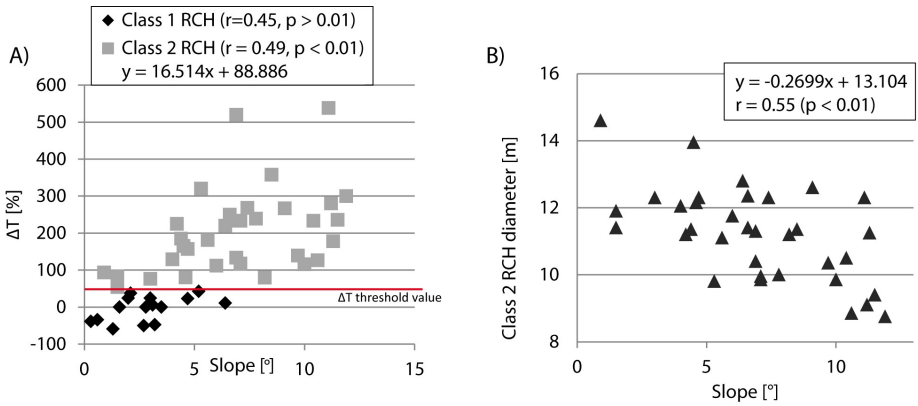


**Abbildung 5.3.** A) Relationship between slope and downslope change in Auh-layer thickness ( $\Delta T$ ) for individual RCH sites; Right) Relationship between slope and class 2 RCH diameter

### 5.5.2 Slope correlation with $\Delta T$ and diameter

We used simple linear regression models to analyze the correlation of  $\Delta T$  and diameter with slope inclination (Fig. 5.3). For class 1 RCHs there is a moderately weak positive and insignificant correlation of  $\Delta T$  with the slope.  $\Delta T$  ranges from -59 % to 42 %, which we regard as variation caused by the colliers efforts to create an even platform on generally flat positions with rough micro relief features (at the meter scale) that are not captured by our DEM-based slope measurement. For class 2 RCHs there is a moderate positive correlation of  $\Delta T$  with slope, suggesting a general increase in Auh-layer thickness toward the downslope end of sites on steeper slopes. From around 5° to 7.5°,  $\Delta T$  rises to a maximum of up to 300 % and then varies between 100 % and more than 500 %. Class 2 RCH's diameter correlates moderately negative with slope, showing a general decrease of site diameter with increasing slope inclination from > 15 m at 1° to around 8 m on 12°.

### 5.5.3 Site pedostratigraphy

#### Auh-layers

The sites stratigraphy and their location alongside the transects is shown in figures 5.4 and 5.5. An overview of average thicknesses for all sites is given in figure 5.6 and Annex Tab. A.3. Nearly every sites position has a primary Auh-layer with the exception of RCH no. 61, upon which no technogenic layer could be classified because of a distinct lighter color and comparably lower or lacking occurrence of charcoal pieces. RCH nos. 38 and 35 are

lacking two and one soil pits, respectively, hence the total number of Auh-layers per position in table 2 does not match the total number of RCH sites. The average first Auh-layer (Auh1) thickness increases from  $20.9 \pm 5.7$  cm in position 1 to  $23.6 \pm 14.9$  cm in position 3. The second Auh-layers (Auh2) average thickness is generally six to nine centimeter smaller than for the Auh1. The third Auh-layer (Auh3) is has an average thickness of  $16.3 \pm 9.7$  cm. Neither Auh1, Auh2, or Auh3 horizon thicknesses significantly correlate with slope inclination (data not shown).

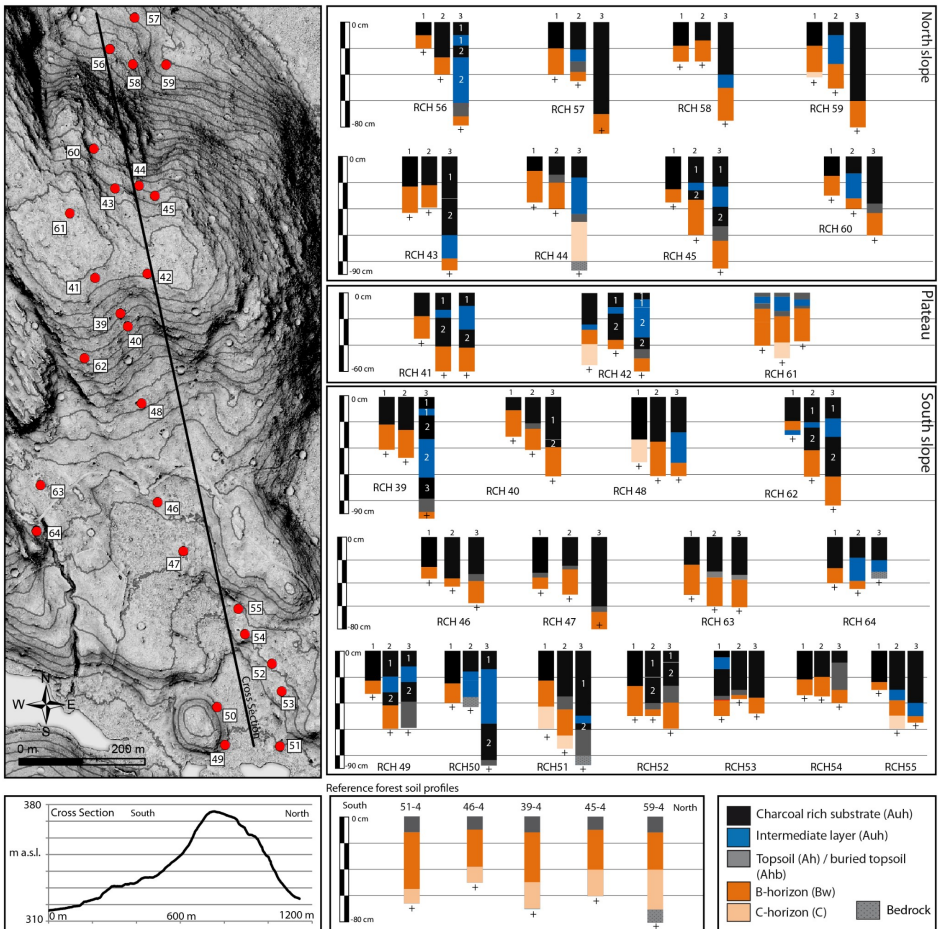


**Abbildung 5.4.** Overview of Wickwire RCH site locations and summary of soil stratigraphy data. The map shows 1.5 m contour lines.

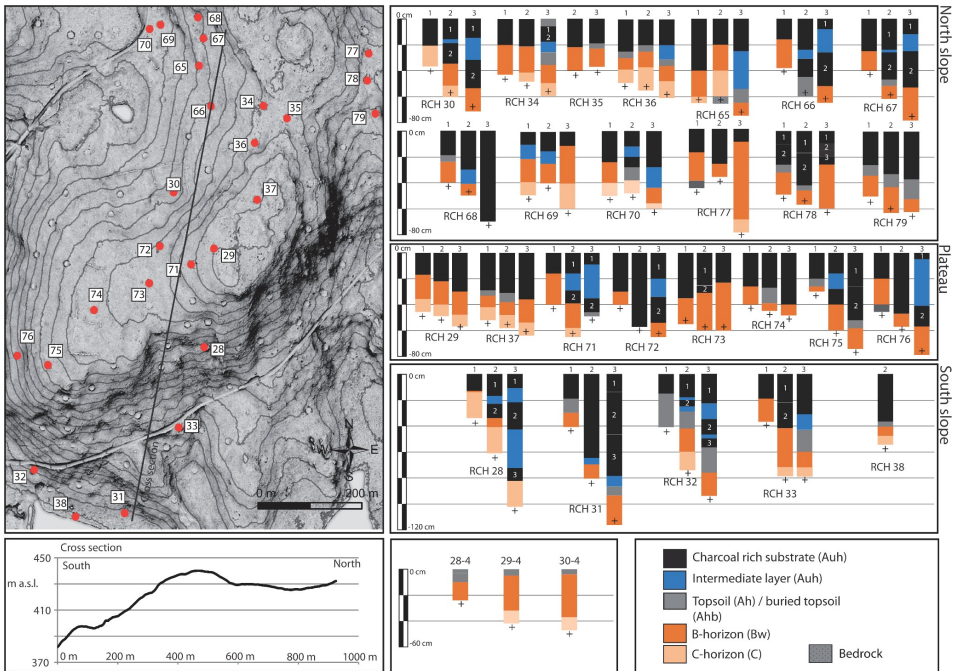


**Abbildung 5.5.** Overview of Hollenbeck RCH site locations and summary of soil stratigraphy data. The map shows 1.5 m contour lines.

### Intermediate Auh-layers

The average thickness of the int Auh1 horizon increases from  $7.6 \pm 4.0$  cm to  $14.4 \pm 7.3$  cm. A second intermediate Auh-layer (int Auh2) is comparably rare. Its average thickness ranges from  $8.5 \pm 4.5$  cm in position 2 to  $24.0 \pm 11.2$  cm in position 3. Neither int Auh1 or int Auh2 horizon thicknesses correlate with the slope inclination (data not shown).

### Forest soil horizons

We could identify buried Ah-horizons (Ahb) on 37 RCH sites, mostly on positions 2 and 3 (Annex A.2), but only very seldom on both at the same site. Their distinguishing characteristics are the lack of macro and micro sized charcoal particles except for scattered pieces at the top of the horizons, a less dark color than the Auh-layers and predominantly a very sharp upper boundary that is even, wavy or interlocked. The average Ahb thickness increases from  $5.0 \pm 2.2$  cm in position 1 to  $8.7 \pm 5.1$  cm in position 3. Although buried Bw-horizons are generally present at nearly every soil profile we sampled, it was only pos-

sible to measure their vertical extent down to the lower boundary at 18 sites. The average Bwb-horizon thickness is barely changing depending on the position on a site. At position 1 it measures  $15.6 \pm 4.6$  cm, and at position 3  $14.3 \pm 2.7$  cm. In the reference forest soil profiles, we measured the thickness of 26 Ah-horizons and 20 complete Bw-horizons. The Ah-horizons have an average thickness of  $9.7 \pm 4.6$  cm. The average Bw-horizon is  $29.1 \pm 8.6$  cm thick. 11 RCH sites show a slight redness of the top end of the Bwb-horizons mostly at position three, indication heat exposure (Hirsch et al. 2018b).

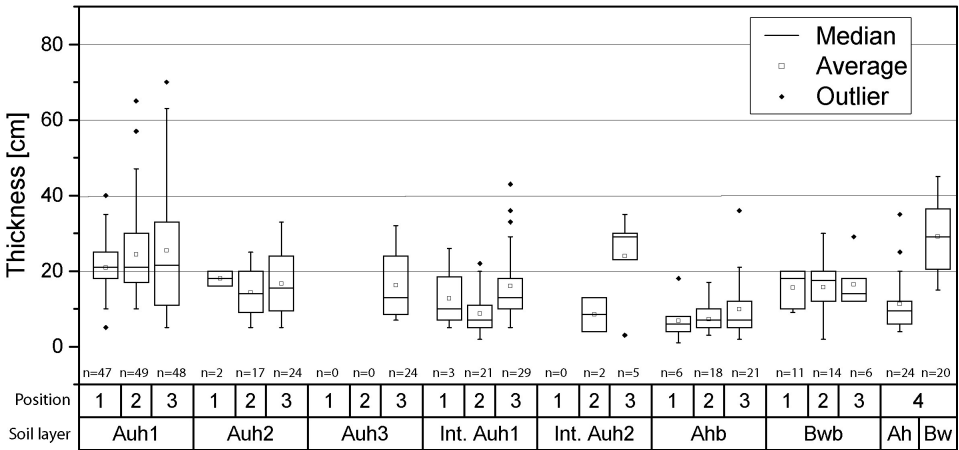


**Abbildung 5.6.** Box and whisker plots comparing average soil horizon thickness and variation at the four positions of a RCH site (1: RCH upslope end; 2: center of the RCH; 3: RCH downslope end; 4: reference forest soil).

### 5.5.4 Variation of bulk density

We detected significant differences in the bulk density of soil horizons by intra- and inter site comparison (Annex A.4). The lowest average bulk density is measured in the Auh1 at position 1 with  $0.66 \pm 0.10$  g per  $\text{cm}^3$ , with an increase to  $0.73 \pm 0.10$  g per  $\text{cm}^3$  on position 3 (Fig. 5.7).

There is a significant difference between position 3 and positions 1 and 2. Furthermore, the bulk density for the Auh1 differs significantly from most other soil horizons, including Auh2. Auh2 and Auh3 combined have an average bulk density of around  $0.82$  g per  $\text{cm}^3$ . An insufficient sample amount in Auh2 at position 1 and in Auh3 overall prevent more detailed analysis. The bulk density for int Auh1 and int Auh2 horizon ranges between  $0.86 \pm 0.07$  g per  $\text{cm}^3$  and  $0.92 \pm 0.17$  g per  $\text{cm}^3$ , with no significant difference between positions. Their bulk densities do not significantly differ in relation to other soil layers, except for Auh1 and

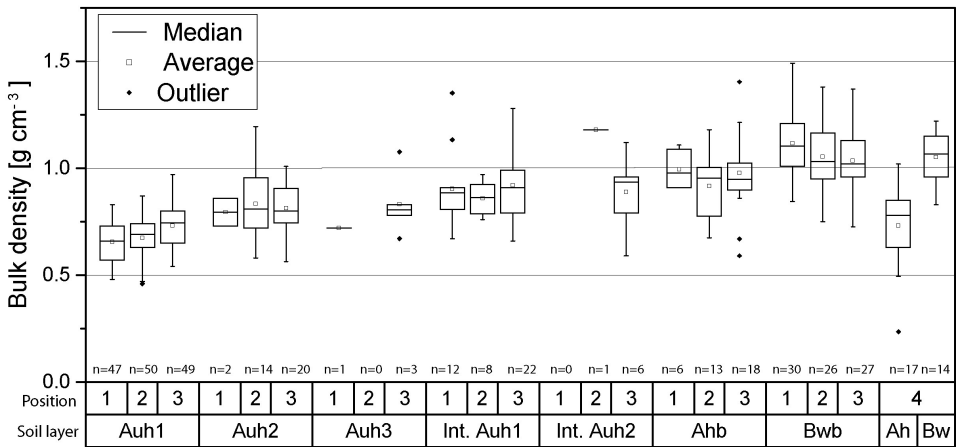


**Abbildung 5.7.** Box and whisker plots comparing soil horizon bulk density and its variation at the four positions of a RCH site (1: RCH upslope end; 2: center of the RCH; 3: RCH downslope end; 4: reference forest soil).

the Bwb-horizon. The Ahb- and Bwb-horizons bulk density ranges between  $0.92 \pm 0.14$  g per  $\text{cm}^3$  and  $1.12 \pm 0.15$  g per  $\text{cm}^3$  for each position, with mostly no significant difference between them. The Ahb-horizon is  $0.3$  g per  $\text{cm}^3$  higher than the reference forest soil Ah-horizon. No significant difference in bulk density can be detected between the buried- and the reference forest soil Bw-horizon.

## 5.6 Synthesis and discussion

### 5.6.1 Generalizing pedostratigraphy and RCH diameter

The following section gives the outline for the model we propose to generalize the pedostratigraphy of the analyzed RCH sites. A previous study has used one type of RCH architecture and only one variable (diameter) to generalize RCH geometry throughout a landscape in the North German Lowland (Bonhage et al. 2020a), which works well in flat terrain and with architectural homogeneous RCHs. We can show that in sloped terrain with multiple-layered RCH types, the slope inclination and the associated differences in pedostratigraphy must be regarded as well. The correlations we show of  $\Delta T$  and diameter with the slope inclination are moderately good, with some degree of heterogeneity that can be attributed to a number of factors. The first is that the colliers could have deliberately used site locations on natural breaks in the slope, which would allow for RCHs with a lower  $\Delta T$  on a steeper general slope. This factor is mentioned by Krebs et al. (2017) in their comprehensive research on site selection criteria for historical charcoal production. However, we could not

find evidence for the intentional usage of slope breaks to build platforms. Due to the potential significant disturbance of buried soil horizons, as seen by the sporadic occurrence of buried A-horizons and the difference in thickness of Bw- and buried Bw-horizons, as well as the potential reworking of Auh-layers during multiple usages of the platforms, a trigonometrical check of the “true” slope the site was built upon, based on the depth of the technogenic Auh-horizons lower boundaries, is unreliable. Second, the Auh-layers with low bulk densities and increased SOM content are potentially prone to compaction due to mechanical compression and the decomposition of SOM. This might be especially the case for the Auh2 layers which are often characterized by slightly sloped horizon boundaries, contrary to historic documents that usually note the importance of a horizontal platform for the construction of the charcoal hearth (e.g., see Warren et al. 2012). Third, the position of the hearth on a platform could be variable. Former studies suggest that each consecutive usage of a site resulted in a larger platform and therefore the possibility to build a larger hearth (Hirsch et al. 2018a, Raab et al. 2017), however, it is possible that a smaller hearth was built on top of a larger platform, and the substrate of the platform was used to cover the wood heap. If in this scenario, for example, substrate was mainly taken from the upslope end of the platform, then  $\Delta T$  would be skewed. Fourth, regarding the RCH diameters, heterogeneity can be caused by faulty or imprecise measurements in the field. Frequently it was not possible to identify clear boundaries of RCH platforms and the forest floor, in the slope parallel direction. Lastly, it must be considered that the colliers, although presumably using regionally appropriate construction techniques based on a principle of minimum energy expenditure, also varied the size of the constructed platforms depending on other factors, e.g., available workforce, intended reuse of sites, or wood availability. However, no further information is available on these aspects.

In light of these uncertainties, we propose a model based on RCH site slope inclination to account for the differences in the sites pedomorphology and diameter. The resulting model is based on two assumptions: First, RCH sites in the study area can be classified into the RCH on slopes and the flatland RCH class that has been reported for this and study areas in Europe. Second, the fact that sites on slopes are usually multilayered and sites on flatland are usually single layered and more or less constant in thickness holds true. We could show that both assumptions can be confirmed for our study area. The resulting two categories of idealized sites and their properties are listed in table 5.3.

The sites are categorized using a threshold value of 4° slope inclination based on results from section 5.5.2. The 4° slope inclination break in the data is crucial for the differentiation of

**Table 5.3.** Parameters for the model of idealized RCH sites suitable for calculating geometry, pedostratigraphical thicknesses and stocks of elements

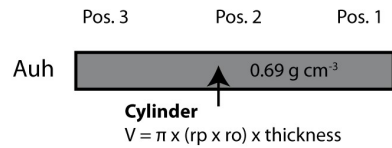
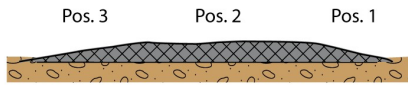
	Ideal class 1 RCH	Ideal class 2 RCH		
$\Delta T$ [%] at position 3	0	$\Delta T = 16.514 \cdot \text{slope} [^\circ] + 88.886$		
Site diameter	11.5 m	Diameter = $-0.2699 \cdot \text{slope} [^\circ] + 13.104$		
Auh-layer Thickness	Position 1,2,3	Position 1	Position 2	Position 3
Auh1	22.6 cm	20.9 cm	22.9 cm	23.6 cm
intermediate Auh	-	-	$(20.9 \cdot \Delta T \cdot 0.01/2) \cdot 0.17$	$(20.9 \cdot \Delta T \cdot 0.01) \cdot 0.27$
Auh2	-	-	$(20.9 \cdot \Delta T \cdot 0.01/2) \cdot 0.32$	$(20.9 \cdot \Delta T \cdot 0.01) \cdot 0.32$
Bulk density $\text{g cm}^{-3}$				
Auh1	$0.69 \text{ g cm}^{-3}$	$0.69 \text{ g cm}^{-3}$	$0.69 \text{ g cm}^{-3}$	$0.69 \text{ g cm}^{-3}$
intermediate Auh	-	-	$0.89 \text{ g cm}^{-3}$	$0.89 \text{ g cm}^{-3}$
Auh2	-	-	$0.82 \text{ g cm}^{-3}$	$0.82 \text{ g cm}^{-3}$

single- and multilayered sites when using the approach outlined in this study. The thickness of Auh-layers is not correlated with slope inclination, therefore an average horizon thickness can be assumed for all sites, which is potentially showcasing their artificial character and the lack of erosive slopewash. Colluvial deposits of substrate onto the RCH platform, whether caused by historic anthropogenic activity or natural processes, should potentially lead to a larger thickness of RCHs Auh-layers on steeper slopes.  $\Delta T$  for class 2 RCHs correlates significantly with slope and can therefore be calculated for site specific inclinations. Under the assumption that the technogenic horizons at position 1 consist solely of a first Auh-layer, all the other layer thicknesses at position 2 and 3 can be calculated. For position 2,  $\Delta T$  is thereby only half as thick as for position 3. The secondary Auh- and intermediate Auh-layer have an additional factor proportional to the summarized technogenic-layer thickness of position 2 and 3. At position 2 the summarized average thickness of the Auh1-, Auh2- and intermediate technogenic layers is 44.5 cm, whereof, based on their average thicknesses, 51 % are made up of the Auh-1 layer, 32 % of the Auh2-layer and 17 % of the intermediate Auh-layer. For position 3 it's a total of 54.3 cm, whereof 41 % are Auh1, 32 % are Auh2 and 27 % are intermediate Auh-layer substrate. The volume of the idealized soil-layer shapes can then be calculated as a cylinder for flat RCHs (Bonhage et al. 2020), and as the sum of three truncated cylinders for slope RCHs (Fig. 5.8). Stocks of elements can be calculated using the volume and average bulk densities for each soil-layer.

Bulk densities for Auh-layers in RCHs are typically lower than the reference forest soils, as is the case for the first Auh-layer in this study. This is most likely linked to the high charcoal content as reported for this area (Hirsch et al. 2018a) and similar sites in Pennsylvania (Mikan & Abrams 1995). The differences in Auh1 and Auh 2 and 3 bulk densities most likely originate from soil compaction affecting the latter two. Differences between position



### Generalization of RCHs on slopes $\leq 4^\circ$



### Generalization of RCHs on slopes $> 4^\circ$

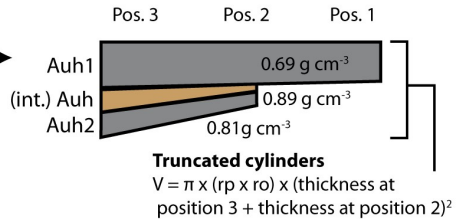
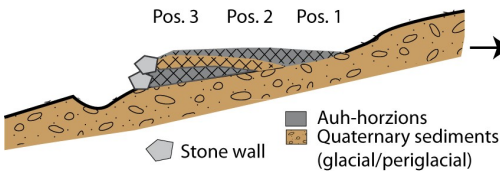


**Abbildung 5.8.** Model for class 1 and 2 RCH architecture with generalized layers and average bulk densities for each soil layer.

1 and 3 may be caused by differences in SOM content on the sites. Future studies need to address the SOM distribution on RCH sites to analyze this aspect. Comparing our results to other studies reveals some similarities, although for a detailed analysis differences in soil texture, SOM content and compaction should be taken into account. For mountainous regions published bulk densities ( $\text{g per cm}^3$ ) vary: 0.61 - 0.76 (Harz mountains, Germany, Borchard et al. 2014), 0.60 (Northern Italy, Criscuoli et al. 2014), 0.70 (Connecticut, USA, Hirsch et al. 2018a), 0.69 (Southern Belgium, Mastrodonato et al. 2019) and 0.65 - 1.04 (Southeastern Pennsylvania, Mikan & Abrams 1995). Higher bulk densities ( $\text{g per cm}^3$ ) in general are reported for sites in less sloped, non-mountainous terrain: 0.7-0.9 (Central Italy, Mastrodonato et al. 2018) and 0.94 - 1.28 (Northeast Germany, Schneider et al. 2020). To our best knowledge, this study is the first to report intra-site variations for multiple Auh and intermediate Auh-layers. Differences in bulk densities may impact physicochemical soil properties important for forest ecological functions (e.g., Buras et al. 2020, Gießelmann et al. 2019, Carrarie et al. 2018). Results from a year-long monitoring experiment show that the topmost 15 cm of technogenic RCH substrate has higher daily and seasonal temperature variations than adjacent forest soils, which is mainly due to the lower bulk density (Schneider et al. 2019). Increased preferential flow in technogenic RCH substrate under dry soil conditions can also lead to a high spatial and temporal variation of water contents. Because these effects are related to structural heterogeneity and hydrophobicity that results from high contents of charcoal and potentially by border effects from the boundary of technogenic- to forest soil substrate (Schneider et al. 2018a), they may be accentuated in multilayered sites.

### 5.6.2 Interregional comparison

A multilayered stratigraphy for RCHs on slopes is described here and in other sites studied in Connecticut, USA (Hirsch et al. 2018, Raab et al. 2017). Stolz & Grunert (2010) describe up to four Auh-layers and corresponding intermediate layers at RCH sites that span a century of charcoal production in Southwest Germany. No information about the stratigraphy is given for RCH platforms in the foreland of the Taunus Mountain Range, Germany, however, sites are described as having a ridge at the downslope end that can be multilayered, representing multiple harvesting phases of a site (Stolz et al. 2012). Schneider et al. (2018b) document sites on slopes in Bavaria, Germany with a striking similarity to sites in this study, i.e. there are multiple Auh- and intermediate Auh-layers that increase in thickness towards the downslope end of the platform. Williams (2019) describes RCHs in Clarion County, Pennsylvania as being single layered and on mean slopes of  $1.7^\circ$  with diameters comparable to our study area, including the somewhat oval shape of the platforms. A LiDAR-based survey of RCH sites in the Blue Mountain Region, Pennsylvania describes that most sites there can be found on slopes of  $8.5^\circ - 11.3^\circ$  Carter (2019), but unfortunately no further information about RCHs soil properties are known for that region. Otherwise, most studies of RCH sites have either no information on their stratigraphy, or describe them as single layered in case of flatland RCHs. The comprehensive comparison of Hirsch et al. (2020) documents several RCH architectural types that do not fundamentally vary for study sites in Central Europe and the US. This potentially indicates that our generalizations regarding the geometry of RCHs as a function of slope can be applied to other areas, since the dependency of layer thicknesses and slope should be the same. However, the lack of data regarding the detailed pedostratigraphy on different positions of RCH sites and its relation to slope for other regions limits the transferability for now, as it cannot be ruled out that multiple usages of RCH sites resulting in clearly discriminable Auh-layers is regionally specific. Furthermore, differences in geology or soil parent material can potentially limit the transferability of our results, e.g., as the presence of hard bedrock on the surface in the Ore Mountains (Saxony, Germany) required a different building technique for RCHs on slopes (Hirsch et al. 2020).

### 5.6.3 Significance for Geoarcheology and beyond

Overall, the study of RCHs in the geoarchaeological context is currently expanding in various disciplines. Advances regarding alteration of soil properties on RCHs and resulting effects on vegetation and fauna in relation to unaffected soils show the profound impact of this historical craft on present day forest ecosystems (e.g. Buras et al. 2020, Máliš et al.

2020) Furthermore, RCHs are potential sites of interest for the analysis of biochar application to soils and its degradation over time (e.g. Kerré et al. 2016, Borchard et al. 2014). Their charcoal content is a time capsule, potentially allowing the reconstruction of past forest compositions and historical wood exploitation. The geoarchaeological value of RCH sites originates not only from the possibility to more or less accurately date them by various techniques or by proxy of nearby historical industries, but also from the astonishing numbers in which they are mapped presently (e.g., Schneider et al. 2020, Rutkiewicz et al. 2019). With this study, we show that it is possible to generalize RCH site shape with a model, allowing the transformation of site specific results onto a landscape scale. This is an important step towards understanding and quantifying the legacy effects of historical landuse on forest ecosystems. In this context, future studies should further assess the detailed stratigraphical properties of complete RCH platforms in different regions of the USA and Central Europe. Furthermore, detailed RCH site mappings on a landscape scale and spatial analysis regarding their topographical position are required to apply and test the presented generalizations.

## 5.7 Summary and Conclusion

This study aims at producing a model to generalize the stratigraphical features of RCHs based on their position in the landscape. We show that RCH sites in western Connecticut exhibit two architectures with diameter and pedostratigraphies correlating to slope inclination. RCHs with an elevated circular construction type are characteristically located on flatter slopes ( $< 4^\circ$ ), while RCHs on levelled platforms are typically found on steeper slopes ( $> 4^\circ$ ). Sites on steeper slopes are usually multilayered and built up by multiple charcoal rich Auh-layers and intermediate Auh-layers consisting of reworked mineral substrate. Based on detailed study of 52 sites, we present a generalized model of RCH architecture that includes slope dependent variations of diameter, downslope Auh-layer thickness variation, individual Auh-layer thicknesses, and bulk density. The results show that an easy to implement model can be used to calculate soil volumes impacted by RCHs in landscapes affected by historical charcoal burning, and to assess effects on forest ecosystems such as additions to soil organic matter, changes in element stocks, and dynamics or modifications of soil biology or vegetation. Lack of data similar to that presented here regarding pedostratigraphy and soil physical properties limits further application into other regions where RCHs are common, such as Central Europe and mid-Atlantic USA. Future challenges include the assessment of the transferability of our generalizations into other regions, which depends on detailed field-based descriptions of the sites pedostratigraphy and its relation to the slope

inclination. Furthermore, RCH site mappings on a landscape scale and knowledge about their soil properties are necessary to apply the presented generalizations.

## 5.8 Acknowledgements

We want to thank Sally Donovan for supporting our field work. Furthermore, we like to thank three anonymous reviewers for comments that helped to significantly improve this manuscript. This research was supported by the German Research Foundation (DFG) under grant number RA 931/8-1. The funding source had no involvement in the study beside financial support.

# 6 Vertical SOC distribution and aromatic carbon in centuries old charcoal-rich Technosols

This chapter is published as: Bonhage, A., Raab, T., Schneider, Fischer, T., Ramezany, S., Ouimet, W., Raab, A. & Hirsch, F. (2022): Vertical SOC distribution and aromatic carbon in centuries old charcoal-rich Technosols. *European Journal of Soil Science*, 73, 4. DOI: 10.1111/ejss.13293 The Annex contains additional, previously unpublished material regarding samples TOC and BPCA-C (measured and predicted) concentrations and pH values.

## 6.1 Abstract

Charcoal-rich Technosols on century-old relict charcoal hearths (RCHs) are the subject of ongoing research regarding potential legacy effects that result from historic charcoal production and subsequent charcoal amendments on forest soil properties and forest ecosystems today. RCHs consist mostly of Auh horizons that are substantially enriched in soil organic carbon (SOC), of which the largest part seems to be of pyrogenic origin (PyC). However, the reported range of SOC and PyC contents in RCH soil also suggests that they are enriched in nonpyrogenic SOC. RCH soils are discussed as potential benchmarks for the long-term influence of biochar amendment and the post-wildfire influences on soil properties. In this study, we utilize a large soil sample dataset ( $n = 1245$ ) from 52 RCH sites in north-western Connecticut, USA, to quantify soil organic carbon contents by total element analysis. The contents of condensed highly aromatic carbon as a proxy for black carbon (BC) were predicted by using a modified benzene polycarboxylated acid (BPCA) marker method in combination with diffuse reflectance infrared Fourier transform spectroscopy-based partial least square regression ( $R^2 = 0.89$ ). A high vertical spatial sampling resolution allows the identification of SOM enrichment and translocation processes. The results show

an average 75 % and 1862 % increase in TOC and BPCA-derived carbon respectively for technogenic Auh horizons compared to reference soils. In addition to an increase in aromatic properties, increased carboxylic properties of the RCH SOC suggest self-humification effects of degrading charcoal and thereby the continuing formation of leachable aromatic carbon compounds, which could have effects on buried soils pedogenic processes. Indeed, we can show BPCA-derived carbon concentrations in intermediate technogenic Cu horizons and buried top/subsoils that suggest vertical translocation of highly aromatic carbon originating in RCH Auh horizons. Topmost Auh horizons show a gradual decrease in TOC contents with increasing depth, suggesting accumulation of recent, non-pyrogenic SOM. Lower aliphatic absorptions in RCH soil spectra suggest different SOM turnover dynamics compared to reference soils. Furthermore, studied RCH soils feature additional TOC enrichment, which cannot be fully explained as of now.

## 6.2 Aims

To better understand the soil carbon dynamics of RCH soils, we utilize the Benzene polycarboxylic acid (BPCA) molecular marker method to gain knowledge about the concentration and vertical distribution of aromatic carbon (BPCA-C). BPCA molecular markers are often used as a proxy to determine pyrogenic carbon concentrations in soils. However, current discussions point out that BPCA markers are specific not only for pyrogenic carbon but also for highly aromatic carbon compounds in general (Gerke 2019, Gerke 2018). The specific aims of the study are:

- To determine TOC and BPCA-C concentrations in a large RCH- and reference soil sample set (n = 1245) using total element analysis and FTIR based chemometric prediction modelling
- To compare TOC and BPCA-C concentrations of RCH-, buried- and reference soil horizons
- To describe the vertical distribution of carbon fractions in RCH soil horizons in high resolution and thereby to study potential redistribution processes and initial pedogenesis in carbon-rich anthropogenic substrates

## 6.3 Methodology

### 6.3.1 Sample preparation and total carbon analysis

Samples were sieved (< 2 mm) and ground to a homogeneous fine powder using a ball mill grinder (Retsch® PM400). Total element carbon and nitrogen analysis was conducted on all samples (n = 1216) using an Elementar® vario Max Cube. A subset of samples (BPCA<sub>quant</sub>, n = 100) was used for quantifying BPCA-derived carbon. BPCA<sub>quant</sub> consists of 52 RCH soil samples (Auh and Cu horizons) and 48 reference soil samples (buried A- and B- and non-RCH-affected A- and B-horizons) taken from representative soil profiles. In total, samples from 8 sites were included in the BPCA<sub>quant</sub> dataset, and thereby, no sample from the same depth of every soil profile was included more than once. As we expect a high degree of heterogeneity in the RCH soil, we do not deem pseudo replication to be an issue. To assess the significance of vertical changes of TOC and PyC concentrations we used the nonparametric comparative Mann–Whitney U tests (SPSS 14, IBM®). We interpreted P values following Muff et al. 2021. Soil acidity (pH) was measured in 0.01 M CaCl<sub>2</sub> (1:2.5 w:w).

### 6.3.2 Benzene polycarboxylic acid (BPCA) determination

We applied the benzene polycarboxylic acid (BPCA) molecular marker method originally proposed by Glaser et al. (1998) and modified by Llorente et al. (2017), further modifying the method to allow for the use of microwave pressure digestion. The method aims at cleaving and oxidizing benzene rings using nitric acid as well as high temperature and pressure, resulting in aromatic carboxylic acids that can be qualitatively and quantitatively analysed (Chang et al. 2018). For this, 0.5 g of sample material was digested with 10 ml of 4 M trifluoroacetic acid (TFA) (Acros®, CAS: 76-05-1) at 130°C for 30 minutes in a MARS 6 microwave digestion system (CEM®). The solid residue was then washed three times by repeated centrifugation at 5500 rpm for 10 minutes, the supernatant was discarded, and fresh distilled water was added each time while stirring. The original protocol used glass fibre filters to separate and wash the solid phase; however, we found the loss of sample material caused by adhesion to the filter to be too high. The washed and dried solid residue was then microwave pressure digested with 6 ml of 65 % HNO<sub>3</sub> at 200°C for 30 minutes. The content of the digestion vessels was then filtered using ashless cellulose filters (Whatman® #41, CAT: 1441-110) and washed several times by rinsing with distilled water. The solid phase is discarded. The BPCA-containing solution was then dried at 60°C and rewetted repeatedly to remove nitric acid residues. The solid residue was then weighed, and its total

carbon content was measured by dry combustion. The results are reported as uncorrected BPCA-C concentrations and corrected black carbon (BC) concentrations using a correction factor of 2.27 (Brodowski et al. 2005). The results of the procedure were checked by FTIR spectral analysis of dried residuals from some RCH samples, which confirmed the presence of BPCA-relevant absorption bands. The spectra (Annex Fig. A3) show CH bendings and deformations of m, o, p-disubstituted aromatics from 1039  $\text{cm}^{-1}$  towards 825  $\text{cm}^{-1}$  and lower wavenumbers, aromatic ring C=C stretching at 1481  $\text{cm}^{-1}$ , strong C=O stretching at 1668  $\text{cm}^{-1}$  and a broad OH stretching at 3500  $\text{cm}^{-1}$  that presumably result from residual moisture in the sample material.

### 6.3.3 PLSR-based BPCA prediction

FTIR DRIFT spectra of undiluted soil samples were acquired with a Bruker® Optics (Germany) TENSOR 27 equipped with a DRIFT module, liquid N<sub>2</sub>-cooled Mercury Cadmium Telluride (MCT) detector and the high-throughput screening extension (HTS-XT) microplate reader. The soil spectra were recorded from 4000–400  $\text{cm}^{-1}$  and averaged over 40 scans at a 4  $\text{cm}^{-1}$  resolution and 10 kHz scan speed. Spectral processing and explorative analysis were conducted using Bruker® OPUS software and the ChemoSpec R package. Spectral bands were assigned using the Wiley's® KnowItAll Informatics System 2020 database or based on literature research. All spectra were baseline corrected and cut at 1300  $\text{cm}^{-1}$  to avoid silica band interferences (Robertson et al. 2015). Partial least squares regression (PLSR) and cross validation on the complete dataset were conducted using the OPUS software package. The software's optimization algorithm was used to find the optimal spectral preprocessing method and the most meaningful wavenumber regions to include in the PLSR analysis.

## 6.4 Results

### 6.4.1 BPCA<sub>quant</sub> soil properties

Table 6.1 lists the specific properties of the BPCAquant soil samples. The TOC concentrations of the BPCAquant Auh horizons are approximately twice as high as those of the reference Ah horizons and nearly reach an average of 100  $\text{g kg}^{-1}$ . BC makes up on average 83 % of the TOC concentration in Auh horizons, in contrast to 7 % for reference soil Ah horizons. The Auh horizons therefore have an average 75 % increase in TOC and an 1862 % increase in BC concentrations compared to the adjacent reference topsoil. The Cu horizons have higher TOC and BC concentrations and BC-TOC ratios than all other mineral horizons. The Bw, Bwb and C horizons have comparably low TOC and BC concentrations,



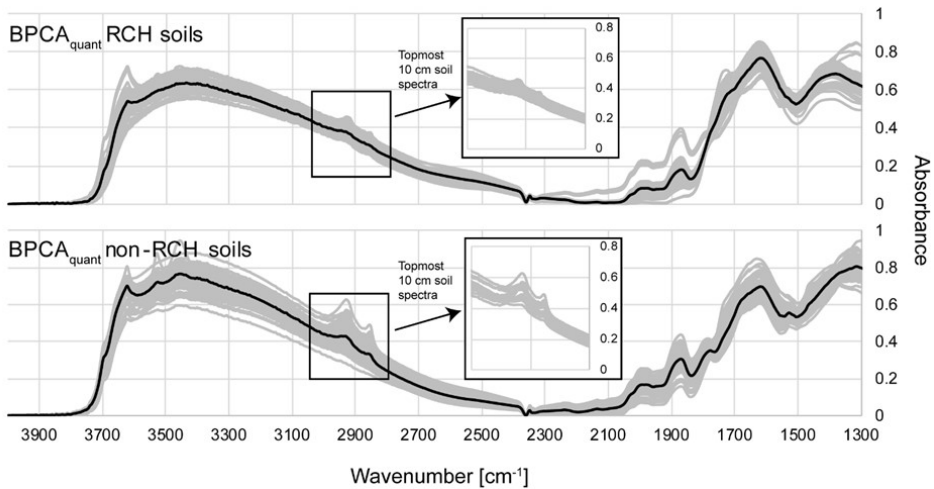
resulting in BC-TOC ratios of approximately 30 %. Ahb horizons, however, have a higher ratio of 54 %, constituting a 137 % increase in BC compared to reference Ah horizons, while their TOC contents are 67 % lower.

**Table 6.1.** Total concentrations of nitrogen (TN), organic carbon (TOC), BPCA-derived carbon (BPCA-C) and black carbon (BC) grouped by soil horizon (mean  $\pm$  standard deviation) for BPCAquant samples. Soil acidity (pH) is given as a range and average. The ratio gives the BC to TOC ratio.

	Soil horizon	pH in CaCl <sub>2</sub>	n	TN	TOC	BPCA-C	BC	Ratio
				[g kg <sup>-1</sup> ]				
RCH soils	Auh	3.5-4.8 (4.2)	42	2.4 $\pm$ 0.9	94.6 $\pm$ 48.1	34.6 $\pm$ 21.8	78.5 $\pm$ 49.4	83
	Cu	4.4-5.0 (4.7)	8	0.9 $\pm$ 0.3	38.4 $\pm$ 24.7	11.3 $\pm$ 8.0	25.6 $\pm$ 18.1	66
	Ahb	4.6-4.8 (4.7)	5	0.5 $\pm$ 0.1	17.4 $\pm$ 4.8	4.2 $\pm$ 2.4	9.5 $\pm$ 5.4	54
Non-RCH soils	Ah	3.6-4.7 (4.1)	11	2.1 $\pm$ 0.8	53.8 $\pm$ 29.0	1.8 $\pm$ 1.3	4.0 $\pm$ 2.9	7
	Bwb	4.3-5.1 (4.8)	10	0.6 $\pm$ 0.2	16.8 $\pm$ 5.4	2.7 $\pm$ 1.1	5.1 $\pm$ 2.4	30
	Bw	4.2-4.9 (4.5)	23	0.7 $\pm$ 0.5	13.3 $\pm$ 9.4	2.0 $\pm$ 1.9	4.5 $\pm$ 4.3	33
	C	4.9	7	0.5 $\pm$ 0.2	8.6 $\pm$ 3.7	1.1 $\pm$ 0.5	2.4 $\pm$ 1.1	27

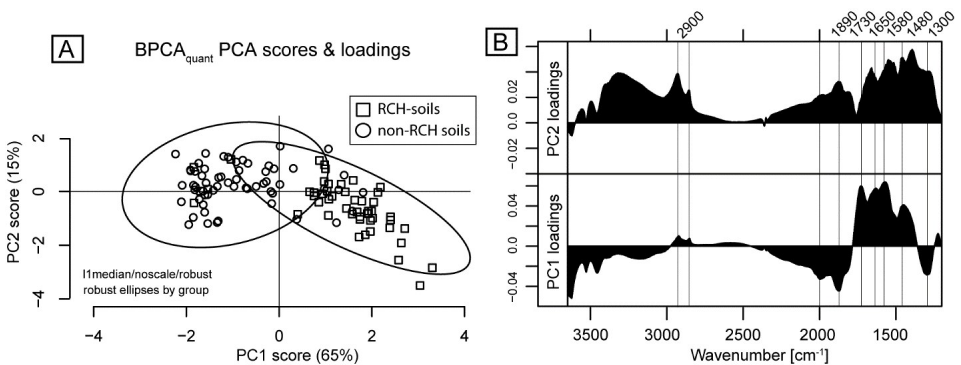
#### 6.4.2 BPCA<sub>quant</sub> spectral properties

Figure 6.1 gives an overview of the BPCAquant soil sample spectra. A principle component analysis of untreated BPCAquant spectra shows a separation of scores into two clusters that correspond to the two soil types: RCH soils have mainly positive scores alongside principal component (PC) 1 and negative scores alongside PC 2, while for non-RCH soils, the order is reversed (Fig. 6.2A). Figure 6.2B shows the corresponding PCA loading values, which can be seen as the weights associated with each principle component, giving an idea about which wavenumber regions are influential for the difference in score values. The main separator along PC 1 are negative loadings for wavenumber regions associated with mineral soil components such as clay minerals (approximately 3500 cm<sup>-1</sup>), SiO<sub>2</sub> overtones (Volkov et al. 2021) (peaking at 1890 cm<sup>-1</sup>), C-O, CH, CH<sub>2</sub> vibrations in alkenes and phenolic groups (Hobley et al. 2014) (approximately 1300 cm<sup>-1</sup>) and positive loadings for the region associated with aromatic carbon C=C and carboxyl C=O (1750 cm<sup>-1</sup> to 1400 cm<sup>-1</sup>). Loadings for PC 2 are mainly positive, and the main differences compared to PC 1 are the stronger influence of aliphatic CH and CH<sub>2</sub> absorptions at approximately 2900 cm<sup>-1</sup> and the absence of any influence by carboxylate C=O absorptions at 1740 cm<sup>-1</sup>. Coincidentally, aliphatic CH absorptions at approximately 2900 cm<sup>-1</sup> are notably less intense in RCH soils (Fig. 6.2). Furthermore, the loadings at absorptions related to C-O, CH, CH<sub>2</sub> vibrations in alkenes and phenolic groups (1300 cm<sup>-1</sup>) are positive in PC 2. The grouping of RCH and non-RCH soil spectra can further be seen in a dendrogram for an exemplary subset of 20 spectra (Annex Fig. A4), where most technogenic and reference soil spectra belong to se-



**Abbildung 6.1.** Diffuse reflectance spectra of BPCAquant RCH soils (Auh, Cu Horizons) and non-RCH soils (Ahh, Bwb, Ah, Bw Horizons). The black line shows the averaged spectra. Close ups of the aliphatic CH absorption wavenumber region exclusively show spectra of soil samples taken from the top 10 cm of a soil profile.

parate groups. However, the Cu horizons TOC content is especially heterogeneous, making some samples more similar to reference spectra, presumably caused by their very low TOC content. We created separate PLSR quantification models for carbon rich Auh and Cu horizons (RCH soils) and reference soils and Cu horizons with low carbon contents (non-RCH soils) to improve the prediction accuracy of BPCA-C concentrations. Cu horizons were included in the calibration dataset of a prediction model based on a threshold of their average TOC content (Table 6.1), where samples with  $< 38.4 \text{ g TOC kg}^{-1}$  are assigned to the non-RCH soil group.



**Abbildung 6.2.** A) Principal component analysis (PCA) score- and B) loading plots for untreated BPCAquant soil sample spectra. RCH soil: Auh & Cu horizons; non-RCH soil: Ahh, Bwb, Ah, Bw and C horizons.

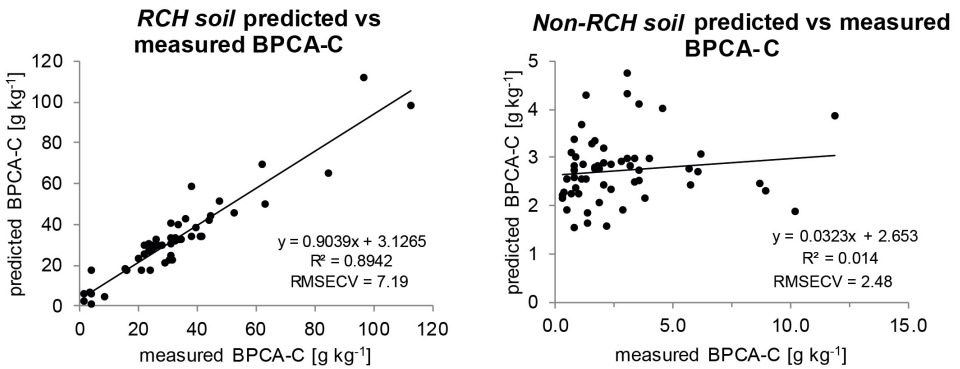


**Abbildung 6.3.** PLSR BPCA-C prediction model evaluation using cross-validation for RCH soil (Auh & Cu horizons) and non-RCH soil (Ahb, Bwb, Ah, Bw, C horizons) BPACquant spectra.

### 6.4.3 PLSR model validation

PLSR can predict BPCA-C concentrations in RCH soils very well ( $r^2 = 0.89$ ); however, it fails to predict concentrations for non-RCH soils ( $r^2 = 0.01$ ) (Fig. 6.3). The reason for this being the very low TOC and BC concentrations in non-RCH soils, which fail to produce a strong enough signal in the spectra. The PLSR regression coefficients for the RCH soil model (Fig. 6.4) suggest that higher BPCA-C concentrations coincide with higher carboxyl C=O absorptions at  $1732\text{ cm}^{-1}$ , aromatic C=C absorptions from ionized carboxyl ( $\text{COO}^-$ ) groups or C=O absorptions at  $1616\text{ cm}^{-1}$  (Rebollo et al. 2008, Volkoy et al. 2021), aromatic C-H vibrations at  $3000\text{--}3100\text{ cm}^{-1}$  and lower absorptions at the aliphatic CH region at  $2800\text{--}3000\text{ cm}^{-1}$  and aromatic C=C stretches associated with lignin at  $1518\text{ cm}^{-1}$  (White et al. 2011, Ferrari et al. 2011, Volkov et al. 2021). Thereby, the coefficients show that BPCA-C concentrations correlate mainly positive with wavenumber regions associated with charcoal contents in soils. Furthermore, inorganic absorptions peaking at  $3622\text{ cm}^{-1}$  are positively correlated with higher BPCA-C concentrations.

Although we separated Cu horizons based on their TOC content for the initial prediction model building, we decided to refrain from this for the further prediction of BPCA-C values, as it would otherwise omit a lot of Cu-horizon spectra from the analysis. This seemed valid, because the measured BPCA-C concentrations for Cu horizons (Tab. 6.1) fall within the calibration range of the RCH soil model.

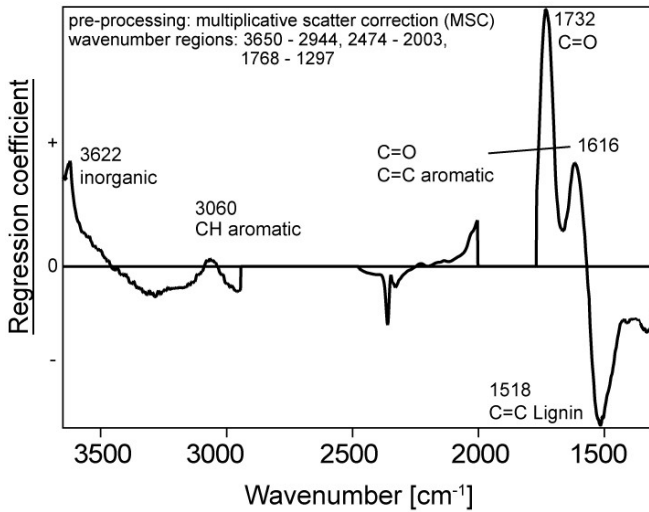


**Abbildung 6.4.** PLSR regression coefficient for RCH soil spectra in the BPCAquant dataset

#### 6.4.4 Variation in soil carbon concentration by horizon

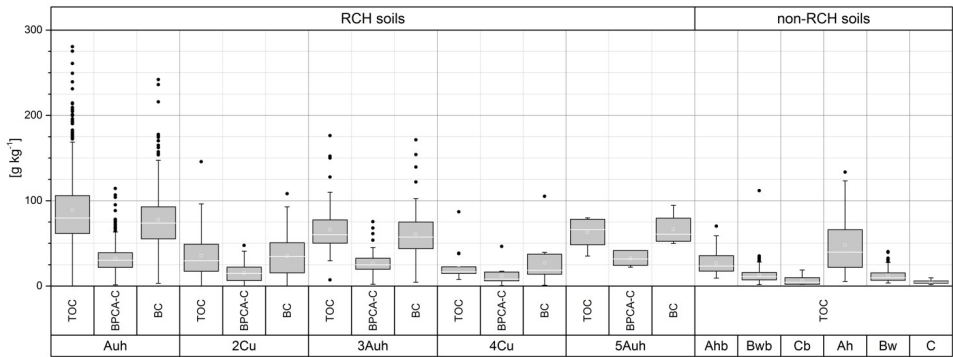


**Abbildung 6.5.** Total carbon (TOC), predicted BPCA-derived carbon (BPCA-C) and calculated black carbon (BC) concentrations for RCH soils and non-RCH soil horizons

An overview of the TOC and predicted BPCA-C and BC concentrations for the complete dataset sorted by soil horizons is given in Figure 6.5, with descriptive statistical values of all soil chemical parameters given in Table 6.2. The TOC concentration of the Auh horizons is highest in the first Auh and decreases in 3Auh and 5Auh. The Auh horizon has similar BC to TOC ratios as seen for the BPCAquant dataset. Notably, the ratio is increasing for deeper Auh horizons. Outliers with exceptionally high TOC and BC concentrations (up to

**Table 6.2.** Concentrations of measured nitrogen (TN), carbon (TOC), predicted BPCA-derived carbon (BPCA-C) and calculated black carbon (BC) concentrations grouped by soil horizon (mean  $\pm$  standard deviation) for all samples. The ratio gives the BPCA-C and BC to TOC ratio.

Horizon	n	TN	TOC		BC	Ratio		Avg. C:N	
				BPCA-C		BPCA-C	BC		
				[g kg <sup>-1</sup> ]					
RCH soils	Auh	600	2.4 $\pm$ 1.0	89.4 $\pm$ 41.0	32.0 $\pm$ 14.9	72.6 $\pm$ 33.8	0.35	0.85	37.2
	2Cu	131	1.0 $\pm$ 0.5	36.1 $\pm$ 23.7	15.1 $\pm$ 9.8	34.2 $\pm$ 22.2	0.41	0.94	36.1
	3Auh	100	1.5 $\pm$ 0.4	66.7 $\pm$ 26.9	26.7 $\pm$ 13.1	60.6 $\pm$ 29.7	0.40	0.90	44.4
	4Cu	15	0.7 $\pm$ 0.2	27.0 $\pm$ 19.8	11.9 $\pm$ 12.0	27.0 $\pm$ 27.2	0.44	1.00	38.5
	5Auh	12	1.3 $\pm$ 0.3	57.8 $\pm$ 14.2	29.2 $\pm$ 6.6	66.2 $\pm$ 14.9	0.50	1.14	44.4
Non-RCH soils	Ah	55	2.5 $\pm$ 2.6	50.5 $\pm$ 43.5	n.a.				20.2
	Ahb	67	1.0 $\pm$ 0.5	26.4 $\pm$ 12.5	n.a.				26.4
	Bw	65	0.7 $\pm$ 0.3	13.2 $\pm$ 8.8	n.a.				18.5
	Bwb	159	0.5 $\pm$ 0.3	12.6 $\pm$ 7.6	n.a.				25.2
	C	27	0.3 $\pm$ 0.1	5.6 $\pm$ 3.5	n.a.				18.6
	Cb	14	0.3 $\pm$ 0.1	7.1 $\pm$ 5.1	n.a.				23.6

281 g kg<sup>-1</sup> and 256 g kg<sup>-1</sup>, respectively) can be explained by large contents of charcoal in the respective samples. The 2Cu and 4Cu horizon TOC concentrations are higher than those of reference soils B and C-horizons, suggesting a carbon admixture to the mineral substrate caused by the hearths operation. Furthermore, the BC to TOC ratios for the 2Cu and 4Cu horizons are higher than those for the BPCA<sub>quant</sub> dataset. Buried A-horizons and B-horizons feature a lower average TOC concentration than unburied reference soils. The C:N ratios of RCH soils are approximately twice as high as those of non-RCH soils.

#### 6.4.5 Vertical distribution of TOC and BPCA-C in RCH soil horizons

The averaged vertical TOC and BPCA-C distribution can only be analysed for Auh, 2Cu and 3Auh horizons, based on the sufficient amount of samples. Depth information (Fig. 6.6) refers to the upper boundary of the horizon, not the ground surface. The Auh horizons contain the highest concentrations of TOC and BPCA-C in the topmost 5 cm, with a decreasing trend until a depth of 20 cm, where they lose 44 % of TOC and 31 % of BPCA-C. For the first 15 cm to 20 cm depth, there is moderate to strong evidence for a systematic difference between BPCA-C and TOC concentrations at each depth increment ( $P \leq 0.1$  and  $P < 0.01$ ). The average BPCA-C:TOC and C:N ratios increase from 32 % to 40 % and from 36 % to 40 %, respectively, in the top 30 cm before slightly dropping and fluctuating with increasing depth. The 2Cu-horizon carbon concentrations decrease up to a depth of 25 cm, where they lose 47 % of the TOC content and 63 % of the BPCA-C concentration. However, evidence for the first weak to moderate systematic difference between increments is only given when comparing carbon concentrations between depths of 5 cm and 20 cm ( $P = 0.10$  and  $P = 0.06$ ). The BPCA-C:TOC ratio decreases from 38 % to 25 % in the first 20 cm,

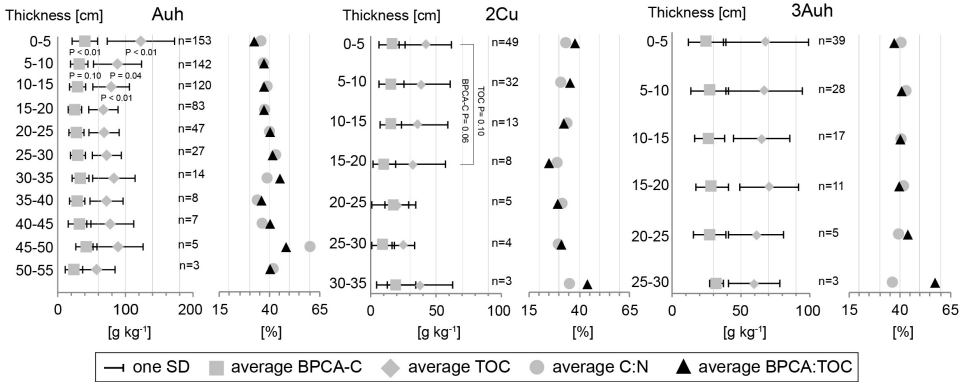


**Abbildung 6.6.** Vertical distribution of total carbon and BC carbon concentrations in RCH soil horizons. P values from Mann–Whitney U testing are given as a measure for evidence of systematic differences between sampling increments ( $P > 0.10$  not shown).

while there is no change in the C:N ratio. The 3AuH horizon carbon concentrations show no vertical trend. The BPCA:C and C:N ratios remain constant until a depth of 20 cm, where they start to diverge. However, the amount of data is very small for depths of 25 cm and 30 cm.

## 6.5 Discussion

### 6.5.1 Spectra-derived soil properties

Analysing the differences in RCH- and non-RCH soil spectra shows two main results: an interaction of mineral and organic absorption intensities and the increased intensity of carboxyl- and aromatic absorptions in RCH soils, as also described by several studies before. We hypothesize that the difference in spectral properties of RCH and non-RCH soils from the BPCAquant dataset mainly results from the large difference in the TOC quantity and quality of the soil samples. PC 1 (Fig. 6.4) potentially shows the effect that higher absorption intensities from organic soil constituents can have on mineral component absorption intensities, namely, that they lower the latter in the spectra. Conversely, lower absorption intensities related to TOC can result in more pronounced mineral absorptions. This effect can be seen in the spectra (Fig. 6.3), where mineral absorptions at approximately  $1900 \text{ cm}^{-1}$  are higher in intensity for non-RCH soils than for RCH soils. PC 1 (Fig. 6.4) shows the importance of wavenumber regions associated with carboxyl C=O and aromatic C=C absorptions, which are higher in intensity in RCH soil spectra (Fig. 6.4). This result is further shown by the PLSR regression coefficients for RCH soils (Fig. 6.6), which are mainly

sensitive to carboxyl and ionized carboxyl  $\text{COO}^-$  groups. The positive correlation coefficients of absorptions in the phyllosilicate region ( $3622\text{ cm}^{-1}$ ) (Fig. 6.6) cannot be reasonably explained as of now, but could very well be a pseudo-predictor caused by the large amount of variables used by the PLSR model.

The spectral properties suggest an ongoing weathering of charcoal in RCH soils. An increase in carboxylic properties has been described for RCH soils (Hardy et al. 2019) and for incubation experiments where fresh and historic charcoal pieces (19th century) were artificially aged for several months, resulting in an increase in carboxylic groups by the oxidation of carbon compounds on the charcoal surface and interior (Cheng et al. 2014, Cheng et al. 2008). This effect can be increased by introducing noncharcoal biomass to the process (Cheng et al. 2006). Cohen-Ofri et al. (2006) termed this effect the “selfhumification” of charcoal, which is further discussed by Ascough et al. 2011. They describe the presence of highly carboxylated aromatic humic acids in aged charcoal, which originate, at least in part, from the weathering of the charcoal itself and not from exogenous sources. Furthermore, the less intense aliphatic CH absorptions at approximately  $2900\text{ cm}^{-1}$  in RCH soils suggest a lower content of relatively labile carbon compounds compared to reference soils. Similar findings are discussed by Abdelrahman et al. 2018, who reported stronger signals for aliphatic carbon from long chained molecules (e.g., waxes and fatty acids) in NMR spectra of forest soils compared to some RCH soils. We suggest that this could be a direct result of the charcoal burning process that acts as a reset point for any noncharcoal carbon compounds in the affected soils, since they are most likely charred during the final burning on a site. Compared to the reference soils, the RCH sites then had a relatively short time to accumulate fresh SOM (approximately 120 to 250 years, Raab et al. 2017), although most SOM has a decadal residence time (Schmidt et al. 2011). Furthermore, other factors that could influence the input and degradation rate of fresh biomass cannot be ruled out, such as changes in vegetation and microbial composition and growth at RCH sites.

### 6.5.2 TOC enrichment of RCH soil

The ratios of PyC to TOC in RCH soils that have been observed in other studies vary strongly, and the variety of methods used to quantify pyrogenic/highly aromatic carbon makes only for a superficial comparison (Table 6.3). Additional RCH soil OC contents in RCH soils have been discussed by several studies, although the majority of them studied RCH sites under long term agricultural use (Burgeon et al. 2020, Kerré et al. 2016, Hernandez-Soriano et al. 2016).

**Table 6.3.** Average total organic carbon (TOC) and pyrogenic/highly aromatic carbon (PyC) concentrations for relict charcoal hearth (RCH) topsoil in temperate forests. The ratio gives the PyC /Charcoal-derived C to TOC ratio.

Study	Methodology	TOC	PyC	Ratio	Additional OC
		[g kg <sup>-1</sup> ]			
Mastrolonardo et al. 2018	Weak nitric acid digestion	129	56	0.43	57 %
Mastrolonardo et al. 2019	Walkley-Black digestion	131	65	0.49	51 %
Hardy et al. 2019	Differential scanning calorimetry	85	53	0.62	38 %
Hardy & Dufey 2017	Walkley-Black digestion	106	82	0.77	23 %
This study	BPCA (no factor)	89	32	0.35	65 %
This study	BPCA (x2.27)	89	72	0.80	20 %

The effect is attributed to sorption and consequent sequestration of dissolved organic matter (DOM) on charcoal surfaces (Borchard et al. 2014), whereby a preferential accumulation of hydrophilic, humic-like compounds can take place (Kerré et al. 2016, Heitkötter & Marschner 2015). Furthermore, charcoal-derived SOM seems to be stabilized through organo-mineral associations in RCH soils (Burgeon et al. 2020), as has been similarly reported for comparably younger biochar-amended soils (Tilston et al. 2016, Singh & Cowie 2014, Zimmermann et al. 2011). Other studies discuss the absorption of potentially more labile, nonaromatic SOM on charcoal surfaces through vertical transport by DOM (e.g., Wagner et al. 2018). Since the additions shown in Table 5 are rather large in some cases, other origins should be discussed as well.

Most obviously, methodological uncertainties could be the reason, which could be increased by the specific nature of OC and PyC in RCH. Different quantification methods for PyC can target different parts of the PyC degradation continuum, and as already discussed, RCH substrate seems to be very heterogeneous in its OC and PyC composition. Besides chemical weathering of charcoal, factors influencing its actual production have to be considered. The temperatures within and below charcoal hearths at production have been detected within a relatively wide range (Powell et al. 2021, Dupin et al. 2019), which can result in incomplete charring of SOM and different degrees of aromaticity (Ascough et al. 2020, Abney et al. 2019). Pyrogenic materials with low-order aromaticity caused by degradation (ageing) or lower pyrolysis temperatures at production have been shown to be susceptible to oxidation in laboratory environments (Ascough et al. 2020), i.e. they could be overlooked by some PyC quantification methods. Furthermore, the presence and quantity of noncharcoal-related products that potentially remain in the soil as a result of RCH burnings (such as resins, tar and potash) and their resistance to commonly used PyC quantification methods



have not yet been studied. Finally, the material that was used to cover the hearth during operation is part of the Auh horizons today and contributes to their TOC. It was most likely a mixture of grass/moss sods, twigs and mineral/topsoil from the adjacent areas and could thereby feature high non-PyC concentrations from the very start.

For the BC quantification method of this study, sources of uncertainty have to be considered. The BPCA-derived carbon in this study can originate from charcoal, aromatic products of the charcoal “self-humification” process and noncharcoal-related aromatic SOM. BPCA markers are used to characterize and quantify organic matrices containing aromatic carbon by splitting up groups of benzene rings and oxidizing them, thereby also including nonpyrogenic aromatic carbon (Chang et al. 2018, Kappenberg et al. 2016, Zimmerman & Mitra 2017). Therefore, the method is reportedly underestimating pyrogenic carbon contents, even for pure charcoal samples, for which ratios of 15 % to 26 % BPCA-C to TOC have been documented (Schneider et al. 2010, Hammes et al. 2007). Correction factors have been established to convert BPCA-derived carbon into pyrogenic carbon, with a factor of 2.27 given as a conservative estimate for estimating black carbon concentrations in soils (Brodowski et al. 2005). Schneider et al. (2010) discuss that any application of conversion factors adds a potential large source of error in the quantification and that the best solution is to just report measured concentrations as they are. However, interpreting our results in terms of ratios without a correction factor would result in a large difference between TOC and BPCA-C concentrations that could not be explained satisfactorily. Nevertheless, problems arise with factor usage since ratios using corrected BPCA-C often surpass 100 % (e.g., Table 6.3), demonstrating that a fixed correction factor is not universally applicable.

For the results of this study, subtracting BPCA-C from TOC concentrations for the first Auh horizon results in a TOC content similar to that of the reference soil Ah horizon (approximately 50 g TOC kg<sup>-1</sup>), which suggests that the Auh horizon has started to accumulate fresh SOM. The higher ratios in the 3Auh and 5Auh horizons could be explained by a much lower or missing input rate of fresh SOM and by a higher degree of aromaticity caused by an older age of these horizons compared to the topmost Auh. The same reasoning applies when looking at BC instead of BPCA-C ratios, despite these ratios being much larger, e.g., non-BC carbon in the topmost Auh horizons now reaches approximately 17 g TOC kg<sup>-1</sup> instead of 50 g TOC kg<sup>-1</sup>. This could also explain the lower absorption intensities of aliphatic carbon spectral features compared to reference Ah horizons. BC ratios of nearly 100 % (and above) for the 2Cu, 4Cu and 5Auh horizons suggest that the TOC in deeper horizons is more or less completely made up of highly aromatic carbon.

In summary, the ubiquitously observed increase in TOC contents compared to reference soils is either caused by methodological sources of uncertainty in quantifying PyC, by the specific composition of RCH OC, or by postburn accumulation of SOM; but likely a combination of all factors.

### 6.5.3 Vertical distribution of carbon

Potential vertical translocation processes can best be assessed from the vertical distribution of carbon in the 2Cu horizon (Fig. 6.6) since it consists of relocated mineral substrate and therefore, a homogeneous carbon distribution at the time of its deposition can be assumed. Although, buried topsoils also show higher ratios of BC, again suggesting a vertical translocation of aromatic carbon or a mechanical admixture of charcoal during the hearths operation. We observe a 177 % to 544 % increase in TOC concentrations for 2Cu horizons compared to non-RCH Bw and C horizons respectively. Thereby, 94 % of the TOC is pyrogenic carbon (Table 6.2). This increase might in part be due to charcoal pieces that are sometimes found in 2Cu horizons of RCHs in the area (Raab et al. 2017), presumably resulting directly from the operation of the hearths (raking, digging). However, the gradual decrease in TOC concentrations and aromaticity in the first 20 cm of the 2Cu horizons also suggests vertical translocation originating in Auh horizons. Evidence of bioturbation has not been detected in our study area.

Comparable vertical transport of pyrogenic carbon is described for wildfire affected- and biochar amended soils in particulate and soluble form (Bellè et al. 2021, Braun et al. 2020). It remains unclear if these processes are still ongoing in RCH soils. However, the evidence of charcoal degradation described here and in other studies suggest the continuing formation of water extractable black carbon in RCH soils. This could be of interest when studying RCH sites located in areas with occurring podsolization. If the natural A horizons are replaced by RCH substrate of up to several decimetres in thickness, this would allow to study the effect of increased amounts of soluble aromatic organic acids on buried E horizons.

The vertical TOC distribution in the top 20 cm of the Auh horizon suggest an accumulation of non-pyrogenic carbon. However, based on FTIR spectra analysis as shown in Fig. 6.3 and discussed in section 6.5.1, the accumulated TOC seems to be of different composition compared to reference topsoils. This could hint at changed SOM turnover dynamics in RCH soils. Mastrodonato et al. (2019) describe a PyC enrichment for the lower part of

RCH substrate for sites in Belgium, which we could not confirm for our sites.

## 6.6 Conclusions

- The spectral properties of our studied RCH soils suggest an increase in aromatic and carboxylic properties when compared to the SOM of reference soils. This hints at ongoing charcoal degradation processes that potentially result in the formation of water extractable aromatic acids.
- The vertical distribution of TOC in topmost Auh horizons suggest an accumulation of recent, non-pyrogenic SOM. However, less intense aliphatic carbon absorptions in RCH soil spectra suggest potentially different SOM turnover dynamics compared to reference soils.
- The ratio of BC contents and TOC contents suggest an accumulation of additional SOM in RCH soils. The origin of this additional SOM seems unclear as of now. It is hypothesized to be a combination of methodological uncertainties when quantifying PyC, a postburn accumulation of SOM and the potential SOM enriched original RCH cover material.
- The vertical distribution of PyC in 2Cu and Ahb horizons suggest a translocation of aromatic carbon compounds from the Auh horizons into buried mineral soils and the continuing formation of water extractable black carbon even after centuries of charcoal incorporation into the soils.

## 6.7 Acknowledgements

We would like to thank Dr. Frank Repmann for facilitating helpful discussions. This research was supported by the German Research Foundation (DFG) under grant number RA 931/8-1. AB conceptualised the study, wrote and revised the manuscript. TR, AS, TF, WW, AR, FH conceptualised the study and edited and revised the manuscript draft. SR contributed to data analysis and visualisation.

*Once upon a time, in days of old,  
Charcoal burners labored in the cold.  
Cutting wood and stacking it just right,  
To create the perfect fire pit site.  
They lit the flame and watched it grow,  
As the wood turned to ash and began to glow.  
Banking the fire to keep it burning bright,  
They tended it day and night.  
When the fire had died down and the coals were white,  
They carefully covered them to smother the light.  
And when the coals had cooled, they raked them out,  
Ready for use in blacksmith's forge or hearth, no doubt.  
Thus, the charcoal burners played their part,  
In the history of fire and the art  
Of creating fuel from the trees,  
A legacy that still lives on, if you please.*

- ChatGPT



# 7 Automated large-scale mapping and analysis of relict charcoal hearths in Connecticut (USA) using a Deep Learning YOLOv4 framework

This chapter is published as: Verschoof-van der Vaart, W., Bonhage, A., Schneider, A., Ouimet, W., Raab, T. (2022): Automated large-scale mapping and analysis of relict charcoal hearths in Connecticut (USA) using a Deep Learning YOLOv4 framework. *Archaeological Prospection*. DOI: 10.1002/arp.1889

## 7.1 Abstract

In the past decade numerous studies have successfully mapped thousands of former charcoal production sites (also called Relict Charcoal Hearths) manually using DEM data from various forested areas in Europe and the north-eastern USA. The presence of these sites causes significant changes in the soil physical and chemical properties, referred to as legacy effects, due to high amounts of charcoal that remain in the soils. The overwhelming amount of charcoal hearths found in landscapes necessitates the use of automated methods to map and analyze these landforms. We present a novel approach based on open source data and software, to automatically detect relict charcoal hearths in large-scale LiDAR datasets (visualized with Simple Local Relief Model). In addition, the approach simultaneously provides both general as well as domain-specific information, which can be used to further study legacy effects. Different versions of the methodology were fine-tuned on data from north-western Connecticut and subsequently tested on two different areas in Connecticut. The results show that these perform adequate, with F1-scores ranging between 0.21 and 0.76, although additional post-processing was needed to deal with variations in LiDAR quality.

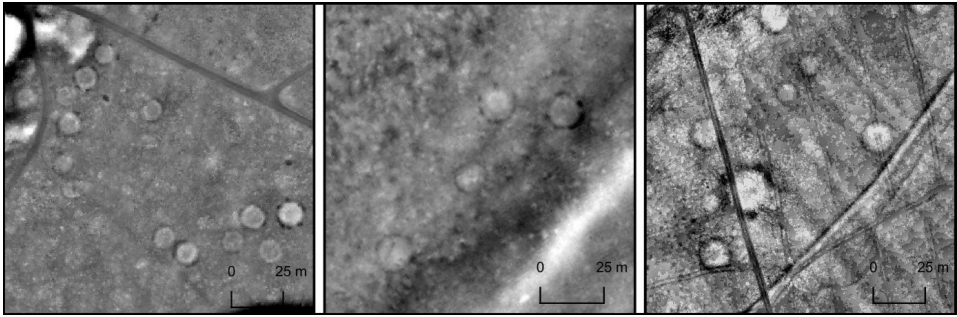


**Abbildung 7.1.** Excerpts of LiDAR data, visualized with Simple Local Relief Model (Hesse, 2010), showing examples of relict charcoal hearths in the Netherlands (left), Connecticut, USA (center), and Germany (right).

After testing the best performing version of the prediction model (with an average F1-score of 0.56) was applied on the entire state of Connecticut. The results show a clear overlap with the known distribution of charcoal hearths in the state, while new concentrations were found as well. This shows the usability of the approach on large-scale datasets, even when the terrain and LiDAR quality varies.

## 7.2 Introduction

Recent archaeological and pedological research has shown the widespread presence of former charcoal production sites, also called Relict Charcoal Hearths (RCHs), across forested areas in Europe and the north-eastern USA (for an extensive overview see Hirsch et al., 2020). These landforms are mainly of pre-industrial age and persist in the present-day landscape as earthworks, i.e., circular-shaped, elevated platforms of up to 30 m in diameter (on average 12 m) surrounded by a shallow ditch or multiple pits. LiDAR-based digital elevation model (DEM) analysis has proven an effective tool to find, map, and investigate them (Figure 7.1).

One of the reasons for investigating RCHs is the value of these objects for geoarchaeological and pedological research. Recent larger scale studies have analysed the spatial association between RCH- and historic industrial sites (Schneider et al., 2020), emphasizing the scale dependent heterogeneity of site densities (Schneider et al., 2022). Relict charcoal hearth sites are often studied for past-landscape- and historic reconstruction efforts (e.g., Dupin et al., 2019; Tolkendorf et al., 2015). The charcoal remaining in these RCHs is of particular value to reconstruct historic forest compositions and abundances (Deforce et al., 2013; Gocel-Chalté et al., 2020). As a result of high amounts of charcoal remaining in the soils,

these sites (categorized as Spolic Technosols; IUSS Working Group World Reference Base, WRB, 2014) have a distinct enrichment of total organic- and pyrogenic carbon (e.g., Borchard et al., 2014; Hirsch et al., 2017), resulting in significant changes of the soil physical and chemical properties (e.g., Donovan et al., 2020; Schneider et al., 2019). This enrichment is also affecting vegetation patterns and dynamics as well as microbial growth and abundance (e.g. Raab et al. 2022). Efforts have been made to quantify the changes caused by historical charcoal burning on today's soil landscapes, referred to as legacy effects, on a larger-than-site specific scale. For instance, Bonhage et al. (2020a) found a positive correlation between local slope, RCH site volume and stratigraphy, i.e., on steeper slopes the sites total volume increases and vice versa. By using a GIS-based modelling approach, it enables the quantification of nutrient- and carbon stocks in RCH sites based on their topographical position. Thereby information about the local topography and the sites surface area is of high interest next to the site's location itself. A uniform and seamless large scale mapping can significantly help to improve the assessment of legacy effects on soil landscapes caused by historic land-use, whether it be in terms of morphology (e.g., how much soil substrate was redistributed) or soil properties (e.g., carbon- and element stocks) and it can help in the effort to identify large scale clusters of site occurrences.

In the past decade various studies have successfully mapped thousands of RCHs by hand using DEM data from various regions (Carrari et al., 2017; Deforce et al., 2013; Hazell et al., 2017; Hesse, 2010; Johnson et al., 2015; Raab et al., 2019; Risbøl et al., 2013; Rutkiewicz et al., 2019). For instance, the manual analysis of DEM data from northwestern Connecticut, USA resulted in the discovery of over 20,000 RCHs (Johnson et al., 2015; Johnson & Ouintet, 2021; Raab et al., 2017; see also Table 1).

This overwhelming number of RCHs, combined with an ever-increasing set of available, high-quality, remotely-sensed data necessitates the use of computer-aided methods for the automatic detection of these objects, thereby alleviating the complications surrounding manual analysis, e.g., biased and heterogeneous detection accuracy (Quintus et al., 2017; Risbøl et al., 2013; Sadr, 2016), and documentation (Bennett et al., 2014; Bevan, 2015). Furthermore, in order to model legacy effects using these enormous numbers of RCHs, automation in the calculation of domain specific information based on their topographical position (e.g., local slope) is needed as well.

Previous research in an effort to automatically detect RCHs has relied on various methods including Template Matching (Schneider et al., 2015; Trier & Pilø, 2012) and Geographic

Object-Based Image Analysis (Witharana et al., 2018), while more recently Machine Learning approaches are being developed and utilized (Anderson, 2019; Bonhage et al., 2021; Carter et al., 2021; Davis & Lundin, 2021; Kazimi et al., 2019, 2020; Oliveira et al., 2021; Suh et al., 2021; Trier et al., 2018, 2021; Verschoof-van der Vaart et al., 2020). Deep Learning (LeCun et al., 2015), a subfield of Machine Learning, predominantly employs Convolutional Neural Networks (CNNs)—hierarchically structured algorithms that generally consist of a (image) feature extractor and classifier (Guo et al., 2016)—that learn to generalize from a large set of labelled examples, rather than relying on a human operator to set parameters or formulate rules. To date, these automated methods are mainly tested in an experimental setting, but have generally not been applied in various contexts or on a large (e.g., regional or national) scale (Verschoof-van der Vaart et al., 2020; but see for instance Berganzo-Besga et al., 2021; Davis et al., 2021; Orenge et al., 2020); with this being the aim of previous initiatives (Trier et al., 2019). Questions remain concerning the usability of these approaches for large-scale surveys and the transferability of these methods when applied outside of the area where they were developed (Cowley et al., 2020; Kermit et al., 2018; Verschoof-van der Vaart & Landauer, 2022). Furthermore, archaeological automated detection can still be considered as being in a developmental stage (Opitz & Herrmann, 2018) and as such studies generally focus on the training and testing of automated methods and the resulting detection rates, while the further analysis and use of the generated archaeological information are often not part of these studies (Davis, 2019). Leading to the understanding that, opportunities to automate the subsequent analysis of detections to gain domain-specific information are rarely explored.

In this paper, we present a novel approach to automatically detect relict charcoal hearths in LiDAR-based digital elevation model (DEM) data. For this, a state-of-the-art Deep Learning object detection framework, YOLOv4, has been transfer-learned, i.e., the model has been pre-trained on a generic image dataset and subsequently fine-tuned on our own dataset, and combined with (GIS) processing algorithms with a focus on being effective and efficient to handle large amounts of spatial data (e.g., entire states). Simultaneously, it is designed to be able to provide both general information (e.g., the location), as well as domain-specific information, such as the area (i.e., the area covered by the RCH's platform and ditch) and average local slope (i.e., the slope in the direct vicinity of the RCH; see Bonhage et al., 2020a; Johnson & Ouimet, 2021), of the objects of interest (see also Verschoof-van der Vaart, 2022). A further aim of this research is to utilize open-source data and software, to make this research more transparent, reproducible, and more readily implementable by other researchers (Schmidt & Marwick, 2020).



### 7.3 Research areas and LiDAR data

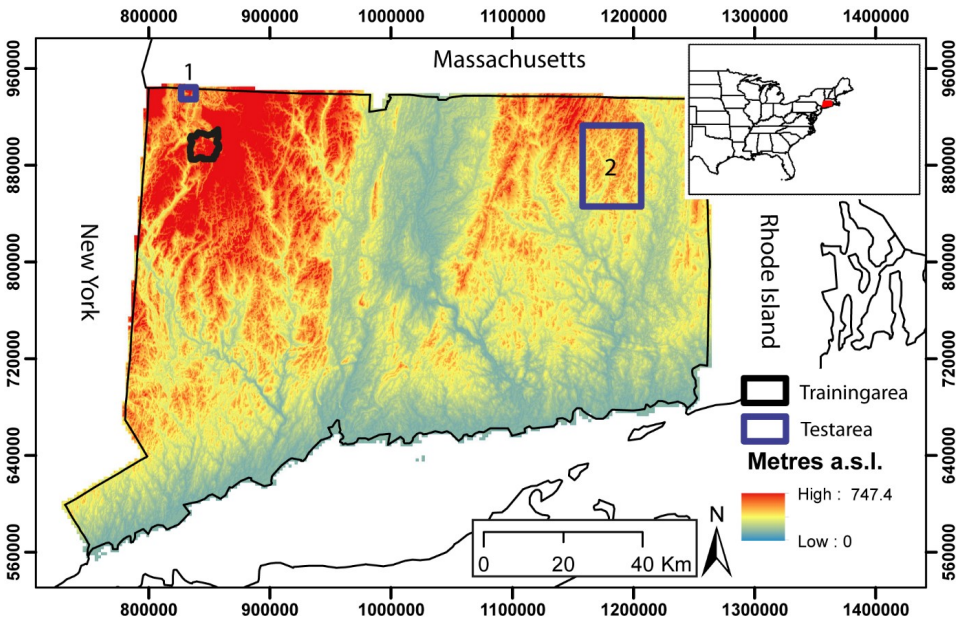


**Abbildung 7.2.** The research areas on an elevation map of Connecticut, USA.

In order to train, test, and apply the developed method, four different, predominantly forested areas were first defined (see Table 7.1 and Figure 7.2). The Huntsville area (circa 40 km<sup>2</sup>) comprises the northern part of the Housatonic State Forest between Huntsville, Cornwall Hollow, and West Cornwall in Litchfield County located in northwestern Connecticut (Figure 7.2, Training area). This wider area is part of the Salisbury Iron district and has a very high density of known RCHs (Johnson et al., 2015; Johnson & Ouimet, 2021; Raab et al., 2017). RCH sites from the Huntsville area have been used for the training of our approach (see Section 7.4.1). To test the developed method, two separate areas in Connecticut were selected. The Canaan area (circa 11 km<sup>2</sup>), or Test area 1, lies circa 10 km north of the Huntsville area near the town of Canaan within the Salisbury Iron district. Due to the close proximity, this area closely resembles the training area in terms of landscape and to a lesser extent in known RCH density (Table 7.1). The discrepancy in forest cover (see <https://www.sciencebase.gov/catalog/item/5b6fa9d4e4b0f5d57878e707>) between these two areas is in large part caused by Washing Lake in the southwest of the Canaan area. The Ashford area (302 km<sup>2</sup>), or Test area 2, lies circa 100 km to the east of the Huntsville area, in Windham County in eastern Connecticut. While this area has a comparable topo-

graphy and forest cover as the Huntsville area, the density of known RCHs is much lower and more comparable to the overall density of RCHs in Connecticut (Table 7.1; see also Suh et al., 2021). The difference in size and RCH density of the two test areas offers opportunities to see the influence of these parameters on the performance of the developed method (see Verschoof-van der Vaart, 2022).

**Table 7.1.** Overview of the research areas and the number and density of manually mapped relict charcoal hearts.

Location	Type	Sq. km	Known RCH	Density (RCH /sq. km)	Forest cover	Ground point / sq. m
Huntsville, Litchfield County CT	Training area	40	3040	76	92%	2.44
Canaan, Litchfield County CT	Test area 1	11	314	29	77%	3.98
Ashford, Windham County CT	Test area 2	302	527	1.75	87%	2.13
State of Connecticut	Application	12189	24051	2	66%	-

After testing, the developed method has been applied on a large-scale. The application area equals the entire state of Connecticut (circa 12,542 km<sup>2</sup>), excluding the training and testing areas. As of this publication, about 24,000 RCHs are known from the entire state of Connecticut according to the publicly available Northeastern US Relict Charcoal Hearth ArcGIS Online Web Map (Ouimet, 2019).

Statewide LiDAR-based DEM data (the 2016 dataset with a raster cell size of 0.6 m) was acquired from the openly accessible repository of the Connecticut Department of Energy and Environmental Protection (<http://www.cteco.uconn.edu>). The global accuracy of this dataset is stated as a horizontal accuracy of ± 1.0 meter and a vertical accuracy of ± 0.138–0.170 meter. In addition, we assessed the quality of the LiDAR data for the three subregions by randomly selecting 10 point cloud las tiles (760 x 760 m each) and then averaging their calculated ground point density, which varied between 2.1 and 4 (Table 7.1).

The downloaded DEM tiles were merged into a single file, which was subsequently split into 25 tiles (around 800 km<sup>2</sup> each) to ease further computational requirements. This procedure was a compromise of reducing the total number of DEM tiles and keeping the files sizes manageable. The 25 DEM tiles were visualized, using the RVT toolbox (see Kokalj & Hesse, 2017), with Simple Local Relief Model (SLRM; Hesse, 2010) and subsequently merged. The choice to use SLRM was based on several factors such as the fact that this visualization most clearly shows the RCHs for the purpose of human observation. Also, in prior automated detection research on RCHs the use of SLRM had led to satisfactory results (Trier et al., 2021; Verschoof-van der Vaart, 2022). We are aware that multiscale visualiza-

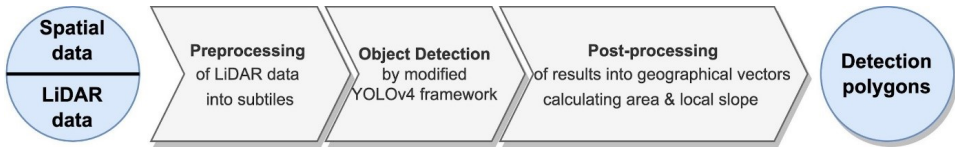


**Abbildung 7.3.** Simplified representation of the ARCHMAGE workflow.

tion techniques can result in better detection results when using deep learning (Guyot et al. 2021). Even though, SLRM produces relatively high results in recent study comparing visualizations (Guyot et al. 202) as well as in less recent publications (Gallwey et al., 2019, Kazimi et al., 2020). More importantly, we choose efficiency over total accuracy, as we are dealing with (very) large-scale datasets. Compared with other visualizations and especially blends and multiscale visualizations, SLRM is more easy to implement and can be utilized using open source tools that allow rapid batch processing of large datasets.

## 7.4 Methodology

The aim of this study is to create an effective and efficient approach to automatically detect RCHs in large amounts of DEM data, while simultaneously providing both general (e.g., location) as well as domain-specific information (e.g., area and local slope). The developed approach (Figure 3), called ARCHMAGE (Automated Relict Charcoal Hearth Mapping And Geospatial Exploration), combines the state-of-the-art object detection framework, YOLOv4 (Bochkovskiy et al., 2020), with different (GIS) processing algorithms. The workflow can be divided into three parts: a preprocessing part that converts the DEM data into input images (subtiles), based on geospatial information about known RCHs (Section 7.4.1); a part concerning the Deep Learning-based object detection (Section 7.4.2); and a post-processing part where the results of the object detection are converted back into geospatial data (Section 7.4.3). In addition, two domain-specific parameters, i.e., area and local slope are calculated.

### 7.4.1 Preprocessing of DEM data into subtiles

To generate a training dataset for the object detection model, all RCHs in the Huntsville area (circa 40 km<sup>2</sup>; see Table 7.1) were manually mapped. The results of a prior analysis of the 2011 LiDAR data of Litchfield County (Johnson et al., 2015) were used as a starting point. This data on the location of RCHs originally consisted of point data, which we converted into polygons, using the outer edge of RCH sites as a maximum extent.

Subsequently, two experts—both with ample experience in the analysis of DEM data—independently marked all other visible RCHs in the DEM data. The annotations were combined and compared in QGIS (QGIS Development Team, 2017). This resulted in a dataset containing 3040 unique RCH sites, of which 2350 were known from the 2015 analysis (see Johnson et al., 2015). The latter shows the problem of heterogeneous detection accuracy between operators in manual analysis, which is further enhanced by the use of DEM data of different date, quality, and different visualizations (see Quintus et al., 2017; Risbøl et al., 2013; Sadr, 2016). To make input subtiles for the YOLOv4 model, a modified version of the dataset generation method developed by Olivier & Verschoof-van der Vaart (2021) was used. This python script uses a spatial dataset of objects (in this case known RCH sites) to crop LiDAR data into smaller images (subtiles) with set dimensions (in this case 500 x 500 pixels or circa 305 x 305 m). For every individual object in the dataset, a subtitle is generated, centered on the location of the object. To avoid bias, a small shift (or jitter) is added so that the RCH is not in the exact center of the subtitle. However, as RCHs are often spatially clustered, these cropped subtiles generally contains multiple RCHs and therefore, a RCH site can appear on multiple subtiles. This ‘re-use’ of objects has proven beneficial, as it not only increases the number of subtiles in the training dataset, but also increases variability (Olivier & Verschoof-van der Vaart, 2021).

**Table 7.2.** The number of subtiles per research area, resulting from the dataset generation.

Location	Number of subtitels
Huntsville, Litchfield County CT (Training area)	1942
	485
Canaan, Litchfield County CT (Test area 1)	143
Ashford, Windham County CT (Test area 2)	3672
State of Connecticut (Application)	214,620

A selection of 2427 RCHs from the 3040 RCHs found in the manually mapped dataset were used to crop the SLRM visualized DEM data of the Huntsville training area. The remaining 613 RCHs were omitted as these were mapped in the prior analysis of Johnson et al. (2015), but could not be verified in the LiDAR data used in this research. Subsequently, all subtiles were randomly split 80/20 into a train and validation dataset (Table 7.2), as is common practice in the training of Deep Learning algorithms (Goodfellow et al., 2016).

As the testing and application areas simply need to be split into equal parts, not based on the location of known RCHs, an additional python script was used that cuts the DEM data into subtiles of 500 x 500 pixels (circa 305 x 305 m) with a 25 pixel (circa 15 m) overlap

to all sides. The latter is done to avoid the dissecting of potential RCHs at the edge of the subtiles. A drawback of this overlap is the occurrence of multiple overlapping predictions (i.e., bounding boxes) on RCHs at the edge of multiple subtiles. This resulted in two test datasets of respectively 143 and 3672 subtiles, while the application dataset consists of 214,620 subtiles (Table 7.2).

## 7.4.2 Object detection with the YOLOv4 framework

The object detection portion of the ARCHMAGE workflow consists of the YOLOv4 detection framework (Bochkovskiy et al., 2020), a recent implementation of the YOLO (“You Only Look Once”) framework (Redmon et al., 2016). YOLOv4 is a so-called ‘one-stage’ detector, which, contrary to ‘two-stage’ detectors such as Faster R-CNN (Ren et al., 2017), combines the two parts of object detection (i.e., object localization and classification) in one process and approaches this as one would a regression problem. More specifically, in YOLOv4 input subtiles are downscaled to a fixed resolution and subsequently divided into an equally spaced grid. For every cell within this grid, a set amount of bounding boxes with confidence scores is predicted as well as a class probability (Bochkovskiy et al., 2020). This approach dramatically decreases the inference time (i.e., the speed of detections), generally without a loss of accuracy. For example, a comparison of the testing time between YOLOv4 and Faster R-CNN on DEM data showed that the former was about 18 times faster than the latter (see Olivier & Verschoof-van der Vaart, 2021). Although speed is normally not the focus of archaeological automated detection research, the aim to develop an effective and efficient approach for large-scale mapping—which involves massive amount of data up to several hundred gigabytes—necessitates a fast inference time without a loss in performance, especially on small objects which the YOLOv4 framework provides (Bochkovskiy et al., 2020; Carranza-García et al., 2021).

### 7.4.2.1 Adjusting YOLOv4 for archaeological object detection

Implementing an off-the-shelf version of an object detection framework, pre-trained on a general-purpose dataset, e.g., Microsoft COCO (Lin et al., 2014), on the task of detecting (archaeological) objects in remotely-sensed data generally results in an unsatisfactory performance (Verschoof-van der Vaart & Lambers, 2019). This is directly related to the differences between the (objects in) images in general-purpose datasets and DEM data (Olivier & Verschoof-van der Vaart, 2021; Verschoof-van der Vaart, 2022). The main problem is that general-purpose datasets contain ‘natural images’ (i.e., photographs of scenes seen in normal, every-day settings) in which objects are generally large and prominent, and occupy a

major portion of the image. Object detection methods normally take advantage of this by downscaling (and pooling) the images, when they pass through the CNN to greatly reduce the computational cost (Guo et al., 2016). For instance, in the YOLOv4 framework input images are downscaled to a fixed size, normally  $416 \times 416$  pixels. However, within DEM data (and remotely-sensed imagery in general) the objects of interest are generally very small, especially in relation to the size of the images. Consequently, downscaling on these images will result in information loss and the removal of small objects, which makes it impossible to detect them (Olivier & Verschoof-van der Vaart, 2021). Therefore, in our versions of YOLOv4, the input size was set to  $512 \times 512$  pixels—while the actual size of the subtiles is  $500 \times 500$  pixels—to prevent the downsampling of the subtiles in the CNN (Table 7.3).

**Table 7.3.** Overview of the general (hyper)parameters for the YOLOv4 framework (before specific modifications) used in this research.

(Hyper)parameter	Value /Type
backbone CNN	CSPDarknet53
input size	$512 \times 512$
batchsize	64
learning rate	initially 0.001
epochs	4000
data augmentation	photometric distortions: brightness, contrast, hue, saturation, and noise; geometric distortion: random scaling, cropping, flipping, and rotating; mosaic
regularization	Dropblock
loss function	CIoU
non-maximum suppression	greedyNMS

Another common problem remains in the fact that the objects of interest in remotely-sensed imagery are often densely clustered but scarcely distributed. This means that while many subtiles in the test and application datasets will be empty, some will contain a large number of RCHs. Traditional object detection methods can generally only detect a select number of objects within a single subtile, although this can be adjusted. Therefore, the maximum number of detections per subtile was increased to 200 in the YOLOv4 framework used in this study (Table 7.3). Finally, several data augmentation techniques (Goodfellow et al., 2016) were implemented to improve the robustness of the model to deal with occlusion and fragmentation of RCHs in the data (for an extensive explanation of augmentation techniques, see Bochkovskiy et al., 2020; Redmon et al., 2016).

**Table 7.4.** Overview of the different versions of the YOLOv4 framework used in this research.

Model	Upsample stride	Loss function	Accuracy metric
1	2	CIoU	mAP@0.5
2	4	CIoU	mAP@0.5
3	2	GIoU	mAP@0.5
4	4	GIoU	mAP@0.5
5	2	GIoU	mAP@0.9
6	4	GIoU	mAP@0.9

In addition to the general adjustments to the YOLOv4 framework, we experimented with different strides, loss functions, and accuracy metrics. To measure the influence of these, six different versions of the YOLOv4 model were created, transfer-learned, and tested on the two test areas (Table 7.4).

### Upsample stride

To further enhance YOLOv4's performance on especially small objects, i.e., smaller than 19 x 19 pixels (the average size of RCH in the dataset is circa 17 x 17 pixels or 11 by 11 m), the upsampling stride in YOLOv4 can be increased. At two points in the framework the image is upsampled, i.e., if the image is upsampled with a stride 2, one pixel is transformed into four pixels in a 2 by 2 area. By increasing the stride parameter from 2 to 4, small objects, which constitute a few pixels, will appear larger in the upsampled image. A downside can be that the element of scale becomes more difficult.

### Loss function

During the training of the CNN, the loss function—a function that calculates the penalties of incorrect classifications into a single number (Goodfellow et al., 2016)—is optimized. A low loss value is generally regarded as an indication for a well-trained approach and therefore high performance (Guo et al., 2016). In the case of object detection, the Intersection Over Union (IoU) is often used as loss function, which gives a measure for the overlap between the predicted bounding box and the ground truth. While this metric gives a good indication for bounding box quality, it completely disregards the positional relation between the predicted bounding box and the ground truth (Rezatofighi et al., 2019). Therefore, YOLOv4 employs an improved version of the IoU, the Complete IoU (CIoU), which uses three parameters, i.e., the overlap between predicted bounding box and ground truth, the distance between the center point of the predicted bounding box and ground truth, and the aspect

ratio between the two (Zheng et al., 2021). However, other loss functions, which also take the position of the bounding box in regard to the ground truth into account, might prove more beneficial. Therefore, several versions (3–6) have been outfitted with the Generalised IoU (GIoU) (Rezatofighi et al., 2019). The GIoU takes into account the distance between the predicted bounding box and ground truth, as well as their overlap by using the size of a box enclosing the prediction and the ground truth.

### Accuracy metric

The last modification involves using GIoU (see above) and changing the metric used to evaluate the quality of detections during training, i.e., the mean average precision, or mAP. This metric is changed from mAP@0.5 to mAP@0.9, which means that only predictions whose overlap with the ground truth is over 0.9 (instead of 0.5) are regarded as True Positives when determining mAP (Everingham et al., 2010). This modification should make the detected bounding boxes more accurate and consequently improve the overall performance of the detection framework.

### 7.4.3 Post processing

The initial post-processing part of the ARCHMAGE workflow consists of three steps: 1) Converting predicted bounding boxes to geospatial polygons and calculate their area; 2) Filter detections by land-use; and 3) Calculate the average slope in the vicinity of the detections. The output of the YOLOv4 model is one text file per subtitle, with a list of detected RCHs comprising of pixel coordinates for the bounding box and a confidence score (range 0–100).

The first post-processing step involves converting these pixel coordinates into a ‘real-world’ coordinate system, so that these can be managed and analysed in a GIS environment (see also Verschoof-van der Vaart & Lambers, 2019). Therefore, a python script, based on the detectionsToCSV script by Olivier & Verschoof-van der Vaart (2021) was used to convert the content of the txt file into a CSV file by connecting every subtitle to the DEM tile from which it originally derived. The real-world coordinates from the DEM tile are used to compute the real-world coordinates of the bounding boxes and add them to the CSV file. Then, the area (i.e., the area covered by the potential RCH’s platform and ditch) is calculated using the formula for the area of an oval, based on the size of the bounding box and the resolution, i.e., cell size, of the DEM tile (Equation 1). However, this initially produced unsatisfactory



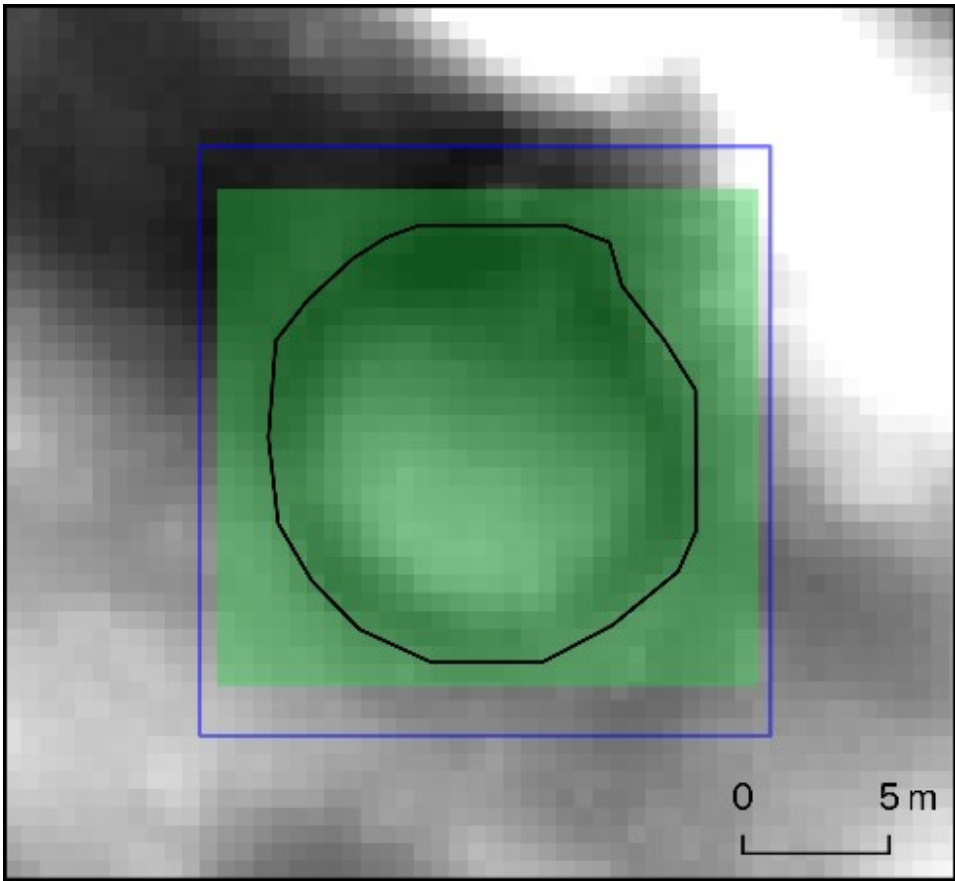


**Abbildung 7.4.** Excerpt of LiDAR data, visualized with Simple Local Relief Model (Hesse, 2010), showing the outline of a RCH (black), the ground truth (green), and the predicted bounding box (blue).

results, as the predicted bounding boxes are generally larger than the actual RCH (Figure 7.4). Further analysis of this problem showed that most ground truths are also larger than the actual RCH, which might have led to larger predicted bounding boxes. To cope with this problem, a negative constant ( $\alpha$  and  $\beta$ ; in this research 5 and 6 pixel respectively) was added to the formula. This resulted in areas much closer to the manually calculated analogs.

### Equation 1

$$Area = * ((width - ) * resolution)/2 * (height - ) * resolution)/2)$$

In the second step of the post-processing the detections are loaded into a GIS environment

and the location of every potential RCH is compared to a spatial layer containing forested areas (see <https://www.sciencebase.gov/catalog/item/5b6fa9d4e4b0f5d57878e707>). All detections situated outside of woodland are discarded, as research has shown that over 95 % of all known RCHs are situated in forested areas (deciduous and conifer forest, Johnson et al., 2015). This aids in filtering out some False Positives created by landscape objects such as swimming pools, roundabouts etc.

Finally, the average slope in the vicinity of the potential RCHs is automatically calculated using a combination of different GIS processing algorithms (see Algorithm 1). This process is comparable to how the average slope surrounding RCHs is manually calculated usually (see for instance Johnson & Ouimet, 2021). For every bounding box, a buffer with 20 m radius is generated. The original bounding box is removed from this buffer to reduce distortions in the average slope value due to slope variation within the RCH. The resulting polygon is compared to a slope map (5 m cell size). Empirically, we found that the median of slope values inside the polygon gave the best results as compared to manually generated average slope values and was less affected by outliers. In addition, the detections are divided into five classes ( $<4^\circ$  /  $4^\circ-8^\circ$  /  $8^\circ-12^\circ$  /  $12^\circ-16^\circ$  /  $>16^\circ$ ), based on the calculated average slope value. The latter is done to make an informed distinction between RCHs on (relatively) flat terrain and more steep terrain.

#### 7.4.4 Implementation details

We used the six versions of the YOLOv4 framework with CSPDarknet53 as the backbone CNN. The CNN was pre-trained on the Microsoft COCO dataset (Lin et al., 2014), and fine-tuned for 4000 epochs with an initial learning rate of 0.001 on our own training dataset (see Section 7.3). During and directly after training, the performance of the six versions of YOLOv4 was determined on the validation dataset. Subsequently the models were used to detect RCHs in the test datasets (see Table 7.1 and 7.2), the results were post-processed (see Section 7.4.3) and evaluated.

The training and testing of the frameworks was implemented on the browser-based Collaboratory platform (Colab Pro+) from Google Research (Google, 2022). Google Colab is a specialized version of Jupyter Notebook, which is cloud-based and offers free computing resources (e.g., GPUs). This platform is connected to Google Drive, where the necessary data (e.g., training and testing dataset, model weights) are stored. Therefore, Colab provides straightforward implementation of the developed models, allows multiple researchers

to access and use the same data and code, and makes dissemination of the developed approach simple.

#### 7.4.5 Performance metrics

To evaluate and compare the performance of our Deep Learning model, the common metrics Recall (R; Equation 2), Precision (P; Equation 3), and F1-score (F1; Equation 4) were calculated (Chicco & Jurman, 2020; Verschoof-van der Vaart, 2022) by determining the number of True Positives (TP), False Positives (FP), and False Negatives (FN). Recall gives a measure of how many relevant objects are selected, while Precision measures how many of the selected items are relevant. The F1-score is the harmonic mean of the Precision and Recall and a single metric of the model's overall performance (Sammut & Webb, 2010). These metrics are restricted between 0 and 1, where higher values indicate better performance.

##### Equation 2

$$Recall = TP / ((TP + FN))$$

##### Equation 3

$$Precision = TP / ((TP + FP))$$

##### Equation 4

$$F1 = 2 * ((Recall * Precision)) / ((Recall + Precision))$$

To obtain the highest F1-scores, we employed threshold moving (Zou et al., 2016). By default, a Deep Learning model uses a certain confidence threshold: detections with a confidence score that equals or exceeds this threshold are included in the results, while detections with a lower confidence score are discarded. This confidence threshold is generally set to an arbitrary number, typically 0.5. However, by changing the threshold and recalculating the performance metric, an optimal trade-off between Recall and Precision can be found, resulting in the highest F1-score (Zou et al., 2016). Therefore, we empirically calculated the optimal confidence threshold for the validation and test datasets and used these (see Table 7.5). While this might complicate the comparison of the performance between datasets, it better shows the capability and maximum performance of the model on that particular dataset.

## 7.5 Results

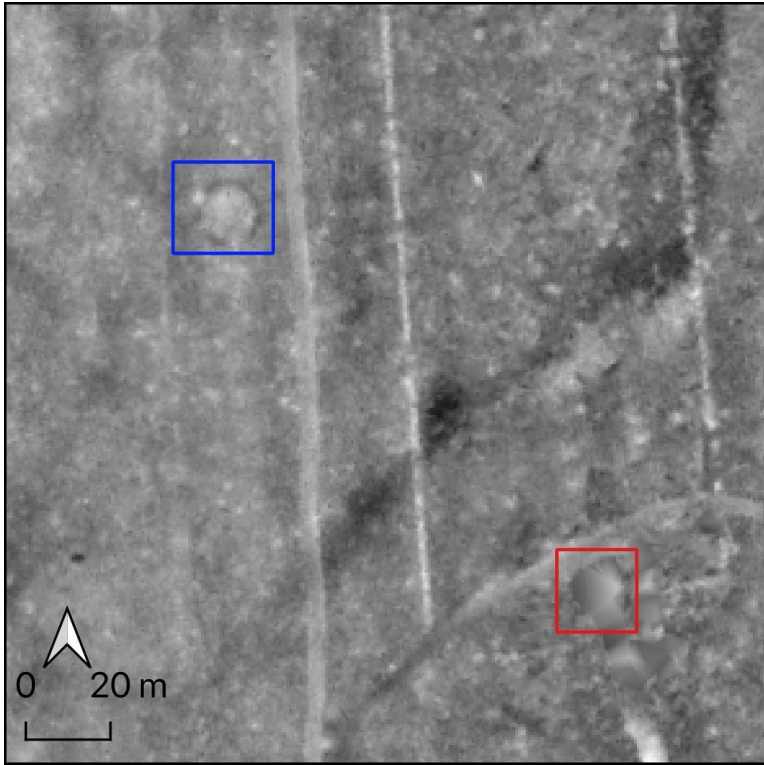
### 7.5.1 General results

Table 7.5 shows the performance of the different versions of the YOLOv4 framework on the validation and test datasets. The performance (F1) on the validation dataset is high, on average 0.88, which demonstrates that the detection method is suitable—at least on a technical level—for this specific task (see Verschoof-van der Vaart, 2022). The performance on both test areas is lower. The performance (F1) on test area 1 is on average 0.73. Although the average Precision (0.86) is very similar to the validation dataset (0.86), a clear drop in average Recall can be observed (0.90 to 0.64). This reduced performance between the validation dataset (or a small, non-random, selective dataset) and test datasets (‘realistic’ datasets representing the real-world situation) has been observed in various studies (Soroush et al., 2020; Verschoof-van der Vaart et al., 2020) and is related to several factors, such as the proportion of positive and negative subtiles (i.e., subtiles with or without archaeological objects), the total number of labelled objects in the area as compared to the size of the area (i.e., the density), the variety in the state of preservation of the archaeological objects (Verschoof-van der Vaart et al., 2020), and land cover conditions (Suh et al., 2021).

**Table 7.5.** The performance (Recall, Precision, F1) of the different versions of the YOLOv4 framework on the validation, and test datasets. Notice the difference in confidence threshold between the different datasets.

Model	Upsam- ple stride	Loss function	Accuracy metric	Validation (conf thresh 0.25)			Test area 1 (conf thresh 0.5)			Test area 2 (conf thresh 0.9)		
				Recall	Precision	F1	Recall	Precision	F1	Recall	Precision	F1
1	2	CIoU	mAP@0.5	0.90	0.85	0.88	0.65	0.89	0.75	0.38	0.15	0.21
2	4	CIoU	mAP@0.5	0.90	<b>0.87</b>	<b>0.89</b>	0.61	0.89	0.73	0.36	0.24	0.28
3	2	GIoU	mAP@0.5	<b>0.91</b>	0.86	0.88	<b>0.71</b>	0.69	0.70	<b>0.52</b>	0.09	0.15
4	4	GIoU	mAP@0.5	0.90	0.87	0.88	0.66	0.88	<b>0.754</b>	0.40	0.18	0.24
5	2	GIoU	mAP@0.9	0.90	0.85	0.87	0.62	0.87	0.72	0.30	0.25	0.27
6	4	GIoU	mAP@0.9	<b>0.91</b>	0.86	0.88	0.60	<b>0.92</b>	0.72	0.25	<b>0.37</b>	<b>0.30</b>

Another factor that can have a considerable impact on the performance of detection are changes in the LiDAR data quality (Bonhage et al., 2021; Suh et al., 2021; Verschoof-van der Vaart & Landauer, 2022). This is clearly illustrated by the large decline in performance between Test area 1 and Test area 2 (Table 7.5). An inspection of the properties of the LiDAR data of both test areas shows that Test area 2 has a lower ground point density than Test area 1 (Table 7.1). This results in the appearance of interpolation errors (Căteanu & Ciubotaru, 2020). These errors are particularly problematic for this research, as their appearance



**Abbildung 7.5.** Excerpt of LiDAR data, in (scale 1:2000), visualized with Simple Local Relief Model (Hesse, 2010), showing a RCH in (blue outline) and an interpolation error in (red outline).

in the interpolated and visualized DEM data is often round, and thereby very comparable to RCHs (Figure 7.5). This results in the severe drop in Precision from on average 0.86 (Test area 1) to on average 0.21 (Test area 2). As a solution to this problem, an additional post-processing step was developed to automatically filter out the majority of FPs resulting from these interpolation errors. Further investigation proved that the slope within the interpolation errors varies little, i.e., the standard deviation (stdev) of the slope within the errors is low. Therefore, a combination of different GIS processing algorithms (Algorithm 2) was developed. For every bounding box (detection polygon), the centroid is computed and a buffer with 4 m radius is generated. The size of the buffer was empirically determined to make sure no edges of the RCHs or the interpolation artefacts were included, while still allowing the computation of the slope standard deviation by including enough raster cells. These buffer polygons are compared to a slope map of the original DEM resolution, which has been created with an added z-factor of 10 and then has been subsequently converted

to integer values to allow the use of the Zonal Statistic Toolbox in ArcGIS. For each buffer polygon, the standard deviation (stdev) of the slope is calculated. Subsequently, the buffer polygon feature tables are joined with the detection polygons based on their location. Every detection polygon with a slope standard deviation lower or equal than the threshold of 4.5 is removed. This threshold was determined by comparing the slope standard deviation of a selection of the interpolation errors.

**Table 7.6.** The original and recalculated performance (Recall, Precision, F1) of the different versions of the YOLOv4 framework on the test datasets. Notice the difference in confidence threshold between test area 1 and 2.

Model	Up-sample stride	Loss function	Accuracy metric	Test area 1 (conf thresh 0.5)			Test area 1 (conf thresh 0.5)		
				Original	Recall	Precision	F1	Recalculated	Precision
1	2	CIoU	mAP@0.5	0.65	0.89	0.749	0.64	0.96	0.757
2	4	CIoU	mAP@0.5	0.61	0.89	0.73	0.61	0.93	0.73
3	2	GIoU	mAP@0.5	0.71	0.69	0.70	0.70	0.76	0.73
4	4	GIoU	mAP@0.5	0.66	0.88	0.754	0.65	0.91	0.759
5	2	GIoU	mAP@0.9	0.62	0.87	0.71	0.62	0.92	0.74
6	4	GIoU	mAP@0.9	0.60	0.92	0.725	0.59	0.94	0.72

Model	Up-sample stride	Loss function	Accuracy metric	Test area 2 (conf thresh 0.9)			Test area 2 (conf thresh 0.9)		
				Original	Recall	Precision	F1	Recalculated	Precision
1	2	CIoU	mAP@0.5	0.38	0.15	0.21	0.37	0.29	0.32
2	4	CIoU	mAP@0.5	0.36	0.24	0.28	0.34	0.42	0.38
3	2	GIoU	mAP@0.5	0.52	0.09	0.15	0.5	0.14	0.21
4	4	GIoU	mAP@0.5	0.40	0.18	0.24	0.39	0.32	0.35
5	2	GIoU	mAP@0.9	0.30	0.25	0.27	0.3	0.43	0.35
6	4	GIoU	mAP@0.9	0.25	0.37	0.30	0.25	0.57	0.34

To evaluate the effectiveness of this post-processing step, the models' performance on Test area 1 and Test area 2 was recalculated (Table 7.6). Based on the results, interpolation errors account for 25 to 41 % of the FPs in Test area 1, while in Test area 2 the percentage lies between 43 and 59 %. The remaining FPs are mainly caused by a variety of natural landforms that 'mimic' RCHs. For Test area 1 a slight decrease in Recall (0–1 point) and an increase in Precision (2–8 points), with an overall increase in performance (F1) between 0 and 3 points can be observed. The impact on the performance of Test area 2 is more notable. While the Recall is only slightly decreasing, the Precision increases by 5–20 points, i.e., the procedure is effective and efficient in predominantly deleting false positive sites. In summation, false positives are generally caused by areas with low ground point density (resulting in in-

terpolation errors), but with a central elevation value higher than the surrounding values. Therefore, these areas can be automatically selected as being detections with low standard deviation of the elevation values.

### 7.5.2 Results of the implementation of specific adjustments

The results (Table 7.5 & 7.6) display that the specific adjustments are of influence on the performance. More specifically, the increase of the upsampling stride seems to have a negative influence on Recall, while improving Precision. Changing the loss function from CIoU to GIoU improves Recall, but decreases Precision. Finally, changing the mAP results in an increase in Precision, but a decrease in Recall. The version of YOLOv4 with the best Recall is model 3, which concerns the base model with GIoU. However, this model also has the lowest Precision of all versions (see Table 7.5 & 7.6). The opposite is true for model 6. This version reached the highest Precision, but has the lowest Recall of all versions (Table 7.5 & 7.6). The models with the overall best performance (F1) in both test areas are model 2 and 4, of which the former uses an increased upsampling stride and the latter an increased upsampling stride and GIoU.

### 7.5.3 Results of the post-processing

To evaluate the automatically computed area (see Equation 1), the results of 25 randomly selected RCHs in Test area 1 were compared to manually determined areas. The results (Figure 7.6) show that on average, the automatically determined area is still an overestimation of the actual area. Even though the overestimation is less than 20 sq. m on average, which we deem an acceptable error.

To evaluate the performance of the average slope algorithm (see Algorithm 1), the results for 50 RCH locations in the training area were compared with manually determined slope values (see Bonhage et al., 2020b). The results show that 46 % (23 out of 50) of the automatically calculated slope values are within 1 degree of the manually determined slopes, while 94 % (47 out of 50) are within 4 degrees. Three locations yield widely different values (> 4-degree difference). A manual investigation of these outliers shows that two are located on a ridge surrounded by low-lying areas (e.g., gullies; Figure 7.7, A & B). For the other outlier (Figure 7.7, C) no clear cause for the discrepancy can be found, although it should be noted that the difference between the two slope values for this location is reasonably low (4.1 degrees) in comparison to the other outliers (6.1 and 9.5 degrees respectively).

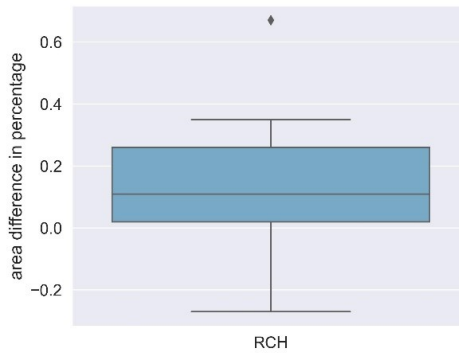


**Abbildung 7.6.** Boxplot graph showing the difference (in fractions) between the automatically and manually determined area of 25 RCHs.

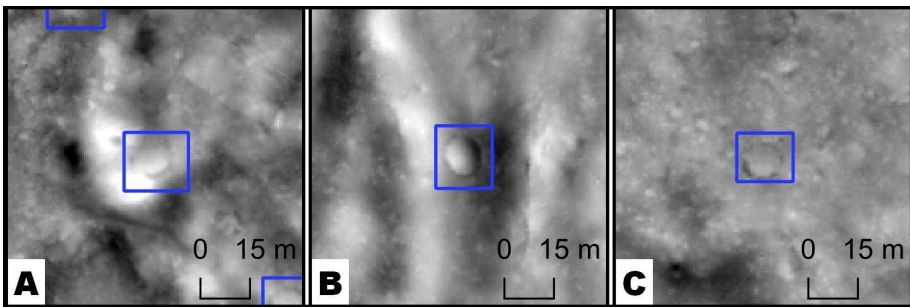


**Abbildung 7.7.** Excerpts of LiDAR data, in scale 1:2000, visualized with Simple Local Relief Model (Hesse, 2010), showing the three predicted RCH locations in blue outline.

#### 7.5.4 Application and Transferability of the ARCHMAGE workflow

Based on the results (section 7.4.3), model 2 was regarded as the most suitable to be used for large scale mapping of RCHs in the entire state of Connecticut. The testing time on circa 214,500 subtiles took about 40 hours on Colab, using a Nvidia T4, P100, or V100 GPU. The results were post-processed (see Section 7.4.3 and 7.5.3), which resulted in 43,197 detections. The distribution of these detections shows a clear concentration in the northwestern part of Connecticut, with up to 194 RCHs per sq. km (see Figure 7.8). The highest concentration can be found in the western part of the Salisbury district, in Sharon County. To get a first impression of the results, a comparison was made to the distribution of known RCHs, obtained through manually mapping, by Anderson (2019). Note that the latter only shows the presence or absence of RCHs, while our results also show the number of RCHs per sq.



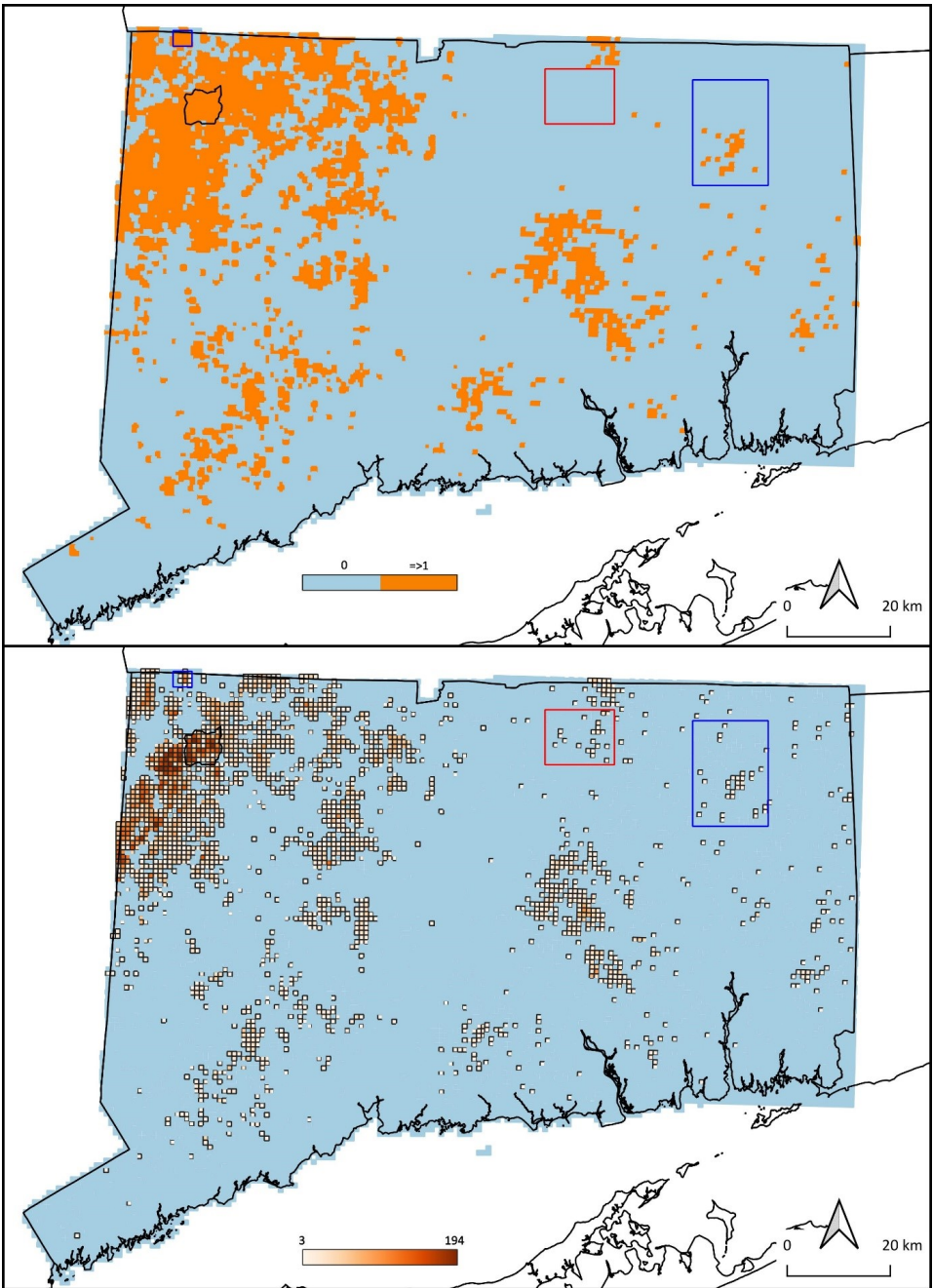


**Abbildung 7.8.** Overview of the distribution of RCHs (per sq. km) in the state of Connecticut, based on prior research by Anderson (2019; top) and current research (bottom). The top figure shows the presence (orange) or absence (light blue) of RCHs. The bottom figure shows the numbers of RCHs per sq. km (in shades of orange) or absence (light blue). Note that cells with less than 3 RCHs are omitted. The Training area is shown in black, the Test areas in blue. The red outline shows the newly discovered concentration of RCHs near West Stafford.

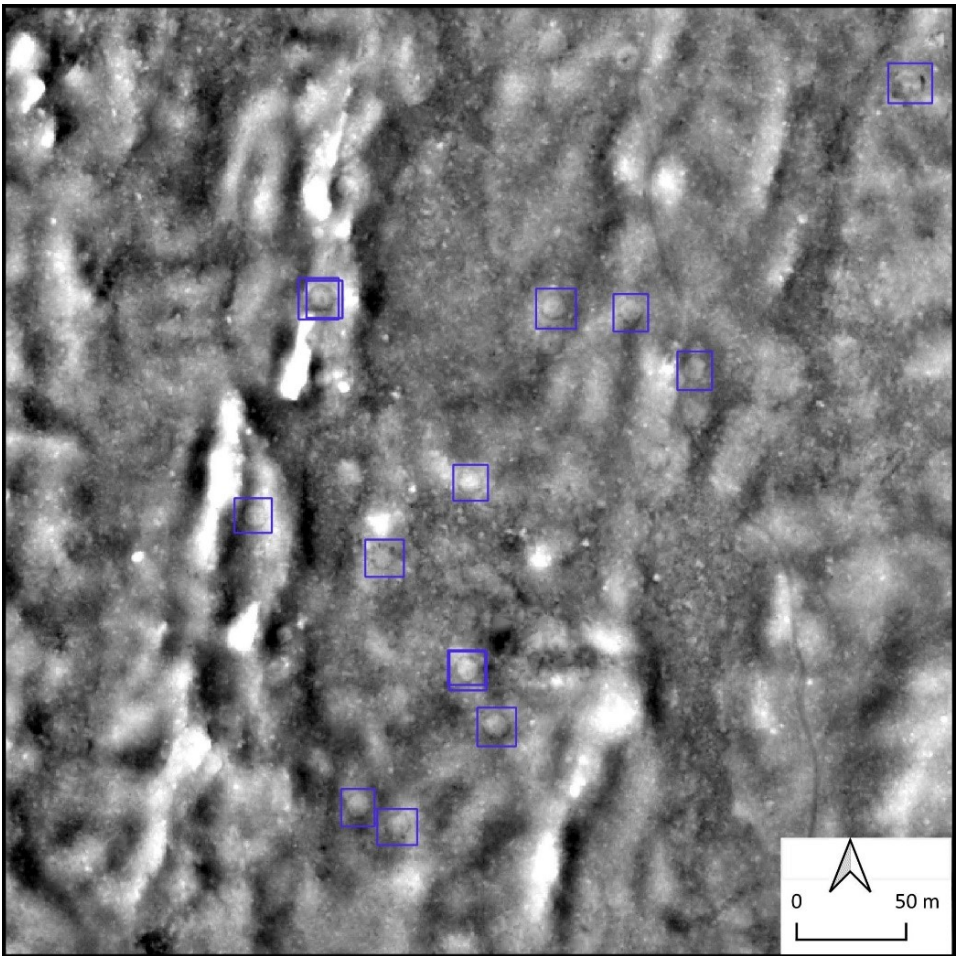


**Abbildung 7.9.** Excerpt of LiDAR data, visualized with Simple Local Relief Model (Hesse, 2010), showing part of the newly discovered cluster of RCHs in Shenipsit State Forest near West Stafford.

km (Figure 7.8). A visual inspection reveals a clear overlap between both distributions, with minor differences between the extents of individual concentrations. A major deviation can be observed in the northeastern part of the state (Figure 7.8, red outline). This was confirmed to be a concentration of previously unknown RCHs in Shenipsit State Forest near the town of West Stafford (Fig. 7.9). This demonstrates that ARCHMAGE is able to successfully detect RCHs over the entire state of Connecticut, even when the terrain and LiDAR quality varies.

## 7.6 Discussion

With the ever-increasing reliance of archaeologists on remotely-sensed data (Opitz & Herrmann, 2018)—with some even advocating for remote sensing as the primary source for archaeological prospection of large areas (Banaszek et al., 2018)—the usability of automated mapping approaches for large-scale archaeological survey becomes ever more important and necessitates investigation (Lambers et al., 2019). However, up-to-now the application of automated methods is generally limited to relatively small test areas, although a trend towards covering larger areas can be observed (e.g., Berganzo-Besga et al., 2021; Carter et al., 2021; Suh et al., 2021). Even though, questions concerning the reliability and transferability of these methods for large spatial scales remain (Cowley et al., 2020; Kermit et al., 2018; Verschoof-van der Vaart & Landauer, 2022). Presumably, the application on large areas is still mostly limited by DEM data availability, problems in handling and processing large amounts of spatial data, and, most pressingly, the uncertainty caused by changes in LiDAR data quality over larger areas. The usability of a method on areas with different topography, land-use, and/or LiDAR data quality is challenging. As shown in this research, variations in LiDAR data quality presumably caused by differences in data acquisition and processing (Opitz & Cowley, 2013) and/or varying land cover conditions (Bonhage et al., 2021; Cowley et al., 2020; Suh et al., 2021) can result in reduced and heterogeneous ground points densities and interpolation errors (Căteanu & Ciubotaru, 2020) that can greatly influence detection performance. As shown in this study (Table 7.5 & 7.6), increasing the spatial scale of the investigated area results in a drastic decrease in performance (see also Trier et al. 2021). Unsurprisingly, the efficiency of automated mapping approaches seems scale dependent (Bonhage et al., 2021). The effect of differences in LiDAR quality have also been noted in other research on automated- (Banasiak et al., 2022; Dolejš et al., 2020; Trier & Pilø, 2012) as well as manual mappings (Risbøl et al., 2013) of archaeological objects in LiDAR data. We showed that these variations in LiDAR data quality could be addressed by an additional post-processing step, without decreasing the information value of the LiDAR data (e.g., by increasing the resolution of the DEM although this could be a valid solution as well). The results of the application (Section 7.5.6) show that with this additional step, ARCHMAGE is able to efficiently and effectively detect RCHs on very large spatial scales.

Another obstacle appears to be the general low density of objects within the test areas. The former is a problem inherent to archaeological automated detection, as archaeological objects are more often absent than present in the landscape (Trier et al., 2021) and consequently the majority of the images in the test datasets will not contain an object of interest.

Identifying objects in such low-density datasets is a challenging task; not only for automated methods but also for domain experts, with a decrease in object density having a negative influence on performance (Soroush et al., 2020; Verschoof-van der Vaart, 2022). When the density of objects decreases it negatively influences performance. This is, apart from the problem with LiDAR data quality outlined above, the most probably cause of the decrease in performance of our method between Test area 1 (high-density: 29 RCHs / sq. km) and Test area 2 (low-density: 1.75 RCHs / sq. km; see also Table 7.1). In addition, the objects within our test datasets are generally small and scarcely distributed, especially compared to objects in more general image datasets, such as the Microsoft COCO dataset (Lin et al., 2014), which are often large and predominately present (see for instance Verschoof-van der Vaart, 2022, Fig. 7.2.). Deep Learning methods take advantage of the large size of objects to reduce computational cost by downscaling images when they pass through a CNN. However, this also removes small objects, rendering them impossible to detect (Olivier & Verschoof-van der Vaart, 2021). Small and scarcely distributed objects lead to the problem of foreground-background class imbalance in object detection (Oksuz et al., 2019), where one class is over-represented, in this case the background class, while the other class (foreground, i.e., the archaeological objects) is under-represented (Luque et al., 2019). This imbalance can have a major impact on the classification and generalization capacity of CNNs, leading to bias and low performance, as these are generally geared towards detecting large, abundantly present objects.

A final challenge when using automated detection on a large scale is the matter of validating the results, as using a singular methodology as the primary source of information, without verifying the results, seems neither scientifically sound, nor desirable (Bennett et al., 2014). However, manually verifying all detections made on such a large spatial scale runs the risk of moving the professional bottleneck (Smith, 2014) from manual analysis to manual verification, especially when automated approaches with middling performance are used. Therefore, either an approach with very high performance is required, or alternative strategies need to be explored to verify the results (Trier et al., 2021; Verschoof-van der Vaart et al., 2020), such as the use of citizen science (Herfort et al., 2019; Lambers et al., 2019). Notwithstanding, the need for detailed verification is very dependent of how the method and its results are embedded within the wider research framework (Banaszek et al., 2018; Cowley et al., 2020; Lambers et al., 2019; Opitz & Herrmann, 2018). In the case of this research, the aim was to develop a method that can be used in subsequent research on legacy effects on a landscape scale (see Section 1). As such, the validation and correctness of every single detection might not be necessary (see also Soroush et al., 2020). Alternatively, a shift may

become necessary from a fixation on individual detections being correct, to the overall patterns being descriptive (Cowley, 2012; Sadr, 2016). While individual detections might not always be correct; the overall patterns in the landscape might be correctly reproduced by the automated method (Gallwey et al., 2019). For instance, the comparison in distribution of RCHs in Connecticut, as shown in Figure 8, can inform us on of the methods 'pattern descriptiveness'. Although the true value of using automated detection would lie in the discovery of RCHs in areas priory devoid of these objects of interest, i.e., deviations from the prevailing pattern.

## 7.7 Conclusion

In this research we presented a novel approach (ARCHMAGE) based on open source data and software to automatically detect relict charcoal hearths (RCHs) in large-scale LiDAR datasets and simultaneously provide general as well as domain-specific information. The workflow consists of three steps: a preprocessing step that converts the DEM data into input images (subtiles), based on geospatial information about known RCHs; a step concerning the Deep Learning-based object detection; and a post-processing step where the results of the object detection are converted back into geospatial data. In addition, two domain-specific parameters, i.e., area and local slope are calculated. Our study shows that ARCHMAGE is able to effectively detect RCHs in Connecticut, with F1-scores ranging between 0.21 and 0.76, although an additional post-processing was needed to deal with variations in LiDAR quality between different test areas. The results of applying best performing version of the prediction model (with an average F1-score of 0.56) on the entire state of Connecticut show a clear overlap with the known distribution of RCHs in the region, while new site clusters were found as well, showing the usability of the approach on large-scale datasets even when the terrain and LiDAR quality varies. Future research will focus on the improvement of the overall workflow and especially the generation of domain specific information. For instance, preprocessing of the LiDAR data to remove interpolation errors would enhance the performance of the workflow. Additional post-processing is envisioned to deal with overlapping bounding boxes, caused by the overlap in the subtiles (which is estimated to occur in circa 4 % of all detections). Another possible angle of research would be to use semantic segmentation (e.g., Guyot et al., 2021) to improve the calculation of domain specific information. Furthermore, the results of the statewide detection and analysis will be used in subsequent research to analyze site distributions as well as morphological- and pedological legacy effects of historic charcoal burning on a landscape scale. The additional information of the sites local slope and surface area will be used to calculate specific site volumes and

subsequently how much soil substrate was moved and what the sites element stocks are. The datasets and methods created in this research will be made freely available in the near future.

## 7.8 Acknowledgements

We are thankful to Jin Wo Suh for facilitating helpful discussions. We also would like to thank Martin Olivier for his assistance on the development of the python scripts and Mark Grimm for proof-reading the manuscript. We are grateful to the reviewers for their constructive comments. This research was funded by the German Research Foundation (DFG) under grant number RA 931/8-1.

# 8 From site to state - Quantifying multi-scale legacy effects of historic landforms from charcoal production on soils in Connecticut, USA

This chapter is published as: Bonhage, A., Raab, T., Schneider, A., Raab, A., Ouimet, W., Völkel, J., Ramezany, S.: From site to state - Quantifying multi-scale legacy effects of historic landforms from charcoal production on soils in Connecticut, USA. *Catena*. <https://doi.org/10.1016/j.catena.2023.107426> The Annex contains additional, previously unpublished material regarding concentrations of exchangeable cations, pedogenic (hydr)oxides and total element concentrations.

## 8.1 Abstract

Relict charcoal hearth (RCH) landforms are relatively small (average diameters of 11 m) and circular microrelief features found in many forests of the North-Eastern USA and Central Europe. Soils on RCHs are special in that they are significantly enriched in organic- (OC) and pyrogenic carbon (PyC), caused by the admixture of charcoal. Many studies have shown that this results in changed soil chemical and physical properties, making RCHs unique soil microhabitats. However, questions about their larger impact on a soil landscape's carbon storage have hardly been studied so far; an aspect that could become more relevant with growing RCH site location databases. Here we show that RCHs can substantially add to a landscape soil organic- and pyrogenic carbon storage. This effect is scale dependent, i.e. a larger scale of observation (1:20,000) will result in significant additions for areas with high site densities (+ 22.6 % OC, 128.6 % PyC), contrary to smaller scales of observation (>1:650,000) where the effect is diminished (+ 0.2 % OC, + 1.2 % PyC). A comparison with

a nationwide soil database (gSSURGO) shows that in areas with high site densities, individual soil unit OC contents are increased by up to 91.6 %. An exemplary comparison to historic terrace/lynchet systems shows that RCHs store vastly more carbon when pedons of the same size are compared. However, if the actual landform surface areas are taken into account, RCHs store a lot less. This is showcasing the spot-like distribution of RCHs on a landscape scale. Furthermore, we broaden the knowledge about RCH site specific properties in Connecticut by a first analysis of pedogenic (hydr-)oxide and exchangeable cation concentrations, with the result indicating increased weathering rates and enrichment of exchangeable  $\text{Ca}^{2+}$ ,  $\text{Mg}^{2+}$  and  $\text{Mn}^{2+}$  in RCH soils.

## 8.2 Aims

We hypothesize that, in addition to site-specific legacy effects, the historic charcoaling industry in Connecticut caused changes to soils that are quantifiable on a landscape scale. With this study, we aim at complementing the existing database of known site-specific RCH soil properties in Connecticut, USA, with a focus on exchangeable cations and pedogenic (hydro-)oxides indicating changes in the mineral phase of the soils affected by the charcoal burning. Furthermore, we aim at gaining information about the extent of legacy effects in the state of Connecticut (USA) on four scales: site (single/individual RCH platform), landscape (1:20,000), county/district (1:650,000) and state (1:1,250,000). In a geopedological approach, we combine available RCH soil chemical and physical properties, determined by this and already published studies and a state wide site mapping. We assess site aggregation patterns and correlations with topographical positions and relief ruggedness parameters. Furthermore, we calculate anthropogenically redistributed soil substrate masses and element stocks of RCHs. With this we aim at gaining a more holistic view of the extent of legacy effects of RCH soils on today's soils and landscapes.

The specific aims of the study are to:

- Determine the RCH- and reference soils horizons total element and pedogenic (hydro-) oxide concentrations to analyse rates of crystallinity and assess weathering activity;
- Determine concentrations of exchangeable cations;
- Statistically analyse morphometric variables of RCH landforms (volume, mass, surface area);
- Analyse RCH locations in terms of terrain ruggedness and topographic position;



- Assess the RCH landforms legacy effect on organic-pyrogenic carbon stocks from a site to a landscape scale.

## 8.3 Methods

### 8.3.1 RCH soil property database

This study builds on data gathered from previously published studies (Bonhage et al. 2020, Bonhage et al. 2022). 52 RCHs along two catenas have been extensively sampled volumetrically in 5 cm vertical spacing (honouring horizon boundaries) on three positions within a site (upslope, middle, downslope); with one reference soil profile being sampled outside each site. TOC concentrations have been measured by dry combustion using a total element analyser (Elementar© Vario Max Cube). Pyrogenic carbon concentrations have been measured using a modified benzene-polycarboxylated acid (BPCA) method with a subsequent conversion factor of 2.27, in combination with a chemometric approach predicting BPCA-C concentrations using FTIR-MIR spectra. Soil acidity (pH) was measured in 0.01 M CaCl<sub>2</sub> (1:2.5 w:w).

### 8.3.2 Soil chemical analysis

Further analysis was conducted on representative subsets of the dataset described in section 3.1. Total element concentrations and cation exchange capacity was measured on 85 samples from 5 RCH sites and 59 samples from 11 reference soils. Total element concentrations are determined by aqua regia (1:3 65 % HNO<sub>3</sub> + 35 % HCl) digestion in a Mars 6 Synthesis microwave system and subsequent element determination using plasma atomic emission spectroscopy (MP-AES 4100, Agilent). Exchangeable elements and effective cation exchange capacity (CEC) are determined according to Hendershot et al. (2006) using BaCl<sub>2</sub> as cation displacement agent with subsequent element determination by MP-AES. Pedogenic (hydro-)oxides are determined for 42 samples from the same 5 RCH sites and for 19 samples from 6 reference soils by using 1g sample material in a sequential extraction (Völkel 1995) with Sodium-Pyrophosphate (Na<sub>4</sub>P<sub>2</sub>O<sub>7</sub>), Ammonium-Oxalate ((NH<sub>4</sub>)<sub>2</sub>C<sub>2</sub>O<sub>4</sub>) and Sodium-Dithionite (Na<sub>2</sub>S<sub>2</sub>O<sub>4</sub>), with element concentrations being determined by atomic absorption spectroscopy (AAS, Thermo Scientific™ iCE™ 3000). The non-parametric Mann-Whitney-U (SPSS 14, IBM) test was applied to check for statistical significance when comparing soil parameters.

### 8.3.3 GIS based quantification of legacy effects

#### 8.3.3.1 Calculating RCH site Volume & Mass

We utilize a recent DEM-based mapping of RCH sites covering the complete state of Connecticut that not only describes the location of sites, but also provides their surface area and the local slope on which they are build (Verschoof-van der Vaart et al. 2022). To calculate RCH site volumes, substrate masses and element stocks, we utilize a process described by Bonhage et al. (2020) that geometrically abstracts RCH sites to cylinders. For sites on slopes, the thickness and stratigraphy are correlated to the local slope of each site (i.e. an RCH sites overall thickness will increase the steeper the slope is its build upon). For sites on flat terrain, an average thickness is assumed. A slope threshold of  $4^\circ$  is used to classify sites as either single-layered flatland sites ( $< 4^\circ$ ) or multi-layered sloped sites ( $> 4^\circ$ ). With this approach, we assume that an RCH is a self-contained epipedon that lies sharply delineated from adjacent pedons within the natural soil landscape. Average bulk densities for RCH soil horizons are used as described by Bonhage et al. (2020): Auh  $0.69 \text{ g cm}^{-3}$ , 2Cu  $0.89 \text{ g cm}^{-3}$  and 3Auh  $0.81 \text{ g cm}^{-3}$ .

#### 8.3.3.2 RCH site distribution

e state-wide site density per  $\text{km}^2$  was calculated using the Point Density toolbox of ArcGIS 10.4.1 (cellsize 10 (feet), circle with radius of 250 m) and then classified for visualisation using Natural Breaks (Jenks) (10 classes). The Terrain ruggedness Index (TRI) and Topographic Position Index (TPI) were calculated based on a DEM with 10-meter cell size based on state wide available LiDAR data (2016, CTECO, <http://www.cteco.uconn.edu/>). The TRI was calculated in SAGA-GIS 8.4.0. The index gives information about topographic heterogeneity by calculating the sum change of elevation values between a grid of eight cells around a target cell (Riley et al. 1999). Lower values of TRI indicate less rugged-, larger values more rugged terrain. For ease of computation, TRI values were grouped into ten classes (1 = low, 10 = high), whereby class boundaries are determined by Natural Breaks (Jenks). To classify landscape positions, we applied the Topographic Position and Landform Analysis workflow implemented in the Land Facet Corridor toolbox (v.1.2.884) for ArcGIS 10.4.1. Thereby, the TPI (standardized elevation) is created and classified according to Weiss (2000) (circle, radius = 50 cells). To classify the 6 slope positions (Ridge, Upper-, Steep Slope, Flats, Lower Slope, Valley) suggested by the author, we use his thresholds for TPI standard deviation units, which proved to be sensible for our study area. To analyse the occurrence of significant spatial clusters of large and small RCH sites, we applied the Getis-Ord  $G_i^*$  sta-

tistic, as implemented in ArcGIS 10.4.1. The test gives information about local pockets of spatial dependence within a dataset (Getis & Ord 1992), i.e. it does not indicate the location of sites that are larger (Hot Spots) or smaller (Cold Spots) than the datasets global mean, but the location of significant spatial clusters (aggregations) of such sites. We used the tool-box Optimized Hot Spot Analysis of ArcGIS 10.4.1 to determine the optimal fixed distance band to 30 nearest neighbours for the Cluster analysis, which is 1265 meters.

### 8.3.3.3 Calculating Forest SOC stocks and comparison with soil survey data

Forest soil SOC stocks for Connecticut are calculated based on a land cover dataset (30 meter cell size) that gives areas for mixed, coniferous and deciduous forests (NLCD 2016 Landcover, <https://www.mrlc.gov/data>) in combination with published concentrations of SOC storage in forest soils (compiled by Tomasso et al. 2014). We averaged the given concentrations for coniferous ( $52.6 \text{ Mg ha}^{-1}$ ) and deciduous ( $78.5 \text{ Mg ha}^{-1}$ ) forests soils to get a mean for mixed forests soils ( $65.5 \text{ Mg h}^{-1}$ ). Total stocks were then calculated by multiplying forest areas with the given SOC stocks per hectare. We estimated PyC stocks for forest soils based on the available average SOC and PyC concentration and ratio for Ah-, Bw, and C-horizons (est. 0 – 50 cm depth) (Bonhage et al. 2022). The result shows that 14.4 % of SOC in forest soils can be estimated to be PyC, which is within the range of usually reported ratios (Reisser et al. 2016).

Additionally, we compare added SOC stocks from RCHs to forest soils using properties from a frequently used nationwide soil database (Gridded Soil Survey Geographic Database, gSSURGO, Soil Survey Staff, 2022). Thereby, carbon stocks for soil units (polygons) are calculated using their given area and carbon concentrations per square meter (0 – 100 cm depth). These soil unit SOC stocks are then compared to the TOC contents of all RCH sites within each polygon.

## 8.4 Results and Discussion

We sorted the results for better reading comprehension. First we discuss site specific results, then, for the larger scale analysis, we grouped the results into site distributions, morphological legacy effects and carbon stock legacy effects.

## 8.4.1 Site scale

### 8.4.1.1 Carbon, pH and exchangeable cations

A recent study (Bonhage et al. 2022) has shown that total organic carbon and pyrogenic carbon concentrations of sites in the Litchfield area (Tab. 1) are well aligned with previously published results for sites in Connecticut and elsewhere (Donovan et al. 2021, Raab et al. 2022). Total organic carbon concentrations, as well as highly aromatic (pyrogenic) carbon concentrations are significantly increased for the Auh and Cu horizons compared to other horizons. Buried horizons, notably the Ahb, have increased PyC concentrations. Soil acidity, measured as pH value, is slightly stronger for Ah and Auh horizons, presumably caused by humification of fresh litter and, additionally, by charcoal degradation processes resulting in the formation of aromatic acids in Auh horizons. Effects on soil pH as seen during initial phases of biochar application (liming effect), are generally not reported for RCH soils, as for most sites there is no distinct difference to reference Ah-horizons (Raab et al. 2022).

**Table 8.1.** Averaged total organic carbon (TOC), pyrogenic carbon (PyC) and pH values for RCH (Auh, Cu), reference (Ah, Bw, C) and buried soil horizons (Ahb, Bwb) (data taken from Bonhage et al. 2022)

	n	TOC+ [g kg <sup>-1</sup> ]	PyC* [g kg <sup>-1</sup> ]	pH [CaCl <sub>2</sub> ]
Auh	42	94.6	78.5	4.2
Cu	8	38.4	25.6	4.7
Ah	5	53.8	4.0	4.1
Ahb	11	17.4	9.5	4.7
Bw	10	13.3	4.5	4.5
Bwb	23	16.8	5.1	4.8
C	7	8.6	2.4	4.9

+ determined by dry combustion, see Bonhage et al. (2022) \* determined by benzene-polycarboxylated-acid markers, see Bonhage et al. (2022)

While the increased CEC of Auh horizons compared to reference Ah horizons (Tab. 2) is not significant ( $p = 0.13$ ), the difference in the sum of certain exchangeable cations is. Thereby, exchangeable  $\text{Ca}^{2+}$ ,  $\text{Mg}^{2+}$  and  $\text{Mn}^{2+}$  concentrations are significantly increased in Auh horizons ( $p < 0.05$ ), while  $\text{Fe}^{3+}$ ,  $\text{K}^{+}$  and  $\text{Na}^{+}$  concentrations are significantly decreased ( $p < 0.05$ ). Increases in  $\text{Ca}^{2+}$  and  $\text{Mg}^{2+}$  concentrations have been reported for RCH soils (Mastrolonardo et al. 2019, Hirsch et al. 2018) and linked to the increased presence of phenolic and carboxylate groups on aged charcoal in soils (Burgeon et al. 2022). Notably, exchangeable  $\text{Mg}^{2+}$  and  $\text{Ca}^{2+}$  are increased in buried horizons as well, although to a comparably lesser degree and only significantly for Bwb-horizons ( $p < 0.05$ ) when compared to reference Bw-horizons. This is potentially indicating vertical leaching of cations,

**Table 8.2.** Cation exchange capacity (CEC in cmolc kg<sup>-1</sup>) and exchangeable cations (in cmolc kg<sup>-1</sup>) for reference (Ah, Bw, C), technogenic (Auh, Cu) and buried soil horizons (Ahb, Bwb). BS (%) and Al (%) give the base- and aluminium saturation

Soil Horizon/	Auh	Cu	Ah	Ahb	Bw	Bwb	C
ex. elements	n = 31	n = 7	n = 14	n = 5	n = 32	n = 24	n = 11
CEC	10.96	8.04	6.40	5.10	3.99	4.19	3.32
Fe	0.01	0.02	0.02	0.01	0.06	0.03	0.02
Al	2.07	1.30	0.45	0.31	2.24	0.54	0.36
Mn	0.16	0.09	0.05	0.02	0.07	0.01	<0.01
Ca	6.14	4.53	2.83	2.24	1.89	1.57	1.51
Na	1.09	1.03	0.98	0.94	1.31	1.15	0.90
K	0.16	0.11	0.09	0.08	0.21	0.10	0.12
Mg	1.26	0.97	0.70	0.58	0.47	0.36	0.36
BS %	73	79	62	91	85	91	89
Al %	25	20	36	8	14	8	10

which could be linked to leaching of aromatic acids originating in the charcoal rich substrate (Bonhage et al. 2022). That is especially relevant for Ca<sup>2+</sup> (Kalinichev & Kirkpatrick 2007). Leaching of K<sup>+</sup>, as reported for RCH sites under agricultural use (Burgeon et al. 2022), cannot be proven for our study area.

#### 8.4.1.2 Pedogenic (hydr-)oxides

The extraction of pedogenic iron, aluminium and manganese can give information about the weathering state of a soil (e.g., Blume 1969). Figure 8.1 shows concentrations of pedogenic oxides and ratios of activity ( $Fe_o/Fe_d$ ), as well as crystallinity ( $Fe_d/Fe_t$ ) (see also Annex Tab. A1). Brunification, the release of iron by weathering of minerals and formation of secondary iron oxides, is the dominant pedogenic process in our study area and can be seen by studying the soil morphology. This process is also reflected in the highest  $Fe_d$  concentrations in Bw horizons of the reference soils. Activity- and crystallinity ratios are slightly increased for RCH and buried soils, with the exception of a markedly higher activity ratio for Ah horizons and almost equal activity ratios for Bwb and Bw horizons (Fig. 8.1). This suggests an increased overall weathering state of iron in soils affected by historical charcoal production, not only in terms of crystalline iron compounds, but also in terms of amorphous ones.

High activity ratios are usually found in Ah-horizons, where organic matter contents can result in unfavourable conditions for crystallisation (Blume & Schwertmann 1969). The disparity between Auh- and Ah- horizons activity ratio could indicate that changes to pedogenic oxides are not the result of an pedogenic process, but rather the direct result of

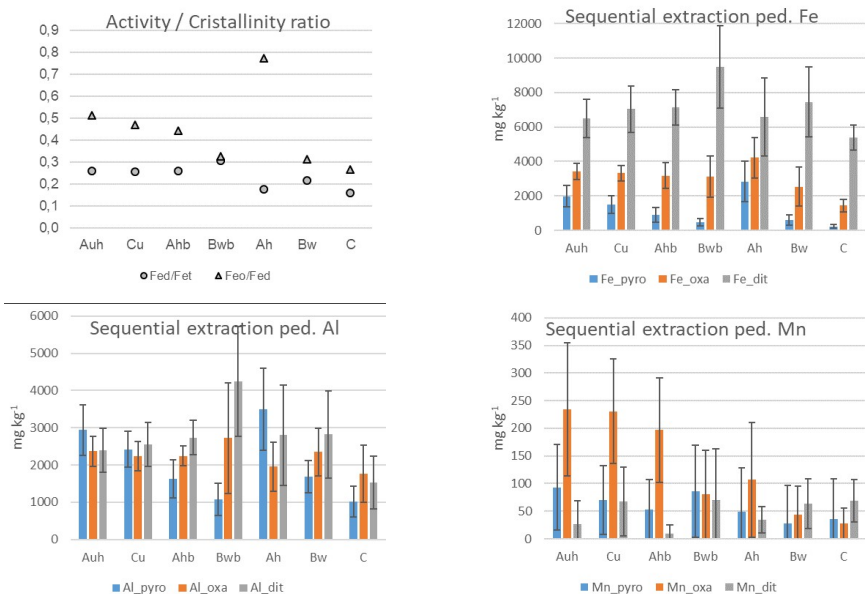


**Abbildung 8.1.** Concentrations of sequentially extracted pedogenic oxides (pyro – pyrophosphate, oxa – oxalate, dit – dithionite) in RCH soil (Auh, Cu), buried soil (Ahb, Bwb) and reference soil (Ah, Bw, C).

heating the mineral substrate during the hearths operation. Qualitative changes to pedogenic iron (hydr-)oxides in RCH- and buried soils haven been described in Germany. Ther- eby, the RCH soil horizons and sometimes the topmost centimeters of buried B-horizons have heat-induced increased contents of magnetite, maghemite and hematite, causing an increase in the magnetic mass susceptibility (Hirsch et al. 2018). This effect of pyrogenic magnetic enhancement is also seen for wildfire affected soils, and is there discussed at least partly to be caused by minerals originating from burned vegetation ash that has been in- corporated into the topsoil (Jordanova et al. 2019a).

Most prominent is the increase of  $Mn_{ox}$  in the Auh, Cu and the buried Ahb horizon, which comes to around +65 % when compared to the reference Ah horizons (Fig. 8.1, Annex A1). Furthermore, for Auh horizons the amount of exchangeable  $Mn^{2+}$  is increased by +128 % compared to Ah horizons ( $p < 0.05$ ). Manganese is accumulated in acidic topsoils by plant uptake of soluble  $Mn^{2+}$  and consequent litter decomposition that leads to the oxidation of  $Mn^{2+}$  to insoluble Mn oxides in the soil environment (Li et al. 2021). The oxidation of mobile  $Mn^{2+}$  is dominantly facilitated by biotic processes (e.g. bacteria and fungi) (Tebo et al. 2004). Abiotic oxidation processes can take place, e.g. oxidation by reaction with Fe-

**Table 8.3.** Total element concentrations of recovered macroscopic charcoal pieces from two RCH sites

Sample ID	Ca	Mg	Mn	Al	Na	K
				mg kg <sup>-1</sup>		
45-3a	7,669	1,275	958	11,850	618	761
45-3b	8,154	1,364	1,009	12,557	704	773
56-3a	9,023	1,251	597	10,266	728	1037
56-3b	8,213	1,127	534	9,316	718	984

oxides, however, they are favoured mostly in alkaline conditions (Li et al. 2021). Relatively high concentrations of total Mn in recovered charcoal pieces (Tab. 8.3) let us assume that charcoal is the main source of additional Mn<sup>2+</sup> in RCH soil. Increase of Mn concentrations are also reported for wildfire affected soils (Jordanova et al. 2019b).

As studies focusing on microbial characteristics of RCH soil are very rare so far, future research should also address the potential effect of increased Mn concentrations on microbial growth in RCH soils. First studies show no significant differences in microbial biomass in RCH soils under agricultural use (Kerre et al. 2017) and some changes in fungal (Garcia-Barreda et al. 2017) and bacterial abundance and composition (Lasota et al. 2021, Gießelmann et al. 2019). Bonhage et al. (2022) found potential evidence for changed SOM turnover dynamics in RCH soils in Connecticut, which is especially interesting in this context given the key role of manganese as a biotic and abiotic oxidizer of soil organic matter (Li et al. 2021). Wildfire affected soils can exhibit changes to microbial activity that influence pedogenic oxide contents of soils (Jordanova et al. 2019b), however it is unknown if this effect happened or is still present in the centuries old RCH soils.

## 8.4.2 Landscape, County and State scale

### 8.4.2.1 State-wide site distribution

In total, 34,692 RCH sites are included in the available state-wide dataset, whereby 8,187 sites (24 %) are located on terrain with a slope < 4°. Therefore, they can be classified as single-layered type 2b RCHs (sites on flat land) according to Hirsch et al. (2020). Conversely, 26,505 sites (76 %) are located on terrain with a slope > 4°, making them multi-layered type 3b RCHs (sites on slopes). We use Connecticut's county and township boundaries as a mean of segmenting the area. The site distribution shows that the largest impact of the historic charcoaling industry took place in Litchfield county, where 60 % of all RCH sites and the highest site densities (310 per km<sup>2</sup>) are found (Fig. 8.2A). Thereby, townships in the Salisbury Iron District (Sharon, Cornwall, Kent, Canaan and Litchfield) have the hig-

hest site occurrences in Litchfield county on mountains along the Housatonic River.

The Getis Gi\* cluster analysis shows the presence of multiple hot spots (cluster with larger sites) and cold spots (cluster with smaller sites) throughout the state of Connecticut (Fig. 8.2B). Thereby, 9,780 sites are part of hot spots and 6,107 part of cold spots. Most notably is the abundance of cold spots in the eastern part of the state versus the occurrence of hot spots in the western part. Hot Spots are especially prevalent in Litchfield county, which further highlights the concentration of charcoaling efforts around the Salisbury Iron District that resulted not only in more, but also bigger RCH sites. Other noticeable site aggregations (100 sites per km<sup>2</sup> or more) are located in south east Hartford, centering around the town Marlborough, in north eastern Fairfield near Newtown along the Housatonic River and in western Hartford near the towns Burlington and Simsbury.

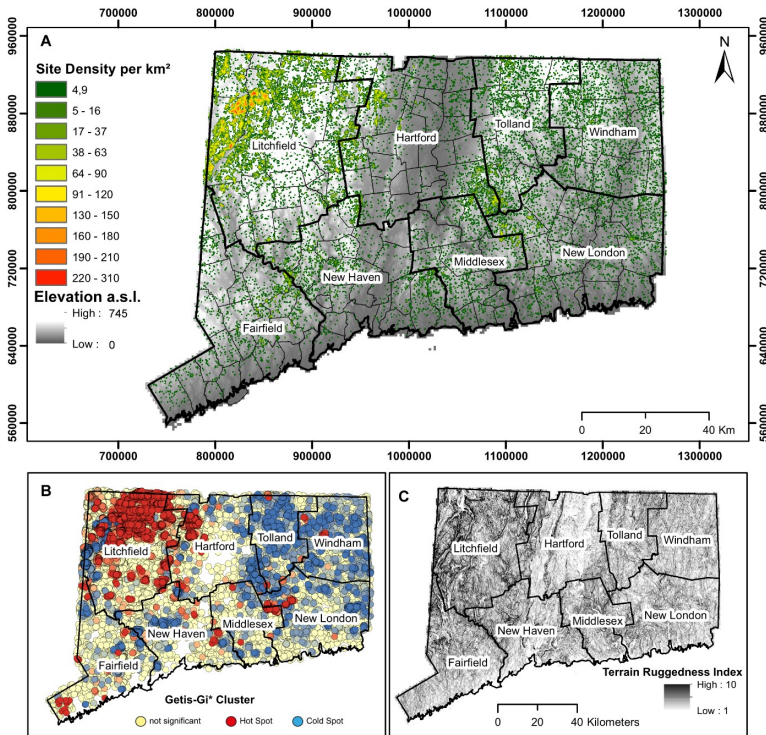


**Abbildung 8.2.** A) RCH site density in the state of Connecticut. Site locations are taken from Verschoof-van der Vaart et al. (2022). DEM data, State- and County boundary polygons are taken from the Connecticut Department of Energy and Environmental Protection (CTECO, <http://www.cteco.uconn.edu/>), Coordinate system WKID: 6434.; B) Map of Getis-Gi\* Clusters for RCH sites areas. Hot Spots indicate significant spatial clusters of larger sites; Cold Spots indicate significant spatial clusters of smaller sites. C) Map of the state-wide Terrain Ruggedness Index (TRI).



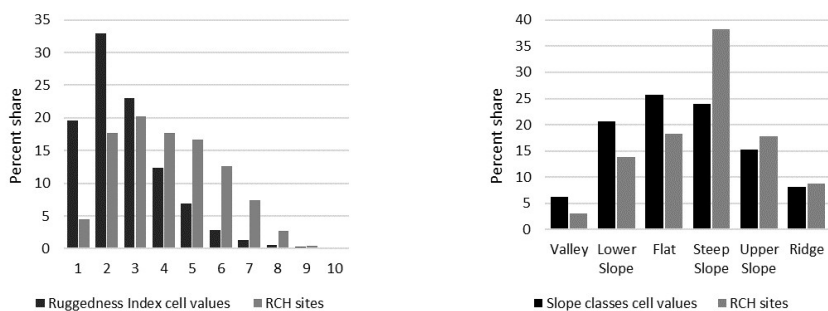


**Abbildung 8.3.** State-wide A) Terrain Ruggedness Index (TRI) cell values for each class (1 level, 10 extremely rugged) compared to RCH site occurrence, B) Topographic Position Index (TPI) cell values for each class compared to RCH site occurrence.

The state-wide Terrain Ruggedness Index (Fig. 8.2c, Fig. 8.3a) indicates an increase in ruggedness towards the western part of Connecticut and the onset of the Appalachian mountain massife, with its highest values being reached in the Salisbury Iron District. TRI cell values  $\leq 5$  make up 95 % of the states total area, while 77 % of RCH sites are located on them. The remaining 23 % of all sites are located on 5 % of the state's area with TRI values  $> 5$ , showing a slight proclivity of site occurrences toward rougher terrain. This is in contrast to findings from Europe, where in two study areas (North German Lowland and Northern Bavaria) RCH site occurrences tended to increase towards flat, less rugged terrain (Schneider et al. 2020). Taking into account TPI derived slope positions (Fig. 8.3b), 37 % of RCH sites are located on steep slopes that make up 24 % of state-wide cell values. Aggregating RCH sites occurrences for TPI classes signifying sloped terrain in general (Ridges, Upper Slope, Steep Slope, Lower Slope) gives a sum of 79 %, while 3 % are found in valley positions, and 18 % on flat terrain. Potentially, there are two major drivers towards the increased abundance of sites on sloped terrain. First, the steepest and most rugged terrain is found in the area of the historic Salisbury Iron District, a mountainous area with abundant opportunities for ore-mining and iron smelting industries. Secondly, the rough conditions encountered by the settlers and early New England inhabitants made it necessary to distribute the landscape pragmatically: land suitable for agriculture was used as such, making upland forests and steep hills a preferred site for charcoal production (Gordon 2001).

Other large scale studies of RCH site distributions in Germany note a similar aggregated pattern, where increased site densities could often be related to the location of historical industrial sites; but also often times lack an obvious spatial relationship, especially in heterogeneous terrain where relief and morphology then become an important factor in site

**Table 8.4.** Measured and calculated morphometrics and mass for relict charcoal hearth sites in the state of Connecticut (average  $\pm$  one standard deviation).

Geographic boundary	RCH sites*	Average RCH surface Area*	Average RCH Volume	Average RCH mass	Total RCH mass
	n	m <sup>2</sup>	m <sup>3</sup>	Mg	Mg
Connecticut St	34,692	183 $\pm$ 52	103 $\pm$ 46	75.6 $\pm$ 35.3	2,622,888
Litchfield Ct	21,573	191 $\pm$ 48	117 $\pm$ 41	86.5 $\pm$ 31.2	1,866,976
Fairfield Ct	1,721	174 $\pm$ 60	87 $\pm$ 47	63.3 $\pm$ 35.8	108,980
Hartford Ct	3,681	183 $\pm$ 54	91 $\pm$ 47	66.4 $\pm$ 35.4	244,500
New Haven Ct	1,714	169 $\pm$ 58	84 $\pm$ 45	61.0 $\pm$ 34.1	104,622
Middlesex Ct	1,143	172 $\pm$ 55	76 $\pm$ 43	55.3 $\pm$ 32.1	63,307
Tolland Ct	1,682	153 $\pm$ 50	70 $\pm$ 42	50.9 $\pm$ 31.3	85,648
Windham Ct	1,447	151 $\pm$ 58	62 $\pm$ 41	44.7 $\pm$ 29.94	64,702
New London Ct	1,731	162 $\pm$ 55	67 $\pm$ 40	48.6 $\pm$ 30.4	84,149

\* Site information taken from Verschoof-van der Vaart et al. (2022)

occurrences (Schneider et al. 2020). Furthermore, cluster of larger and smaller sites within areas of high RCH site densities have been discussed as resulting from charcoaling activities during different time periods, a rapid overabundance of wood (e.g. caused by calamities) or other local peculiarities that influenced the intensity of charcoal production (Raab A. et al. 2017).

#### 8.4.2.2 Morphological legacies

State wide, the estimated average surface area of all sites is  $183 \pm 52 \text{ m}^2$  (Tab. 8.4), which means their average diameter is  $15.2 \pm 8.1$  meters. For type 3b sites on slopes, the average diameter is  $15.3 \pm 8.0$  meters, for type 2b sites on flatlands its  $15.0 \pm 8.7$  meters. This is well above the average (field mapped) size of sites in study areas previously reported in the county of Litchfield, that show averages of around 11.5 meters by Bonhage et al. (2020) and 9.5 meters by Raab T. et al. (2017). We see two possible reasons for this. Firstly, the majority of sites mapped in the aforementioned studies are within a cold spot (Fig. 8.4A close up). Secondly, the difference between field- and DEM-based measured sites can be considerable, as the determination of exact dimensions and edges of sites on DEMs is inherently inaccurate when compared to field mappings. The DEM based mapping tends to overestimation (Verschoof-van der Vaart et al. 2022).

The average RCH site has a volume of  $103 \pm 46 \text{ m}^3$  and mass of  $7.6 \pm 3.5 \text{ Mg}$  (Tab. 8.4). For type 3b sites on slopes the average is  $122 \pm 34 \text{ m}^3$ , for type 2b sites on flatland it is  $40 \pm 13 \text{ m}^3$ , which shows that sloped sites have more mass due to being multi-layered and their general construction principle. In total, our estimation shows that colliers moved and re-distributed more than  $2.6 \times 10^6 \text{ Mg}$  of soil substrate state-wide for the charcoaling industry

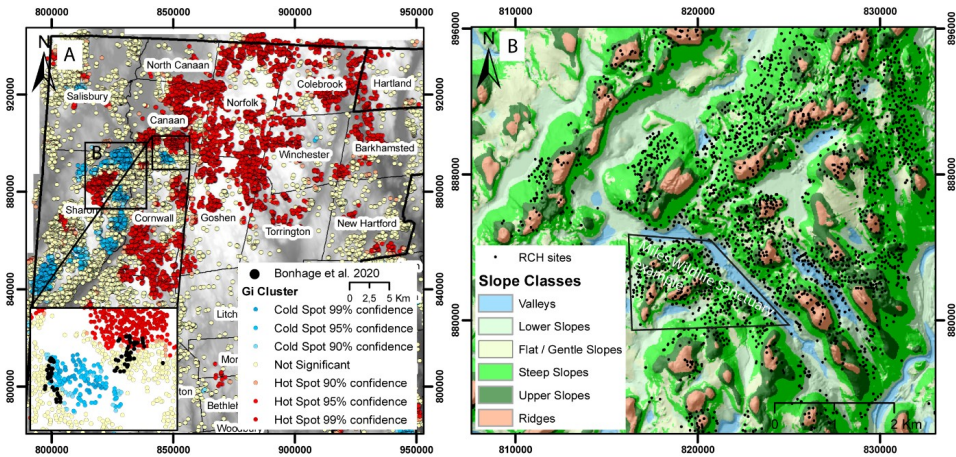


**Abbildung 8.4.** A) RCH site Getis-Gi\* cluster along the Housatonic River in Litchfield County, Connecticut. B) Detail view of RCH locations related to slope positions and boundary of the Miles Wildlife Sanctuary site aggregation example. Site locations are taken from Verschoof van-der Vaart et al. (2022). DEM data, State- and County boundary polygons are taken from the Connecticut Department of Energy and Environmental Protection (CTECO, <http://www.cteco.uconn.edu/>).

(Tab. 8.4), whether it be by building the platform, or reusing available RCH substrate for multiple burnings. For comparison, the Hoover Dam constructed in the 1930s is made up of  $6.6 \cdot 10^6$  Mg of concrete .

Giving an example on a county scale, the site aggregation spanning the townships Salisbury, Canaan, Sharon and Cornwall (Fig. 8.4A), consists of 4,919 RCH sites on appr.  $77 \text{ km}^2$  (or 7700 ha). With a total RCH mass of 419,108 Mg, this comes to 5,442 Mg moved substrate per  $\text{km}^2$  (or 54 Mg per ha). Decreasing the scale further to a landscape scale for an arbitrary example within the aggregation, there are 377 RCH sites on  $2.3 \text{ km}^2$  (or 230 ha) in the Miles Wildlife Sanctuary south of the Mine Mountain in the township Sharon (Fig. 8.4B). With a total RCH mass of 31,416 Mg, this comes to 13,696 Mg per  $\text{km}^2$  (or 136 Mg per ha; or 13.6 kg per  $\text{m}^2$ ) of relocated substrate.

### 8.4.2.3 SOC and PyC carbon stock legacy

Based on the morphological features identified and the calculations done, the average SOC stock in RCHs on a state scale is 6.1 Mg, of which 4.9 Mg are pyrogenic carbon (Tab. 5) with most of the carbon being stored in Litchfield county. Given as content per ha, the legacy effect on carbon stocks is comparably small, even in Litchfield county with 0.61 Mg SOC per ha (or 0.06 kg per  $\text{m}^2$ ).

**Table 8.5.** Calculated average ( $\pm$  one standard deviation) and total stocks of total organic carbon (TOC) and pyrogenic carbon (PyC) for RCH soils in Connecticut

Geographic boundary	RCH sites	av TOC stock	av PyC Stock	Mg		Mg per ha	
				tot TOC stock	tot PyC Stock	TOC	PyC
Connecticut St	34,692	6.1 $\pm$ 2.6	4.9 $\pm$ 2.1	210,935	170,466	0.17	0.14
Litchfield Ct	21,573	6.8 $\pm$ 2.3	5.6 $\pm$ 1.9	148,227	119,776	0.61	0.49
Fairfield Ct	1721	5.2 $\pm$ 2.7	4.2 $\pm$ 2.2	8949	7229	0.05	0.04
Hartford Ct	3682	5.5 $\pm$ 2.7	4.4 $\pm$ 2.1	20,084	16,230	0.10	0.08
New Haven Ct	1714	5.0 $\pm$ 2.6	4.1 $\pm$ 2.1	8615	6956	0.05	0.04
Middlesex Ct	1143	4.6 $\pm$ 2.4	3.6 $\pm$ 1.9	5300	4287	0.05	0.04
Tolland Ct	1682	4.3 $\pm$ 2.4	3.4 $\pm$ 1.9	7149	5776	0.07	0.05
Windham Ct	1447	3.8 $\pm$ 2.3	3.1 $\pm$ 1.8	5494	4447	0.04	0.03
New London Ct	1731	4.1 $\pm$ 2.3	5.8 $\pm$ 1.9	7115	5761	0.04	0.03

**Table 8.6.** Calculated SOC and PyC stocks for forested areas compared to carbon stored in Connecticut's RCH soils

Boundary	Forest type	Area [ha] <sup>x</sup>	Stocks [Mg]			Addition by RCH		
			Forest SOC <sup>y</sup>	Forest PyC	RCH SOC	RCH PyC	SOC	PyC
<b>State-wide</b>								
	Mixed	277,498	18,176,130	2,617,363	31,999	25,858	0.2 %	1.0 %
	Evergreen	59,452	3,127,153	450,310	2,016	1,632	0.2 %	0.4 %
	Deciduous	901,615	70,776,760	10,191,853	165,861	134,005	0.2 %	1.3 %
	Total						0.2 %	1.2 %
<b>Salisbury Iron District</b>								
	Mixed	33,177	2,173,103	312,927	18,875	15,238	0.9 %	4.9 %
	Evergreen	4,929	259,267	37,334	1,015	821	0.4 %	2.2 %
	Deciduous	83,345	4,383,959	631,290	108,671	87,823	2.5 %	13.9 %
	Total						1.9 %	10.6 %
<b>M. W. Sanctuary aggregation</b>								
	Deciduous	208	10,964	1,579	2,476	2,030	22.6 %	128.6 %

<sup>x</sup> based on NLCD 2016 Landcover (Conus) data, <https://www.mrlc.gov/data/nlcd-2016-land-cover-conus>

<sup>y</sup> based on SOC stocks compiled by Tomasso et al. (2014)

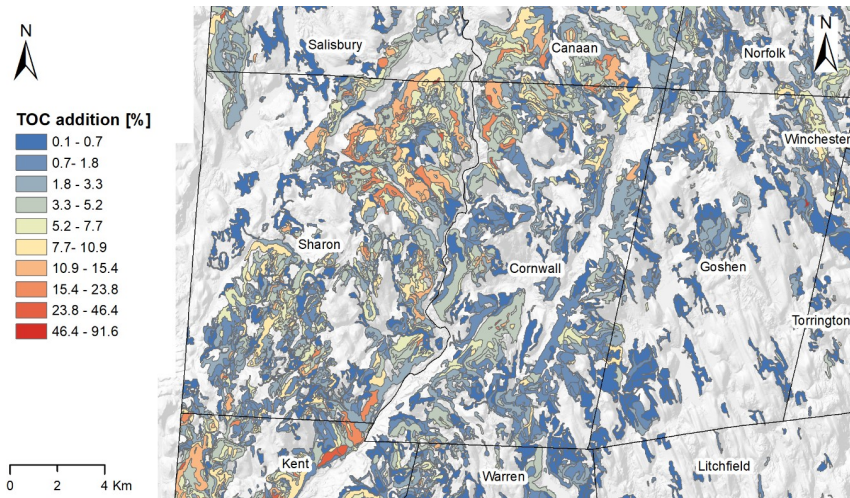


**Abbildung 8.5.** Soil unit polygons from the Gridded Soil Survey Geographic Database (gSSURGO, Soil Survey staff 2022) with added total organic carbon stocks from RCHs compared to forest soil stocks (0 – 100 cm depth)

However, the RCH legacy effects on carbon stocks are shown to be scale dependent (Schneider et al. 2022). Additions of SOC and PyC per area increase with decreasing scale of observation (Tab. 8.6) from very little (0.2 %) to significant (22.6 %). Since most of the carbon stored in RCH is pyrogenic and the forest soil contains comparably less PyC than SOC, the effect on PyC stocks is more severe, especially for deciduous forest areas (up to +128.6 %).

When compared to TOC stocks of soil units from the gSSURGO database, RCHs add between 0.1 % to 91.6 % of additional TOC to individual polygons (Fig. 8.5). Reisser et al. (2016) estimated global PyC stocks in soils, with results showing a range from around 2.6 to 40.1 Mg PyC ha<sup>-1</sup> globally. On a state-wide scale, our results would add only very little to this range (0.14 Mg PyC ha<sup>-1</sup>), however, on a county and landscape scale, additions of 1.1 Mg PyC ha<sup>-1</sup> and 9.7 Mg PyC ha<sup>-1</sup> can be seen (Tab. 8.6).

### 8.4.3 Comparison of historic land-use

To better determine the scale of the magnitude of legacy effects from RCH soils, we compare the RCH landform masses of the Miles Wildlife Sanctuary aggregation with another landform resulting from historical land use, an agricultural terrace/lynchet system in Belgium (Tab. 7) (Cucchiario et al. 2021).

Looking solely at the surface area of the landforms, 1 ha of RCH landform comprises of

**Table 8.7.** Comparison of morphometrics and SOC stocks from RCHs and historical terrace/lynchet systems.

	RCH		Terrace/Lynchet <sup>x</sup>		
	Total	per ha landform	per ha landscape	Total <sup>x</sup>	per ha landscape <sup>y</sup>
Landform surface area	7.2 ha		0.03 ha	18 ha	
Landform Volume	42,549 m <sup>3</sup>	5,909 m <sup>3</sup>	185 m <sup>3</sup>	89,105 m <sup>3</sup>	4,950 m <sup>3</sup>
Landform mass	31,416 Mg	4,363 Mg	137 Mg	122,965 Mg	6,831 Mg
Landform SOC stock	2,518 Mg	350 Mg	11 Mg	1,390 Mg	77 Mg

x Data taken from Cucchiaro et al. (2021), table 5, study area Belgium; y own calculations

more volume, mass and notably higher SOC stocks than the exemplary historical terrace system. However, due to the spot-like distribution of RCH sites, a dilution takes place when taking into account actual landscape surface areas. The miles Wildlife Sanctuary aggregation has 7.2 ha of RCH landform area, but they are located on 230 ha of landscape, thereby making up only 3 % of the total area, whereas the terrace system landform is the landscape itself. Looking at actual morphometric values per ha landscape, RCHs metrics are then an order of magnitude lower than for the terrace systems, with SOC stocks being 7 times lower (Tab. 8.7).

## 8.5 Conclusions and Outlook

Site specific legacy effects (Fig. 8.6A) of the historic charcoaling industry on recent soils have been described in Connecticut by multiple studies (Bonhage et al. 2022, Bonhage et al. 2021, Donovan et al. 2021, Hirsch et al. 2018, Raab et al. 2017). By a first analysis of pedogenic (hydr-)oxides, we found evidence for increased weathering rates in RCH soils. Contents of exchangeable and oxalate extractable manganese are increased and could result in changes to the RCH soils microbiome. Both aspects of increased weathering rates and higher manganese concentrations merit further research. RCH soils in the area also feature decreased available phosphorous concentrations (Donovan et al. 2021). We show that high spatial variation of site densities, as described for areas in Germany (Schneider et al. 2021), is also characteristic for the Connecticut RCH landscape. This results in local pockets of significant additions to soil organic carbon and especially pyrogenic carbon stocks (Fig. 8.6B-D). For pyrogenic carbon stocks, these effects can become noticeable at a county scale (1:650,000). On a landscape scale (1:20,000), additions to TOC and PyC stocks are significant in regions with high RCH site density. In summary, we can draw the following main conclusions from this study:

- RCH soils are selectively enriched in exchangeable  $\text{Ca}^{2+}$ ,  $\text{Mg}^{2+}$ ,  $\text{Mn}^{2+}$ , and there is evidence of vertical translocation of cations into buried soils.

- RCH soils are enriched in oxalate extractable manganese
- RCH sites feature an aggregated spatial pattern throughout Connecticut, concentrated in the historic Salisbury Iron District.
- There are spatially significant clusters of smaller and larger RCH sites throughout the state.
- On a state scale, RCHs add to soil organic and pyrogenic carbon stocks; this effect becomes more noticeable with increasing scale of observation.

Hence, RCH sites should be recognized as important anthropogenic landforms with remarkable legacy effects on today's soils and a landscapes soil carbon budget. Although RCHs have and still are influencing and changing local soil habitat conditions, it remains open how the increases to local soil organic carbon stocks e.g. influence calculations and modelling of a soil landscapes carbon sequestration rate or stocks of pyrogenic carbon. The relatively small area of RCHs and therefore their small share on a landscapes overall surface area is a main challenge for the accurate consideration by existing soil surveys.

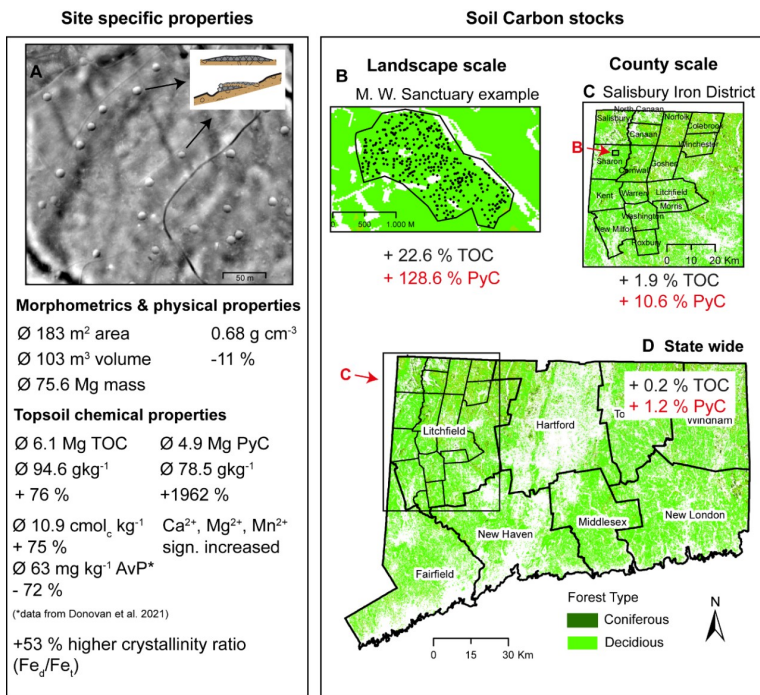


**Abbildung 8.6.** Synthesis of A) site specific RCH soil properties. Percentages are in relation to reference forest topsoil properties; Large scale legacy effects on soil organic carbon and soil pyrogenic carbon stocks on a B) landscape, C) County and D) State scale.

## 8.6 Acknowledgements

We would like to thank two reviewers for comments and suggestions that improved this manuscript. This research was supported by the German Research Foundation (DFG) under grant number RA 931/8-1.



## 9 Synthesis

Based on the results shown in the last chapters, **Q1 (Can we prove the distribution of soils as stated in H1 in our study area?)** can be answered positively. We can confirm the initial assumption (**H1**) about the distribution of soils that was derived from other known RCH soil-landscapes in Europe and pre-studies in Litchfield county. Results from **Q1** are the foundation for subsequently answering **Q2**.

**Q2 (Can we prove “legacy effects” of charcoal burning on soil properties?)** can also be answered positively and therefore, the assumption of significant differences in properties of RCH soils (**H2**) can be confirmed. The studied RCH soils feature changed soil physical and chemical properties. Most notably they have increased stocks of organic- and pyrogenic carbon which add to a landscapes overall soil carbon stock.

The overall research question: “**How and to what extent are historical charcoal burning activities controlling the distribution, development and properties of recent soils?**” is therefore answered. The charcoaling industry in Connecticut resulted in unique landscapes where the natural forest soil has been altered in terms of its morphology and chemical properties. The resulting new, anthropogenic soils have a comparably small signature on the overall landscape in terms of surface area, but nevertheless remarkable legacy effects. For singular landforms, the effect comprises of noticeably changed soil properties with potential implications for soil fertility and the soil microbiome. For RCH-landscapes, the legacy affects soil organic and pyrogenic carbon stocks.

The following section addresses each research question respectively. A graphical overview of the results is given at the end of the chapter.

### **Q1.1 What is the average depth and the typical soil horizon sequence found on RCH soils and natural (reference soils)?**

The results from measuring 52 RCH sites in Litchfield County described in chapter 5 show their stratigraphic properties and average soil horizon thicknesses. RCH soils feature at least one technogenic horizon (Auh) with specific soil properties caused by the large contents of charcoal and organic substances. If a site is multilayered, intermediate mineral layers (Cu) will separate at least two Auh horizons. The exact origin of the Cu horizons substrate is not determined conclusively, it is most likely a mixture of former topsoil (Ah) and mineral soil (Bw, C) horizons. Former topsoils underneath RCHs are mostly unrecognizable and only seldomly preserved in truncated form. Buried Bw-horizons (Bwb) are most commonly present. Reference soils in the area are mainly Cambisols with an Ah, Bw, C horizon stratigraphy. The (topmost) Auh horizons average thickness ranges between 20.9 cm and 23.6 cm, depending on the position within a site, while the reference soils Ah horizons average thickness is 9.7 cm. Conceptually, RCH landforms are replacing the natural forest topsoil (locally) with an A horizon more than twice as thick and with significantly different soil properties. The stratigraphy and thickness of RCH sites is influenced by the local slope that they are located on, which leads into the next question.

### **Q1.2 Does the topographic position control the distribution and morphometrical parameters of RCH soils?**

In **chapter 5** it is shown that the topographic (slope) position of an RCH site influences its stratigraphy and its soil horizons thickness. Sites on flat terrain are generally single-layered, with an Auh, (2Ahb), 2Bwb, 2Cb stratigraphy, while sites on slopes are generally multilayered, with an Auh, 2Cu, 3Auh, (4Ahb), 4Bwb, 4Cb stratigraphy (there can be more than 2 Auh horizons in some cases). It has been shown that a slope threshold of  $4^\circ$  serves well to predict which type of site it is ( $>4^\circ$  = multilayered,  $<4^\circ$  = singlelayered). The local slope also influences the thickness of technogenic layers (except for the topmost Auh), meaning a sites overall thickness will increase with increased steepness of the slope it was built upon. The slope threshold and slope dependent site thickness has important implications for calculating site specific substrate volume and subsequential element stocks and has been acknowledged in the subsequent model calculations. **Chapter 8** shows that RCH sites in Connecticut are preferably located on steep slopes and generally on more rugged terrain. To say that these features are solely explanatory for the RCH site distribution in Connecticut is not entirely validated, as most likely the availability of iron ore (that also spawned

the Salisbury Iron District) in the Appalachian Mountain region of NW Connecticut plays a large part in the presence of iron furnaces and, by proxy, the charcoaling industry.

### **Q2.1 How are carbon concentrations and carbon quality controlled by the legacies of charcoal burning?**

**Chapter 6** illustrates the significant changes in soil organic carbon contents within RCH soils compared to reference soils. Average total carbon contents of Auh horizons are increased by 75 % compared to Ah horizons. Highly aromatic carbon (pyrogenic carbon) is increased by 1862 % compared to reference soils, originating in the large amounts of charcoal stored in the Auh horizons. Intermediate Cu horizons feature overall lower TOC concentrations than Ah horizons, but are also increased in PyC by more than a magnitude. Buried Ah horizons (Ahb) are decreased in TOC contents, presumably caused by the influence of heath during the hearths operation and the stopped input of fresh SOC when it was buried. However, they also feature larger PyC concentrations. The large soil sample dataset in combination with a chemometric FTIR spectra-based approach and the high resolution vertical sampling approach allowed to draw conclusions about vertical TOC concentrations beyond a site specific scale. Topmost Auh horizons feature signs of accumulation of non-pyrogenic organic matter while intermediate Cu horizons feature signs of translocation of highly aromatic carbon, originating from the Auh horizons that they are buried by. Analysing the FTIR spectra showed increased carboxylic properties in the organic matter of Auh horizons, most likely as a result of ongoing charcoal degradation (aging) processes that release highly aromatic and mobile humic acids. Furthermore, potential changes in the organic matter turnover dynamics in Auh horizons could be seen, as aliphatic carbon compounds features are decreased in intensity. Overall, these results highlight that RCH Auh horizons are heavily enriched in highly aromatic organic matter, not solely in pyrogenic matter. This distinction can potentially be important, as laboratory methods quantifying pyrogenic matter in soils could misinterpret the true soil organic matter composition of RCH soils.

### **Q.2.2 Is there an effect of charcoal burning on soil physical properties?**

In very recent years the state-of-knowledge regarding soil physical properties of RCH soils has been improved significantly. Results from this thesis confirm the primary effect discovered in other study areas, which is the lower bulk density of RCH soils. To answer subsequent research questions regarding carbon stocks, the bulk density was a crucial parameter

to determine. Chapter 5 shows for one that the Auh horizons bulk density is considerably lower compared to reference Ah horizons and also that the bulk density in general is variable among the technogenic RCH soil horizons. This was taken into account for calculating carbon stocks of RCH sites.

### **Q2.3 Is there a change in element concentrations besides organic- and pyrogenic carbon?**

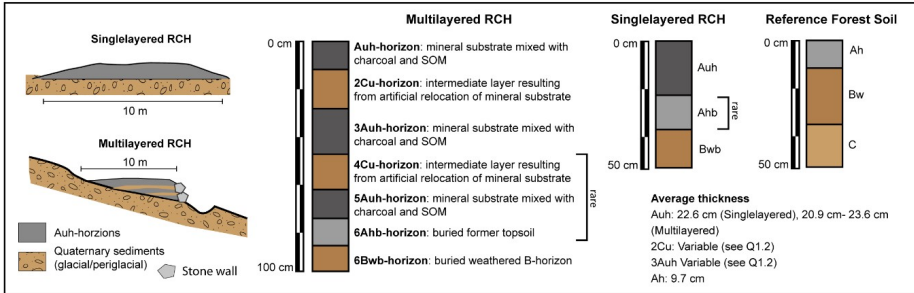
**Chapter 8** reveals that the studied RCH soils are enriched in elements besides carbon. They feature higher concentrations of exchangeable  $\text{Ca}^{2+}$ ,  $\text{Mg}^{2+}$  and  $\text{Mn}^{2+}$ , originating most likely from the charcoal addition to the soil. RCH soils feature generally increased activity and crystallinity ratios of pedogenic iron, indicating an increased state of mineral weathering, although it remains unclear if this is caused by the burning event(s), or by pedogenic effects originating in the altered chemical properties of RCH soils. Oxalate extractable manganese is increased by 100 % compared to reference Ah horizons, which could potentially hint at influences on the microbiome of RCH soils.

### **Q2.4 How can we quantify legacy effects on a site-specific scale and on a soil landscape scale?**

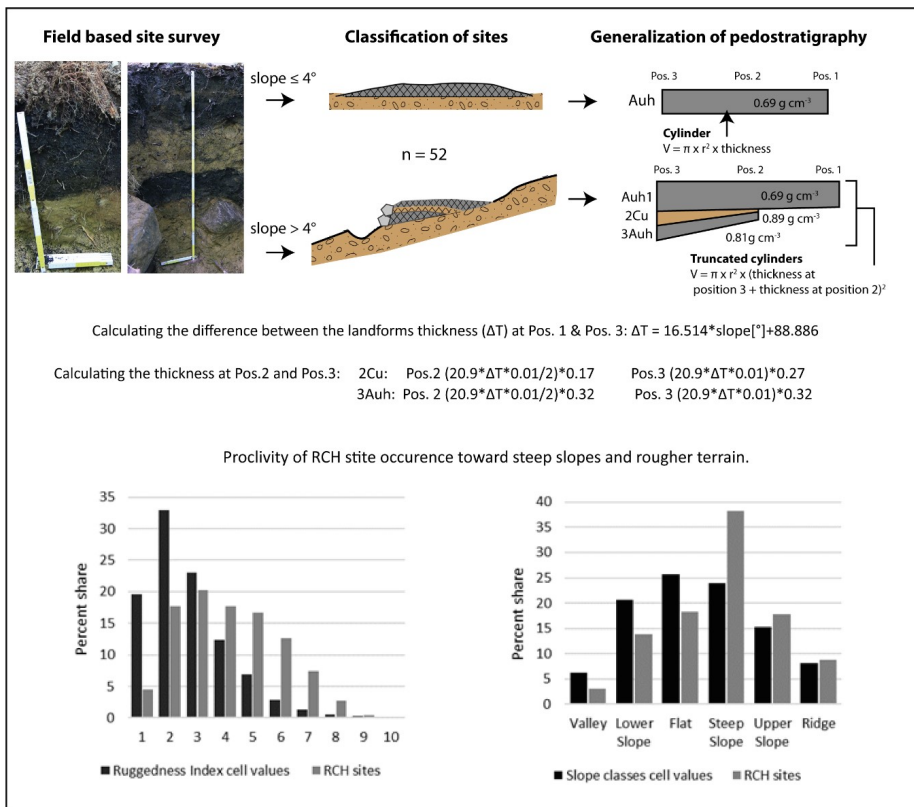
Quantifiable legacy effects in the context of this thesis refer to element stocks and landform attributes. The approach to calculate RCH landform volumes and thereby substrate masses developed in **chapter 5** is the basis for quantifying the legacy effects. With this model, the two types of RCH sites can be geometrically abstracted as cylinders based on the local slope they are located on ( $4^\circ$  threshold), whereby a fixed thickness is presumed for single-layered sites, and a slope-dependent thickness is presumed for multi-layered sites. Using average bulk densities for the RCH soil horizons allows the calculation of element stocks, thereby a focus was set to carbon and pyrogenic carbon stocks based on element concentrations determined in **chapter 6**. The initial target of analysing 52 RCH sites this way could be greatly expanded by a state wide site mapping, as outlined in **chapter 7**. The ARCHMAGE (Automated Relict Charcoal Hearth Mapping and Geospatial Exploration) workflow was designed to not only infer site locations, but also automatically extract information regarding each sites local slope and surface area, key parameters needed for calculating RCH sites volume. Therefore, this approach works on a site specific and on a soil landscape scale. **Chapter 8** shows that legacy effects are scale dependent, with increasing influence on local soil carbon stocks when there is a high RCH site density and a large scale ( $\leq 1:650,000$ ) of observation.

**Q1: Can we prove the distribution of soils as stated in H1?**

**Q1.1 What is the average depth and typical soil horizon sequence found on RCH soils and natural (reference soils)?**

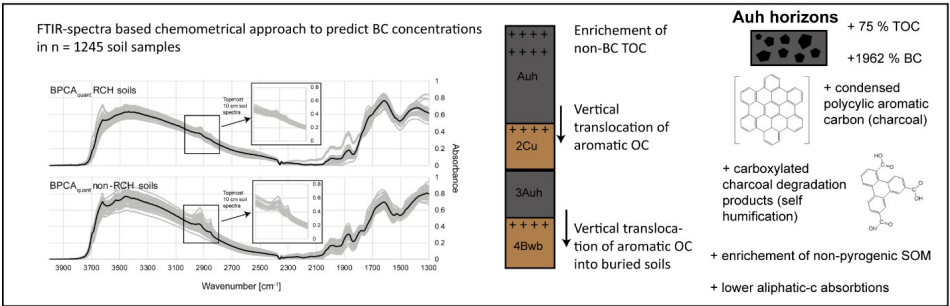


**Q1.2 Does the topographic position control the distribution and morphometrical parameters of RCH soils?**

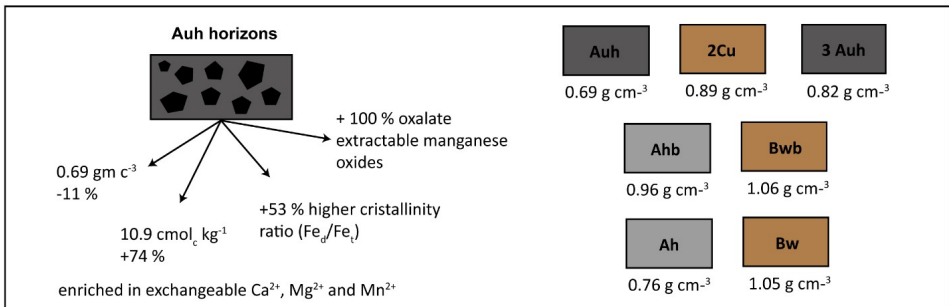


**Q2: Can we prove „legacy effects“ of charcoal burning on soil properties?**

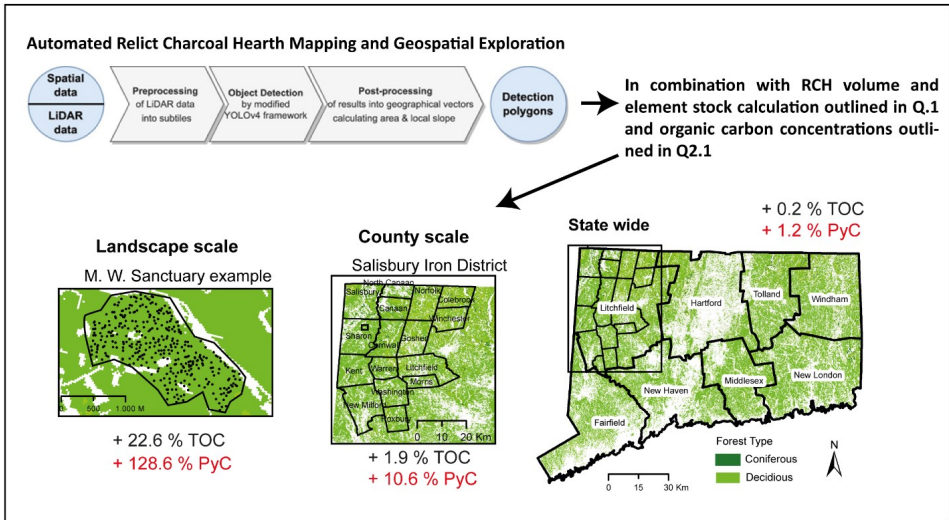
**Q2.1 How are carbon concentrations and carbon quality controlled by the legacies of charcoal burning?**



**Q2.2 & Q2.3 Is there an effect on soil physical properties and element concentrations beside TOC and BC?**



**Q2.4 How can we quantify legacy effects on a site-specific scale and on a soil landscape scale?**



## 10 Outlook

The extensive field survey- and soil sampling campaigns of this research project resulted in a unique dataset of morphological-, stratigraphical- and soil properties of 52 RCH sites, with more than 1245 soil samples gathered from 154 soil profiles. This, in combination with cutting-edge deep learning based site mapping and geospatial exploration enabled a novel and powerful analysis of the impact the historical charcoal burning has on today's soils and soil landscapes carbon stocks in Connecticut. The studies presented in this thesis are well aligned with the state-of research regarding the landform analysis of RCHs that has advanced during recent years and in terms of spatial scale, they are unique so far. The results produced new insights about the often assumed, but seldomly proved legacy effects, which lead to new potential research questions:

- **Is the model to calculate RCH landform volume and mass transferable to other study areas in New England or Worldwide?** Multiple studies have shown that the RCH stratigraphy in other areas is very similar to the one observed in this thesis. For sloped sites, the basic relationship of local slopes and overall site thickness should hold true, but the occurrence of intermediate mineral layers could be a local peculiarity of our study area (although it has been described for sites in Pennsylvania and Germany).
- **Are pedogenic processes of buried soils influenced by the vertical input of aromatic carbon and cations with the soil solution?** Especially for buried E-horizons, this could be of interest to study the effect increased and/or altered environmental conditions on podsolization rates.
- **Is there a change in C-turnover rates in RCH soils?** The lower intensity of aliphatic absorptions in FTIR spectra for samples in the first 10 cm of Auh horizons begs the questions of what causes this effect. Is it caused by (relatively) young age of these topsoils, increased mineralisation rates of labile OM, or is it caused by spectral effects

diminishing the intensity of aliphatic-C specific wavenumber regions in MIR FTIR spectra?

- **Does the increase in exchangeable and oxalate extractable manganese has an effect on the microbiome and faunal growth on RCH soils?** Manganese is an essential nutrient for plant growth and the increased concentrations of exchangeable  $Mn^{2+}$  could influence local growth conditions. Increased oxalate extractable Mn-oxides concentrations could hint at increased soil microbial activity in RCH soils.
- **Can the ARCHMAGE workflow be applied in other regions in New England?** It was designed to be able to process large amounts of DEM data efficiently. Can further areas be surveyed when the DEM data quality and resolution differs across larger areas? Can the algorithm to reduce false positive detections caused by bad DEM data quality expanded and/or improved for other areas?
- **If it can be transferred, can other regions of high RCH site densities in New England be detected?** Other states in the New England region had historic iron industries and thereby charcoal production. Can similar site densities and aggregation patterns and thereby legacy effects be discovered?
- **How is the RCH site distribution in Connecticut spatially correlated with historic manufacturers and landscape features (ponds, roads etc.)?** The distribution of RCH sites in general, and the distribution of smaller and larger sites specifically, could hint at different local conditions influencing the charcoaling industries, or different timespans of charcoal production.
- **Do RCH carbon stock additions to landscapes need to be included in soil surveys?** As was shown, the effect on local C- and Pyc stocks can be significant. But the spot-like distribution of RCH sites in a landscapes results in relatively small hot spots of carbon additions.



# 11 References

## A

- Abdelrahman, H., Hofmann, D., Berns, A.E., Meyer, N., Bol, R., Borchard, N. (2018): Historical charcoal additions alter water extractable, particulate and bulk soil C composition and stabilization. *Journal of Plant Nutrition and Soil Science*. <https://doi.org/10.1002/jpln.201800261>
- Abney, R.B., Berhe, A.A. (2018): Pyrogenic Carbon Erosion: Implications for Stock and Persistence of Pyrogenic Carbon in Soil. *Frontiers in Earth Science*. DOI: 10.3389/feart.2018.00026
- Abney, R.B., Jin, L., Berhe, A.A. (2019): Soil properties and combustion temperature: Controls on the decomposition rate of pyrogenic organic matter. *Catena*. DOI: 10.1016/j.catena.2019.104127
- Anderson, E. (2019). Mapping Relict Charcoal Hearths in the Northeast US Using Deep Learning Convolutional Neural Networks and LIDAR Data. Master's theses. 1387. University of Connecticut. [https://opencommons.uconn.edu/g\\_s\\_theses/1387](https://opencommons.uconn.edu/g_s_theses/1387)
- Ascough, P.L., Brock, F., Collinson, M.E., Painter, J.D., Lane, D. W., Bird, M. (2020): Chemical Characteristics of Macroscopic Pyrogenic Carbon Following Millennial-Scale Environmental Exposure. *Frontiers in Environmental Science*. DOI: 10.3389/fenvs.2019.00203
- Ascough, P.L., Bird, M.I., Francis, S.M., Lebl, T. (2011): Alkali extraction of archaeological and geological charcoal: evidence for diagenetic degradation and formation of humic acids. *Journal of Archaeological Science*. DOI: 10.1016/j.jas.2010.08.011

## B

- Banasiak, P. Z., Berezowski, P. L., Zapłata, R., Mielcarek, M., Duraj, K., & Stereńczak, K. (2022): Semantic Segmentation (U-Net) of Archaeological Features in Airborne Laser Scanning—Example of the Białowieża Forest. *Remote Sensing*. <https://doi.org/10.3390/RS14040995>

- Banaszek, L., Cowley, D., & Middleton, M. (2018): Towards National Archaeological Mapping. Assessing Source Data and Methodology—A Case Study from Scotland. *Geosciences*. <https://doi.org/10.3390/geosciences8080272>
- Bayuzick S., Guarin, D., Bonhage, A., Hirsch, F., Diefenbach, D.R., McDil, M., Raab, T., Drohan, P.J. (2022a): Small anthropogenic landforms from past charcoal production control moisture dynamics and chemistry in northcentral Appalachian soils. *Geomorphology*. DOI: 10.1016/j.geomorph.2022.108379
- Bayuzick, S., Guarin, D., Benavides, J., Bonhage, A., Hirsch, F., Diefenbach, D.R., McDill, M., Raab, T., Drohan, P.J. (2022b): Soil and geomorphic patterns within relict charcoal hearths could represent unique ecosystem niches. *Geomorphology*. DOI: 10.1016/j.geomorph.2022.108525
- Bellè, S.L., Berhe, A.A., Hagedorn, F., Santin, C., Schiedung, M., van Meerveld, I., Abvien, S. (2021): Key drivers of pyrogenic carbon redistribution during a simulated rainfall event. *Biogeosciences*. DOI: 10.5194/bg-18-1105-2021
- Bennett, R., Cowley, D., & De Laet, V. (2014): The data explosion: Tackling the taboo of automatic feature recognition in airborne survey data. *Antiquity*. <https://doi.org/10.1017/S0003598X00050766>
- Berganzo-Besga, I., Orenco, H. A., Lumbreras, F., Carrero-Pazos, M., Fonte, J. & Vilas-Estévez, B. (2021): Hybrid MSRM-Based Deep Learning and Multitemporal Sentinel 2-Based Machine Learning Algorithm Detects near 10k Archaeological Tumuli in North-Western Iberia. *Remote Sensing*, 13, 4181, <https://doi.org/10.3390/rs13204181>
- Bevan, A. (2015): The data deluge. *Antiquity*. <https://doi.org/10.15184/aqy.2015.102>
- Bird, M.I, Wynn, J.G. Saiz, G., Wurster C.M., McBeath, A. (2015): The pyrogenic carbon cycle. *Annual Reviews of Earth and Planetary Sciences*. DOI: 10.1146/annurev-earth-060614-105038
- Bista, P., Ghimire, R., Machado, D., Pritchett, L. (2019): Biochar Effects on Soil Properties and Wheat Biomass vary with Fertility Management. *Agronomy*. DOI: 10.3390/agronomy9100623
- Blume, H.P. (1969): The fate of Iron during soil formation in humid-temperate environments. In: Stucki, J.W., Goodman, B.A., Schwertmann, U.: *Iron in soils and clay minerals*. NATO ASI series Vol 217. ISBN: 90-277-2613-2
- Blume, H.P. & Schwertmann, U. (1969): Genetic evaluation of profile distribution of aluminum, iron and manganese oxides. *Soil Science Society of America Journal* 33. 438-444.
- Bochkovskiy, A., Wang, C.-Y., & Liao, H.-Y. M. (2020): YOLOv4: Optimal Speed and Accuracy of Object Detection. In arXiv: Vol. 2004.109.

- Bond, J. (2007): Medieval charcoal-burning in England. Arts and crafts in medieval rural environment. In: *Ruralia VI*, 277-294.
- Bonhage, A., Raab, T., Schneider, A., Fischer, T., Ramezany, S., Ouimet, W., Raab, A., Hirsch F. (2022): Vertical SOC distribution and aromatic carbon in centuries old charcoal-rich Technosols. *European Journal of Soil Science*. DOI: 10.1111/ejss.13293
- Bonhage, A., Raab, A., Eltaher, M., Raab, T., Breuß, M., & Schneider, A. (2021): A modified Mask region-based convolutional neural network approach for the automated detection of archaeological sites on high-resolution light detection and ranging-derived digital elevation models in the North German Lowland. *Archaeological Prospection*. <https://doi.org/10.1002/arp.1806>
- Bonhage, A., Hirsch, F., Schneider, A., Raab, A., Raab, T. (2020a): Long term anthropogenic enrichment of soil organic matter stocks in forest soils - detecting a legacy of historical charcoal production. *Forest Ecology and Management* <https://doi.org/10.1016/j.foreco.2019.117814>
- Bonhage, A., Hirsch, F., Raab, T., Schneider, A., Raab, A., & Ouimet, W. (2020b): Characteristics of small anthropogenic landforms resulting from historical charcoal production in western Connecticut, USA. *Catena*, 195, 104896. <https://doi.org/10.1016/j.catena.2020.104896>
- Bonhôte, J., Davasse, B., Dubois, C., Isard, V., Métailié, J.P. (2002): Charcoal kilns and environmental history in the eastern Pyrenees (France). In: *A Methodological Approach, Second International Meeting of Anthracology, 2000, Paris, France*, 219–228.
- Borchard, N., Ladd, B., Eschemann, S., Hegenberg, D., Maria Möseler, B.M., Amelung, W. (2014): Black carbon and soil properties at historical charcoal production sites in Germany. *Geoderma*. [dx.doi.org/10.1016/j.geoderma.2014.05.007](https://doi.org/10.1016/j.geoderma.2014.05.007)
- Braun, M., Kappenberg, A., Sandhage-Hofmann, A., Lehndorff, E. (2020): Leachable soil black carbon after biochar application. *Organic Geochemistry*. DOI: 10.1016/j.orggeochem.2020.103996
- Brodowski, S., Rodionow, A., Haumaier, L., Glaser, B., Amelung, W. (2005): Revised black carbon assessment using benzene polycarboxylic acids. *Organic Geochemistry*. DOI: 10.1016/j.orggeochem.2005.03.011
- Buras, A., Hirsch, F., Schneider, A., Scharnweber, T., van der Maaten, E., Cruz-García, R., Raab, T., Wilmking, M. (2020): Reduced above-ground growth and wood density but increased wood chemical concentrations of Scots pine on relict charcoal hearths. *Science of the total environment*. <https://doi.org/10.1016/j.scitotenv.2020.137189>

- Burgeon, V., Fouché, J., Garré, S., Dehkordi, R. H., Colinet, G., Cornelis, J.-T. (2022): Young and century-old biochars strongly affect nutrient cycling in a temperate agroecosystem. *Agriculture, Ecosystems & Environment*. DOI: 10.1016/j.agee.2021.107847
- Burgeon, V., Fouché, J., Leifeld, J., Chenu, C., Cornélis, J.-T. (2020): Organo-mineral associations largely contribute to the stabilization of century-old pyrogenic organic matter in cropland soils. *Geoderma*. DOI: 10.1016/j.geoderma.2020.114841

## C

- Carranza-García, M., Torres-Mateo, J., Lara-Benítez, P., & García-Gutiérrez, J. (2021): On the performance of one-stage and two-stage object detectors in autonomous vehicles using camera data. *Remote Sensing*. <https://doi.org/10.3390/rs13010089>
- Carrari, E., Ampoorter, E., Bussotti, F., Coppi, A., Nogales, A.G., Pollastrini, M., Verheyen, K., Selvi, F. (2018): Effects of charcoal hearth soil on forest regeneration: Evidence from a two-year experiment on tree seedlings. *Forest Ecology and Management*. [doi.org/10.1016/j.foreco.2018.05.038](https://doi.org/10.1016/j.foreco.2018.05.038)
- Carrari, E., Ampoorter, E., Bottalico, F., Chirici, G., Coppi, A., Travaglini, D., Verheyen, K., Selvi, F. (2017): The old charcoal kiln sites in Central Italian forest landscapes. *Quaternary International*. DOI: 10.1016/j.quaint.2016.10.027
- Carrari, E., Ampoorter, E., Verheyen, K., Coppi, A., Selvi, F. (2016): Former charcoal kiln platforms as microhabitats affecting understorey vegetation in Mediterranean forests. *Applied Vegetation Science*. Doi: 10.1111/avsc.12238
- Carter, B. P., Blackadar, J. H., & Conner, W. L. A. (2021): When Computers Dream of Charcoal Using Deep Learning, Open Tools, and Open Data to Identify Relict Charcoal Hearths in and around State Game Lands in Pennsylvania. *Advances in Archaeological Practice*. <https://doi.org/10.1017/aap.2021.17>
- Carter, B. P. (2019): Identifying landscape modification using open data and tools: The charcoal hearths of the Blue Mountain, Pennsylvania. *Historical Archaeology*. <https://doi.org/10.1007/s41636-019-00171-1>
- Cațeanu, M., & Ciubotaru, A. (2020): Accuracy of ground surface interpolation from airborne laser scanning (ALS) data in dense forest cover. *ISPRS International Journal of Geo-Information*. <https://doi.org/10.3390/ijgi9040224>
- Chang, Z., Tian, L., Li, F., Zhou, Y., Wu, M., Steinberg, C.E.W., Dong, X., Pan, B., Xing, B. (2018): Benzene polycarboxylic acid - A useful marker for condensed organic matter, but not for only pyrogenic black carbon. *Science of the Total Environment*. DOI: 10.1016/j.scitotenv.2018.01.145

- Cheng, C.H., Lin, T.-P., Lehmann, J., Fang, L.J., Yang, Y.-W., Menyailo, O.V., Chang, K.H., Lai, J.-S. (2014): Sorption properties for black carbon (wood char) after long term exposure in soils. *Organic Geochemistry*. DOI: 10.1016/j.orggeochem.2014.02.013
- Cheng, C.H., Lehmann, J., Engelhard, M.H. (2008): Natural oxidation of black carbon in soils: Changes in molecular form and surface charge along a climosequence. *Geochimica et Cosmochimica Acta*. DOI: 10.1016/j.gca.2008.01.010
- Cheng, C.H., Lehmann, J., Thies, J.E., Burton, S.D., Engelhard, M.H. (2006): Oxidation of black carbon by biotic and abiotic processes. *Organic Geochemistry*. DOI: 10.1016/j.orggeochem.2006.06.022
- Chicco, D., & Jurman, G. (2020): The advantages of the Matthews correlation coefficient (MCC) over F1 score and accuracy in binary classification evaluation. *BMC Genomics*. <https://doi.org/10.1186/s12864-019-6413-7>
- Cohen-Ofri, I., Weiner, L., Boaretto, E., Mintz, G., Weiner, S. (2006): Modern and fossil charcoal: aspects of structure and diagenesis. *Journal of Archaeological Science*. DOI: 10.1016/j.jas.2005.08.008
- Cowley, D. (2012): In with the new, out with the old? Auto-extraction for remote sensing archaeology. *Proceedings of SPIE*. <https://doi.org/10.1117/12.981758>
- Cowley, D., Banaszek, L., Geddes, G., Gannon, A., Middleton, M., & Millican, K. (2020): Making LiGHT Work of Large Area Survey? Developing Approaches to Rapid Archaeological Mapping and the Creation of Systematic National-scaled Heritage Data. *Journal of Computer Applications in Archaeology*. <https://doi.org/10.5334/jcaa.49>
- Criscuoli, I.; Alberti, G.; Baronti, S.; Favilli, F.; Martinez, C.; Calzolari, C.; Pusceddu, E.; Rumpel, C.; Viola, R.; Miglietta, F. (2014): Carbon sequestration and fertility after centennial time scale incorporation of charcoal into soil. *PLOS ONE*. DOI: 10.1371/journal.pone.0091114
- Criscuoli, I., Baronti, S., Alberti, G., Rumpel, C., Giordan, M., Camin, F., Ziller, L., Martinez, C., Pusceddu, E., Miglietta, F. (2017): Anthropogenic charcoal-rich soils of the XIX century reveal that biochar leads to enhanced fertility and fodder quality of alpine grasslands. *Plant and Soil*. DOI 10.1007/s11104-016-3046-3
- Cucchiaro, S., Paliaga, G., Fallu, D.J., Pears, B.R., Walsh, K., Zhao, P., Van Oost, K., Snape, L., Lang, A., Brown, A.G., Tarolli, P. (2021): Volume estimation of soil stored in agricultural terrace systems: A geomorphometric approach. *Catena*. DOI: 10.1016/j.catena.2021.105687

## D

- Davis, D. S., (2019). Object-Based Image Analysis: A Review of Developments and Future Directions of Automated Feature Detection in Landscape Archaeology. *Archaeological Prospection*. <https://doi.org/10.1002/ARP.1730>
- Davis, D. S., Caspari, G., Lipo, C. P., & Sanger, M. C. (2021): Deep Learning Reveals Extent of Archaic Native American Shell-Ring Building Practices. *Journal of Archaeological Science*. <https://doi.org/10.1016/j.jas.2021.105433>.
- Davis, D. S., & Lundin, J. (2021): Locating Charcoal Production Sites in Sweden Using LiDAR, Hydrological Algorithms, and Deep Learning. *Remote Sensing*. <https://doi.org/10.3390/rs13183680>
- Deforce, K., Boeren, I., Adriaenssens, S., Bastiaens, J., De Keersmaeker, L., Haneca, K., Tys, D., & Vandekerckhove, K. (2013). Selective woodland exploitation for charcoal production. A detailed analysis of charcoal kiln remains (ca. 1300–1900 AD) from Zoersel (northern Belgium). *Journal of Archaeological Science*. <https://doi.org/10.1016/J.JAS.2012.07.009>
- Dehkordi, R.H., Denis, A., Fouche, J., Burgeon, V., Cornelis, J.-T., Tychon, B., Gomez, E.P., Meersmans, J. (2020): Remotely-sensed assessment of the impact of century-old biochar on chicory crop growth using high-resolution UAV-based imagery. *International Journal of Applied Earth Observation and Geoinformation*. DOI: 10.1016/j.jag.2020.102147
- Dolejš, M., Pacina, J., Veselý, M., & Brétt, D. (2020): Aerial Bombing Crater Identification: Exploitation of Precise Digital Terrain Models. *ISPRS International Journal of Geoinformation*. <https://doi.org/10.3390/ijgi9120713>
- Donovan S., Ignatiadis M., Ouimet W., Dethier D. & Hren M. (2021): Gradients of geochemical change in relic charcoal hearths soils, Northwestern Connecticut, USA. *Catena*. DOI: 10.1016/j.catena.2020.104991
- Dupin, A., Sordoillet, D., Fréville, K., Girardclos, O., Gauthier, E. (2019): The taphonomic characterization of a charcoal production platform. Contribution of an innovative pair of methods: Raman analysis and micromorphology. *Journal of Archaeological Science*. <https://doi.org/10.1016/j.jas.2019.05.003>
- Dupin, A., Girardclos, O., Fruchart, C., Laplaige, C., Nuninger, L., Dufraisse, A., Gauthier, E. (2017): Anthracology of charcoal kilns in the forest of Chailluz (France) as a tool to understand Franche-Comte forestry from the mid-15th to the early 20th century AD. *Quaternary International*. <http://dx.doi.org/10.1016/j.quaint.2017.03.008>

## E

- Eriksson, O., Lundin, L. G. (2021): Legacies of historic charcoal production affect the forest flora in a Swedish mining district. *Nordic Journal of Botany*. DOI: 10.1111/njb.03312
- Everingham, M., Van Gool, L., Williams, C. K. I., Winn, J., & Zisserman, A. (2010): The PASCAL Visual Object Classes (VOC) Challenge, *International Journal of Computer Vision*. <https://doi.org/10.1007/s11263-009-0275-4>

## F

- FAO (2006) Guidelines for soil description (4th ed.) Rome: Food and Agriculture Organization of the United Nations.
- Ferrari, E., Francioso, O., Nardi, S., Saladini, M., Ferro, N.D., Morari, F. (2011): DRIFT and HR MAS NMR characterization of humic substances from a soil treated with different organic and mineral fertilizers. *Journal of Molecular Structure*. DOI: 10.1016/j.molstruc.2011.05.035

## G

- Gallwey, J., Eyre, M., Tonkins, M., & Coggan, J. (2019): Bringing Lunar LiDAR Back Down to Earth: Mapping Our Industrial Heritage through Deep Transfer Learning. *Remote Sensing*. <https://doi.org/10.3390/rs11171994>
- Garcia-Berreda, S.; Molina-Grau, S.; Forcadell, R.; Sánchez, S.; Reyna, S. (2017): Long-term soil alteration in historical charcoal hearths affects Tuber melanosporum mycorrhizal development and environmental conditions for fruiting. *Mycorrhiza*. DOI 10.1007/s00572-017-0773-0
- Gates, R.M. (1951): A report on the bedrock geology of the Litchfield Quadrangle with Geological map. State geological and natural history survey. Available Online: <https://portal.ct.gov/-/media/DEEP/geology/QuadReports/QR1pamphletRev.pdf>
- Gerke, J. (2019): Black (pyrogenic) carbon in soils and waters: a fragile data basis extensively interpreted. *Chemical and Biological Technologies in Agriculture*. DOI: 10.1186/s40538-019-0151-6
- Gerke, J. (2018): Concepts and Misconceptions of Humic Substances as the Stable Part of Soil Organic Matter: A Review. *Agronomy*. DOI: 10.3390/agronomy8050076
- Getis, A., Ord, J.K. (1992): The analysis of spatial association by use of distance statistics. *Geographical Analysis*. [doi.org/10.1111/j.1538-4632.1992.tb00261.x](https://doi.org/10.1111/j.1538-4632.1992.tb00261.x)
- Gießelmann U.C., Borchard N., Traunspurger W. & Witte K. (2019): Long-term effects of charcoal on nematodes and other soil meso- and microfaunal groups at historical kiln-sites – a pilot study. *European Journal of Soil Biology*. DOI: 10.1016/j.ejsobi.2019.103095

- Glaser, B., Haumaier, L., Guggenberger, G., Zech, W. (1998): Black carbon in soils: the use of benzenecarboxylic acids as specific markers. *Organic Geochemistry*. DOI: 10.1016/S0146-6380(98)00194-6
- Glisczynski, F.v., Pude, R., Amelung, W., Sandhage-Hofmann, A. (2016): Biochar-compost substrates in short-rotation coppice: effects on soil and trees in a three-year field experiment. *Journal of Plant Nutrition and Soil Science*. DOI: 10.1002/jpln.201500545
- Gocel-Chalté, D., Guerold, F., Knapp, H., & Robin, V. (2020): Anthracological analyses of charcoal production sites at a high spatial resolution: the role of topography in the historical distribution of tree taxa in the northern Vosges mountains, France. *Vegetation History and Archaeobotany*. <https://doi.org/10.1007/S00334-020-00769-Z>
- Goodfellow, I., Bengio, Y., & Courville, A. (2016): *Deep Learning*. The MIT Press. ISBN: 9780262035613
- Google. (2022): Google Research Colaboratory. <https://colab.research.google.com/>
- Gordon R.B. (2001): *A Landscape Transformed: The Ironmaking District of Salisbury, Connecticut*. Oxford University Press. ISBN: 9780195128185
- Guo, Y., Liu, Y., Oerlemans, A., Lao, S., Wu, S., & Lew, M. S. (2016): Deep learning for visual understanding: A review. *Neurocomputing*. <https://doi.org/10.1016/j.neucom.2015.09.116>
- Gustafsson, Ö., Bucheli, T.D., Kukulska, Z., Andersson, M., Largeau, C., Rouzaud, J.N. et al. (2001): Evaluation of a protocol for the quantification of black carbon in sediments. *Global Biogeochemical Cycles*. <https://doi.org/10.1029/2000GB001380>
- Guyot, A., Lennon, M., & Hubert-Moy, L. (2021): Objective comparison of relief visualization techniques with deep CNN for archaeology. *Journal of Archaeological Science*. <https://doi.org/10.1016/j.jasrep.2021.103027>

## H

- Hammes, K.; Schmidt, M.; Smerink, R.; Currie, L.; Ball, W.; Nguyen, T.; Louchouart, P.; Houel, S.; Gustafsson, Ö.; Elmquist, M.; Cornelissen, G.; Skjemstad, J.; Masiello, C.; Song, J.; Peng, P.; Mitra, S.; Dunn, J.; Hatcher, P.; Hockaday, W.; Smith, D.; Hartkopf-Fröder, C.; Böhmer, A.; Lüer, B.; Huebert, B.; Amelung, W.; Brodowski, S.; Huang, L.; Zhang, W.; Gschwend, P.; Flores-Cervantes, X.; Largeau, C.; Rouzaud, J-N.; Rumpel, C.; Guggenberger, G.; Kaiser, K.; Rodionov, A.; Gonzales-Villa, F.; Gonzalez-Perez, J.; de la Rosa, J.; Manning, D.; López-Capel, E.; Ding, L. (2007): Comparison of quantification methods to measure fire-derived (black/elemental) carbon in soils and sediments using reference materials from soil, water, sediment and the atmosphere. *Global Biogeochemical Cycles*. doi:10.1029/2006GB002914



- Hardy, B., Sleutel, S., Dufey, J.E. Cornelis, J.-T. (2019): The Long-Term Effect of Biochar on Soil Microbial Abundance, Activity and Community Structure Is Overwritten by Land Management. *Frontiers in Environmental Science*. DOI: 10.3389/fenvs.2019.00110
- Hardy, B., Cornelis, J-T., Houben, D., Leifeld, J., Lambert, R., Dufey, J.E. (2017): Evaluation of the long-term effect of biochar on properties of temperate agricultural soil at pre-industrial charcoal kiln sites in Wallonia, Belgium. *European Journal of Soil Science*. doi: 10.1111/ejss.12395
- Hardy, B.; Dufey, J.E. (2017): The resistance of centennial soil charcoal to the “Walkley-Black” oxidation. *Geoderma*, DOI: 10.1016/j.geoderma.2017.05.001
- Hardy, B., (2017): Pre-industrial Charcoal Kiln Sites in Wallonia, Belgium: Spatial Distribution, Effects on Soil Properties and Long-term Fate of Charcoal in Soil. *Université catholique de Louvain*. <http://hdl.handle.net/2078.1/184605>
- Hardy, B., Cornelis, J-T, Houben D., Lambert, R., Dufey, J.E. (2016): The effect of pre-industrial charcoal kilns on chemical properties of forest soil of Wallonia, Belgium. *European Journal of Soil Science*. doi: 10.1111/ejss.12324
- Hart, J.L., Van der Gevel, S., Mann, D.F., (2008): Legacy of charcoaling in a western highland rim forest in Tennessee. *The American Midland Naturalist*. <http://www.jstor.org/stable/20491325>.
- Hazell, Z., Crosby, V., Oakey, M., & Marshall, P. (2017): Archaeological investigation and charcoal analysis of charcoal burning platforms, Barbon, Cumbria, UK. *Quaternary International*. <https://doi.org/10.1016/j.quaint.2017.05.025>
- Heitkötter, J.; Marschner, B. (2015): Interactive effects of biochar ageing in soils related to feedstock, pyrolysis temperature, and historic charcoal production. *Geoderma*. DOI: 10.1016/j.geoderma.2015.01.012
- Hendershot W.H., Lalonde, H., Duquette, M. (2006): Chapter 18 – Ion exchange and exchangeable cations. In: Carter, M.R. Gregorich, E.G. (2006): *Soil sampling and methods of analysis* 2nd ed. CRC Press. ISBN-13: 978-0-8493-3586-0.
- Herfort, B., Li, H., Fendrich, S., Lautenbach, S., & Zipf, A. (2019): Mapping Human Settlements with Higher Accuracy and Less Volunteer Efforts by Combining Crowdsourcing and Deep Learning. *Remote Sensing*. <https://doi.org/10.3390/rs11151799>
- Hernandez-Soriano, M.C.; Kerré, B.; Goos, P.; Hardy, B.; Dufey, J.; Smolders, E. (2016): Long-term effect of biochar on the stabilization of recent carbon: soils with historical inputs of charcoal. *GCB Bioenergy*, DOI: 10.1111/gcbb.12250
- Hesse, R. (2010): LiDAR-derived Local Relief Models - a new tool for archaeological prospection. *Archaeological Prospection*. <https://doi.org/10.1002/arp.374>

- Hirsch, F., Schneider, A., Bonhage, A., Raab, A., Drohan, P., Raab, T. (2020): An initiative for a morphologic-genetic catalog of relict charcoal hearths from Central Europe. *Geoarchaeology*. <https://doi.org/10.1002/gea.21799>
- Hirsch, F., Raab, T., Ouimet, W., Dethier, D., Schneider, A., Raab, A. (2018a): Soils on historic charcoal hearths: Terminology and chemical properties. *Soil Science Society of America*. doi:10.2136/sssaj2017.02.0067
- Hirsch, F., Schneider, A., Bauriegel, A., Raab, A., Raab, T. (2018b): Formation, classification, and properties of soils at two relict charcoal hearth sites in Brandenburg, Germany. *Frontiers of Environmental Science*. doi: 10.3389/fenvs.2018.00094
- Hobley, E., Zoor, L.C., Shrestha, H.R., Bennett, L.T., Weston, C.J., Baker, T.G. (2019): Prescribed fire affects the concentration and aromaticity of soluble soil organic matter in forest soils. *Geoderma*. DOI: 10.1016/j.geoderma.2019.01.035
- Hochholzer, H., Stocker, J., Bentley, W.R. (2010): Connecticut's Forest resource assessment strategy 2010. Available online [https://portal.ct.gov/-/media/DEEP/forestry/assessment\\_and\\_strategy/AssessmentStrategypdf.pdf](https://portal.ct.gov/-/media/DEEP/forestry/assessment_and_strategy/AssessmentStrategypdf.pdf)

## I

- IUSS Working Group WRB (2014): World Reference Base for Soil Resources 2014, update 2015. FAO, Rome, 181.
- IUSS Working Group WRB. (2022): World Reference Base for Soil Resources. International soil classification system for naming soils and creating legends for soil maps. 4 th edition. International Union of Soil Sciences (IUSS), Vienna, Austria.

## J

- Jabin, M., Guiltherme, E., Topp, W. (2006): Sind historische Meilerplatten hot spots für die Bodenfauna in Buchenwäldern? In: Greven, H., Lenz, N. (Eds.), *Entomologie heute* 18, pp. 45–53.
- Johnson, K., Ouimet, W., Raslan, Z. (2015): Geospatial and LiDAR-based analysis of 18th to early 20th century timber harvesting and charcoal production in Southern New England. *Geological Society of America Abstracts with Programs*. 47, 3. p 65.
- Johnson, M.K., Ouimet, W.B. (2014): Rediscovering the lost archaeological landscape of southern New England using airborne light detection and ranging LiDAR. *Journal of Archaeological Science*. <http://dx.doi.org/10.1016/j.jas.2013.12.004>

## K

- Kalinichev, A.G. & Kirkpatrick, R.J. (2007): Molecular dynamics simulation of cationic complexation with natural organic matter. *European Journal of Soil Science*. DOI: 10.1111/j.1365-2389.2007.00929.x
- Kappenberg, A., Bläsing, M., Lehdorff, E., Amelung, W. (2016): Black carbon assessment using benzene polycarboxylic acids: Limitations for organic-rich matrices. *Organic Geochemistry*. DOI: 10.1016/j.orggeochem.2016.01.009
- Karimi Moayed, N., Vandenberghe, D.A.G., Deforce, K., Bastiaens, J., Ghyselbrecht, E., Debeer, A.E., De Smedt, P., De Clercq, W., De Grave, J. (2020): Bypassing the Suesseffect: age determination of charcoal kiln remains using OSL dating. *Journal of Archaeological Science*. <https://doi.org/10.1016/j.jas.2020.105176>
- Kasozi, G.N., Zimmerman, A.R., Nkedi-Kizza, P., Gao, B. (2010): Catechol and humic acid sorption onto a range of laboratory produced black carbon (biochars). *Environmental science and technology*. DOI: 10.1021/es1014423
- Kazimi, B., Thiemann, F., & Sester, M. (2019): Semantic Segmentation of Manmade Landscape Structures in Digital Terrain Models. *ISPRS Annals of the Photogrammetry, Remote Sensing and Spatial Information Sciences*. <https://doi.org/10.5194/isprs-annals-IV-2-W7-87-2019>
- Kazimi, B., Malek, K., Thiemann, F., & Sester, M. (2020): Effectiveness of DTM Derivatives for Object Detection Using Deep Learning. In: CHNT 25, 2020 – Abstracts (pp. 1–4). Proylaem.
- Kermit, M., Reksten, J. H., & Trier, Ø. D. (2018): Towards a national infrastructure for semi-automatic mapping of cultural heritage in Norway. In M. Matsumoto & E. Uleberg (Red.), *Oceans of Data. Proceedings of the 44th Conference on Computer Applications and Quantitative Methods in Archaeology* (pp. 159–172). Archaeopress.
- Kerré, B., Willaert, B., Smolders, E. (2017): Lower residue decomposition in historically charcoal -enriched soils is related to increased adsorption of organic matter. *Soil Biology & Biochemistry*. <http://dx.doi.org/10.1016/j.soilbio.2016.10.007>
- Kerré, B.; Bravo, C.T.; Leifeld, J.; Cornelissen, G.; Smolders, E. (2016): Historical soil amendment with charcoal increases sequestration of non-charcoal carbon: a comparison among methods of black carbon quantification. *European Journal of Soil Science*. doi: 10.1111/ejss.12338
- Knapp, H., Nelle, O., Kirleis, W. (2015): Charcoal usage in medieval and modern times in the Harz Mountains Area, Central Germany: Wood selection and fast overexploitation of the woodlands. *Quaternary International*. <http://dx.doi.org/10.1016/j.quaint.2015.01.053>

- Kokalj, Ž. & Somrak, M. (2019): Why not a single image? Combining visualisations to facilitate fieldwork and on-screen mapping. Remote sensing. doi:10.3390/rs11070747
- Kokalj, Ž. & Hesse, R. (2017): Airborne Laser Scanning Raster Data Visualization: A Guide to Good Practice. Založba ZRC. ISBN: 978-961-254-984-8
- Krebs, P., Pezzatti, G. B., Stocker, M., Bürgi, M., Conedra, M. (2017): The selection of suitable sites for traditional charcoal production: ideas and practice in southern Switzerland. Journal of historical Geopgraphy. <http://dx.doi.org/10.1016/j.jhg.2017.04.002>
- Kučera, A., Holí, L., Knott, R., Adamec, Z., Volánek, J., Bajer, A. (2022): The Soil Environment of Abandoned Charcoal Kiln Platforms in a Low-Altitude Central European Forest. Forests. DOI: 10.3390/f14010029
- Kurth, V. J., MacKenzie, M. D., & DeLuca, T. H. (2006). Estimating charcoal contents in forest mineral soils. Geoderma. <https://doi.org/10.1016/j.geoderma.2006.08.003>

## L

- Lambers, K., Verschoof-van der Vaart, W. B., & Bourgeois, Q. P. J. (2019): Integrating remote sensing, machine learning, and citizen science in Dutch archaeological prospection. Remote Sensing. <https://doi.org/10.3390/rs11070794>
- Lasota, J., Babiak, T., Błońska, E. (2022): C:N:P stoichiometry associated with biochar in forest soils at historical charcoal production sites in Poland. Geoderma Regional. DOI: 10.1016/j.geodrs.2022.e00482
- Lasota, J., Błońska, E., Babiak, T., Piaszczyk, W., Stępniewska, H., Jankowiak R., Boroń, P., Boroń, A.L. (2021): Effect of Charcoal on the Properties, Enzyme Activities and Microbial Diversity of Temperate Pine Forest Soils. Forests. DOI: 10.3390/f12111488
- LeCun, Y., Bengio, Y., & Hinton, G. (2015): Deep learning. Nature. <https://doi.org/10.1038/nature14539>
- Leifeld, J. (2007): Thermal stability of black carbon characterised by oxidative differential scanning calorimetry. Organic Geochemistry. <https://doi.org/10.1016/j.orggeochem.2006.08.004>
- Li, H., Santos, F., Butler, K., Herndon, E. (2021): A Critical Review on the Multiple Roles of Manganese in Stabilizing and Destabilizing Soil Organic Matter. Environmental Science Technology. DOI: 10.1021/acs.est.1c00299
- Lim, B. & Cachier, H. (1996): Determination of black carbon by chemical oxidation and thermal treatment in recent marine and lake sediments and Cretaceous–Tertiary clays. Chemical Geology. [https://doi.org/10.1016/0009-2541\(96\)00031-9](https://doi.org/10.1016/0009-2541(96)00031-9)

- Lin, T.-Y., Maire, M., Belongie, S., Hays, J., Perona, P., Ramanan, D., Dollár, P., & Zitnick, C. L. (2014): Microsoft COCO: common objects in context. *Lecture Notes in Computer Science*. [https://doi.org/10.1007/978-3-319-10602-1\\_48](https://doi.org/10.1007/978-3-319-10602-1_48)
- Llorente, M., Turrión, M.-B., Glaser, B. (2018): Rapid and economical quantification of black carbon in soils using a modified benzene polycarboxylic acids (BPCA) method. *Organic Geochemistry*. DOI: 10.1016/j.orggeochem.2017.11.005
- Ludemann, T. (2010): Past fuel exploitation and natural forest vegetation in the Black Forest, the Vosges and neighbouring regions in western Central Europe. *Palaeogeography, Palaeoclimatology, Palaeoecology*. doi:10.1016/j.palaeo.2009.09.013
- Ludemann, T., (2003): Large-scale reconstruction of ancient forest vegetation by anthracology - a contribution from the Black Forest. *Phytocoenologia*. DOI: 10.1127/0340-269X/2003/0033-0645
- Luque, A., Carrasco, A., Martín, A., & de las Heras, A. (2019): The impact of class imbalance in classification performance metrics based on the binary confusion matrix. *Pattern Recognition*. <https://doi.org/10.1016/j.patcog.2019.02.023>

## M

- Máliš, F., Bobek, P., Hédl, R., Chudomelová, M., Petřík, P., Ujházy, K., Ujházyová, M., Kopecký, M. (2020): Historical charcoal burning and coppicing suppressed beech and increased forest vegetation heterogeneity. *Journal of Vegetation Science*. <https://doi.org/10.1111/jvs.12923>
- Mastrolonardo, G., Calderaro, C., Cocozza, C., Hardy, B., Dufey, J., Cornelis, J.-T. (2019): Long-term effect of charcoal accumulation in hearth soils on tree growth and nutrient cycling. *Frontiers of Environmental Sciences*. doi.org/10.3389/fenvs.2019.00051
- Mastrolonardo, G., Francioso, O., Certini, G. (2018): Relic charcoal hearth soils: A neglected carbon reservoir. Case study at Marsiliana forest, Central Italy. *Geoderma*. doi.org/10.1016/j.geoderma.2017.11.036
- Máliš, F., Bobek, P., Hédl, R., Chudomelová, M., Petřík, P., Ujházy, K., Ujházyová, M., Kopecký, M. (2020): Historical charcoal burning and coppicing suppressed beech and increased forest vegetation heterogeneity. *Journal of Vegetation Science*. DOI: 10.1111/jvs.12923
- Mikan, C.J., Abrams, M.D. (1995): Altered forest composition and forest development on historic charcoal hearths in southeastern Pennsylvania. *Canadian Journal of Forest Research*. doi.org/10.1139/x26-213
- Muff, S.; Nilssen, E.B., O'Hara, R.B., Nater, C.R. (2021): Rewriting results sections in the language of evidence. *Trends in Ecology & Evolution*. DOI: 10.1016/j.tree.2021.10.009

## N

NASA Shuttle Radar Topography Mission (SRTM) (2013). Shuttle Radar Topography Mission (SRTM) Global. Distributed by OpenTopography. <https://doi.org/10.5069/G9445JDF>. Accessed: 2023-01-30

## O

- Oksuz, K., Cam, B. C., Kalkan, S., & Akbas, E. (2019): Imbalance problems in object detection: A review. In arXiv. <https://arxiv.org/pdf/1909.00169>
- Oliveira, C., Aravecchia, S., Pradalier, C., Robin, V., & Devin, S. (2021): The use of remote sensing tools for accurate charcoal kilns' inventory and distribution analysis: Comparative assessment and prospective. *International Journal of Applied Earth Observation and Geoinformation*. <https://doi.org/10.1016/j.jag.2021.102641>
- Olivier, M., & Verschoof-van der Vaart, W. B. (2021): Implementing State-of-the-Art Deep Learning Approaches for Archaeological Object Detection in Remotely-Sensed Data: The Results of Cross-Domain Collaboration. *Journal of Computer Applications in Archaeology*. <https://doi.org/10.5334/jcaa.78>
- Opitz, R., & Cowley, D. (2013): *Interpreting Archaeological Topography. Airborne Laser Scanning, 3D Data and Ground Observation*. Oxbow Books. ISBN: 9781842175163
- Opitz, R., & Herrmann, J. (2018): Recent trends and long-standing problems in archaeological remote sensing. *Journal of Computer Applications in Archaeology*. <https://doi.org/10.5334/JCAA.11>
- Orengo, H. A., Conesa, F. C., Garcia-Molsosa, A., Lobo, A., Green, A. S., Madella, M., & Petrie, C. A., (2020): Automated Detection of Archaeological Mounds Using Machine-Learning Classification of Multisensor and Multitemporal Satellite Data, *PNAS*. <https://doi.org/10.1073/pnas.2005583117>
- Ouimet, W. (2019): Northeastern US relict charcoal hearth mapper. <https://connecticut.maps.arcgis.com/apps/webappviewer/index.html?id=102f6831a12843878ea8081aec41029d>

## P

- Pollet, S., Chabert, A., Burgeon, V., Corn'elis, J.-T., Fouch'e, J., Gers, C., Hardy, B., Pey, B., (2022): Limited effects of century-old biochar on taxonomic and functional diversities of collembolan communities across land-uses. *Soil Biology & Biochemistry*. <https://doi.org/10.1016/j.soilbio.2021.108484>
- Powell, A.J., Wheeler, J., Batt, C.M. (2012): Identifying archaeological wood stack charcoal production sites using geophysical prospection: magnetic characteristics from a modern

wood stack charcoal burn site. *Journal of Archaeological Science*. DOI: 10.1016/j.jas.2011.11.005

## Q

QGIS Development Team. (2017). QGIS Geographic Information System (3.4). Open Source Geospatial Foundation Project. <http://qgis.org>

Quintus, S., Day, S. S., & Smith, N. J. (2017). The efficacy and analytical importance of manual feature extraction using lidar datasets. *Advances in Archaeological Practice*. <https://doi.org/10.1017/aap.2017.13>

## R

Raab, A., Bonhage, A., Schneider, A., Raab, T., Rösler, H., Heußner, K. U., & Hirsch, F. (2019): Spatial distribution of relict charcoal hearths in the former royal forest district Tauer (SE Brandenburg, Germany). *Quaternary International*. <https://doi.org/10.1016/j.quaint.2017.07.022>

Raab, A., Takla, M., Raab, T., Nicolay, A., Schneider, A., Rösler, H., Heußner, K.U. Bönisch, E. (2015): Pre-industrial charcoal production in Lower Lusatia (Brandenburg, Germany): Detection and evaluation of a large charcoal-burning field by combining archaeological studies, GIS-based analyses of shaded-relief maps and dendrochronological age determination. *Quaternary International*. DOI: 10.1016/j.quaint.2014.09.041

Raab, T., Raab, A., Bonhage, A., Schneider, A., Hirsch, F., Birkhofer K., Drohan, P., Wilmking, M., Kreyling J., Malik, I., Wistuba, M., van der Maarten, E., van der Maarten-Theunissen, M., Urich, T. (2022): Do small landforms have large effects? A review on the legacies of pre-industrial charcoal burning. *Geomorphology*. DOI: 10.1016/j.geomorph.2022.108332

Raab T., Hirsch, F., Oumiet, W., Johnson, K.M., Dethier, D., Raab, A. (2017): Architecture of relict charcoal hearths in northwestern Connecticut, USA. *Geoarchaeology*. DOI: 10.1002/geoa.21614

Rebollo, N.R., Cohen-Ofri, I., Popovitz-Biro, R., Bar-Yosef, O., Meignen, L., Goldberg, P., Weiner, S., Boaretto, E. (2008): Structural Characterization of Charcoal Exposed to High and Low Ph: Implications for 14C Sample Preparation and Charcoal Preservation. *Radio-carbon*. DOI: 10.1017/s0033822200033592

Redmon, J., Divvala, S., Girshick, R., & Farhadi, A. (2016): You Only Look Once: Unified, Real-Time Object Detection. arXiv preprint, 1506.02640.

Reisser, M., Purves, R.S., Schmidt, M.W.I., Abvien S. (2016): Pyrogenic Carbon in Soils: A Literature-Based Inventory and a Global Estimation of Its Content in Soil Organic Carbon and Stocks. *Frontiers in Earth Science*. DOI: 10.3389/feart.2016.00080

- Ren, S., He, K., Girshick, R., & Sun, J. (2017): Faster R-CNN: Towards real-time object detection with region proposal networks. *IEEE Transactions on Pattern Analysis and Machine Intelligence*. <https://doi.org/10.1109/TPAMI.2016.2577031>
- Rezatofighi, H., Tsoi, N., Gwak, J., Sadeghian, A., Reid, I., & Savarese, S. (2019): Generalized intersection over union: A metric and a loss for bounding box regression. *Proceedings of the IEEE Computer Society Conference on Computer Vision and Pattern Recognition*. <https://doi.org/10.1109/CVPR.2019.00075>
- Riley, S., DeGloria, S.D., Elliot, R. (1999): A terrain ruggedness index that quantifies topographic heterogeneity. *Intermountain Journal of Sciences* 5, 1-4. pp- 23-27.
- Risbøl, O., Bollandsås, O. M., Nesbakken, A., Ørka, H. O., Naeset, E., & Gobakken, T. (2013): Interpreting cultural remains in airborne laser scanning generated digital terrain models: effects of size and shape on detection success rates. *Journal of Archaeological Science*. <https://doi.org/10.1016/j.jas.2013.07.002>
- Robertson, A.H.J., Main, A.M., Robinson, L.J., Dawson, L.A. (2015): In Situ FTIR analysis of soils for forensic applications. *Spectroscopy Supplements Vol. 30 Issue 8*, pp. 22-30
- Rutkiewicz, P., Malik, I., Wistuba, M., Osika, A. (2019): High concentration of charcoal hearths remains as legacy of historical ferrous metallurgy in southern Poland. *Quaternary International*. [doi.org/10.1016/j.quaint.2019.04.015](https://doi.org/10.1016/j.quaint.2019.04.015)

## S

- Sadr, K. (2016): The impact of coder reliability on reconstructing archaeological settlement patterns from satellite imagery: A case study from South Africa. *Archaeological Prospection*. <https://doi.org/10.1002/arp.1515>
- Sammut, C., & Webb, G. I. (2010): *Encyclopaedia of Machine Learning*. Springer. <https://doi.org/10.1007/978-0-387-30164-8>
- Schmidt, M.W.I., Skjemstad, J.O., Czimczik, C.I., Glaser, B., Prentice, K.M., Gelinas, Y., Kuhlbusch, A.J. (2001): Comparative analysis of black carbon in soils. *Global Biogeochemical Cycles*. DOI: 10.1029/2000gb001284
- Schmidt, S. C., & Marwick, B. (2020): Tool-Driven Revolutions in Archaeological Science. *Journal of Computer Applications in Archaeology*. <https://doi.org/10.5334/jcaa.29>
- Schneider, A., Bonhage, A., Hirsch, F., Raab, A., & Raab, T. (2022): Hot spots and hot zones of soil organic matter in forests as a legacy of historical charcoal production. *Forest Ecology and Management*. <https://doi.org/10.1016/J.FORECO.2021.119846>
- Schneider, A., Bonhage, A., Raab, A., Hirsch, F., Raab, T. (2020a): Large-scale mapping of anthropogenic relief features - legacies of past forest use in two historical charcoal production areas in Germany. *Geoarchaeology*. <https://doi.org/10.1002/gea.21782>



- Schneider, A., Hirsch, T., Bonhage, A., Raab, A., Raab, T. (2020b): The soil moisture regime of charcoal-enriched land use legacy sites. *Geoderma*. <https://doi.org/10.1016/j.geoderma.2020.114241>
- Schneider, A., Hirsch, F., Raab, A., Raab, T. (2019): The temperature regime of a charcoal-enriched land use legacy soil. *Soil Science Society of America*. DOI: 10.2136/sssaj2018.12.0483
- Schneider, A., Hirsch, F., Raab, A., Raab, T. (2018a): Dye tracer visualization of infiltration patterns in soils on relict charcoal hearths. *Frontiers of Environmental Science*. doi: 10.3389/fenvs.2018.00143
- Schneider, A., Hirsch, F., Raab, A., Raab, T. (2018b): Bodenkundlich-geomorphologische Untersuchung von Meilerplätzen um Weiherhammer. *Beiträge zur Archäologie in der Oberpfalz und in Regensburg*. 12. 433-448. ISSN 1617-4461
- Schneider, A., Takla, M., Nicolay, A., Raab, A., Raab, T. (2014): A template-matching approach combining morphometric variables for automated mapping of charcoal kiln sites. *Archaeological Prospection*. DOI: 10.1002/arp.1497
- Schneider, M.P.W., Hilf, M., Vogt, U.F., Schmidt, M.W.I. (2010): The benzene polycarboxylic acid (BPCA) pattern of wood pyrolyzed between 200°C and 1000°C. *Organic Geochemistry*. DOI: 10.1016/j.orggeochem.2010.07.001
- Sing, B.P., Cowie, A.L. (2014): Long-term influence of biochar on native organic carbon mineralisation in a low-carbon clayey soil. *Scientific Reports*. DOI: 10.1038/srep03687
- Słowiński, M., Szewczyk, K., Jonczak, J., Związek, T., Łuców, D., Halaś, A., Obremska, M., Słowińska S., Róg D., Mroczkowska, A., Noryśkiewicz, A. M., Chojnacka, A., Ważny T., Gmińska-Nowak, B., Kramkowski M., Barbarino, V., Tyszkowski S., Kruczkowska, B., Kowalska A., Kołaczowska, E., Swoboda, P., Kardasz, C., Niedzielski M., Konopski M., Brykała D. (2022): A novel multiproxy approach to detect the impact of charcoal production on the natural environment in NW Poland - Project concept and preliminary results. *Geographica Polonica*. DOI: 10.7163/GPol.0233
- Smith, M. L. (2014): Citizen science in archaeology. *American Antiquity*. <https://doi.org/10.7183/0002-7316.79.4.749>
- Soil Survey Staff 2014: *Keys to soil taxonomy*. 12th ed. USDA-NRCS, Washington, DC.
- Soil Survey Staff (2022): *The Gridded Soil Survey Geographic (gSSURGO) Database for Connecticut*. United States Department of Agriculture, Natural Resources Conservation Service. Available online at <https://gdg.sc.egov.usda.gov/>. October 2022.
- Soil Survey Staff (2014): *Kellogg Soil Survey Laboratory Methods Manual*. Soil Survey Investigations Report No. 42, Version 5.0.R. Burt and Soil Survey Staff (ed.). US Department

of Agriculture, Natural Resources Conservation Services.

- Soroush, M., Mehrtash, A., Khazraee, E., & Ur, J. A. (2020): Deep Learning in Archaeological Remote Sensing: Automated Qanat Detection in the Kurdistan Region of Iraq. *Remote Sensing*. <https://doi.org/10.3390/rs12030500>
- Stolz, C., Böhnke, S., Grunert, J. (2012): Reconstructing 2500 years of land use history on the Kemel Heath Kemeler Heide, southern Rhenish Massif, Germany. 61. 169-183. doi:10.1016/j.quaint.2009.08.022
- Stolz, C., Grunert, J. (2010): Late Pleistocene and Holocene landscape history of the central Palatinate forest Pfälzerwald, south-western Germany. *Quaternary International*. DOI 10.3285/eg.61.2.05
- Stone, J. R., Schafer, J. P., London, E. H., DiGiacomo-Cohen, M. L., Lewis, R. S., Thompson, W. B. (2005): Quaternary geologic map of Connecticut and Long Island Sound Basin. Reston, VA: U.S. Geological Survey.
- Suh, J. W., Anderson, E., Ouimet, W., Johnson, K. M., & Witharana, C. (2021): Mapping Relict Charcoal Hearths in the Northeast US Using Deep Learning Convolutional Neural Networks and LIDAR Data. *Remote Sensing*. <https://doi.org/10.3390/rs13224630>

## T

- Tarolli, P., Cao, W., Sofia, G., Evans, D., Ellis, E.C. (2019): From features to fingerprints: A general diagnostic framework for anthropogenic geomorphology. *Progress in Physical Geography*. DOI: 10.1177/0309133318825284
- Tebo, B.M., Bargar, J.R., Clement, B.G., Dick, G.J., Murray, K. J., Parker, D., Verity, R., Webb, S.M. (2004): Biogenic manganese oxides: Properties and Mechanisms of Formation. *Annual Review of Earth and Planetary Sciences*. DOI: 10.1146/annurev.earth.32.101802.120213
- Tolksdorf, J.F., Kaiser, K., Petr, L., Herbig, C., Kočár, P., Heinrich, S., Wilke, F. D. H., Theuerkauf, M., Fülling, A., Schubert, M., Schröder, F., Křivánek, R., Schulz, L., Bonhage, A., Hemker, C. (2020): Tracing past human impact in a mountain area: geoarchaeology of the medieval glass kiln site Ullersdorf, Erzgebirge Germany. *Regional Environmental Change*. <https://doi.org/10.1007/s10113-020-01638-1>
- Tolksdorf, J.F., Elburg, R., Schröder, F., Knapp, H., Herbig, C., Westphal, T., Schneider, B., Fülling, A., Hemker, C. (2015): Forest exploitation for charcoal production and timber since the 12th century in an intact medieval mining site in the Niederpöbel Valley (Erzgebirge, Eastern Germany). *Journal of Archaeological Science: Reports*. <http://dx.doi.org/10.1016/j.jasrep.2015.10.018>

- Tomasso, L.P., Leighton, M. (2014): The Impact of Land Use Change for Greenhouse Gas Inventories and State-Level Climate Mediation Policy: A GIS Methodology Applied to Connecticut. *Journal of Environmental Protection*. DOI: 10.4236/jep.2014.517149
- Tilston, E.L., Ascough P.L., Garnett, M.H., Bird, M.I. (2016): Quantifying Charcoal Degradation and Negative Priming of Soil Organic Matter with a <sup>14</sup>C-Dead Tracer. *Radiocarbon*. DOI: 10.1017/rdc.2016.45
- Trier, Ø. D., Reksten, J. H., & Løseth, K. (2021): Automated mapping of cultural heritage in Norway from airborne lidar data using faster R-CNN. *International Journal of Applied Earth Observation and Geoinformation*. <https://doi.org/10.1016/j.jag.2020.102241>
- Trier, Ø. D., Salberg, A.-B., & Pilø, L. H. (2018): Semi automatic mapping of charcoal kilns from airborne laser scanning data using deep learning. In M. Matsumoto & E. Uleberg (Red.), *CAA 2016: Oceans of Data*. Proceedings of the 44th Conference on Computer Applications and Quantitative Methods in Archaeology (pp. 219–231). Archaeopress.
- Trier, D.T., Cowley, D.C., Waldeland, A. U. (2018): Using deep neural networks on airborne laser scanning data: Results from a case study of semi-automatic mapping of archaeological topography on Arran, Scotland. *Archaeological Prospection*. DOI: 10.1002/arp.1731
- Trier, Ø. D., & Pilø, L. H. (2012): Automatic Detection of Pit Structures in Airborne Laser Scanning Data. *Archaeological Prospection*. <https://doi.org/10.1002/arp.1421>

## V

- Van Rossum, G., & Drake, F. L. (2009). *Python 3 Reference Manual*. CreateSpace. ISBN: 978-1-4414-1269-0
- Verschoof-van der Vaart, W. B., Bonhage, A., Schneider, A., Ouimet, W., Raab, T. (2022): Automated large-scale mapping and analysis of relict charcoal hearths in Connecticut (USA) using a Deep Learning YOLOv4 framework. *Archaeological Prospection*. DOI: 10.1002/arp.1889
- Verschoof-van der Vaart, W. B., & Landauer, J. (2022): Testing the transferability of CarcassonNet. A Case study to detect hollow roads in Germany and Slovenia. Proceedings of the 25th Conference on Cultural Heritage and New Technologies, CHNT25. <https://doi.org/10.11588/propylaeum.1045>
- Verschoof-van der Vaart, W. B. (2022): Learning to Look at LiDAR. Combining CNN-based object detection and GIS for archaeological prospection in remotely-sensed data. Leiden University.
- Verschoof-van der Vaart, W. B., Lambers, K., Kowalczyk, W., & Bourgeois, Q. P. J. (2020): Combining Deep Learning and Location-Based Ranking for Large-Scale Archaeological

Prospection of LiDAR Data from The Netherlands. *ISPRS International Journal of Geo-Information*. <https://doi.org/10.3390/ijgi9050293>

Verschoof-van der Vaart, W.B., Lambers, K. (2019): Learning to look at LiDAR: The use of R-CNN in the automated detections of archaeological objects on LiDAR data from the Netherlands. *Journal of Computer Applications in Archaeology*. DOI: <http://doi.org/10.5334/jcaa.32>

Volkov, D., Rogova, O., Proskurnim, M. (2021): Organic Matter and Mineral Composition of Silicate Soils: FTIR Comparison Study by Photoacoustic, Diffuse Reflectance, and Attenuated Total Reflection Modalities. *Agronomy*. DOI: [10.3390/agronomy11091879](https://doi.org/10.3390/agronomy11091879)

Völkel, J. (1995): Periglacial covers and soils of the Bavarian Forest and adjacent areas (Germany). *Zeitschrift für Geomorphologie, Supplementary Issues, Volume 96*.

von Kortzfleisch, A., (2008): *Die Kunst der schwarzen Gesellen. Köhlerei im Harz*. Papierflieger. 978-3-89720-988-6 (ISBN)

## W

Wagner, T.V., Mouter, A.K., Parsons, J.R., Sevnik, J., van der Plicht, J., Jansen, B. (2018): Molecular characterization of charcoal to identify adsorbed SOM and assess the effectiveness of common SOM-removing pretreatments prior to radiocarbon dating. *Quaternary Geochronology*. DOI: [10.1016/j.quageo.2017.10.006](https://doi.org/10.1016/j.quageo.2017.10.006)

Walkley, A. (1947): A critical examination of a rapid method for determining organic carbon in soils—effect of variations in digestion conditions and of inorganic soil constituents. *Soil Science*. 63, pp. 251–264.

Warren, G., McDermott, C., O'Donnell, L., Sands, R. (2012): Recent excavations of charcoal production platforms in the Glendalough Valley, Co. Wicklow. *Journal of Irish Archaeology*. <http://hdl.handle.net/10197/6578>

Weiss, A.D. (2000): Topographic position and landform analysis. Available Online: [http://www.jennessent.com/downloads/tpi-poster-tnc\\_18x22.pdf](http://www.jennessent.com/downloads/tpi-poster-tnc_18x22.pdf)

Williams, C.E. (2019): LiDAR prospection of relict charcoal hearths of the Shippenville Furnace region, Clarion County, Pennsylvania. *Pennsylvania Archaeologist*. 89.

White, K.E., Reeves, J.B. Coale F.J. (2011): Mid-infrared diffuse reflectance spectroscopy for the rapid analysis of plant root composition. *Geoderma*. DOI: [10.1016/j.geoderma.2011.08.009](https://doi.org/10.1016/j.geoderma.2011.08.009)

Witharana, C., Ouimet, W.B., Johnson, K.M. (2018): Using LiDAR and GEOBIA for automated extraction of 18th -late 19th century relict charcoal hearths in southern New England. *GIScience & Remote Sensing*. <https://doi.org/10.1080/15481603.2018.1431356>

## Y

Young, M.J., Johnson, J.E. Abrams, M.D. (1996): Vegetative and edaphic characteristics on relic charcoal hearths in the Appalachian Mountains. *Vegetatio*. <https://doi.org/10.1007/BF0004520>

## Z

Zheng, Z., Wang, P., Ren, D., Liu, W., Ye, R., Hu, Q., & Zuo, W. (2021): Enhancing Geometric Factors in Model Learning and Inference for Object Detection and Instance Segmentation. *IEEE Transactions on Cybernetics*. <https://doi.org/10.1109/TCYB.2021.3095305>

Zimmerman, A.R., Mitra, S. (2017): Trial by Fire: On the Terminology and Methods Used in Pyrogenic Organic Carbon Research. *Frontiers in Earth Science*. DOI: 10.3389/feart.2017.00095

Zimmerman, A.R., Gao, B., Ahn, M.-Y. (2011): Positive and negative carbon mineralization priming effects among a variety of biochar-amended soils. *Soil Biology and Biochemistry*. DOI: 10.1016/j.soilbio.2011.02.005

Zou, Q., Xie, S., Lin, Z., Wu, M., & Ju, Y. (2016): Finding the Best Classification Threshold in Imbalanced Classification. *Big Data Research*. <https://doi.org/10.1016/j.bdr.2015.12.001>

## **Annex**

The Annex contains additional results from field- and laboratory work that were used in the thesis and the publications, but were not displayed in the respective chapters.

## Chapter 5

**Table A1.** Physical and chemical soil properties for a representative RCH site and corresponding reference forest soil.

RCH no. and pit position	Depth [cm]	Soil horizon	Bulk density [g cm <sup>-3</sup> ]	pH in CaCl <sub>2</sub>
39-4 reference forest soil	0-12	Ah	0.55	4.1
	12-50	Bw	-	4.5 - 4.7
	50-80	C	-	4.7
39-1	0-21	Auh	0.51	3.5 - 4.3
	21-40	2Bwb	-	4.5
39-2	0-25	Auh	0.67	4.6 - 4.8
	25-50+	Bw2	-	4.8
39-3	0-9	Auh	0.73	4.4
	9-14	2Auh (int)	0.94	4.8
	14-32	3Auh	0.74	3.9 - 4.9
	32-61	4Auh (int)	0.94	4.7 - 4.8
	61-77	5 Auh	0.67	4.4 - 4.8
	77-87	fAh	1.14	4.8
	87-120+	Bw	0.96	4.2 - 4.4

**Table A2.** Descriptive statistics of all measured soil horizons thickness for every position on the RCH sites and for reference forest soil profiles. Only Bwb- and Bw-horizons where the subsequent C-horizon was visible are included (SDW = Standard deviation, CV= Coefficient of variation).

Soil horizon	Position	N	Average thickness [cm]	SDW [cm]	CV
Auh	1	47	20.9	5.7	0.3
	2	49	22.9	8.1	0.4
	3	48	23.6	14.9	0.6
Auh2	1	2	18.0	-	-
	2	17	14.4	6.1	0.4
	3	24	17.4	8.5	0.5
Auh3	1	0	-	-	-
	2	0	-	-	-
	3	4	16.3	9.7	0.6
Int Auh	1	3	8.3	2.5	0.3
	2	21	7.6	4.0	0.5
	3	29	14.4	7.3	0.5
Int Auh2	1	0	-	-	-
	2	2	8.5	-	-
	3	5	24.0	11.2	0.5
Ahb	1	6	5.0	2.2	0.4
	2	18	6.7	2.6	0.4
	3	21	8.7	5.1	0.4
Bwb	1	11	15.6	4.6	0.3
	2	14	15.7	6.7	0.4
	3	6	14.3	2.7	0.2
Forest Ah	4	24	9.7	4.5	0.5
Forest Bw	4	20	29.1	8.6	0.3

**Table A3.** Coefficient matrix of Mann-Whitney-U test results comparing bulk density for soil horizons (/ p > 0.05 (not significant), \* p ≤ 0.05, \*\* p ≤ 0.01, \*\*\* p ≤ 0.001)

Position	Auh1			Auh2			Ahb			Bwb			int Auh1			int Auh2	Ah	Bw
	1	2	3	2	3	1	2	3	1	2	3	1	2	3	3	4	4	
Auh1	1	X	/	**	***	***	***	***	***	***	***	***	***	***	***	**	**	***
	2		X	**	***	**	***	***	***	***	***	***	***	***	**	*	***	
	3			X	*	*	***	***	***	***	***	***	***	***	/	/	***	
Auh2	2				X	/	*	/	*	***	***	***	/	/	/	/	***	
	3					X	**	/	**	***	***	***	/	/	/	/	***	
Ahb	1						X	/	/	/	/	/	*	*	/	/	***	
	2							X	/	***	/	*	/	/	/	/	*	
	3								X	**	/	/	/	*	/	/	***	
Bwb	1									X	/	/	***	***	***	**	***	
	2										X	/	**	***	**	*	***	
	3											X	**	**	/	/	***	
int Auh1	1													X	/	/	/	
	2														X	/	/	
	3															X	/	
int Auh2	3															X	/	
Ah	4																X	
Bw	4																	

**Table A4.** Descriptive statistics of soil horizons bulk densities for every position on the RCH sites and for reference forest soil profiles.

Soil horizon	Position	N	Average bulk density [g per cm <sup>3</sup> ]	SDW [g cm <sup>-3</sup> ]	CV
Auh	2	50	0.67	0.09	13
	3	49	0.73	0.10	13
Auh2	1	2	0.80	-	-
	2	14	0.83	0.16	19
	3	20	0.81	0.12	14
Auh3	1	0	-	-	-
	2	0	-	-	-
	3	3	0.80	0.02	3
Int Auh	1	12	0.90	0.17	19
	2	8	0.86	0.07	9
Int Auh2	3	22	0.92	0.17	18
	1	0	-	-	-
	2	1	1.18	-	-
Ahb	3	6	0.89	0.16	18
	1	6	1.00	0.08	8
	2	13	0.92	0.14	15
Bwb	3	18	0.98	0.18	19
	1	30	1.09	0.13	12
	2	26	1.05	0.15	14
Forest Ah	3	27	1.04	0.14	13
	4	17	0.76	0.14	19
Forest Bw	4	14	1.05	0.12	11



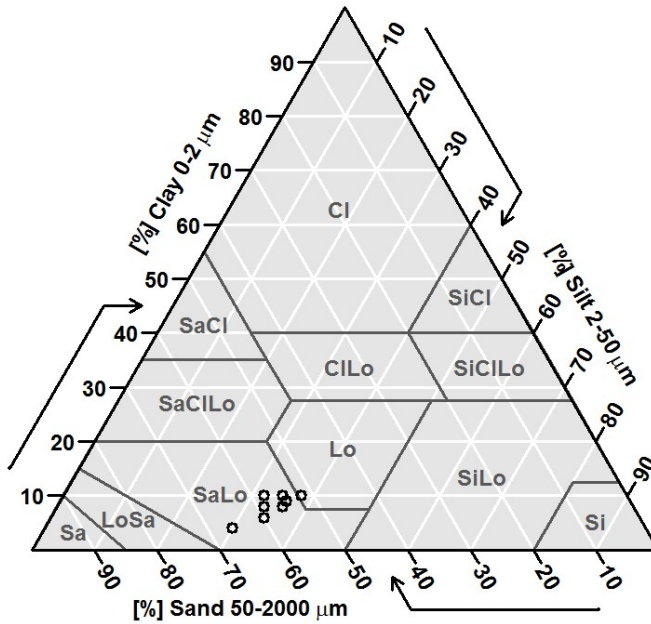


**Abbildung A1.** Soil texture for RCH sites no. 28, 29, 30, 32, 33 (averaged per site) and their respective reference forest soil profiles (USDA texture triangle)

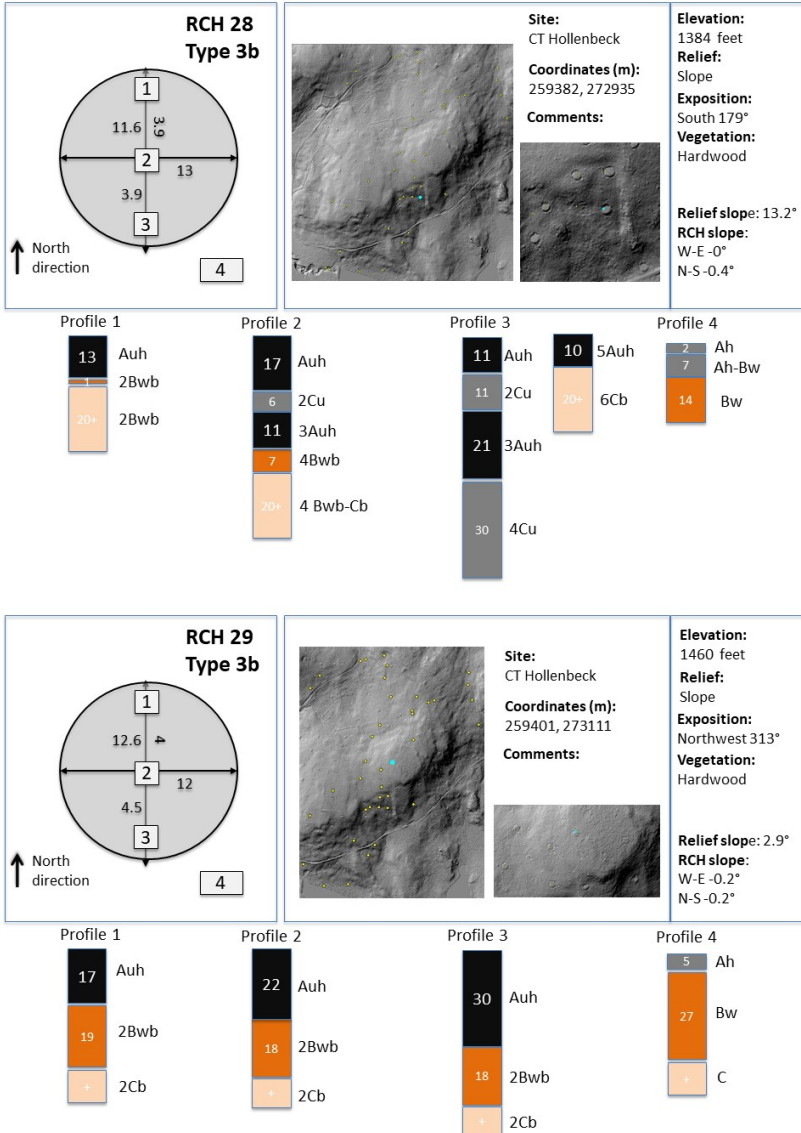
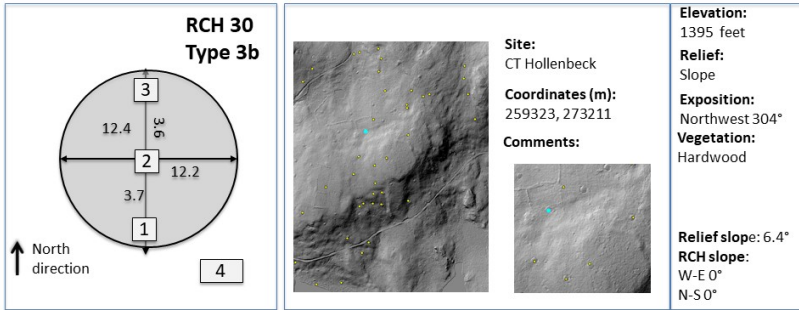
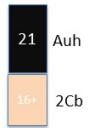


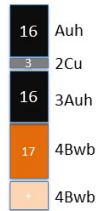
**Abbildung A2.** Site Stratigraphy. The following morphometric and stratigraphic information regarding the 52 RCH sites sampled in Litchfield County has not been published with Chapter 5, but is included in this thesis for completeness. The soil horizons classification varies slightly compared to chapter 5.



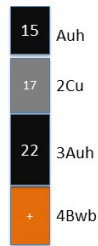
Profile 1



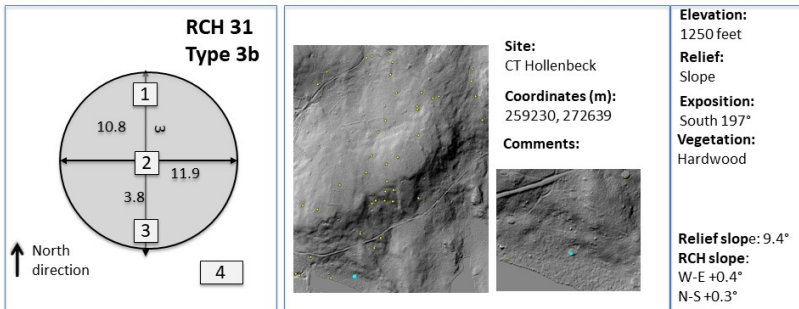
Profile 2



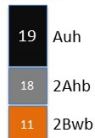
Profile 3



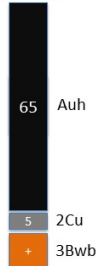
Profile 4



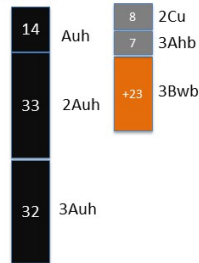
Profile 1



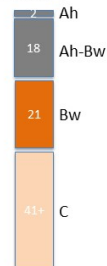
Profile 2

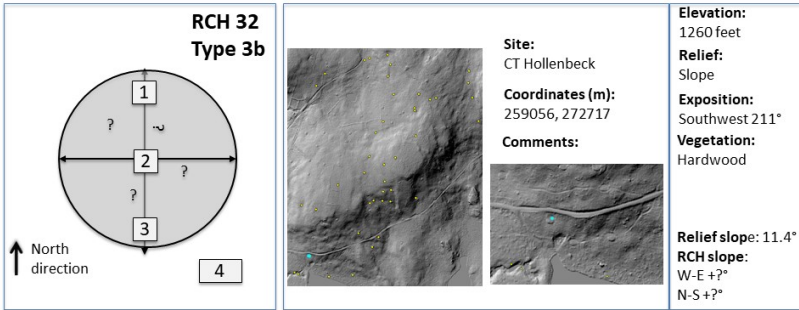


Profile 3

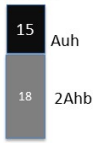


Profile 4

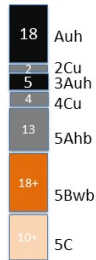




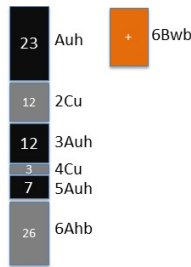
Profile 1



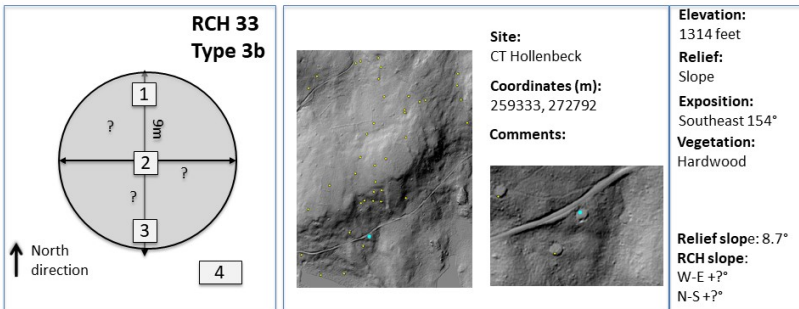
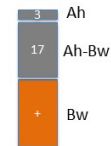
Profile 2



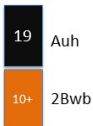
Profile 3



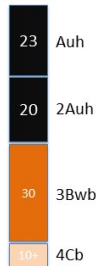
Profile 4



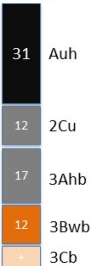
Profile 1



Profile 2

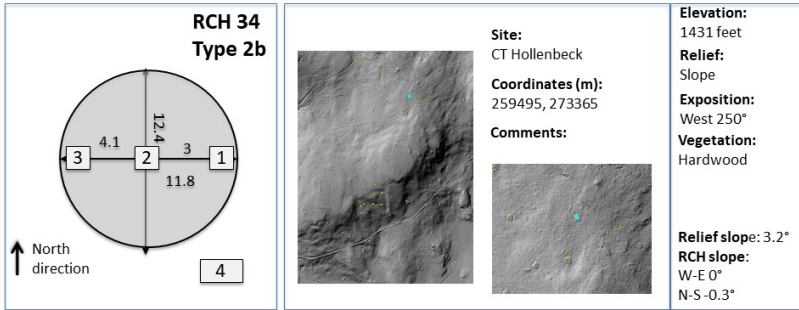


Profile 3

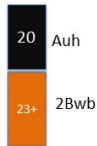


Profile 4

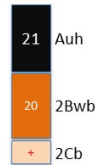




Profile 1



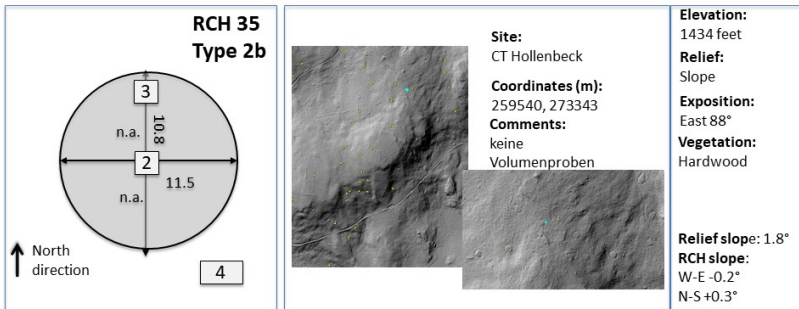
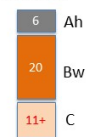
Profile 2



Profile 3



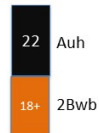
Profile 4



Profile 1

n.a.

Profile 2

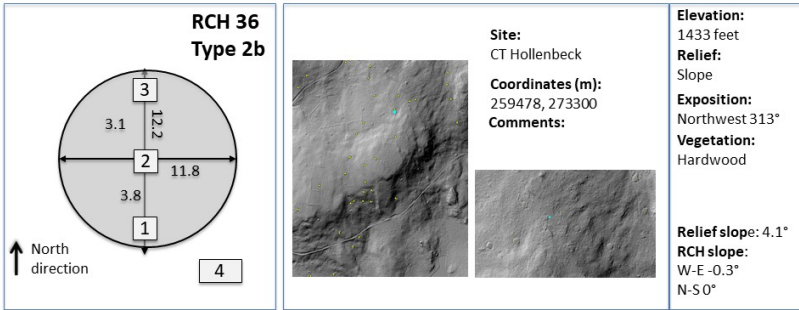


Profile 3

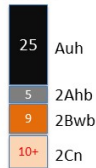


Profile 4

see 34-4



Profile 1



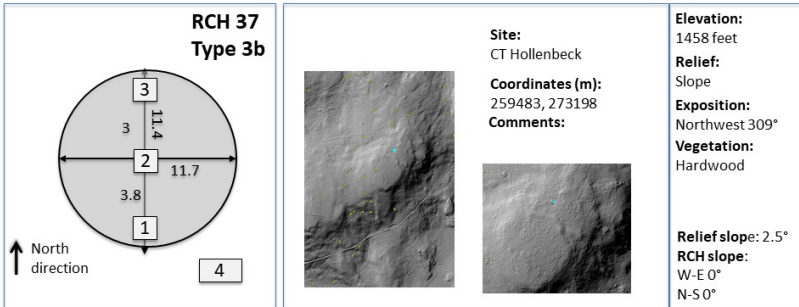
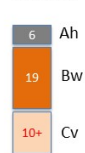
Profile 2



Profile 3



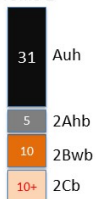
Profile 4



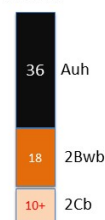
Profile 1



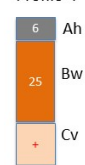
Profile 2

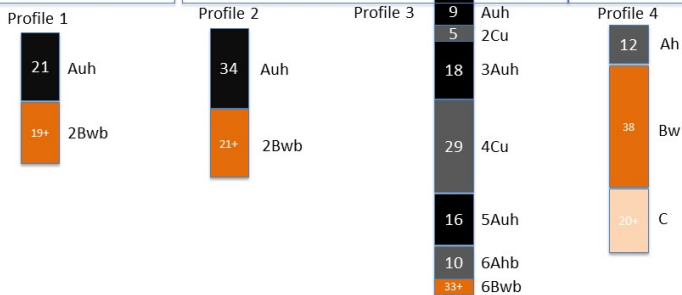
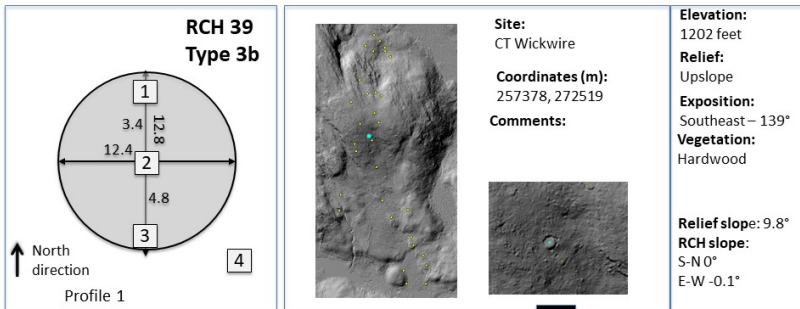
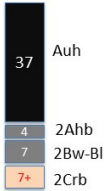
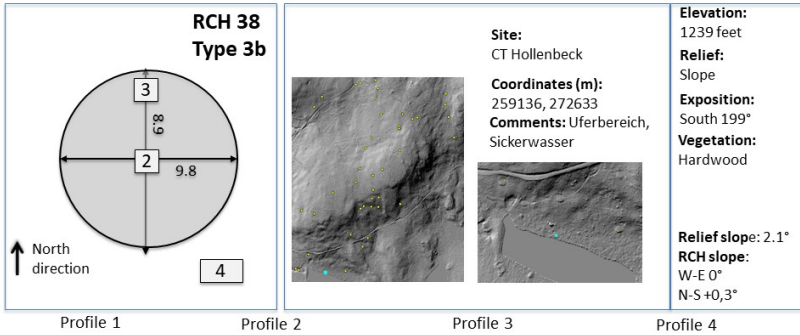


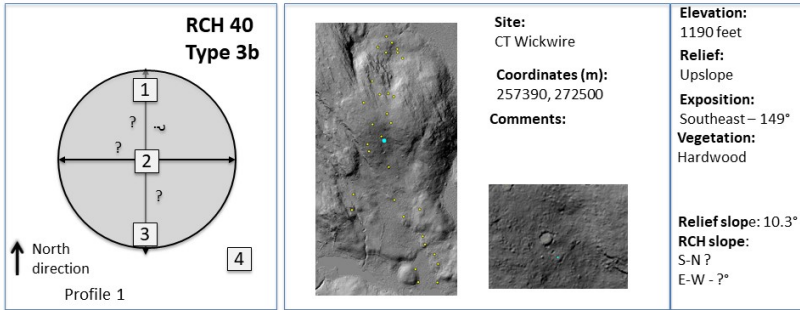
Profile 3



Profile 4



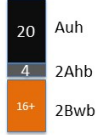




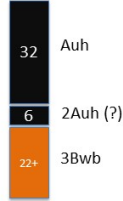
Profile 1



Profile 2

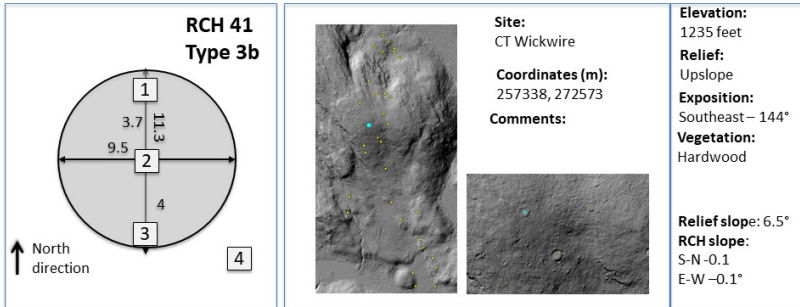


Profile 3

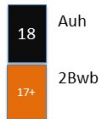


Profile 4

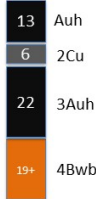
nicht  
bebrobt



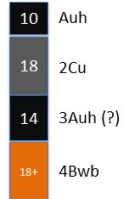
Profile 1



Profile 2



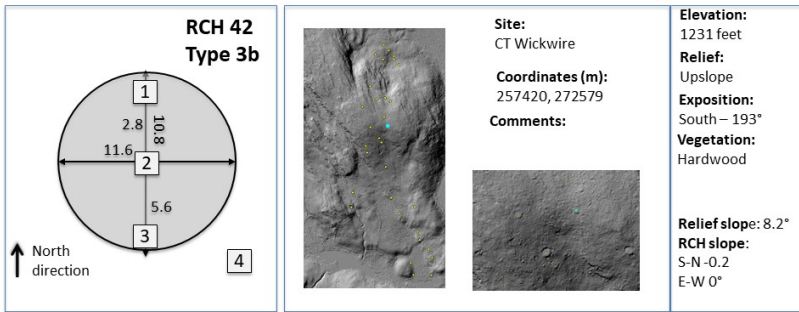
Profile 3



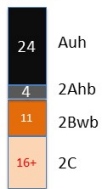
Profile 4



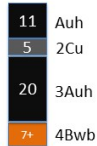




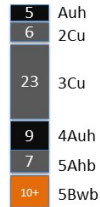
Profile 1



Profile 2

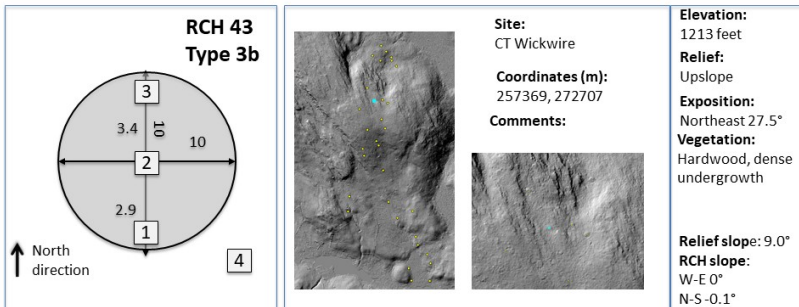


Profile 3

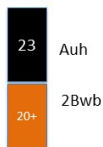


Profile 4

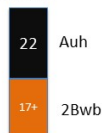
nicht  
beprobt



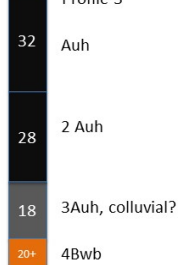
Profile 1



Profile 2

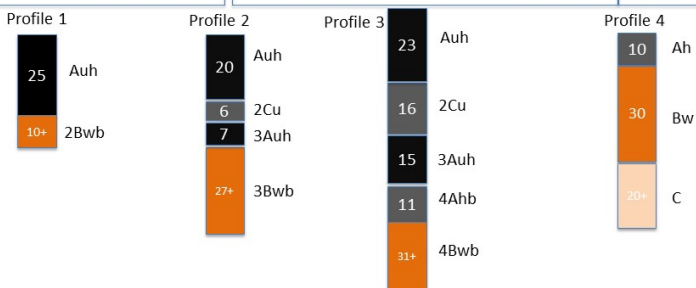
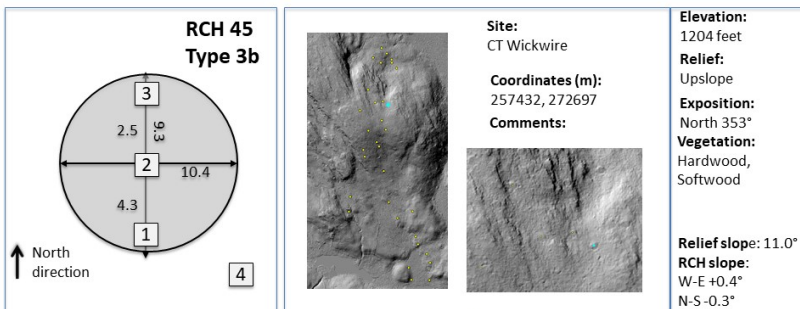
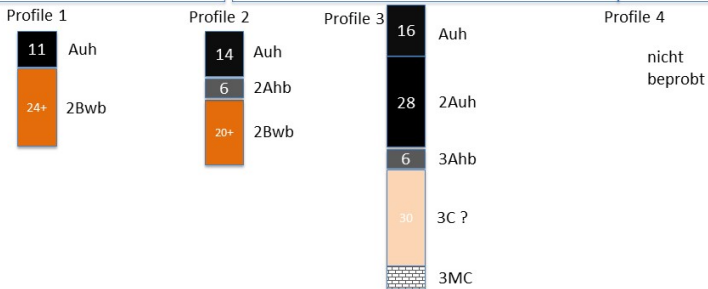
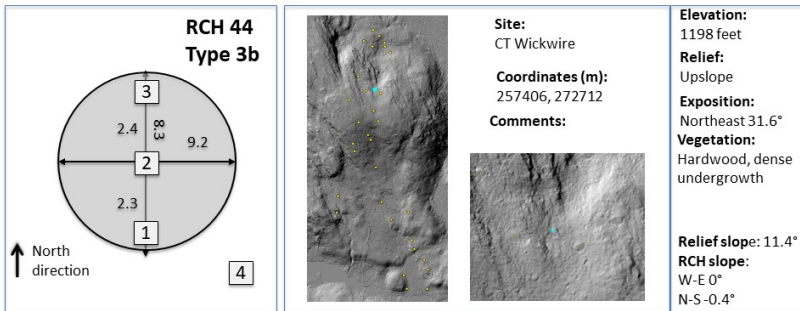


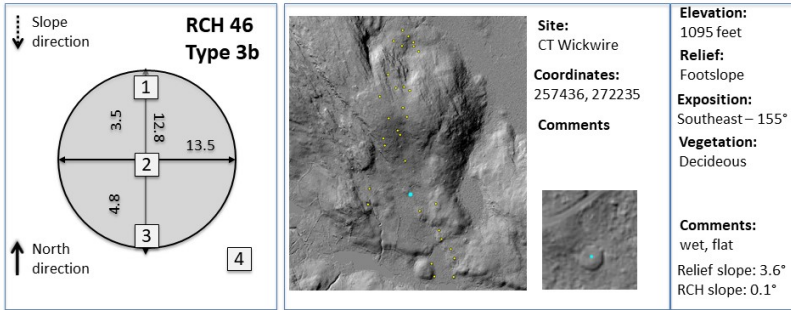
Profile 3



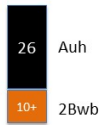
Profile 4

nicht  
beprobt

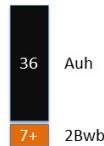




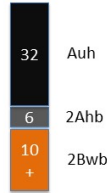
Profile 1



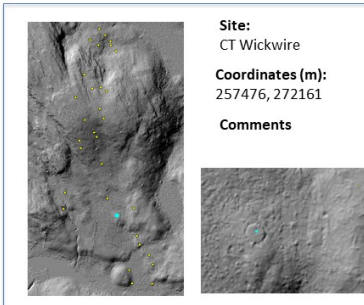
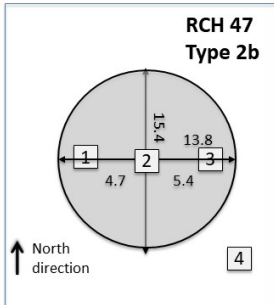
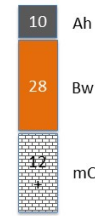
Profile 2



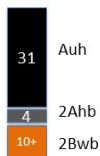
Profile 3



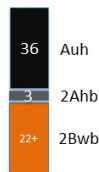
Profile 4



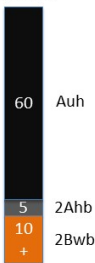
Profile 1



Profile 2



Profile 3



Profile 4

Same as 46  
nicht  
bepröbt

**RCH 48  
Type 3b**

North direction

**Site:**  
CT Wickwire

**Coordinates (m):**  
257411, 270383

**Comments:**  
multiple usages, ditches,  
heavy disturbances

**Elevation:**  
1132 feet

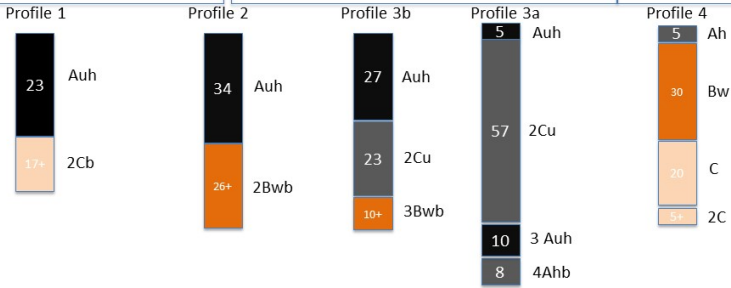
**Relief:**  
slope

**Exposition:**  
Southeast – 155°

**Vegetation:**  
Hardwood

**Relief slope:** 6.6°

**RCH slope:**  
W-E  
S-N -



**RCH 49  
Type 3b**

North direction

**Site:**  
CT Wickwire

**Coordinates (m):**  
257542, 271869

**Comments:**  
wall structure nearby,  
groundwater

**Elevation:**  
1039 feet

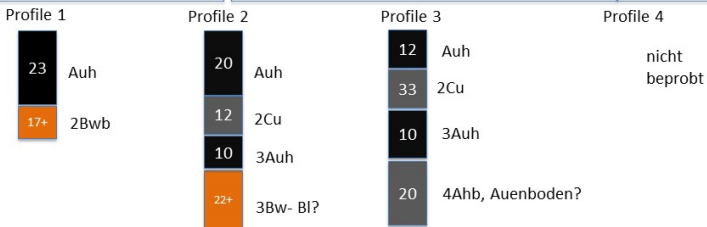
**Relief:**  
Flat- Wetland

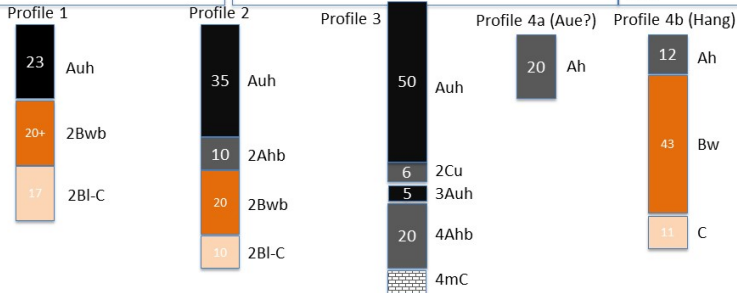
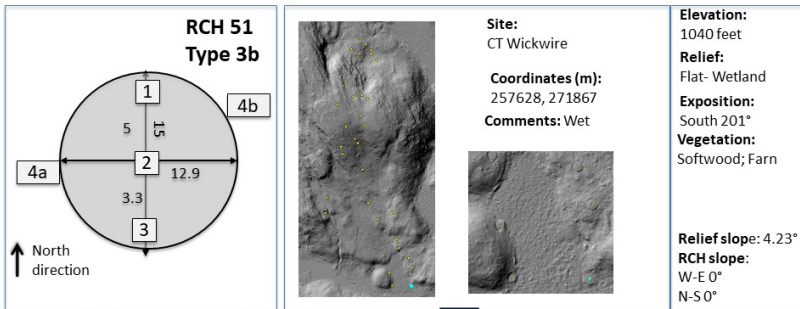
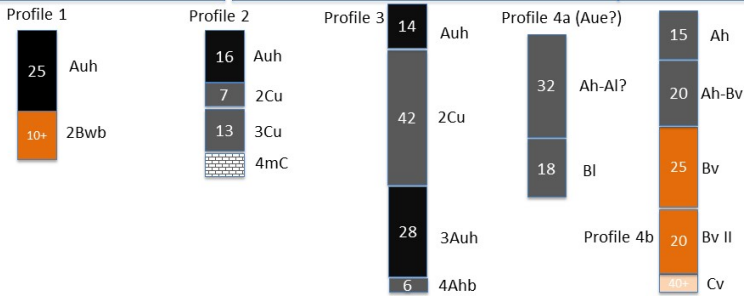
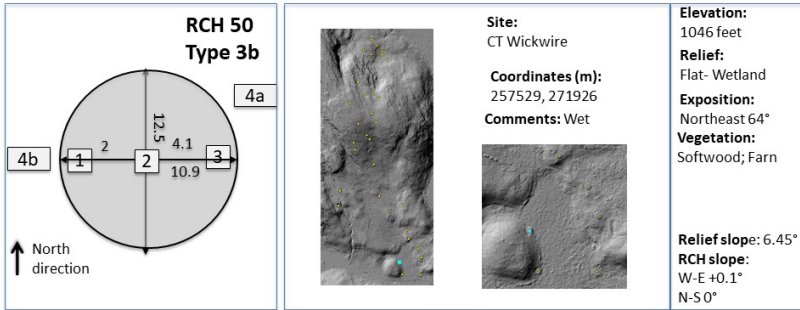
**Exposition:**  
Southeast – 144°

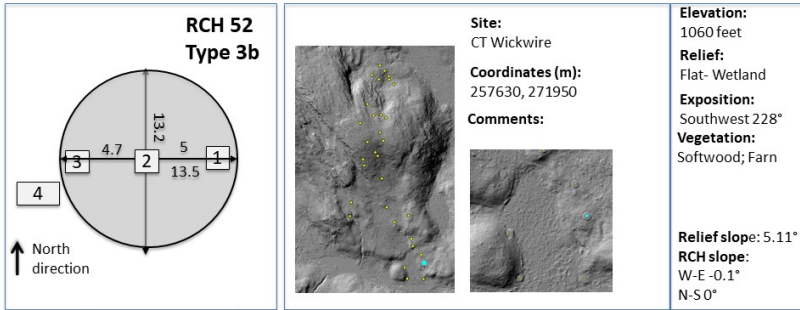
**Vegetation:**  
Softwood, Pine

**Relief slope:** 8.3°

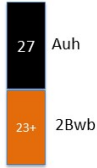
**RCH slope:**  
W-E 0°  
S-N -0°



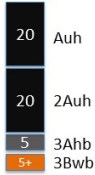




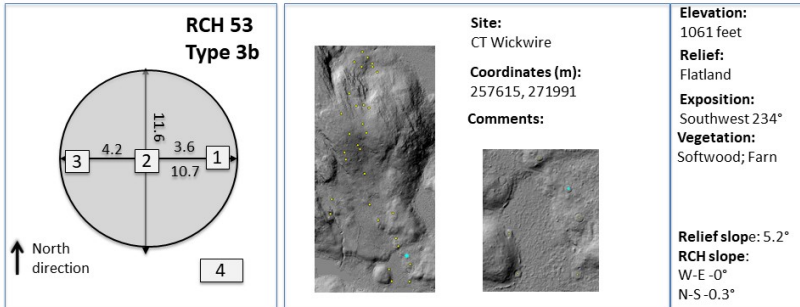
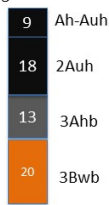
Profile 1



Profile 2



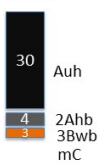
Profile 3



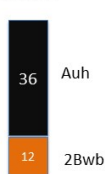
Profile 1



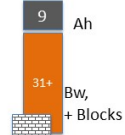
Profile 2

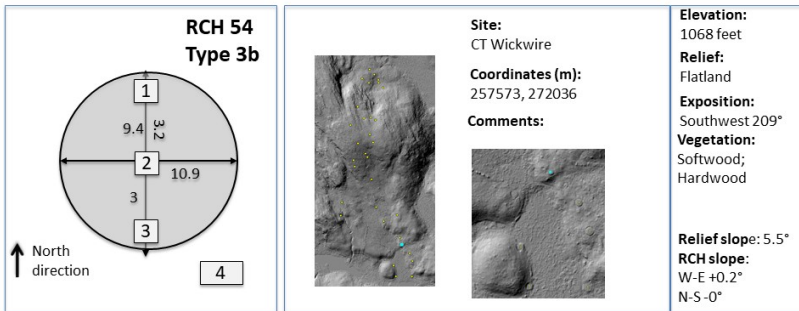


Profile 3

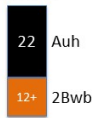


Profile 4b (slope)

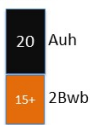




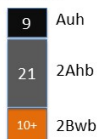
Profile 1



Profile 2

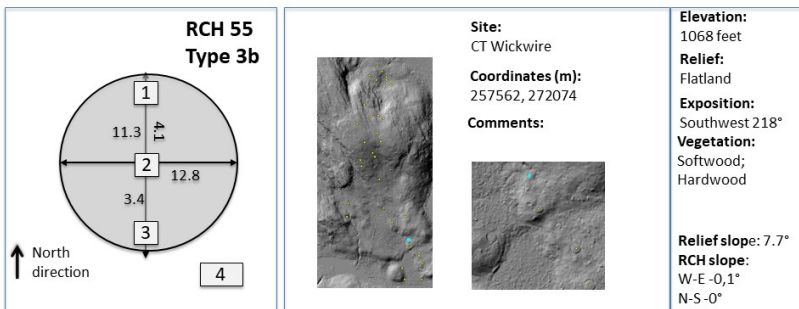


Profile 3



Profile 4

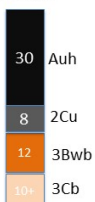
nicht  
beprobt



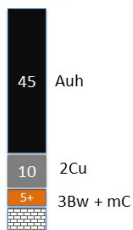
Profile 1



Profile 2

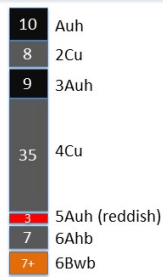
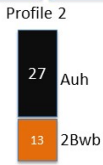
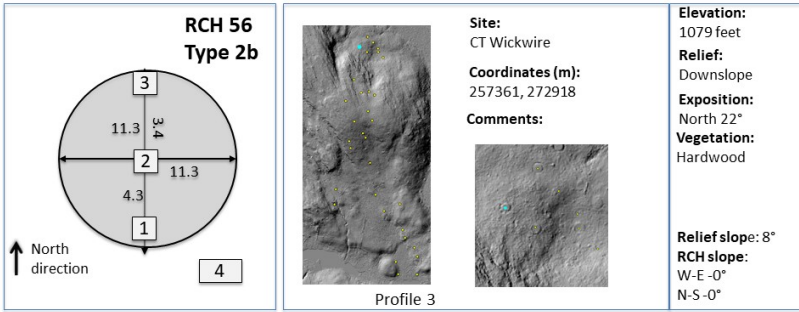


Profile 3



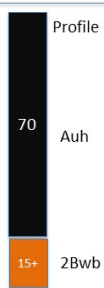
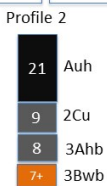
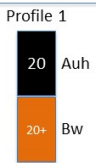
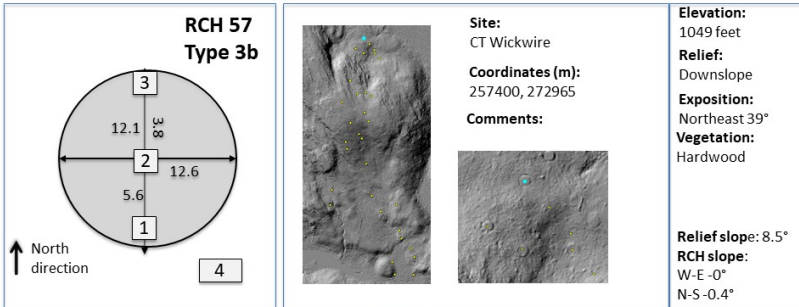
Profile 4

nicht  
beprobt



Profile 4

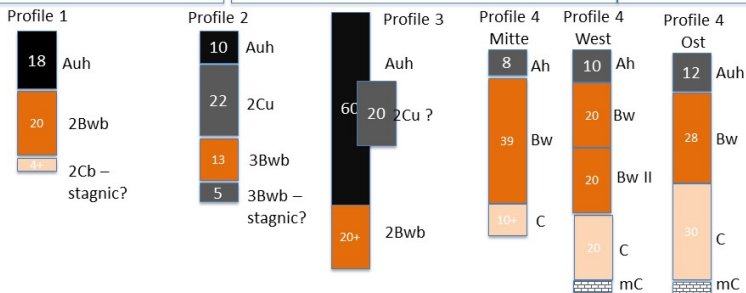
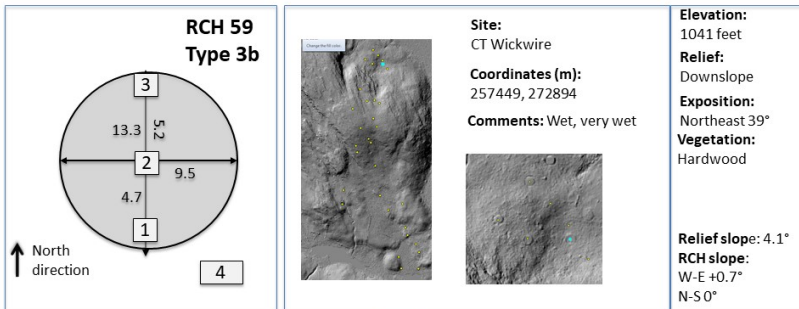
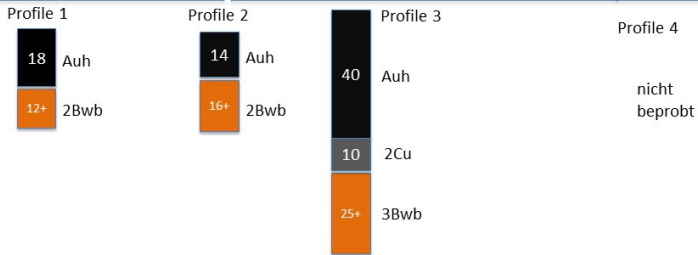
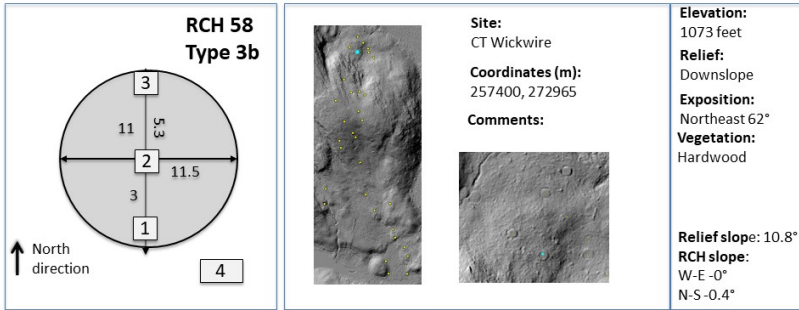
nicht  
beprobt

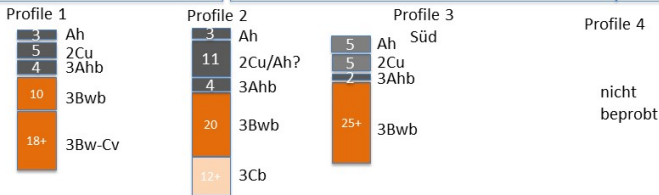
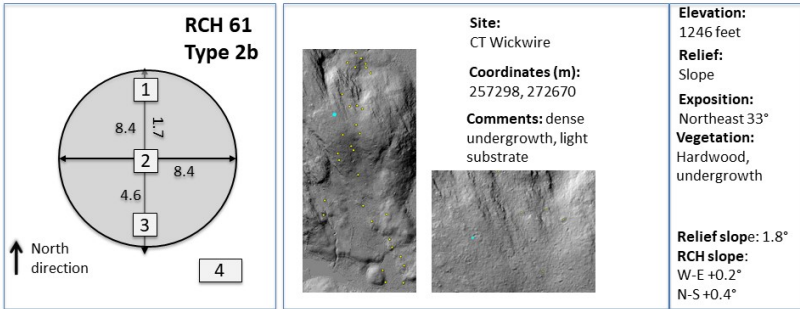
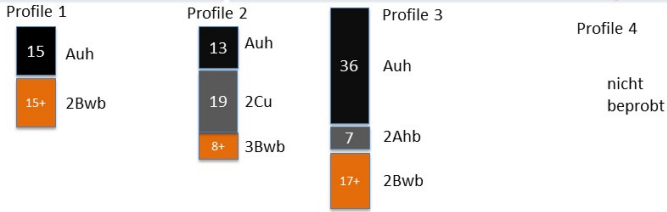
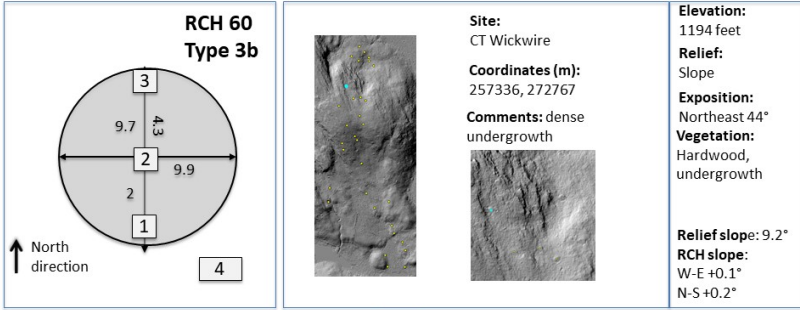


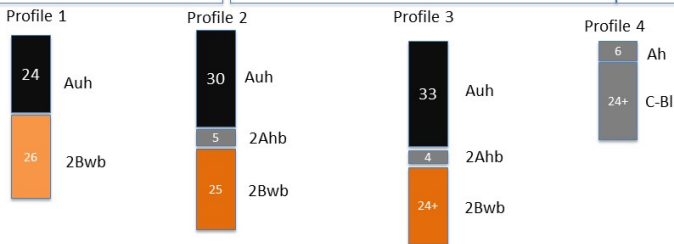
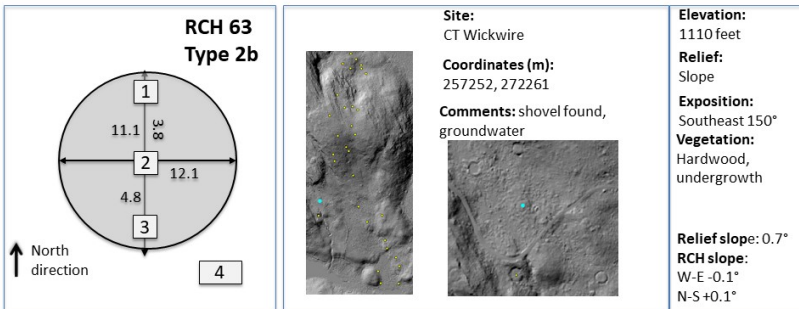
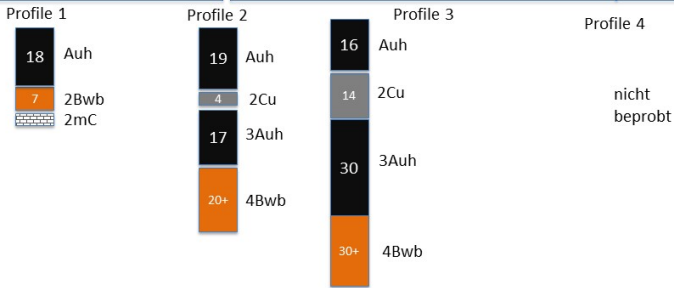
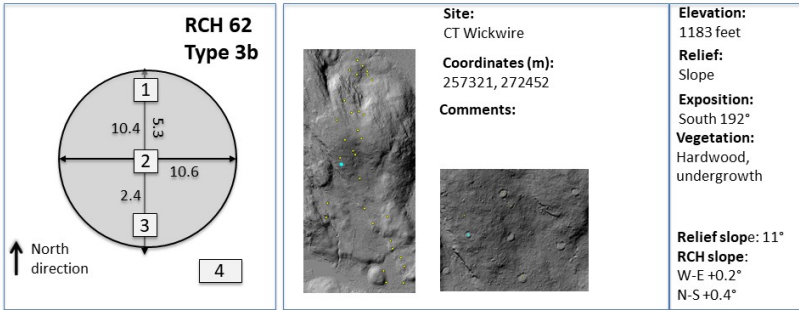
Profile 4

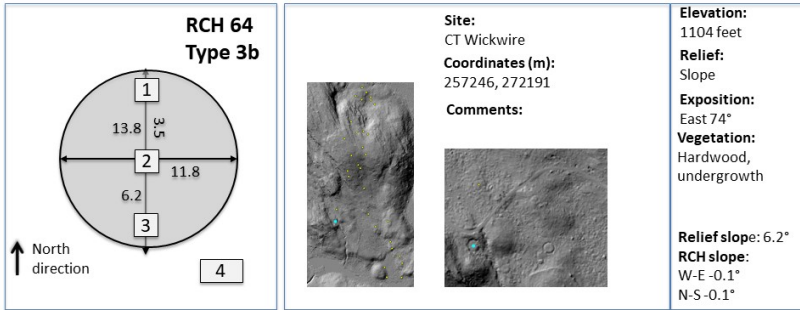
nicht  
beprobt



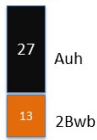




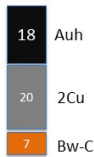




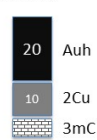
Profile 1



Profile 2

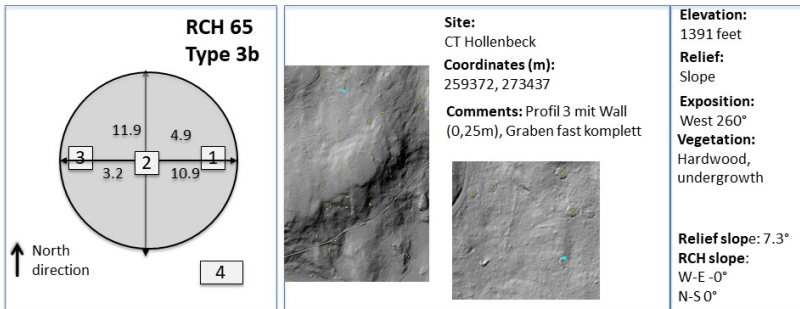


Profile 3

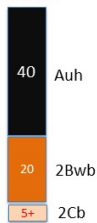


Profile 4

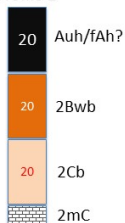
nicht  
beprobt



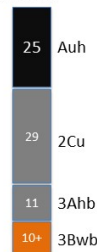
Profile 1



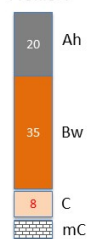
Profile 2

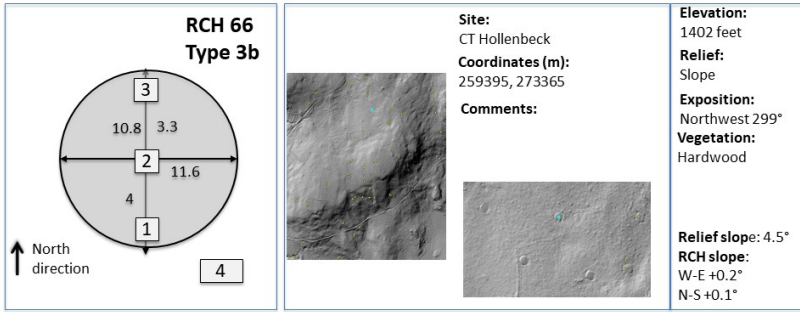


Profile 3

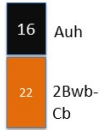


Profile 4

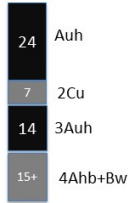




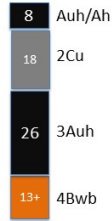
Profile 1



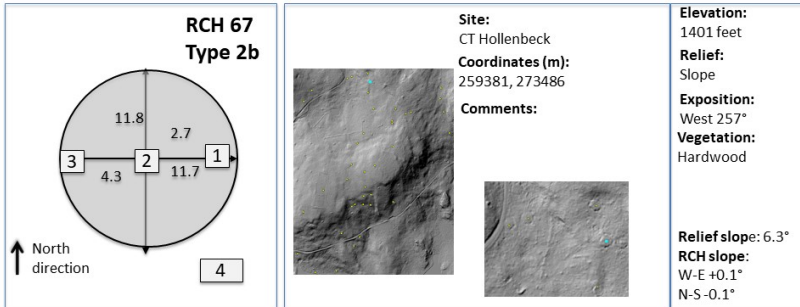
Profile 2



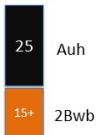
Profile 3



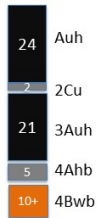
Profile 4



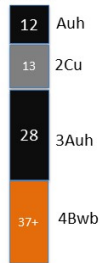
Profile 1



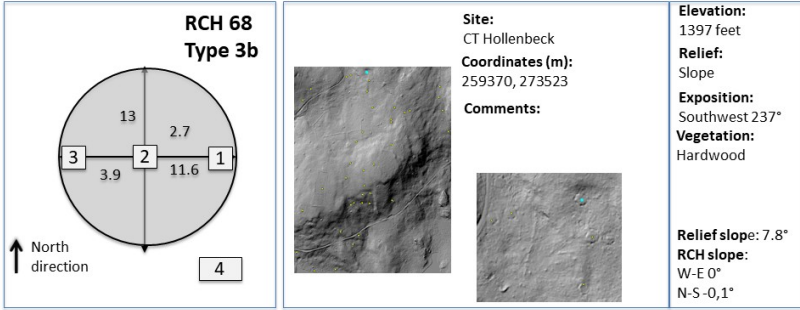
Profile 2



Profile 3



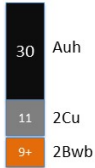
Profile 4



Profile 1



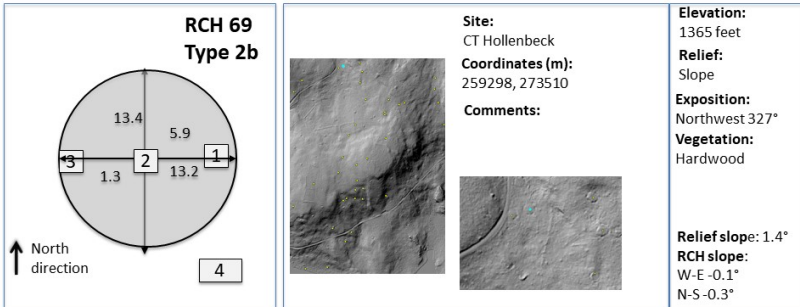
Profile 2



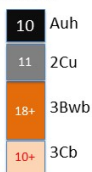
Profile 3



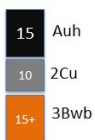
Profile 4



Profile 1



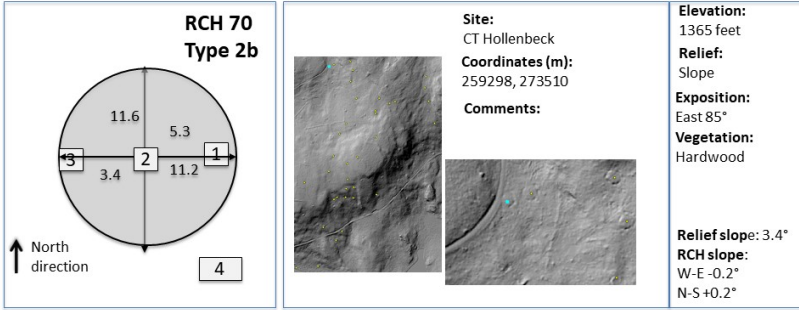
Profile 2



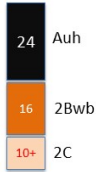
Profile 3



Profile 4



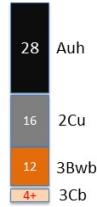
Profile 1



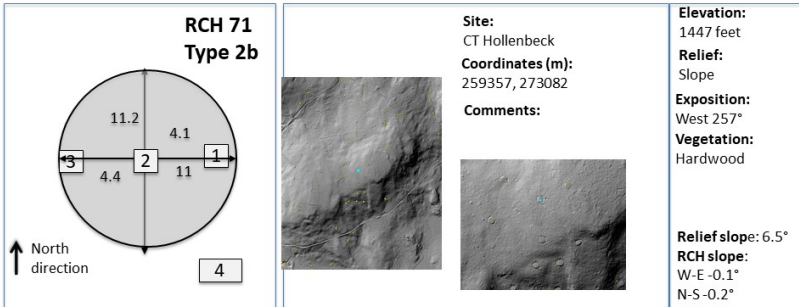
Profile 2



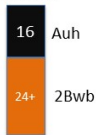
Profile 3



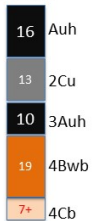
Profile 4



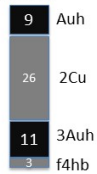
Profile 1



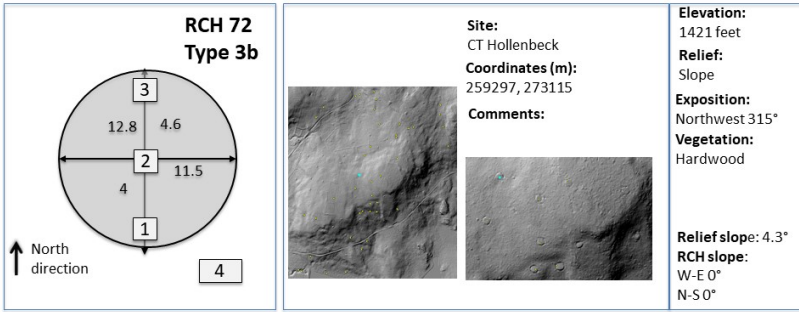
Profile 2



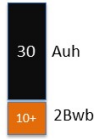
Profile 3



Profile 4



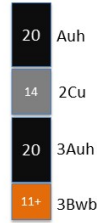
Profile 1



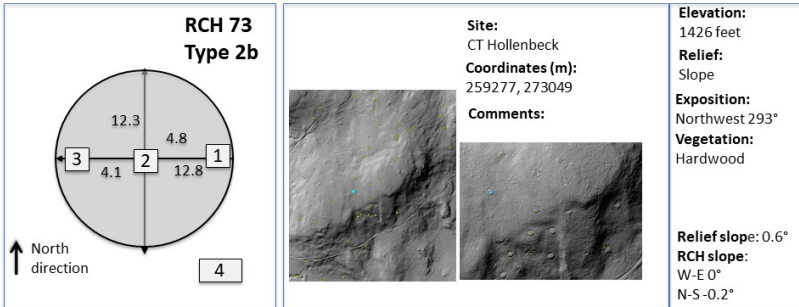
Profile 2



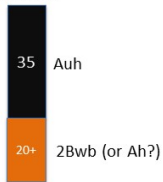
Profile 3



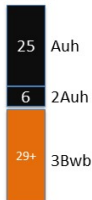
Profile 4



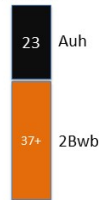
Profile 1



Profile 2

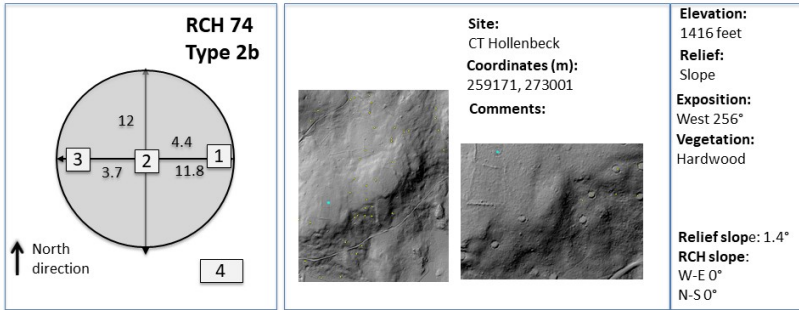


Profile 3

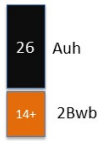


Profile 4

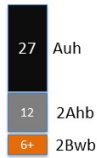




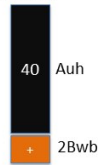
Profile 1



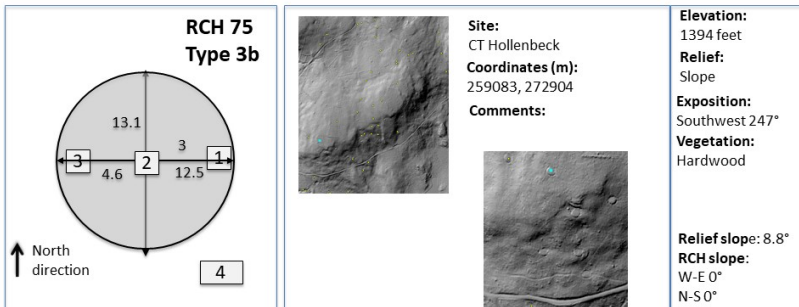
Profile 2



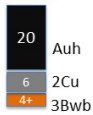
Profile 3



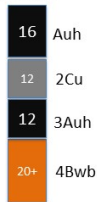
Profile 4



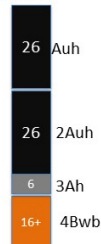
Profile 1



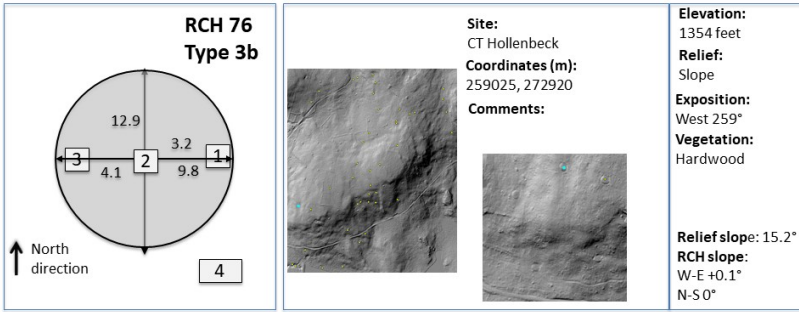
Profile 2



Profile 3



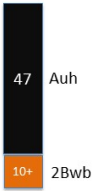
Profile 4



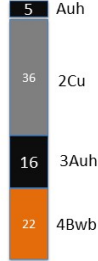
Profile 1



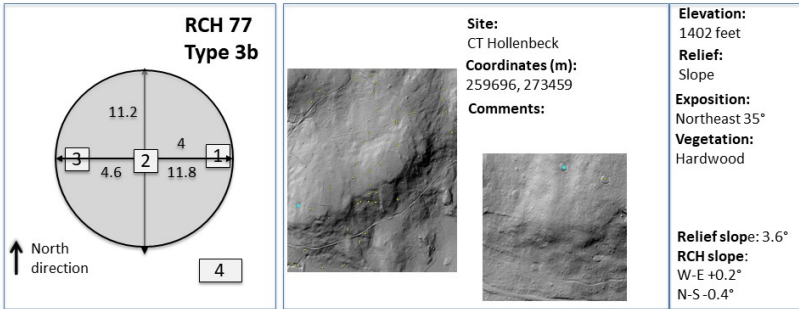
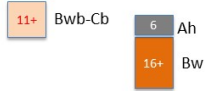
Profile 2



Profile 3



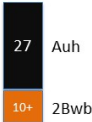
Profile 4



Profile 1



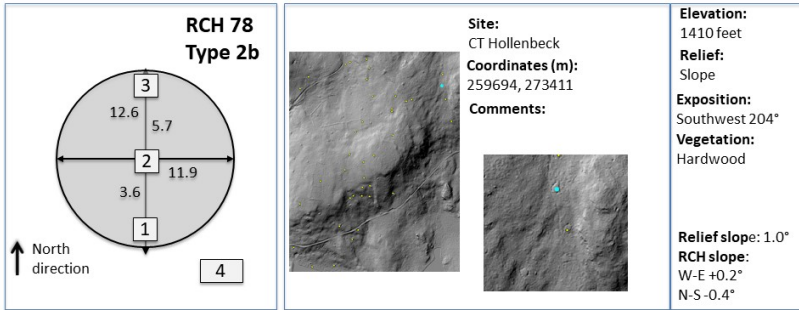
Profile 2



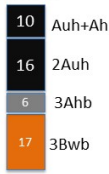
Profile 3



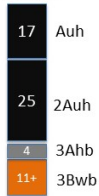
Profile 4



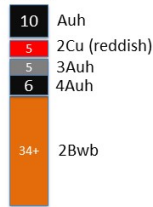
Profile 1



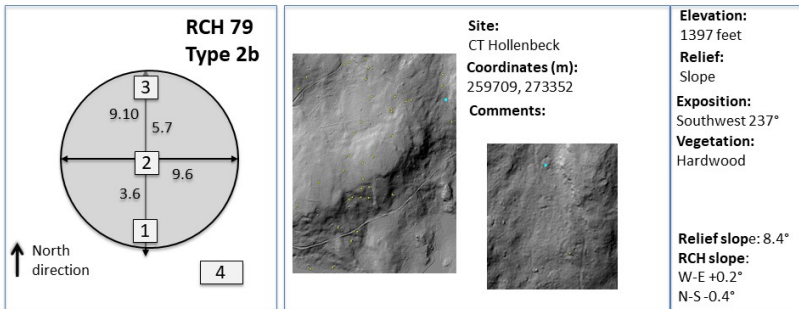
Profile 2



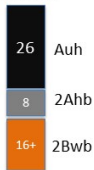
Profile 3



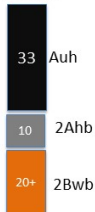
Profile 4



Profile 1



Profile 2



Profile 3a



Profile 3b



Profile 4

## Chapter 6

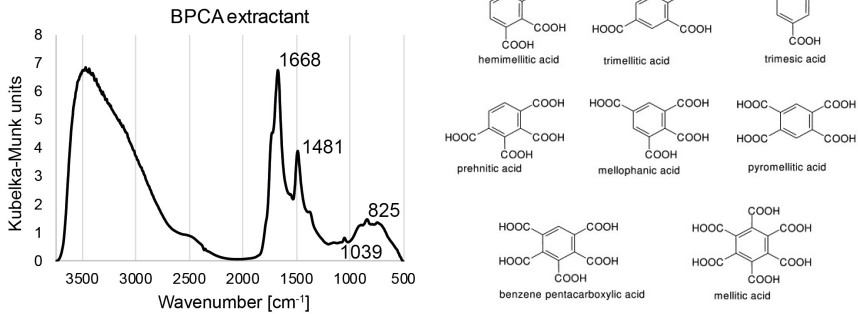


**Abbildung A28.** MIR spectra of dried benzenecarboxylic acid (BPCA) residue showing absorptions for aromatic C=C ( $\leq 1481\text{ cm}^{-1}$ ), carboxyl C=O ( $1668\text{ cm}^{-1}$ ) as well as a broad OH absorption band ( $3500\text{ cm}^{-1}$ ). Additionally, shown are possible structures of BPCA (reproduced from Brodowski et al. 2005).

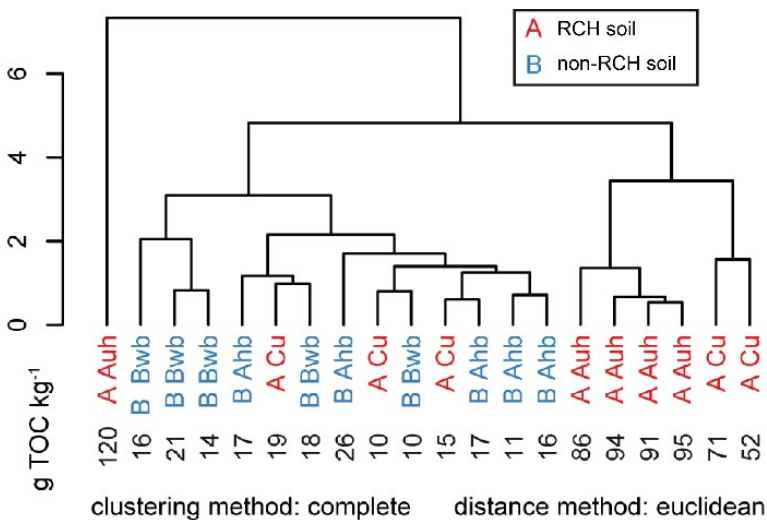


**Abbildung A29.** Hierarchical cluster analysis of 20 exemplary BPCA soil sample spectra and their total organic carbon concentration (TOC).

**Table A5.** List of measured (C, N) and predicted (BPCA) soil properties for volumetric samples.

RCH no.	Depth [cm]	Horizon	C %	N%	BPCA %	RCH no.	Depth [cm]	Horizon	C %	N%	BPCA %
28-1	0-5	Auh	12.20	0.08	10.66	29-3	0-5	Auh	9.45	0.26	3.31
	5-10	Auh	8.53	0.22	3.32		5-10	Auh	9.60	0.21	3.82
	13-14	2Bwb					10-15	Auh	9.15	0.19	3.44
	18-21	2Bwb	0.41	0.02	0.25		15-20	Auh	5.26	0.14	1.77
28-2							20-25	Auh	6.53	0.15	2.88
	0-5	Auh	12.57	0.25	5.02	25-30	Auh	6.47	0.15	2.28	
	5-10	Auh	7.65	0.19	2.95	30-35	2Bwb	3.00	0.11	0.32	
	10-15	Auh	7.70	0.21	2.96	35-40	2Bwb	1.92	0.09	0.28	
	17-22	2Cu	3.35	0.10	1.37	48-53	2Cb	1.00	0.05	-	
	23-28	3Auh	5.56	0.14	2.22						
28-3	34-39	4Bwb	0.93	0.03	-	29-4	0-5	Ah	8.05	0.33	0.41
							5-10	Bw	3.94	0.18	0.31
	0-5	Auh	11.48	0.30	4.19		10-15	Bw	2.76	0.13	0.30
	5-10	Auh	9.17	0.23	3.28		15-20	Bw	1.90	0.10	0.30
	11-16	2Cu	3.12	0.09	0.81		20-25	Bw	1.36	0.08	0.25
	16-21	2Cu	2.93	0.09	0.64		25-30	Bw	0.92	0.06	0.22
	22-27	3Auh	6.84	0.16	2.63		32-37	C	0.96	0.05	0.21
	27-32	3Auh	6.91	0.15	3.06						
	32-37	3Auh	5.85	0.14	2.10	30-1	0-5	Auh	11.08	0.47	3.32
	37-42	3Auh	5.86	0.12	2.66		5-10	Auh	9.56	0.34	3.18
43-48	4Cu	0.93	0.04	0.35	10-15		Auh	7.10	0.23	3.25	
48-53	4Cu	1.03	0.04	0	15-20		Auh	8.44	0.25	3.59	
53-58	4Cu	2.02	0.07	0.62	21-26		2Cb	1.94	0.08	-	
58-63	4Cu	1.66	0.07	0.35	26-31		2Cb	0.93	0.05	-	
63-68	4Cu	1.83	0.08	0.23	31-36		2Cb	0.97	0.05	-	
?											
28-4	73-78	5Auh	4.97	0.11	2.27	30-2	0-5	Auh	12.30	0.45	4.41
	78-83	5Auh	5.37	0.14	2.20		5-10	Auh	9.96	0.29	4.20
	87-92	6Cb	1.47	0.07	-		10-15	Auh	7.98	0.23	3.35
							15-24	2Cu	5.59	0.14	2.97
	2-7		0.00	0.00	0.28		24-29	2Cu	4.46	0.12	2.11
29-1	9-14	Ah	0.00	0.00	0.25		29-34	3Auh	3.46	0.10	1.48
	14-19	Bw	0.75	0.04	0.22		35-40	3Auh	0.72	0.03	0.50
	19-24	Bw	0.89	0.04	0.24						
	25-30	Bw-C	0.70	0.03	0.19	30-3	0-5	Auh	10.13	0.41	3.83
	30-35	Bw-C	0.59	0.03	0.19		5-10	Auh	7.71	0.28	3.19
							10-15	Auh	3.49	0.14	1.58
	0-5	Auh	13.59	0.37	4.59		12-17	Auh	3.19	0.12	1.66
5-10	Auh	9.86	0.27	3.43		17-22	2Cu	2.15	0.09	0.00	
10-15	Auh	9.79	0.27	3.40		22-27	2Cu	2.72	0.10	1.38	
17-22	2Bwb	2.18	0.07	0.33		27-32	2Cu	2.59	0.09	1.09	
22-27	2Bwb	1.44	0.05	0.28		32-37	3Auh	4.71	0.15	1.18	
29-2							37-42	3Auh	5.85	0.12	3.18
	0-5	Auh	11.70	0.28	4.16		42-47	3Auh	6.16	0.14	2.49
	5-10	Auh	9.70	0.23	3.95		53-58	4Bwb	1.10	0.06	-
	10-15	Auh	8.90	0.21	3.17		58-63	4Bwb	1.11	0.06	-
	15-20	Auh	9.10	0.22	3.27						
	22-27	2Bwb	1.60	0.07	0.29	30-4	0-5	Ah	3.95	0.25	-
	27-32	2Bwb	1.50	0.06	0.29		5-10	Ah-Bw	2.12	0.13	-
							10-15	Ah-Bw	2.41	0.14	-
32-37	2Bwb	1.30	0.05	0.28	15-20		Ah-Bw	1.65	0.09	-	
29-4	40-45	2Cb	1.00	0.05	-						
							21-26	Bw	1.50	0.09	-
							26-31	Bw	0.71	0.05	-
							33-38	C	0.44	0.03	-
							38-43	C	0.41	0.03	-

RCH no.	Depth [cm]	Horizon	C %	N%	BPCA %	RCH no.	Depth [cm]	Horizon	C %	N%	BPCA %	
31-1	0-5	Auh	15.38	0.41	4.47	32-3	0-5	Auh	9.23	0.38	2.76	
	5-10	Auh	12.45	0.31	4.14		5-10	Auh	7.21	0.23	3.15	
	10-15	Auh	9.99	0.25	3.66		10-15	Auh	6.97	0.19	2.90	
	15-20	Auh	9.68	0.24	3.88		15-20	Auh	4.69	0.16	2.07	
31-2	0-5	Auh	13.55	0.37	4.48	32-4	23-28	2Cu	2.27	2.09	1.50	
	5-10	Auh	11.98	0.32	4.50		28-33	2Cu	4.29	0.12	2.32	
	11-16	Auh	10.45	0.28	4.22		35-40	3Auh	4.33	0.16	2.25	
	15-20	Auh	9.36	0.24	3.63		40-45	3Auh	4.10	0.11	2.70	
	20-25	Auh	9.04	0.22	3.24		50-55	4 Auh	4.05	0.13	2.28	
	25-30	Auh	9.28	0.22	3.72		57-62	5Ahb	0.92	0.06	0.44	
	30-35	Auh	10.10	0.20	3.99		62-67	5Ahb	1.29	0.08	0.34	
	35-40	Auh	8.47	0.17	3.57		67-72	5Ahb	1.52	0.09	0.51	
	40-45	Auh	8.19	0.15	3.82		85-90	5Bwb	1.33	0.08	-	
	45-50	Auh	11.46	0.13	5.77							
	50-55	Auh	4.83	0.10	1.61		0-5	Ah	2.47	0.15	-	
	31-3	0-5	Auh	9.67	0.24		4.21	33-2	5-10	Ah	2.08	0.13
5-10		Auh	8.49	0.24	3.96	20-25	Ah		1.20	0.07	-	
9-14		Auh	7.24	0.20	3.54	25-30	Bw		0.60	0.04	-	
14-19		2Cu	2.88	0.09	2.28	0-5	Auh		18.04	0.35	6.80	
19-24		2Cu	2.66	0.09	1.61	5-10	Auh		9.74	0.19	3.96	
24-29		2Cu	2.30	0.08	1.55	10-15	Auh		6.43	0.15	3.31	
29-34		2Cu	3.06	0.09	2.15	15-20	Auh		5.35	0.16	2.30	
34-39		2Cu	3.80	0.11	2.04	20-25	Auh		8.19	0.15	4.15	
39-44		2Cu	7.22	0.16	3.70	25-30	2Auh		14.99	0.21	7.55	
47-52		3Auh	6.35	0.16	3.58	30-35	2Auh		15.22	0.22	6.79	
52-57		3Auh	6.25	0.19	3.66	35-40	2Auh		7.77	0.16	4.10	
57-62		3Auh	7.99	0.22	3.72	42-47	3Bwb		1.69	0.05	-	
62-67	3Auh	7.82	0.16	4.16	48-56	3Bwb	0.22	0.01	-			
67-72	3Auh	6.29	0.13	3.94	56-62	3Bwb	0.17	0.01	-			
72-77	3Auh	4.71	0.11	3.29	33-3	0-5	Auh	11.76	0.29	4.67		
77-82	3Auh	4.39	0.11	2.50		5-10	Auh	13.35	0.29	5.51		
82-87	3Auh	3.51	0.09	2.34		10-15	Auh	12.11	0.23	6.25		
89-94	4Cb	0.98	0.05	-		15-20	Auh	8.05	0.17	3.13		
						20-25	Auh	8.36	0.18	3.55		
31-4	2-7	Ah	2.46	0.13	-	25-30	Auh	9.51	0.18	4.00		
	10-15	Ah	1.52	0.08	-	31-36	2Cu	1.70	0.05	0.93		
32-1	0-5	Auh	-	-	-	38-43	2Cu	1.69	0.05	0.51		
	5-10	Auh	-	-	-	43-48	3Ahb	2.08	0.05	-		
	10-15	Auh	-	-	-	43-48	3Ahb	2.25	0.07	-		
	15-20	2Bwb	-	-	-	53-58	3Bwb	1.17	0.04	-		
32-3	0-5	Auh	10.46	0.34	4.27	33-4	0-5	Ah	-	-	-	
	5-10	Auh	17.50	0.32	6.02		5-10	Ah	-	-	-	
	10-15	Auh	6.92	0.19	3.22							
	20-25	2Auh	0.91	0.04			33-1	0-5	Auh	20.93	0.53	6.02
	25-30	3Cu					5-10	Auh	10.47	0.29	4.17	
	30-35	4Ahb	6.43	0.27	2.32		10-15	Auh	7.98	0.19	3.38	
34-1	35-40	4Ahb	5.85	0.18	2.69	34-1	0-5	Auh	18.28	0.43	4.90	
	42-47	4Bwb	6.12	0.14	2.98		5-10	Auh	6.16	0.19	2.13	
	47-52	4Bwb	3.31	0.09	0.41		10-15	Auh	4.91	0.13	1.98	
	52-57	4Bwb	0.71	0.04	0.20		15-20	Auh	6.10	0.20	1.85	
							25-30	2Bwb	1.13	0.06	-	

RCH no.	Depth [cm]	Horizon	C %	N%	BP CA %	RCH no.	Depth [cm]	Horizon	C %	N%	BP CA %
34-2	0-5	Auh	11.65	0.36	3.04		30-35	2Bwb	0.64	0.03	-
	5-10	Auh	8.39	0.22	2.98		37-42	2Cb	0.49	0.02	-
	10-15	Auh	5.34	0.16	1.81						
	15-20	Auh	8.80	0.18	3.45	36-3	0-5	Auh	15.51	0.42	4.60
	20-25	2Bwb	2.31	0.09	-		5-10	Auh	12.23	0.28	4.82
	26-31	2Bwb	1.20	0.06	-		10-15	Auh	7.83	0.20	2.57
	31-36	2Bwb	0.92	0.05	-		15-20	Auh	6.75	0.17	2.53
34-3	41-46	2Cb	0.62	0.04	-		20-25	2Auh	5.89	0.14	2.29
							25-30	2Auh	4.36	0.12	1.33
	0-5	Auh	12.29	0.38	-		36-41	3Bwb	1.54	0.05	-
	6-11	Auh	8.15	0.21	3.00		41-46	3Bwb	0.88	0.03	-
	11-16	Auh	10.95	0.22	3.43		48-53	3Cb	0.52	0.30	-
	18-23	2Cu	1.85	0.07	0.88						
	26-31	3Ahb	2.66	0.10	-	36-4	0-5	Ah	6.82	0.31	-
34-4	41-46	3Bwb	1.27	0.07	-		6-11	Bw	2.90	0.15	-
							11-16	Bw	1.54	0.08	-
	0-5	Ah	6.72	0.27	-		25-30	C	0.57	0.03	-
	6-11	Bw	3.26	0.16	-						
	11-16	Bw	1.51	0.08	-	37-1	0-5	Auh	10.52	0.33	3.02
	16-21	Bw	1.07	0.06	-		5-10	Auh	6.77	0.23	2.15
	21-26	Bw	0.60	0.04	-		10-15	Auh	6.41	0.21	2.37
35-2	26-31	C	0.59	0.04	-		15-20	Auh	5.23	0.17	1.82
	31-36	C	0.57	0.04	-		20-25	Auh	7.56	0.17	2.82
	36-41	C	0.58	0.03	-		29-34	2Ahb	1.73	0.05	0.64
							35-40	2Bwb	0.72	0.03	-
	0-5	Auh	11.81	0.24	3.89						
	5-10	Auh	8.18	0.15	2.84	37-2	0-5	Auh	8.15	0.22	3.29
	10-15	Auh	8.05	0.15	2.62		5-10	Auh	6.11	0.14	2.86
35-3	15-20	Auh	4.30	0.09	1.80		10-15	Auh	5.31	0.11	2.25
	22-27	2Bwb	2.23	0.08	-		15-20	Auh	5.37	0.14	2.12
	27-32	2Bwb	1.39	0.06	-		20-25	Auh	8.70	0.17	3.24
							31-36	2Ahb	1.81	0.07	0.62
	0-5	Auh	13.15	0.41	2.88		38-43	2Bwb	1.05	0.05	-
	5-10	Auh	8.31	0.19	2.40						
	10-15	Auh	7.16	0.16	2.47	37-3	0-5	Auh	12.91	0.29	4.18
36-1	15-19	Auh	6.77	0.15	1.84		5-10	Auh	10.72	0.28	3.82
	19-23	Ahb	5.21	0.12	-		10-15	Auh	7.87	0.24	2.54
	23-28	2Bwb	2.81	0.09	-		15-20	Auh	6.56	0.19	2.44
	28-32	2Bwb	0.95	0.04	-		20-25	Auh	8.03	0.20	3.08
							25-30	Auh	7.37	0.16	2.95
	0-5	Auh	10.41	0.28	3.53		30-35	Auh	6.32	0.15	2.38
	5-10	Auh	6.62	0.20	2.28		36-41	2Bwb	1.68	0.06	-
36-2	10-15	Auh	5.74	0.17	1.84		41-46	2Bwb	0.89	0.04	-
	15-20	Auh	5.83	0.17	2.07						
	20-25	Auh	8.48	0.20	3.48	37-4	0-5	Ah	12.32	0.54	-
	25-30	Ahb	2.86	0.08	0.74		7-12	Bw	4.03	0.18	-
	30-35	2Bwb	1.82	0.06	-		12-17	Bw	2.32	0.11	-
	39-44	2Bwb	0.74	0.03	-		17-22	Bw	1.55	0.08	-
							22-27	Bw	1.50	0.08	-
36-2	0-5	Auh	8.54	0.25	3.03		27-32	Bw	1.81	0.09	-
	5-10	Auh	7.53	0.18	2.79						
	10-15	Auh	7.57	0.18	2.94	38	0-5	Auh	17.23	0.40	4.78
	15-20	Auh	6.55	0.16	2.39		5-10	Auh	10.84	0.26	4.23
	20-25	2Ahb	2.28	0.07	-		10-15	Auh	10.82	0.23	4.57
	25-30	2Bwb	0.77	0.03	-		15-20	Auh	8.06	0.24	3.89

RCH no.	Depth [cm]	Horizon	C %	N%	BPCA %	RCH no.	Depth [cm]	Horizon	C %	N%	BPCA %
	20-25	Auh	7.02	0.22	3.24	41-1	0-5	Auh	28.06	0.49	9.51
	30-35	Auh	6.96	0.38	3.68		5-10	Auh	13.45	0.30	4.41
	37-42	2Ahb	1.55	0.09	-		18-23	2Bwb	2.94	0.11	-
	42-47	2Bw-BI	0.95	0.06	-		23-28	2Bwb	1.57	0.07	-
39-1	0-5	Auh	27.53	0.58	10.40	41-2	0-5	Auh	7.17	0.15	2.87
	5-10	Auh	19.05	0.33	6.77		5-10	Auh	4.98	0.11	2.78
	10-15	Auh	12.55	0.26	4.39		13-18	2cu	5.30	0.13	2.48
	15-20	Auh	5.51	0.15	2.25		19-24	3Auh	6.97	0.15	3.26
	20-25	2Bwb	1.67	0.06	-		24-29	3Auh	8.70	0.13	4.41
							31-36	4Bwb	3.22	0.13	-
39-2	0-5	Auh	19.02	0.42	6.82						
	5-10	Auh	14.23	0.27	5.07	41-3	0-5	Auh	6.26	0.22	1.86
	10-15	Auh	14.36	0.22	5.50		5-10	Auh	2.65	0.11	0.96
	15-20	Auh	10.57	0.18	4.52		10-15	2Cu	2.10	0.07	0.68
	25-30	2Bwb	0.77	0.04	-		15-20	2Cu	1.07	0.05	0.17
							28-33	3Auh	17.63	0.35	6.14
39-3	0-5	Auh	8.81	0.23	2.93		37-42	3Auh	10.78	0.18	4.51
	5-10	Auh	5.39	0.16	1.62		42-47	4Ahb	3.26	0.11	-
	10-15	2Cu	6.89	0.19	2.75		47-52	4Bwb	2.30	0.10	-
	15-20	3Auh	7.16	0.20	2.49						
	32-37	3Cu	1.94	0.07	0.62	42-1	0-5	Auh	12.47	0.32	3.29
	37-42	3Cu	1.56	0.07	0.61		5-10	Auh	9.22	0.21	2.77
	42-47	3Cu	1.01	0.05	0.04		10-15	Auh	10.71	0.23	3.89
	47-52	3Cu	1.48	0.10	-0.03		15-20	Auh	7.84	0.18	2.59
	59-64	4Auh	7.10	0.20	3.06		24-28	2Ahb	2.02	0.06	0
	64-69	4Auh	6.68	0.66	2.71		28-33	2Bwb	1.14	0.05	-
	72-77	4Auh	6.57	2.81	2.65		33-38	2Bwb	0.67	0.04	-
	77-82	5Ahb	1.08	7.25	-						
	82-87	5Ahb	1.59	0.07	-	42-2	0-5	Auh	14.36	0.33	4.48
	87-92	5Bwb	1.20	0.06	-		5-10	Auh	13.30	0.24	4.46
							11-16	2Cu	5.81	0.16	2.15
39-4	0-5	Ah	11.99	0.51	-		16-21	3Auh	8.29	0.18	3.15
	5-10	Ah	3.82	0.19	-		21-26	3Auh	7.76	0.15	3.30
	10-15	Bw	2.54	0.13	-		26-31	3Auh	6.46	0.15	2.53
40-1	0-5	Ah	6.43	0.21	1.19	42-3	0-5	Auh	21.35	0.38	7.14
	5-10	Ah	3.45	0.13	0.77		5-10	2Cu	3.97	0.14	1.10
	10-15	2Bwb	2.12	0.09	-		10-15	2Cu	6.78	0.18	2.16
							15-20	2Cu	9.19	0.20	2.91
40-2	0-5	Auh	7.17	0.23	2.52		20-25	2Cu	9.33	0.20	2.56
	5-10	Auh	8.99	0.25	2.68		25-30	2Cu	14.58	0.25	4.76
	10-15	Auh	8.72	0.21	3.21		34-39	3Auh	10.97	0.22	4.19
	15-20	Auh	7.16	0.18	2.62		43-48	4Ahb	4.15	0.12	-
	20-24	2Ahb	3.03	0.12	-		50-55	4Bwb	2.02	0.08	-
40-3	0-5	Auh	6.76	0.18	2.40	43-1	0-5	Auh	19.27	0.29	4.66
	5-10	Auh	4.48	0.11	1.93		5-10	Auh	14.75	0.25	4.71
	10-15	Auh	3.67	0.09	1.51		10-15	Auh	10.36	0.23	3.96
	15-20	Auh	1.86	0.07	0.61		15-20	Auh	10.41	0.23	3.79
	20-25	Auh	1.68	0.06	0.84		25-30	2Bwb	0.82	0.04	-
	32-38	2Auh	3.07	0.08	1.54						
	38-43	3Bwb	1.20	0.05	-	43-2	0-5	Auh	13.64	0.29	4.71
							5-10	Auh	8.55	0.19	3.39
							10-15	Auh	7.95	0.18	2.58



RCH no.	Depth [cm]	Horizon	C %	N%	BPCA %	RCH no.	Depth [cm]	Horizon	C %	N%	BPCA %
	15-20	Auh	5.41	0.14	1.65		33-38	2Cu	6.89	0.11	2.68
	23-28	2Bwb	2.03	0.07	-		39-44	3Auh	6.72	0.12	2.48
							44-49	3Auh	6.08	0.11	2.23
43-3	0-5	Auh	15.49	0.34	4.33		54-59	4Ahb	2.64	0.07	-
	5-10	Auh	8.44	0.20	3.00		60-65	4Ahb	1.76	0.06	-
	10-15	Auh	8.52	0.18	3.04						
	15-20	Auh	9.36	0.16	4.08	46-1	0-5	Auh	17.86	0.43	5.16
	20-25	Auh	6.15	0.13	2.66		5-10	Auh	10.90	0.27	3.65
	32-37	2Auh	6.11	0.13	2.19		10-15	Auh	11.51	0.26	3.75
	37-42	2Auh	5.01	0.17	1.92		15-20	Auh	7.98	0.35	2.78
	42-47	2Auh	5.67	6.32	2.06		20-25	Auh	6.26	0.15	2.11
	47-52	2Auh	9.98	11.54	3.86		26-31	2Bwb	1.87	0.07	-
43-4	0-5	Ah	6.87	0.25	-	46-2	0-5	Auh	13.53	0.34	4.01
	5-10	Ah	3.09	0.13	-		5-10	Auh	10.08	0.22	3.55
	10-15	Bw	1.63	0.08	-		10-15	Auh	6.17	0.15	2.37
	15-20	Bw	1.19	0.06	-		15-20	Auh	5.64	0.12	2.23
	20-25	Bw	1.01	0.05	-		20-25	Auh	7.75	0.18	2.87
44-1	0-5	Auh	9.93	0.27	3.02	46-3	0-5	Auh	11.96	0.33	4.16
	5-10	Auh	3.53	0.12	0.76		5-10	Auh	9.45	0.22	3.30
							10-15	Auh	9.69	0.22	4.82
44-2	0-5	Auh	19.21	0.36	6.93		15-20	Auh	7.80	0.21	3.06
	5-10	Auh	7.11	0.18	2.26		20-25	Auh	6.66	0.17	2.67
	14-20	2Ahb	2.32	0.07	-		25-30	Auh	6.76	0.18	2.94
							32-37	2Ahb	1.73	0.06	-
44-3	0-5	Auh	7.21	0.20	2.14						
	5-10	Auh	4.76	0.13	1.77	46-4	0-5	Ah	8.98	0.39	-
	16-21	2Cu	1.91	0.07	0.15		5-10	Ah	5.13	0.23	-
	21-26	2Cu	1.02	0.05	0		25-30	Bw	0.83	0.05	-
	26-31	2Cu	0.91	0.05	0						
	31-36	2Cu	0.80	0.04	0	47-1	0-5	Auh	12.35	0.44	3.73
	36-41	2Cu	0.86	0.05	0		5-10	Auh	10.74	0.35	3.44
	44-49	3Ahb	1.02	0.05	-		10-15	Auh	9.27	0.27	3.07
	49-54	3Ahb	1.40	0.06	-		15-20	Auh	6.18	0.21	1.67
							20-25	Auh	4.20	0.16	1.51
45-1	0-5	Auh	9.78	0.27	2.94		31-36	2Ahb	2.26	0.10	0
	5-10	Auh	7.65	0.17	2.25		36-41	2Bwb	1.05	0.05	-
	10-15	Auh	6.89	0.15	2.14						
	15-20	Auh	6.23	0.14	1.74	47-2	0-5	Auh	23.11	0.55	7.82
							5-10	Auh	11.85	0.30	4.07
45-2	0-5	Auh	12.60	0.35	3.95		10-15	Auh	10.15	0.22	4.05
	5-10	Auh	8.38	0.20	2.96		15-20	Auh	9.48	0.23	4.09
	10-15	Auh	8.58	0.17	3.19		20-25	Auh	9.66	0.23	4.20
	15-20	Auh	6.17	0.14	2.18		25-30	2Ahb	4.05	0.13	-
	20-25	2Cu	5.29	0.11	1.72						
	25-30	3Auh	5.38	0.10	1.71	47-3	0-5	Auh	24.93	0.91	5.47
	33-38	4Bwb	1.06	0.03	-		5-10	Auh	17.94	0.53	4.67
							10-15	Auh	14.43	0.43	3.87
45-3	0-5	Auh	8.34	0.19	2.55		15-20	Auh	9.33	0.32	2.41
	5-10	Auh	6.11	0.15	1.81		20-25	Auh	7.95	0.26	2.32
	10-15	Auh	8.24	0.15	3.42		25-30	Auh	9.40	0.27	3.70
	15-20	Auh	8.43	0.16	3.11		30-35	Auh	9.95	0.28	3.73
	23-28	2Cu	5.56	0.12	1.81		35-40	Auh	5.89	0.21	2.09
	28-33	2Cu	7.03	0.13	2.47		40-45	Auh	5.27	0.20	1.65

RCH no.	Depth [cm]	Horizon	C %	N%	BPCA %	RCH no.	Depth [cm]	Horizon	C %	N%	BPCA %
	50-55	2Ahb	3.59	0.15	-		23-28	Auh	1.05	0.04	0.79
	55-60	2Ahb	2.66	0.12	-						
						49-2	0-5	Auh	14.01	0.38	5.34
48-1	0-5	Auh	10.29	0.28	4.07		5-10	Auh	14.68	0.38	5.32
	15-20	Auh	2.82	0.10	1.00		10-15	Auh	5.77	0.18	2.88
	20-25	Auh	4.14	0.12	1.67		15-20	Auh	3.52	0.13	1.97
	25-30	Auh	4.72	0.15	2.07		20-25	2Cu	3.47	0.14	1.48
	32-32	Auh	0.47	0.02	0.52		27-32	2Cu	5.87	0.27	1.10
	44-49	2Cb	0.20	0.01	-						
						49-3	0-5	Auh	10.63	0.38	3.49
48-2	0-5	Auh	8.22	0.23	2.33		5-10	Auh	5.99	0.23	2.29
	5-10	Auh	11.99	0.20	4.88		15-20	2Cu	3.74	0.14	1.76
	10-15	Auh	8.58	0.17	4.25		20-25	2Cu	2.69	0.11	1.22
	15-20	Auh	7.83	0.20	3.20		25-30	2Cu	3.57	0.15	1.75
	20-25	Auh	7.74	0.19	3.55		30-35	2Cu	3.66	0.15	1.60
	34-39	2Bwb	1.33	0.04	-						
						50-1	0-5	Auh	7.54	0.28	1.96
48-3A	0-5	Auh	6.67	0.17	2.70		5-10	Auh	6.66	0.24	2.99
	5-10	2Cu	1.78	0.07	0.49		10-15	Auh	7.26	0.23	3.46
	10-15	2Cu	1.04	0.05	0.40		15-20	Auh	4.81	0.17	1.66
	15-20	2Cu	0.81	0.03	0.25						
	20-25	2Cu	1.06	0.04	0	50-2	0-5	Auh	9.92	0.40	3.32
	25-30	2Cu	0.97	0.04	0		5-10	Auh	8.71	0.30	3.62
	30-35	2Cu	1.36	0.04	0.10		10-15	Auh	5.75	0.24	2.97
	35-40	2Cu	1.48	0.04	0.01		16-21	2Cu	0.88	0.04	1.94
	48-53	2Cu	1.28	0.04	0						
	53-58	2Cu	1.49	0.04	0.18	50-3	0-5	Auh	7.56	0.30	2.65
	62-67	3Auh	5.07	0.09	2.15		5-10	Auh	4.57	0.19	2.09
	67-72	3Auh	4.76	0.09	2.14		10-15	Auh	5.00	0.15	3.18
	72-77	4Bwb	0.83	0.03	-		15-20	2Cu	0.79	0.03	0.49
							20-25	2Cu	0.97	0.04	1.04
48-3B	0-5	Auh	14.49	0.36	4.35		25-30	2Cu	0.87	0.04	0.96
	5-10	Auh	8.28	0.18	2.49		30-35	2Cu	1.28	0.04	1.41
	10-15	Auh	7.67	0.17	3.08		35-40	2Cu	2.96	0.10	1.32
	15-20	Auh	7.70	0.16	3.25		45-50	2Cu	2.51	0.10	1.48
	20-25	Auh	9.76	0.16	5.41		50-55	2Cu	2.51	0.10	2.03
	27-32	2Cu	7.38	0.11	3.21		56-61	3Auh	3.49	0.12	2.38
	32-37	2Cu	5.51	0.09	2.39		61-66	3Auh	4.30	0.13	2.45
	43-48	2Cu	4.99	0.09	2.24		66-71	3Auh	4.54	0.14	2.64
	50-55	3Bwb	1.27	0.04	-		71-76	3Auh	5.09	0.15	2.77
	55-60	3Bwb	0.53	0.02	-		76-81	3Auh	5.27	0.15	2.48
							81-86	3Auh	8.60	0.25	3.84
48-4	0-5	Ah	4.25	0.15	-		86-91	4Ahb	5.89	0.39	-
	5-10	Bw	1.27	0.07	-						
	10-15	Bw	0.80	0.04	-	50-4A	0-5	Ah	13.34	0.73	-
	15-20	Bw	0.60	0.04	-		5-10	Ah	7.75	0.41	-
	20-25	Bw	0.73	0.04	-		10-15	Ah	4.94	0.28	-
	33-38	Bw	0.43	0.06	-		15-20	Ah	3.11	0.20	-
	38-43	C	0.33	0.02	-		32-37	Go	2.15	0.12	-
	43-48	C	0.31	0.02	-						
	57-63	C	0.24	0.02	-	50-4B	0-5	Ah	3.99	0.27	-
							5-10	Ah	2.17	0.14	-
49-1	0-5	Auh	7.89	0.28	2.93		10-15	Ah	1.74	0.11	-
	5-10	Auh	7.74	0.27	3.25		15-20	Bw	1.09	0.06	-
	10-15	Auh	4.63	0.18	2.65		20-25	Bw	0.97	0.05	-

RCH no.	Depth [cm]	Horizon	C %	N %	BCPA %	RCH no.	Depth [cm]	Horizon	C %	N %	BCPA %
	25-30	Bw	1.31	0.08			30-35	2Auh	10.57	0.21	3.93
							35-40	2Auh	7.66	0.16	2.67
51-1	0-5	Auh	12.25	0.45	5.36						
	5-10	Auh	9.60	0.36	5.12	52-3	0-5	Auh	6.00	0.24	2.19
	10-15	Auh	9.59	0.36	4.66		9-14	Auh	5.88	0.18	2.13
	15-20	Auh	6.98	0.30	3.32		14-19	Auh	6.18	0.19	2.20
	23-28	2Bwb	1.50	0.08	0.65		19-24	Auh	6.70	0.20	1.84
	28-33	2Bwb	0.78	0.04	0.38		27-32	Auh	2.59	0.10	0.54
	33-38	2Bwb	0.59	0.04	0.33		32-37	2Ahb	2.08	0.08	-
	45-50	2C	1.87	0.09	-						
						53-1	0-5	Auh	20.10	0.52	7.68
51-2	0-5	Auh	18.01	0.46	5.95		5-10	2Cu	9.10	0.28	4.09
	5-10	Auh	14.98	0.33	5.82		10-15	2Cu	8.76	0.23	3.85
	10-15	Auh	11.75	0.27	4.69		15-20	3Auh	8.49	0.22	3.72
	15-20	Auh	14.41	0.35	6.32		20-25	3Auh	7.82	0.22	3.46
	20-25	Auh	10.70	0.28	3.87		30-35	3Auh	8.97	0.23	3.85
	25-30	Auh	10.79	0.19	5.29		35-40	3Auh	9.36	0.18	4.49
	30-35	Auh	12.52	0.18	5.70		38-43	4Bwb	1.51	0.07	0.37
	35-40	2Ahb	7.02	0.17	-		43-48	4Bwb	0.60	0.04	0.70
	40-45	2Ahb	4.98	0.22	-						
						53-2	0-5	Auh	16.17	0.49	4.51
51-3	0-5	Auh	10.47	0.46	2.36		5-10	Auh	11.60	0.31	3.98
	5-10	Auh	7.55	0.28	3.02		10-15	Auh	10.16	0.26	3.43
	10-15	Auh	6.57	0.21	2.21		15-20	Auh	5.67	0.16	2.21
	15-20	Auh	8.14	0.20	3.20		30-35	2Ahb	2.30	0.09	0.15
	20-25	Auh	7.45	0.18	3.64						
	25-30	Auh	7.17	0.19	3.62	53-3	0-5	Auh	14.55	0.44	5.24
	30-35	Auh	8.12	0.22	3.31		5-10	Auh	13.71	0.35	5.96
	35-40	Auh	9.31	0.29	3.60		10-15	Auh	16.23	0.28	7.26
	40-45	Auh	6.79	0.17	2.18		15-20	Auh	12.11	0.24	5.39
	45-50	Auh	8.76	0.26	4.01		20-25	Auh	10.69	0.18	5.65
	50-55	2Cu	3.14	0.09	1.37		25-30	Auh	7.15	0.12	3.74
	55-60	3Auh	12.77	0.24	5.37						
	60-65	4Ahb	3.57	0.15	-	53-4	0-5	Ah	10.18	0.50	-
	65-70	4Ahb	3.57	0.21	-		5-10	Ah	3.90	0.19	-
							10-15	Bw	1.37	0.08	-
51-4b	0-5	Ah	6.27	0.34	-						
	5-10	Ah	6.28	0.34	-	54-1	0-5	Auh	10.22	0.34	4.01
	10-15	Bw	3.01	0.15	-		5-10	Auh	7.89	0.25	2.55
	15-20	Bw	2.10	0.10	-		10-15	2Auh	8.68	0.25	2.85
	20-25	Bw	0.90	0.05	-		22-27	2Bwb	3.07	0.13	-
	25-30	Bw	0.60	0.03	-						
	30-35	Bw	0.67	0.04	-	54-2	0-5	Auh	13.26	0.37	4.79
							5-10	Auh	5.05	0.18	3.08
52-1	0-5	Auh	17.90	0.49	5.45						
	5-10	Auh	9.36	0.28	3.28	54-3	0-5	Auh	3.84	0.17	1.71
	10-15	Auh	7.20	0.22	2.59		5-10	Auh	1.74	0.10	0.17
	15-20	Auh	8.90	0.23	3.04						
						54-1	0-5	Auh	10.22	0.34	4.01
52-2	0-5	Auh	10.5	0.6	3.91		5-10	Auh	7.89	0.25	2.55
	5-10	Auh	6.3	5.0	1.96		10-15	Auh	8.68	0.25	2.85
	10-15	Auh	6.0	11.8	1.88		22-27	2Bwb	3.07	0.13	-
	15-20	Auh	4.6	23.6	1.17						
	20-25	2Auh	5.6	35.8	1.93	54-2	0-5	Auh	13.26	0.37	4.79
	25-30	2Auh	10.1	0.2	3.84		5-10	Auh	5.05	0.18	3.08

RCH no.	Depth [cm]	Horizon	C %	N %	BPCA %	RCH no.	Depth [cm]	Horizon	C %	N %	BPCA %
53-4	0-5	Auh	3.8	0.2	1.71						
	5-10	Auh	1.7	0.1	0.17						
						57-2	0-5	Auh	19.21	0.52	7.50
55-1	0-5	Auh	11.7	0.4	3.64		5-10	Auh	12.31	0.27	5.74
	5-10	Auh	5.0	0.2	1.37		13-18	Auh	10.27	0.21	5.22
	10-15	Auh	8.8	0.2	3.14		21-26	2Cu	4.86	0.12	2.38
	15-20	Auh	8.2	0.2	2.73		26-31	2Cu	2.43	0.09	0.03
							31-36	3Ahb	3.59	0.10	-
55-2	0-5	Auh	10.8	0.3	3.66						
	5-10	Auh	10.6	0.3	3.69	57-3	0-5	Auh	10.89	0.32	3.68
	10-15	Auh	9.1	0.2	3.82		5-10	Auh	9.26	0.21	3.71
	15-20	Auh	8.8	0.2	3.09		10-15	Auh	7.91	0.18	3.52
	20-25	Auh	7.2	0.2	2.81		20-25	Auh	5.88	0.15	0.34
	30-35	2Cu	3.8	0.1	1.61		25-30	Auh	2.25	0.08	1.87
							45-50	Auh	5.31	0.16	2.63
55-3	0-5	Auh	8.1	0.3	2.52						
	5-10	Auh	6.0	0.2	1.29	58-1	0-5	Auh	19.96	0.41	5.62
	10-15	Auh	5.7	0.2	1.26		5-10	Auh	17.73	0.35	5.04
	15-20	Auh	6.7	0.2	2.21		10-15	Auh	13.67	0.28	4.10
	20-25	Auh	7.8	0.2	2.96		18-23	2Cb	0.57	0.03	-
	25-30	Auh	7.0	0.2	2.50						
	40-45	Auh	7.8	0.2	3.07	58-2	0-5	Auh	15.47	0.29	5.11
	45-50	2Auh	7.0	0.2	3.19		5-10	Auh	14.81	0.34	5.27
	50-55	2Auh	6.8	0.1	3.40		14-19	2Bwb	2.12	0.06	-
							19-24	2Bwb	1.27	0.05	-
56-1	0-5	Auh	9.1	0.3	2.32						
	5-10	Auh	4.5	0.1	1.80	58-3	0-5	Auh	11.99	0.29	3.46
	10-15	2Bwb	1.0	0.0	-		5-10	Auh	10.26	0.23	4.04
							10-15	Auh	11.15	0.21	3.85
56-2	0-5	Auh	11.4	0.4	3.19		15-20	Auh	6.71	0.16	2.68
	5-10	Auh	7.5	0.1	2.48		20-25	Auh	7.79	0.17	3.29
	10-15	Auh	8.6	0.2	2.29		25-30	Auh	7.85	0.16	3.58
	15-20	Auh	5.7	0.1	2.45		30-35	Auh	6.57	0.15	2.45
	27-32	2Bwb	0.5	0.0	-		40-45	2Cu	4.69	0.13	1.59
							45-50	2Cu	6.41	0.16	2.72
56-3	0-5	Auh	11.7	0.3	4.45		50-55	3Bwb	0.91	0.05	-
	5-10	Auh	7.8	0.2	2.75		55-60	3Bwb	0.91	0.05	-
	10-15	2Cu	6.9	0.2	2.47						
	15-20	2Cu	8.2	0.2	3.00	59-1	0-5	Auh	19.35	0.55	5.08
	20-25	3Auh	6.6	0.1	2.54		5-10	Auh	15.53	0.40	5.06
	25-30	3Cu	3.8	0.1	1.73		10-15	Auh	12.52	0.33	4.38
	30-35	3Cu	-	-	-		23-28	2Bwb	0.50	0.03	0.26
	35-40	3Cu	8.7	0.1	4.63		38-42	2Cb	0.19	0.02	-
	40-45	3Cu	3.8	0.1	1.24						
	45-50	3Cu	3.8	0.1	1.65	59-2	0-5	Auh	16.77	0.52	5.23
	50-55	3Cu	0.8	0.0	0		5-10	Auh	13.56	0.36	4.92
	55-60	3Cu	2.2	0.1	0.82		10-15	2Cu	9.62	0.25	3.65
	62-67	3Cu	1.7	0.1	0.11		15-20	2Cu	6.83	0.18	2.52
	67-72	4Ahb	1.7	0.1	-		20-25	2Cu	4.69	0.13	1.41
	72-77	4Bwb	1.4	0.0	-		25-30	2Cu	3.04	0.09	0.04
	77-82	4Bwb	3.3	0.1	-		30-35	3Bwb	1.71	0.08	-
							35-40	3Bwb	1.62	0.09	-
57-1	0-5	Auh	17.63	0.45	6.19						
	5-10	Auh	12.97	0.30	5.54	59-3	0-5	Auh	15.54	0.58	4.06
	10-15	Auh	12.92	0.29	6.19		5-10	Auh	11.65	0.38	3.57

RCH no.	Depth [cm]	Horizon	C %	N %	BPCA %	RCH no.	Depth [cm]	Horizon	C %	N %	BPCA %
	10-15	Auh	10.24	0.31	3.50	60-2	0-5	Auh	10.58	0.29	3.16
	15-20	Auh	10.10	0.30	3.15		5-10	Auh	6.17	0.17	2.64
	20-25	Auh	9.44	0.25	3.62		10-15	Auh	3.12	0.10	1.02
	25-30	Auh	9.41	0.24	3.45		15-20	2Cu	4.77	0.12	2.02
	30-35	Auh	9.36	0.22	3.48		20-25	2Cu	3.17	0.08	1.69
	37-42	Auh	9.49	0.22	3.56		32-37	3Bwb	0.70	0.04	-
	42-47	Auh	15.75	0.24	6.92						
	47-52	Auh	14.40	0.24	6.23	60-3	0-5	Auh	7.73	0.22	2.95
	52-57	Auh	9.41	0.19	4.19		5-10	Auh	6.50	0.18	2.43
	60-65	2Bwb	0.70	0.04	-		10-15	Auh	7.94	0.17	2.44
							15-20	Auh	7.89	0.14	3.74
59-4M	0-5	Ah	6.60	0.28	-		20-25	Auh	8.04	0.14	4.06
	5-10	Ah	6.60	0.29	-		25-30	Auh	7.39	0.11	3.65
	10-15	Bw	2.49	0.12	-		36-41	2Ahb	2.18	0.06	-
	15-20	Bw	1.05	0.07	-		42-48	2Bwb	3.52	0.11	-
	20-25	Bw	0.78	0.05	-						
	25-30	Bw	0.73	0.05	-	61-1	0-5	Auh	14.74	0.28	4.30
	33-38	Bw	0.52	0.04	-		5-10	2Cu	4.90	0.14	1.22
	38-43	Bw	0.38	0.04	-		10-15	3Ahb	2.72	0.07	0.40
	47-52	C	0.16	9.05	-		15-20	3Bwb	1.33	0.05	0.10
							20-25	3Bwb	0.90	0.04	0
59-4O	0-5	Ah	6.21	0.26	-		25-30	3Cb	0.79	0.04	-
	5-10	Ah	3.60	0.17	-						
	12-17	Bw	2.53	0.12	-	61-2	0-5	Auh	9.93	0.24	3.67
	23-28	Bw	1.10	0.06	-		5-10	2Cu	4.20	0.13	0.66
	28-33	Bw	0.80	0.04	-		14-19	3Ahb	2.67	0.07	0.02
							19-24	3Bwb	1.89	0.07	0.44
59-4W	0-5	Ah	6.23	0.28	-		10-15	3Bwb	2.62	0.06	0.26
	5-10	Ah	2.46	0.12	-		25-30	3Bwb	0.90	0.04	0
	10-15	Bw	1.18	0.06	-		38-43	3Cb	0.80	0.03	-
	15-20	Bw	0.55	0.03	-						
	20-25	Bw	0.49	0.03	-	61-3	0-5	Auh	19.97	0.37	4.01
	30-35	2Bw	0.52	0.03	-		10-15	Ahb	4.54	0.14	0.65
	35-40	2Bw	0.39	0.02	-		15-20	2Bwb	3.21	0.12	-
	40-45	2Bw	0.38	0.02	-		20-25	2Bwb	1.93	0.09	-
	45-50	2Bw	0.36	0.02	-						
						62-1	0-5	Auh	23.92	0.57	7.79
	0-5	Auh	10.12	0.29	2.82		5-10	Auh	15.80	0.37	3.83
	5-10	Auh	7.12	0.20	1.53		10-15	Auh	6.84	0.20	1.35
	10-15	Auh	7.85	0.19	2.04		18-23	2Bwb	1.06	0.07	-
	15-20	2Bwb	1.91	0.06	-						
	20-25	2Bwb	0.73	0.03	-						
						62-2	0-5	Auh	12.92	0.25	5.01
	0-5	Auh	10.58	0.29	3.16		5-10	Auh	19.58	0.29	7.50
	5-10	Auh	6.17	0.17	2.64		10-15	Auh	14.69	0.20	5.00
	10-15	Auh	3.12	0.10	1.02		19-24	2Cu	4.66	0.12	0.71
	15-20	2Cu	4.77	0.12	2.02		25-30	3Auh	9.81	0.22	2.63
	20-25	2Cu	3.17	0.08	1.69		30-35	3Auh	9.58	0.21	2.55
	32-37	3Bwb	0.70	0.04	-						
						62-3	0-5	Auh	9.44	0.25	2.02
60-1	0-5	Auh	10.12	0.29	2.82		5-10	Auh	6.32	0.18	1.72
	5-10	Auh	7.12	0.20	1.53		10-15	Auh	4.67	0.13	1.41
	10-15	Auh	7.85	0.19	2.04		16-21	2Cu	7.50	0.16	2.71
	15-20	2Bwb	1.91	0.06	-		21-26	2Cu	4.10	0.12	1.18
	20-25	2Bwb	0.73	0.03	-		30-35	3Auh	7.98	0.16	2.81

RCH no.	Depth [cm]	Horizon	C %	N %	BPCA %	RCH no.	Depth [cm]	Horizon	C %	N %	BPCA %
	35-40	3Auh	7.12	0.15	2.32		15-20	Auh	4.72	0.13	0.76
	45-50	3Auh	3.09	0.10	0.19		20-25	Auh	4.94	0.12	1.90
	50-55	3Auh	5.74	0.13	1.74		25-30	Auh	7.21	0.15	1.44
	55-60	3Auh	4.66	0.12	1.34		30-35	Auh	13.16	0.19	5.09
	60-65	4Bwb	1.56	0.07	-		35-40	Auh	2.34	0.10	0.14
							40-45	2Bwb	1.30	0.06	-
63-1	0-5	Auh	15.06	0.47	4.58		45-50	2Bwb	0.34	0.02	-
	5-10	Auh	9.17	0.25	3.99		60-65	2Cb	0.19	0.01	-
	10-15	Auh	3.86	0.13	2.07						
	15-20	Auh	5.52	0.16	2.40	65-2	0-5	Ah	4.59	0.28	-
	24-29	2Cu	2.80	0.10	1.71		5-10	Ah	1.92	0.11	-
							10-15	Ah	1.73	0.10	-
63-2	0-5	Auh	14.65	0.41	2.97		30-35	Bw	0.97	0.06	-
	5-10	Auh	10.90	0.30	3.67		35-40	Bw	0.62	0.04	-
	10-15	Auh	10.10	0.26	3.63		45-50	C	0.61	0.04	-
	15-20	Auh	10.08	0.26	3.99		55-60	C	0.37	0.02	-
	20-25	Auh	9.52	0.24	3.69						
	25-30	Auh	8.12	0.21	3.15	65-3	0-5	Auh	5.41	0.22	1.77
	30-35	2Ahb	5.43	0.16	2.05		5-10	Auh	4.24	0.16	1.67
	35-40	2Bwb	3.44	0.13			10-15	Auh	5.32	0.16	1.61
							15-20	Auh	6.89	0.18	2.41
63-3	0-5	Auh	11.63	0.41	2.96		25-30	2Cu	1.40	0.08	0.02
	5-10	Auh	8.80	0.28	2.90		30-35	2Cu	1.34	0.08	0
	10-15	Auh	8.15	0.26	3.48		35-40	2Cu	1.38	0.08	0
	15-20	Auh	8.26	0.26	2.87		54-59	3Ahb	1.81	0.11	-
	20-25	Auh	8.17	0.26	2.89		59-64	3Ahb	1.24	0.08	-
	25-30	Auh	7.87	0.25	2.14						
	33-38	2Ahb	4.12	0.19		65-4	0-5	Ah	4.54	0.27	-
	38-43	2Bwb	1.28	0.06			5-10	Ah	2.31	0.14	-
							25-30	Bw	0.84	0.05	-
63-4	0-5	Ah	27.18	1.86	-						
	8-13	C	1.06	0.08	-	66-1	0-5	Auh	9.66	0.28	3.17
	13-18	C	0.54	0.04	-		5-10	Auh	4.60	0.14	1.89
							10-15	Auh	4.67	0.13	2.36
64-1	0-5	Auh	18.03	0.52	6.49		16-21	2Bwb	0.58	0.04	-
	5-10	Auh	7.89	0.25	3.06		21-26	2Bwb	0.37	0.03	-
	10-15	Auh	4.93	0.17	2.17						
	15-20	Auh	4.02	0.16	1.72	66-2	0-5	Auh	7.25	0.20	3.45
	27-32	2Bwb	1.68	0.09	-		5-10	Auh	6.60	0.14	3.18
							10-15	Auh	5.83	0.16	2.16
64-2	0-5	Auh	17.60	0.59	4.33		15-20	Auh	5.36	0.15	1.87
	5-10	Auh	11.73	0.33	4.04		24-29	2Cu	5.40	0.15	2.22
	10-15	Auh	7.71	0.24	2.67		36-41	3Auh	3.14	0.12	1.30
	15-20	Auh	4.26	0.15	1.80		45-50	4Ahb	2.90	0.07	-
	20-25	2Cu	3.17	0.12	1.61		50-55	4Ahb	1.06	0.07	-
	25-30	2Cu	4.92	0.16	2.44						
	30-35	2Cu	4.35	0.15	1.93	66-3	0-5	Auh	6.45	0.27	1.54
							8-13	2Cu	2.21	0.10	0.43
64-3	0-5	Auh	16.86	0.51	5.79		32-37	3Auh	5.06	0.16	2.21
	5-10	Auh	7.71	0.26	3.34		37-42	3Auh	5.29	0.16	0.56
	10-15	Auh	6.14	0.19	2.41		42-47	3Auh	4.83	0.18	1.84
							47-52	3Auh	5.32	0.16	2.02
65-1	0-5	Auh	6.2	0.2	1.19		52-57	4Bwb	1.53	0.09	2.21
	5-10	Auh	4.7	0.1	1.15		57-62	4Bwb	0.93	0.06	-
	10-15	Auh	-	-	-						

RCH no.	Depth [cm]	Horizon	C %	N %	BCPA %	RCH no.	Depth [cm]	Horizon	C %	N %	BCPA %
67-1	0-5	Auh	8.32	0.28	3.87	69-1	0-5	Auh	8.19	0.32	1.98
	5-10	Auh	6.62	0.21	2.89		5-10	Auh	7.11	0.24	2.22
	10-15	Auh	6.99	0.18	2.51		10-15	2Cu	4.32	0.16	1.67
	15-20	Auh	5.74	0.14	1.41		15-20	2Cu	1.73	0.09	0.49
	25-30	2Bwb	2.52	0.08	-						
	30-35	2Bwb	0.86	0.04	-	69-2	0-5	Auh	7.58	0.32	1.64
					5-10		Auh	6.74	0.23	2.31	
67-2	0-5	Auh	21.45	0.41	8.82		10-15	Auh	8.26	0.19	3.21
	5-10	Auh	13.55	0.24	4.06		15-20	2Cu	4.98	0.14	2.43
	10-15	Auh	8.59	0.18	2.59		20-25	2Cu	2.77	0.10	1.58
	15-20	Auh	5.36	0.14	2.85	25-30	3Bwb	1.22	0.07	-	
	20-25	Auh	5.99	0.15	3.18	35-40	3Bwb	0.76	0.05	-	
	25-30	2Cu	7.48	0.18	2.41						
	35-40	2Cu	5.55	0.14	-	69-3	0-5	Auh	5.52	0.20	1.21
	47-52	3Ahb	2.28	0.07	-		5-10	Auh	3.77	0.13	1.51
	52-57	3Ahb	1.40	0.05	-		10-15	2Bwb	1.40	0.07	-
							15-20	2Bwb	1.27	0.07	-
							25-30	2Bwb	0.79	0.04	-
67-3	0-5	Auh	5.10	0.23	0.86		30-35	2Bwb	0.44	0.02	-
	5-10	Auh	3.18	0.14	0.67		35-40	2Bwb	0.35	0.02	-
	12-17	2Cu	2.60	0.09	1.12		40-45	2C	0.19	0.01	-
	17-22	2Cu	4.42	0.12	1.65		45-50	2C	0.18	0.01	-
	20-25	2Cu									
	25-30	3Auh	7.87	0.17	3.57						
	30-35 I	3Auh	6.68	0.15	3.07	70-1	0-5	Auh	5.88	0.27	2.43
	30-35 II	3Auh	6.00	0.14	3.01		5-10	Auh	5.41	0.20	2.88
	35-40	3Auh	5.62	0.16	2.18		15-20	Auh	4.98	0.16	2.93
	40-45	3Auh	4.42	0.14	1.67		24-29	2Bwb	1.46	0.06	-
45-50	3Auh	4.55	0.14	2.61							
	53-58	4Bwb	2.44	0.08	-	70-2	0-5	Auh	5.53	0.26	2.05
	58-63	4Bwb	1.60	0.07	-		5-10	Auh	4.14	0.15	2.18
					10-15		2Cu	4.31	0.15	2.11	
68-1	0-5	Auh	16.88	0.44	4.81		20-25	3Auh	4.06	0.14	1.96
	5-10	Auh	10.97	0.29	3.41		28-33	4Ahb	3.74	0.13	-
	10-15	Auh	7.15	0.18	2.49		33-38	4Ahb	3.46	0.13	-
							50-55	4Cb	0.32	0.03	-
68-2	0-5	Auh	12.21	0.42	3.99						
	5-10	Auh	9.30	0.24	3.32	70-3	0-5	Auh	5.43	0.28	1.67
	10-15	Auh	7.80	0.20	3.22		5-10	Auh	4.70	0.22	1.64
	15-20	Auh	6.89	0.15	2.69		10-15	Auh	3.81	0.18	1.25
	20-25	Auh	7.34	0.16	2.86		15-20	Auh	3.29	0.14	1.22
	41-46	2Bwb	1.02	0.04	-		20-25	Auh	3.59	0.13	1.54
							28-33	2Cu	1.86	0.09	0.79
					33-38		2Cu	1.00	0.06	0.51	
68-3	0-5	Auh	9.49	0.28	3.55		38-43	2Cu	0.63	0.05	0.74
	5-10	Auh	4.97	0.16	2.26		44-49	3Bwb	0.43	0.03	-
	10-15	Auh	6.27	0.17	2.64		49-54	3Bwb	0.48	0.04	-
	15-20	Auh	6.62	0.16	2.87		60-65	4Cb	0.20	0.02	-
	20-25	Auh	5.46	0.14	2.26						
	30-35	Auh	8.92	0.22	3.95						
	35-40	Auh	10.07	0.19	5.07	71-1	0-5	Auh	10.34	0.29	4.02
	43-48	Auh	5.66	0.19	3.03		5-10	Auh	8.87	0.23	3.12
48-53	Auh	4.63	0.05	2.44	10-15		Auh	5.29	0.17	1.97	
53-58	Auh	3.03	0.10	1.33	16-21		2Bwb	1.20	0.07	4.09	
58-63	Auh	2.84	0.09	1.04	21-26		2Bwb	0.60	0.04	3.33	
	80-85	2Bwb	0.47	0.03	-						

RCH no.	Depth [cm]	Horizon	C %	N %	BPCA %	RCH no.	Depth [cm]	Horizon	C %	N %	BPCA %
71-2	0-5	Auh	11.26	0.29	3.80		20-25	Auh	5.14	0.15	1.34
	5-10	Auh	7.56	0.14	2.22		25-30	2Auh	6.54	0.18	2.52
	10-15	Auh	8.60	0.13	0.50		31-36	3Bwb	1.55	0.07	-
	15-20	2Cu	5.66	0.10	2.79						
	20-25	2Cu	2.64	0.08	1.96	73-3	0-5	Auh	5.55	0.21	1.67
	29-34	3Auh	7.12	0.14	-		5-10	Auh	8.13	0.21	2.99
	34-39	3Auh	4.60	0.12	-		10-15	Auh	6.57	0.18	2.45
	39-44	4Bwb	1.92	0.07	-						
	44-49	4Bwb	1.34	0.07	-	74-1	0-5	Auh	13.48	0.36	3.85
	49-54	4Bwb	0.78	0.04	-		5-10	Auh	7.27	0.21	2.86
							10-15	Auh	6.04	0.17	2.30
71-3	0-5	Auh	8.05	0.24	3.24		15-20	Auh	6.63	0.18	2.87
	5-10	Auh	3.02	0.11	1.69		20-25	Auh	6.75	0.18	2.95
	10-15	2Cu	1.76	0.07	0.75						
	15-20	2Cu	2.00	0.08	0.95	74-2	0-5	Auh	8.72	0.30	3.15
	20-25	2Cu	2.56	0.08	1.14		5-10	Auh	7.52	0.24	3.29
	25-30	2Cu	3.07	0.10	1.17		10-15	Auh	8.00	0.25	3.41
	35-40	3Auh	7.34	0.17	2.72		15-20	Auh	6.48	0.21	2.10
	40-45	3Auh	3.95	0.14	1.11		27-32	2Ahb	2.46	0.13	-
	46-51	4Ahb	3.92	0.15	-		32-37	2Ahb	2.52	0.14	-
	51-56	4Bwb	2.54	0.14	-		37-42	2Ahb	2.37	0.12	-
	80-85	4Cb	0.29	0.02	-						
					74-3	0-5	Auh	9.82	0.38	2.66	
72-1	0-5	Auh	17.36	0.46	6.81		5-10	Auh	3.48	0.18	0.92
	5-10	Auh	8.88	0.27	3.97		10-15	Auh	3.31	0.19	0.52
	10-15	Auh	6.06	0.20	2.56		15-20	Auh	3.03	0.18	0.55
	15-20	Auh	4.63	0.14	1.89		20-25	Auh	2.88	0.18	0.65
	20-25	Auh	4.45	0.12	1.61						
	30-35	2Bwb	1.03	0.05	-	75-1	0-5	Auh	20.46	0.43	6.70
						5-10	Auh	12.10	0.37	3.70	
72-2	0-5	Auh	11.66	0.36	3.74		20-25	2Ahb	1.51	0.20	-
	5-10	Auh	7.57	0.24	2.74						
	10-15	Auh	6.26	0.18	3.00	75-2	0-5	Auh	14.30	1.68	4.22
	15-20	Auh	4.84	0.14	2.58		5-10	Auh	14.49	3.10	4.78
	20-25	Auh	4.99	0.15	2.24		10-15	Auh	15.06	4.14	5.89
	25-30	Auh	6.28	0.19	2.78		16-21	2Cu	3.94	7.11	2.23
	32-37	Auh	6.55	0.17	3.01		21-26	2Cu	6.17	13.43	2.62
	37-42	Auh	5.68	0.75	2.51						
						75-3	0-5	Auh	5.72	0.25	2.14
	72-3	0-5	Auh	9.24	7.39	3.06		12-17	Auh	3.95	0.17
	5-10	Auh	7.43	15.72	3.50		25-30	3Auh	5.82	0.20	2.34
	10-15	Auh	6.47	0.18	2.80		30-35	3Auh	9.55	0.26	4.33
	15-20	Auh	4.63	0.15	1.81		35-40	3Auh	10.26	0.28	4.43
	20-25	2Cu	5.07	0.15	2.08		40-45	3Auh	10.92	0.25	4.49
	25-30	2Cu	4.18	0.14	1.71		45-50	3Auh	9.90	0.23	4.29
	34-39	3Auh	8.00	0.20	3.37		52-57	4Ahb	3.53	0.13	-
	39-44	3Auh	7.26	0.17	3.26						
	44-49	3Auh	7.55	0.18	3.15	76-1	0-5	Auh	20.69	0.45	5.75
	54-59	4Bwb	2.70	0.11	-		5-10	Auh	13.11	0.32	2.92
	59-64	4Bwb	1.00	0.05	-		10-15	Auh	12.39	0.29	3.85
							20-25	2Bwb	0.99	0.06	-
73-2	0-5	Auh	9.38	0.24	3.23						
	5-10	Auh	9.10	0.21	2.81	76-2	0-5	Auh	14.82	0.35	5.86
	10-15	Auh	7.31	0.19	2.12		5-10	Auh	11.83	0.24	3.88
	15-20	Auh	6.36	0.16	2.43		10-15	Auh	8.81	0.17	1.96



RCH no.	Depth [cm]	Horizon	C %	N %	BPCA %	RCH no.	Depth [cm]	Horizon	C %	N %	BPCA %
	15-20	Auh	8.49	0.15	2.16		35-40	3Bwb	1.08	0.05	-
	20-25	Auh	10.29	0.15	3.50		40-45	3Bwb	0.53	0.04	-
	25-30	Auh	9.03	0.15	3.29		45-50	3Bwb	0.42	0.03	-
	30-35	Auh	5.77	0.26	1.98						
	35-40	Auh	6.27	3.14	2.43	78-2	0-5	Auh	7.91	0.26	1.95
	40-45	Auh	4.79	0.92	1.78		5-10	Auh	6.94	0.19	1.56
	47-52	2Bwb	2.97	3.13	-		10-15	Auh	5.82	0.17	1.61
							20-25	3Auh	6.04	0.12	1.15
76-3	0-5	Auh	7.92	4.74	2.08		25-30	3Auh	5.82	0.11	1.35
	5-10	2Cu	3.01	8.67	0.68		30-35	3Auh	5.33	0.10	1.32
	10-15	2Cu	3.01	13.64	0.82		35-40	3Auh	3.95	0.11	0.70
	15-20	2Cu	2.40	21.03	0.26		45-50	4Ahb	2.17	0.09	-
	25-30	2Cu	2.37	0.10	0.52		50-55	4Bwb	0.82	0.05	-
	30-35	2Cu	2.11	0.09	0.65						
	35-40	2Cu	2.40	0.09	0.17	78-3	0-5	Auh	8.44	0.26	1.38
	41-46	3Auh	7.69	0.18	3.05		5-10	Auh	4.94	0.16	1.33
	46-51	3Auh	7.55	0.15	2.96		10-15	2Cu	2.96	0.11	0.43
	51-56	3Auh	5.00	0.11	2.06		15-20	2Cu	2.07	0.11	0.32
	57-62	3Cu	2.25	0.08	0.63		20-25	3Auh	2.96	0.12	0.30
	62-67	3Cu	2.24	0.08	1.02		20-25b	3Auh	3.59	0.15	0.48
	80-85	4Bwb	0.46	0.03	-		26-31	4Bwb	2.01	0.10	-
							31-36	4Bwb	0.74	0.04	-
77-1	0-5	Auh	26.09	0.55	11.42		36-41	4Bwb	0.60	0.04	-
	5-10	Auh	11.66	0.27	3.87		41-44	4Bwb	0.49	0.03	-
	10-15	Auh	6.88	0.18	1.97		46-51	4Bwb	0.45	0.03	-
	18-23	2Bwb	1.45	0.12	-						
	23-28	2Bwb	0.88	0.29	-	79-1	0-5	Auh	6.41	0.23	1.90
	28-33	2Bwb	0.75	0.05	-		5-10	Auh	6.25	0.21	1.50
							10-15	Auh	5.06	0.18	1.12
77-2	0-5	Auh	10.55	0.34	2.38		15-20	Auh	4.30	0.16	0.85
	5-10	Auh	6.67	0.20	1.90		20-25	Auh	3.44	0.12	1.16
	10-15	Auh	4.80	0.14	1.04		26-31	2Ahb	1.82	0.09	0.30
	17-22	Auh	5.43	0.15	1.33		34-39	2Bwb	1.29	0.07	-
	22-27	Auh	6.91	0.18	2.41		39-44	2Bwb	0.75	0.04	-
	27-32	2Bwb	2.57	0.10	-						
	32-37	2Bwb	0.90	0.05	-	79-2	0-5	Auh	7.77	0.29	1.69
							5-10	Auh	7.39	0.25	1.90
77-3	0-5	Auh	6.71	0.26	1.41		10-15	Auh	6.16	0.17	2.01
	5-10	Auh	5.82	0.18	1.67		15-20	Auh	5.76	0.15	1.94
	10-15	2Bwb	3.11	0.11	-		20-25	Auh	6.90	0.14	2.86
	15-20	2Bwb	1.22	0.07	-		25-30	Auh	9.14	0.14	4.49
	20-25	2Bwb	0.65	0.05	-		33-38	2Ahb	2.43	0.10	0.49
	30-35	2Bwb	0.56	0.04	-		38-43	2Ahb	1.66	0.08	0.49
	35-40	2Bwb	0.49	0.03	-		43-48	2Bwb	0.73	0.04	-
	40-45a	2Bwb	0.49	0.03	-		48-52	2Bwb	0.45	0.03	-
	40-45b	2Bwb	0.43	0.03	-						
	45-50	2Bwb	0.23	0.02	-	79-3a	0-5	Auh	7.78	0.31	2.04
	80-85	2Cb	0.20	0.02	-		5-10	Auh	7.46	0.23	2.03
							10-15	Auh	5.32	0.16	1.27
78-1	0-5	Auh	9.71	0.36	1.71		15-20	Auh	4.49	0.13	1.76
	5-10	Auh	5.60	0.27	1.30		20-25	Auh	4.86	0.14	1.77
	10-15	2Auh	5.38	0.29	1.05		25-30	Auh	3.81	0.13	1.01
	20-25	2Auh	4.56	0.13	1.03		37-42	Ahb	2.41	0.10	1.03
	25-30	3Ahb	3.62	0.11	-		42-47	Ahb	1.90	0.08	0.48
	28-33	3Ahb	3.31	0.11	-		55-60	2Bwb	0.83	0.05	-

RCH no.	Depth [cm]	Horizon	C %	N %	BPCA %
	60-65	2Bwb	0.62	0.04	-
	70-75	2Cb	0.43	0.03	-
79-3b	0-5	Auh	6.91	0.31	-
	5-10	Auh	3.01	0.17	-
	10-15	2Cu	2.24	0.16	-
A1	0-5	Ah	6.43	0.23	-
	5-10	Bw	3.13	0.13	-
	10-15	Bw	1.92	0.09	-
	15-20	Bw	0.87	0.05	-
	20-25	Bw	0.67	0.04	-
	25-30	Bw	0.79	0.04	-
	33-38	Bw	0.57	0.04	-
	38-43	C	0.64	0.04	-
	43-48	C	0.46	0.03	-
A3	0-5	Ah	2.21	0.13	-
	5-10	Ah	1.35	0.08	-
	10-15	Ah	1.09	0.06	-
	15-20	Ah	0.80	0.04	-
	20-25	Ah	0.54	0.03	-
	33-38	Bw	0.35	0.02	-

**Tabelle A6.** Calibration dataset of measured BPCA-C values for the chemometric BPCA-C prediction.

RCH no.	Depth [cm]	Horizon	BPCA %	RCH no.	Depth [cm]	Horizon	BPCA %	RCH no.	Depth [cm]	Horizon	BPCA %
28-1	0-5	Auh	9.7		5-10	Auh	0.4		25-30	C	0.1
	5-10	Auh	3.1		15-20	Auh	3.1		32-37	C	0.2
28-2	0-5	Auh	4.8		32-37	2Cu	0.6	30-4	0-5	Ah	0.2
	5-10	Auh	2.7		37-42	2Cu	0.4		5-10	Ah	0.1
28-3	0-5	Auh	2.5		42-47	2Cu	0.2		10-15	Bw	0.2
	5-10	Auh	4.2		47-52	2Cu	0.3		15-20	Bw	0.1
29-1	0-5	Auh	5.0		59-64	2Cu	2.5		21-26	C	0.1
	5-10	Auh	3.6		64-69	3Auh	2.2		26-31	C	0.0
	10-15	Auh	4.1		72-77	3Auh	2.2		33-38	C	0.1
29-2	0-5	Auh	3.6	45-1	0-5	Auh	2.8		38-43	C	0.1
	5-10	Auh	3.2		5-10	Auh	3.2	32-4	0-5	Ah	0.1
	10-15	Auh	3.0		10-15	Auh	-		5-10	Ah	0.1
	15-20	Auh	2.9		15-20	2Cu	2.4		20-25	Bw	1.5
29-3	0-5	Auh	3.3	45-2	0-5	Auh	3.1		25-30	Bw	0.4
	5-10	Auh	3.7		5-10	Auh	2.2	39-4	0-5	Ah	0.3
	10-15	Auh	3.7		10-15	Auh	2.3		5-10	Ah	0.3
	15-20	Auh	2.1		20-25	2Cu	1.3		10-15	Bw	0.3
	20-25	Auh	2.5		25-30	2Cu	1.4	39-3	77-82	Ahb	0.2
	25-30	Auh	2.9	45-3	23-28	2Cu	1.5		82-87	Ahb	0.4
39-1	0-5	Auh	10.7			28-33	2Cu	2.1		87-92	Bwb
	5-10	Auh	8.5	28-4	9-14	Bw	0.1	45-3	54-59	Ahb	0.9
	10-15	Auh	4.5		14-19	Bw	0.1		60-65	Ahb	0.4
15-20	Auh	1.9	19-24		Bw	0.1	32-37		Ahb	0.3	
	25-30	Bwb	4.6		25-30	Bw	0.1	46-4	0-5	Ah	1.2
39-2	0-5	Auh	6.2		30-35	Bw	0.3			5-10	Ah
	5-10	Auh	5.9	29-4	0-5	Ah	0.2		25-30	Bw	0.3
	10-15	Auh	3.8		5-10	Bw	0.4	59-40	0-5	Ah	0.1
	15-20	Auh	0		10-15	Bw	0.3			5-10	Ah
	25-30	Auh	0.1		15-20	Bw	0.1		12-17	Bw	0.1
39-3	0-5	Auh	1.8		20-25	C	0.1		23-28	Bw	0.9

RCH no.	Depth [cm]	Horizon	BPCA %
	28-33	Bw	0.2
59-4W	0-5	Ah	0.1
	5-10	Ah	0.1
	10-15	Bw	0.1
	15-20	Bw	0.0
	20-25	Bw	0.0
	30-35	Bw	0.0
	35-40	Bw	0.2
	40-45	Bw	0.1
29-1	17-22	Bwb	0.2
	22-27	Bwb	0.3
29-2	22-27	Bwb	0.3
	27-32	Bwb	0.2
	32-37	Bwb	0.2
29-3	30-45	Bwb	0.2
	35-40	Bwb	0.2
45-2	33-38	Bwb	0.6
46-1	26-32	Bwb	0.3

**Table A7.** Soil acidity (pH in CaCl<sub>2</sub>) for studied soil samples.

RCH no.	Depth [cm]	Horizon	pH	RCH no.	Depth [cm]	Horizon	pH	RCH no.	Depth [cm]	Horizon	pH	
28-1	0-5	Auh	3.9		5-10	Auh	4.4		25-30	C	4.9	
	5-10	Auh	3.9		15-20	Auh	3.9		32-37	C	-	
28-2	0-5	Auh	3.9		32-37	2Cu	4.8	30-4	0-5	Ah	4.3	
	5-10	Auh	3.9		37-42	2Cu	4.8		5-10	Ah	4.6	
	10-15	Auh	4.2									
28-3	0-5	Auh	4.1		42-47	2Cu	4.9		10-15	Bw	4.6	
	5-10	Auh	4.1		47-52	2Cu	4.9		15-20	Bw	4.8	
29-1	0-5	Auh	4.1		59-64	2Cu	4.7		21-26	C	-	
	5-10	Auh	4.1		64-69	3Auh	4.9		26-31	C	-	
	10-15	Auh	4.1		72-77	3Auh	4.5		33-38	C	-	
29-2	0-5	Auh	4.1	45-1	0-5	Auh	4.3		38-43	C	-	
	5-10	Auh	4.1		5-10	Auh	4.3		32-4	0-5	Ah	4.5
	10-15	Auh	4.2		10-15	Auh	4.3			5-10	Ah	4.7
	15-20	Auh	4.2		15-20	2Cu	-			20-25	Bw	4.7
29-3	0-5	Auh	4.2	45-2	0-5	Auh	4.3		25-30	Bw	4.7	
	5-10	Auh	4.2		5-10	Auh	4.3		39-4	0-5	Ah	4.3
	10-15	Auh	4.4		10-15	Auh	4.7			5-10	Ah	4.3
	15-20	Auh	4.4		20-25	2Cu	4.9			10-15	Bw	4.5
	20-25	Auh	4.7		25-30	2Cu	5.0		39-3	77-82	Ahb	4.8
39-1	25-30	Auh	4.7	45-3	23-28	2Cu	4.4		82-87	Ahb	4.8	
	0-5	Auh	3.5		28-33	2Cu	4.4			87-92	Bwb	4.4
	5-10	Auh	3.5	28-4	9-14	Bw	-	45-3	54-59	Ahb	4.6	
	10-15	Auh	4.3		14-19	Bw	4.8			60-65	Ahb	4.6
	15-20	Auh	4.3		19-24	Bw	4.8		46-3	32-37	Ahb	4.6
	25-30	Bwb	4.5		25-30	Bw	4.9		46-4	0-5	Ah	3.8
39-2	0-5	Auh	4.7		30-35	Bw	4.9		5-10	Ah	3.8	
	5-10	Auh	4.7		29-4	0-5	Ah		4.2	25-30	Bw	4.3
	10-15	Auh	4.7			5-10	Bw		4.8	59-40	0-5	Ah
	15-20	Auh	4.8		10-15	Bw	4.8		5-10	Ah	3.9	
	25-30	Auh	4.8		15-20	Bw	4.8			12-17	Bw	4.4
39-3	0-5	Auh	4.4		20-25	C	4.9		23-28	Bw	4.4	

RCH no.	Depth [cm]	Horizon	pH
	28-33	Bw	4.4
59-4W	0-5	Ah	3.6
	5-10	Ah	3.6
	10-15	Bw	4.3
	15-20	Bw	4.3
	20-25	Bw	4.2
	30-35	Bw	4.5
	35-40	Bw	4.5
	40-45	Bw	4.4
29-1	17-22	Bwb	5.0
	22-27	Bwb	5.0
29-2	22-27	Bwb	5.0
	27-32	Bwb	5.0
	32-37	Bwb	5.1
29-3	30-45	Bwb	5.0
	35-40	Bwb	4.6
45-2	33-38	Bwb	5.0
46-1	26-32	Bwb	4.3

## Chapter 8

**Table A8.** Average element concentrations by sequential extraction in RCH and reference soils. T - total, P – pyrophosphate extractable, Ox – oxalate extractable, D – Dithionite extractable

			Auh	Cu	Ahb	Bwb	Ah	Bw	C
Fe	T	mg kg <sup>-1</sup>	25619	27606	27448	30809	33866	36249	33594
	Py		1960	1676	900	475	3244	571	238
	Ox		3436	3355	3181	3107	4600	2464	1437
	Di		6705c	7117	7151	9487	5954	7825	5383
Al	T	mg kg <sup>-1</sup>	22538	24379	23626	27905	24198	25766	25422
	Py		2757	2558	1631	1083	3904	1605	1014
	Ox		2421	2154	2242	2719	2012	2259	1764
	Di		2460	2589	2737	4244	2539	3015	1533
Mn	T	mg kg <sup>-1</sup>	715	662	557	435	711	614	454
	Py		99	93	53	85	57	24	36
	Ox		221	206	196	80	124	37	27
	Di		33	56	9	70	30	63	68
Ca	T	mg kg <sup>-1</sup>	4772	3578	2949	2977	4759	4337	5093
Na	T		889	827	812	910	977	948	916
K	T		3495	3839	3635	4120	2735	3363	4972
Mg	T		4132	4832	4729	5421	5005	6185	7991

**Tabelle A9.** Effective cation exchange capacity (CEC) and exchangeable cations for RCH soils

RCH no.	Depth [cm]	Horizon	Fe	Mg	Al	Ca	Na	K	Mn	CEC
<b>cmolc kg<sup>-1</sup></b>										
39-1	0-10	Auh	0.03	1.53	7.40	5.49	1.38	0.34	0.35	16.52
39-1	10-21	Auh	0	0.84	2.07	3.78	1.04	0.11	0.18	8.02
39-1	21-31	Bwb	0	0.59	0.73	2.73	0.99	0.06	0.05	5.16
39-2	0-15	Auh	0.00	4.10	2.87	1.32	1.10	0.20	0.52	10.10
39-2	15-25	Auh	0.00	5.63	3.00	2.40	1.15	0.15	0.43	12.76
39-2	25-30	Auh	0.00	0.79	0.27	3.27	0.91	0.06	0.05	5.35
39-2	30-40	Bwb	0.00	0.89	0.00	3.06	0.81	0.03	0.02	4.81
39-2	40-50	Bwb	0.00	0.74	0.00	3.18	0.81	0.05	0.02	4.79
39-3	0-9	Auh	0.00	0.79	4.87	3.27	1.17	0.20	0.13	10.43
39-3	9-14	Cu	0.00	0.54	1.40	2.34	0.84	0.12	0.12	5.36
39-3	14-22	2Auh	0.01	1.73	1.93	7.44	0.97	0.14	0.20	12.42
39-3	22-32	2Cu	0.00	1.23	0.87	5.79	0.99	0.14	0.08	9.10
39-3	32-41	2Cu	0.01	0.69	0.13	2.40	0.68	0.08	0.04	4.04
39-3	41-51	2Cu	0.00	1.19	0.20	3.36	1.02	0.11	0.08	5.95
39-3	51-61	2Cu	0.00	0.69	0.13	2.58	0.81	0.09	0.05	4.36
39-3	61-71	3Auh	0.00	2.42	1.13	2.10	1.46	0.17	0.13	7.41
39-3	71-77	3Auh	0.00	1.88	1.33	9.81	1.02	0.14	0.18	14.36
39-3	77-81	Ahb	0.01	0.79	0.27	3.30	0.81	0.09	0.09	5.36
39-3	81-87	Ahb	0.00	0.54	0.20	1.89	0.76	0.08	0.07	3.54
39-3	87-100	Bwb	0.00	0.64	0.20	1.80	1.15	0.09	0.02	3.90
39-3	100-120	Bwb	0.00	0.30	0.60	1.38	0.84	0.09	0.02	3.23
41-1	0-8	Auh	0.01	0.35	2.99	1.24	0.82	0.14	0.15	5.69
41-1	10-18	Auh	0.00	0.51	2.25	1.70	0.82	0.10	0.23	5.61
41-1	18-35	Bwb	0.00	0.42	0.35	2.21	0.95	0.09	0.03	4.05
41-2	0-13	Auh	0.00	1.81	3.11	5.87	0.98	0.17	0.79	12.73
41-2	13-19	Cu	0.00	1.42	0.97	8.96	0.77	0.09	0.22	12.43
41-2	19-31	2Auh	0.00	2.10	0.78	18.78	0.88	0.09	0.24	22.88
41-2	31-40	Bwb	0.00	0.28	0.33	1.36	0.76	0.07	0.02	2.81
41-2	40-50	Bwb	0.02	0.71	0.19	2.10	0.92	0.06	0.03	4.03
41-3	0-10	Auh	0.02	0.33	1.13	1.29	0.90	0.11	0.04	3.81
41-3	10-20	Cu	0.02	0.39	0.96	1.12	0.89	0.09	0.04	3.50
41-3	20-28	Cu	0.02	0.46	0.97	1.40	0.96	0.08	0.02	3.91
41-3	28-42	2Auh	0.02	0.44	1.41	1.49	1.05	0.10	0.09	4.60
41-3	42-50	Bwb	0.01	0.40	0.46	1.58	1.08	0.09	0.03	3.66
41-3	50-60	Bwb	0.01	0.41	0.59	1.56	0.90	0.08	0.02	3.57
45-1	0-15	Auh	0.01	0.73	1.80	2.42	1.04	0.14	0.13	6.28
45-1	15-20	Auh	0.01	1.46	1.73	5.78	2.15	0.14	0.10	11.36
45-1	25-35	Bwb	0.06	0.67	0.37	1.93	1.16	0.10	0.01	4.30
45-2	0-10	Auh	0.05	0.80	1.61	2.51	1.47	0.18	0.09	6.72
45-2	10-20	Auh	0.02	2.06	2.08	9.34	1.47	0.19	0.10	15.27
45-2	20-26	Cu	0.02	2.09	1.24	10.15	1.28	0.14	0.09	15.01
45-2	26-33	2Auh	0.02	1.77	0.67	12.78	1.06	0.10	0.06	16.47
45-2	33-40	Bwb	0.01	0.97	0.11	3.69	0.90	0.08	0.03	5.79
45-2	40-50	Bwb	0.02	0.92	0.18	2.43	0.97	0.08	0.02	4.61
45-2	50-60	Bwb	0.01	0.91	0.07	2.37	1.05	0.08	0.01	4.50
45-3	0-13	Auh	0.02	0.54	1.80	1.33	0.94	0.12	0.09	4.85
45-3	13-23	Auh	0.01	0.76	1.48	2.55	1.01	0.10	0.10	6.02
45-3	23-33	Cu	0.02	1.18	1.93	4.61	1.13	0.12	0.12	9.09
45-3	34-44	2Auh	0.02	0.78	0.84	2.90	0.80	0.08	0.05	5.46
45-3	44-54	2Auh	0.01	0.72	0.94	2.20	0.79	0.08	0.06	4.79
45-3	54-66	Ahb	0.01	1.31	1.33	4.66	1.30	0.14	0.08	8.83
45-3	66-76	Bwb	0.03	0.79	0.66	2.60	1.23	0.11	0.09	5.52
45-3	76-86	Bwb	0.02	0.55	0.58	2.32	0.94	0.08	0.03	4.53
45-3	86-96	Bwb	0.00	0.55	0.43	2.01	0.86	0.08	0.01	3.94
46-1	0-8	Auh	0.06	0.95	3.92	3.62	1.64	0.26	0.13	10.59
46-1	8-16	Auh	0.01	0.71	1.52	3.20	0.49	0.10	0.08	6.11



RCH no.	Depth [cm]	Horizon	Fe	Mg	Al	Ca	Na	K	Mn	CEC
46-1	16-26	Auh	0.01	0.72	1.15	4.35	0.92	0.10	0.04	7.29
46-1	26-36	Bwb	0.01	0.50	0.43	2.72	0.77	0.08	0.01	4.52
46-2	0-8	Auh	0.01	1.35	2.67	13.09	0.94	0.25	0.58	18.88
46-2	8-16	Auh	0.00	1.99	0.24	28.56	0.80	0.08	0.13	31.79
46-2	16-26	Auh	0.00	2.74	0.09	38.16	0.83	0.08	0.08	41.98
46-2	26-36	Auh	0.00	2.74	0.39	25.69	0.93	0.09	0.09	29.92
46-2	36-43	Bwb	0.01	0.88	0.21	4.71	0.97	0.08	0.01	6.87
46-3	0-12	Auh	0.04	0.68	2.68	2.71	1.17	0.22	0.08	7.58
46-3	12-22	Auh	0.00	0.58	1.21	2.13	1.07	0.12	0.07	5.18
46-3	22-32	Auh	0.00	1.02	1.68	5.51	1.29	0.22	0.09	9.82
46-3	32-40	Ahb	0.02	0.49	0.24	2.82	0.90	0.07	0.01	4.55
46-3	40-50	Bwb	0.02	0.30	0.27	1.47	0.89	0.07	0.00	3.02
46-3	50-60	Bwb	0.03	0.51	0.07	2.30	0.86	0.06	0.01	3.83
56-1	0-10	Auh	0.01	0.45	1.36	1.55	0.91	0.16	0.05	4.48
56-1	10-20	Bwb	0.03	0.34	0.52	1.77	0.86	0.08	0.01	3.62
56-2	0-9	Auh	0.01	0.52	2.00	1.75	0.98	0.23	0.09	5.59
56-2	9-18	Auh	0.01	0.49	1.51	1.77	1.05	0.17	0.08	5.09
56-2	18-27	Auh	0.03	0.55	0.92	2.32	1.09	0.20	0.04	5.15
56-2	27-40	Bwb	0.03	0.34	0.03	1.30	1.05	0.10	0.00	2.85
56-3	0-10	Auh	0.06	0.71	2.34	2.32	1.41	0.25	0.05	7.14
56-3	10-18	Cu	0.04	0.69	1.56	3.13	1.38	0.16	0.04	7.00
56-3	18-27	2Auh	0.05	0.88	2.68	3.10	1.28	0.17	0.03	8.19
56-3	27-32	2Cu	0.03	0.48	0.73	2.04	1.09	0.11	0.02	4.49
56-3	32-42	2Cu	0.03	0.90	0.80	3.92	0.94	0.09	0.02	6.71
56-3	42-52	2Cu	0.02	0.51	0.59	1.92	0.90	0.09	0.01	4.03
56-3	52-62	2Cu	0.04	0.67	0.45	2.41	1.16	0.11	0.00	4.85
56-3	62-65	2Cu	0.04	0.47	0.23	1.68	1.04	0.08	0.03	3.56
56-3	65-72	Ahb	0.05	0.38	0.21	1.47	1.09	0.08	0.00	3.27
56-3	72-85	Bwb	0.04	0.35	0.08	1.24	0.93	0.06	0.00	2.70

**Tabelle A10.** Effective cation exchange capacity (CEC) and exchangeable cations for Reference soils

RCH no.	Depth [cm]	Horizon	Fe	Mg	Al	Ca	Na	K	Mn	CEC
				<b>cmolc kg<sup>-1</sup></b>						
28-4	0-9	Ah	0.07	0.50	1.67	2.15	1.67	0.24	0.41	6.71
28-4	17-25	Ah	0.05	0.34	0.25	1.63	1.24	0.11	0.11	3.73
28-4	25-37	Bw	0.07	0.50	0.08	1.90	1.44	0.11	0.11	4.21
28-4	37-49	Bw	0.05	0.34	0.09	1.79	1.36	0.09	0.02	3.75
29-4	0-5	Ah	0.05	0.42	3.43	1.81	1.69	0.28	0.12	7.79
29-4	5-15	Bw	0.05	0.41	0.42	2.07	1.64	0.14	0.01	4.76
29-4	15-22	Bw	0.05	0.43	0.30	1.88	1.48	0.12	0.01	4.28
29-4	22-32	Bw	0.05	0.32	0.33	1.59	1.35	0.12	0.01	3.77
29-4	32-42	C	0.05	0.36	0.16	1.68	1.45	0.12	0.01	3.82
30-4	0-4	Ah	0.06	0.59	2.55	2.14	1.46	0.32	0.12	7.26
30-4	4-14	Bw	0.04	0.45	0.73	1.92	1.33	0.17	0.03	4.68
30-4	14-21	Bw	0.05	0.39	0.40	1.68	1.26	0.14	0.02	3.94
32-4	0-3	Ah	0.06	0.54	0.75	2.17	1.49	0.25	0.06	5.32
32-4	3-11	Ah	0.06	0.46	1.80	1.93	1.41	0.21	0.06	5.93
32-4	11-20	Ah	0.04	0.49	0.11	2.29	1.49	0.12	0.02	4.57
32-4	20-34	Bw	0.05	0.42	0.34	1.92	1.60	0.13	0.03	4.49
33-4	0-5	Ah	0.05	0.45	0.83	2.14	1.41	0.16	0.06	5.10
33-4	5-10	Ah	0.06	0.55	2.06	2.67	1.65	0.30	0.11	7.40
33-4	10-15	Bw	0.04	0.45	0.04	2.06	1.30	0.09	0.00	4.00
33-4	15-20	Bw	0.06	0.38	0.08	1.90	1.67	0.13	0.01	4.22
33-4	20-25	Bw	0.06	0.34	0.07	1.83	1.78	0.14	0.01	4.23
33-4	25-30	Bw	0.08	0.55	0.24	3.18	2.54	0.23	0.02	6.84
33-4	30-35	Bw	0.06	0.45	0.37	2.19	1.88	0.18	0.01	5.15

RCH no.	Depth [cm]	Horizon	Fe	Mg	Al	Ca	Na	K	Mn	CEC
cmolc kg <sup>-1</sup>										
33-4	35-40	Bw	0.06	0.37	0.41	1.86	1.81	0.16	0.04	4.71
39-4	0-12	Ah	0.05	0.33	2.79	0.95	0.78	0.22	0.09	5.22
39-4	12-20	Bw	0.00	0.25	0.53	1.01	0.78	0.08	0.03	2.66
39-4	20-35	Bw	0.00	0.33	0.31	0.83	0.69	0.06	0.02	2.25
39-4	35-50	Bw	0.00	0.29	0.25	1.32	0.64	0.05	0.01	2.56
39-4	50-65	C	0.00	0.36	0.10	1.50	0.65	0.04	0.02	2.66
39-4	65-80	C	0.00	0.36	0.09	1.49	0.63	0.04	0.01	2.61
41-4	0-10	Ah	0.03	0.48	2.82	1.83	1.20	0.19	0.06	6.61
41-4	10-20	Bw	0.01	0.47	0.72	1.82	1.12	0.11	0.02	4.29
41-4	20-30	Bw	0.01	0.30	0.67	1.27	1.24	0.09	0.02	3.60
41-4	30-40	Bw	0.03	0.52	0.60	1.73	1.12	0.10	0.02	4.11
45-4	0-10	Ah	0.12	0.55	4.29	2.33	1.05	0.21	0.02	8.57
45-4	10-20	Ah	0.05	0.42	1.66	1.74	1.31	0.12	0.01	5.31
45-4	20-30	Bw	0.01	0.36	0.95	1.40	0.91	0.10	0.00	3.72
45-4	30-40	Bw	0.00	0.30	0.50	1.12	0.80	0.07	0.00	2.80
45-4	40-50	C	0.01	0.41	0.32	1.75	0.78	0.06	0.01	3.34
45-4	50-60	C	0.00	0.39	0.36	1.39	0.93	0.06	0.01	3.15
46-4	0-10	Ah	0.06	0.52	3.70	1.49	0.99	0.25	0.01	7.01
46-4	10-20	Bw	0.01	0.30	0.68	0.98	0.75	0.12	0.00	2.83
46-4	20-30	Bw	0.00	0.51	0.70	2.20	1.05	0.10	0.00	4.57
46-4	30-38	Bw	0.00	0.31	0.24	1.38	0.76	0.06	0.00	2.75
46-4	38-50	C	0.01	0.41	0.08	1.32	0.67	0.05	0.01	2.55
59-4Ost	0-12	Ah	0.08	0.43	3.18	1.50	1.03	0.17	0.00	6.40
59-4Ost	12-20	Bw	0.07	0.50	0.78	2.05	1.29	0.13	0.00	4.81
59-4Ost	20-30	Bw	0.10	0.43	3.03	1.88	1.16	0.10	0.02	6.72
59-4Ost	30-40	Bw	0.04	0.24	1.34	1.18	1.00	0.20	0.00	4.00
59-4Ost	40-50	C	0.03	0.31	1.72	1.27	0.75	0.05	0.00	4.12
59-4Ost	50-70	C	0.04	0.38	0.33	1.56	0.96	0.08	0.00	3.35
59-4Ost	70-75	C	0.05	0.42	0.40	2.07	1.62	0.58	0.00	5.14
59-4W	0-10	Ah	0.13	0.55	4.00	1.57	1.20	0.31	0.00	7.26
59-4W	10-20	Bw	0.05	0.28	0.83	1.17	0.88	0.08	0.00	3.29
59-4W	20-30	Bw	0.04	0.27	0.42	1.22	0.90	0.08	0.00	2.94
59-4W	30-40	Bw	0.03	0.34	0.32	1.38	0.88	0.10	0.00	3.04
59-4W	40-50	Bw	0.03	0.38	0.83	1.73	0.96	0.06	0.00	4.00
59-4W	50-60	C	0.02	0.28	0.18	1.15	0.72	0.04	0.00	2.40
59-4W	60-70	C	0.03	0.36	0.22	1.50	1.07	0.24	0.00	3.42

**Tabelle A11.** Total element concentrations for RCH soils

RCH no.	Depth [cm]	Hori-zon	Fe	Mg	Al	Ca	Na	K	Mn
$\text{mg kg}^{-1}$									
39-1	0-10	Auh	19296.46	2873.87	17616.68	3845.69	981.94	3036.62	576.78
39-1	10-21	Auh	26221.14	5019.44	30785.83	4544.76	1624.34	6954.57	928.61
39-1	21-31	Bwb	30978.13	6267.90	27326.07	2189.77	1034.13	4493.63	542.73
39-2	0-15	Auh	22473.43	4393.34	22449.43	5864.32	968.59	4392.78	1372.63
39-2	15-25	Auh	22658.16	4362.57	21489.72	6565.91	932.28	3916.67	1172.47
39-2	25-30	Auh	28246.68	4575.51	30071.05	2458.07	1000.07	4062.72	608.43
39-2	30-40	Bwb	29144.00	5358.19	28311.14	2268.62	1000.70	4010.79	453.53
39-2	40-50	Bwb	28250.49	5580.01	26918.94	2126.67	971.65	4142.36	469.30
39-3	0-9	Auh	22981.35	4147.95	21214.10	2544.10	932.19	3159.20	468.19
39-3	9-14	Cu	25116.37	5245.25	23354.46	2318.61	958.05	4040.93	748.40
39-3	14-22	2Auh	23913.10	4762.07	23873.38	4446.44	1043.11	4283.87	998.94
39-3	22-32	2Cu	26742.91	5337.45	26224.28	3546.92	1087.01	4756.22	844.75
39-3	32-41	2Cu	30714.10	5471.91	26916.09	2147.72	923.60	3761.75	564.57
39-3	41-51	2Cu	29459.20	5039.77	26532.73	2173.48	936.94	3749.16	856.74
39-3	51-61	2Cu	29669.16	5396.25	25998.28	2037.83	869.28	3717.14	659.84
39-3	61-71	3Auh	27816.19	5510.00	23968.52	4768.96	965.58	4659.68	861.06
39-3	71-77	3Auh	26989.09	5418.93	22894.97	4746.29	937.69	4261.92	762.99

RCH no.	Depth [cm]	Horizon	Fe	Mg	Al	Ca	Na	K	Mn
mg kg <sup>-1</sup>									
39-1	0-10	Auh	19296.46	2873.87	17616.68	3845.69	981.94	3036.62	576.78
39-1	10-21	Auh	26221.14	5019.44	30785.83	4544.76	1624.34	6954.57	928.61
39-1	21-31	Bwb	30978.13	6267.90	27326.07	2189.77	1034.13	4493.63	542.73
39-2	0-15	Auh	22473.43	4393.34	22449.43	5864.32	968.59	4392.78	1372.63
39-2	15-25	Auh	22658.16	4362.57	21489.72	6565.91	932.28	3916.67	1172.47
39-2	25-30	Auh	28246.68	4575.51	30071.05	2458.07	1000.07	4062.72	608.43
39-2	30-40	Bwb	29144.00	5358.19	28311.14	2268.62	1000.70	4010.79	453.53
39-2	40-50	Bwb	28250.49	5580.01	26918.94	2126.67	971.65	4142.36	469.30
39-3	0-9	Auh	22981.35	4147.95	21214.10	2544.10	932.19	3159.20	468.19
39-3	9-14	Cu	25116.37	5245.25	23354.46	2318.61	958.05	4040.93	748.40
39-3	14-22	2Auh	23913.10	4762.07	23873.38	4446.44	1043.11	4283.87	998.94
39-3	22-32	2Cu	26742.91	5337.45	26224.28	3546.92	1087.01	4756.22	844.75
39-3	32-41	2Cu	30714.10	5471.91	26916.09	2147.72	923.60	3761.75	564.57
39-3	41-51	2Cu	29459.20	5039.77	26532.73	2173.48	936.94	3749.16	856.74
39-3	51-61	2Cu	29669.16	5396.25	25998.28	2037.83	869.28	3717.14	659.84
39-3	61-71	3Auh	27816.19	5510.00	23968.52	4768.96	965.58	4659.68	861.06
39-3	71-77	3Auh	26989.09	5418.93	22894.97	4746.29	937.69	4261.92	762.99
39-3	77-81	Ahb	28529.10	5688.28	24470.31	2369.81	892.58	4155.34	727.25
39-3	81-87	Ahb	29182.00	4995.55	26792.12	2326.70	904.10	3860.51	712.22
39-3	87-100	Bwb	29938.99	5955.40	25497.96	2018.36	895.61	3925.98	379.37
39-3	100-120	Bwb	30857.22	6658.66	25308.40	2173.09	893.17	4477.50	394.11
41-1	0-8	Auh	22173.90	3801.43	21276.85	3269.68	868.59	3982.39	656.29
41-1	10-18	Auh	26086.01	4838.95	24622.09	2638.14	897.28	4470.36	852.85
41-1	18-35	Bwb	32673.34	5881.54	31378.35	3187.97	897.04	5077.93	443.64
41-2	0-13	Auh	26705.08	4733.27	25361.51	4654.13	832.52	4698.42	2251.03
41-2	13-19	Cu	29093.49	5279.32	26084.20	5464.08	840.51	4261.38	935.02
41-2	19-31	2Auh	28099.51	5187.91	24962.94	6162.09	792.94	4221.84	1157.62
41-2	31-40	Bwb	33164.79	4748.02	35907.35	2578.98	823.02	4323.98	499.74
41-2	40-50	Bwb	35447.22	6204.97	37213.81	2047.89	903.90	5040.22	584.31
41-3	0-10	Auh	33962.00	6037.16	27938.29	3330.34	788.12	3875.11	613.57
41-3	10-20	Cu	32978.12	5811.43	27433.67	3129.04	760.11	3867.92	621.04
41-3	20-28	Cu	29268.16	4853.19	25611.15	2487.13	769.02	4052.99	518.48
41-3	28-42	2Auh	34791.00	6198.63	27908.49	4574.03	815.69	4016.62	824.10
41-3	42-50	Bwb	34772.63	5206.67	34412.13	2157.49	865.03	4333.92	583.39
41-3	50-60	Bwb	36694.08	6967.26	34943.51	2392.54	963.72	4750.07	514.60
45-1	0-15	Auh	27338.56	3828.65	26126.01	2851.12	806.13	3761.77	707.44
45-1	15-20	Auh	29101.69	4316.74	27427.78	3752.95	863.64	3474.83	638.64
45-1	25-35	Bwb	31815.50	5884.20	31401.21	2868.23	1107.59	5036.09	397.95
45-2	0-10	Auh	27357.12	4148.85	25856.44	3111.36	862.63	3924.91	693.76
45-2	10-20	Auh	27803.78	4547.04	25311.10	6449.37	1309.73	3950.04	680.56
45-2	20-26	Cu	27559.12	4028.41	25223.48	4245.07	921.86	3671.28	680.41
45-2	26-33	2Auh	25994.22	3662.30	25045.79	5525.70	909.43	3895.03	688.23
45-2	33-40	Bwb	29912.01	5155.94	27900.13	3452.50	941.07	3951.46	465.08
45-2	40-50	Bwb	29831.44	5168.48	27386.66	2653.96	857.44	3602.09	407.64
45-2	50-60	Bwb	30707.03	5651.31	27158.25	1937.80	701.23	3488.62	362.65
45-3	0-13	Auh	25191.43	3535.83	23711.12	4729.23	1169.30	3519.11	618.28
45-3	13-23	Auh	25392.34	3469.07	22997.81	3203.20	794.26	3237.54	761.39
45-3	23-33	Cu	25853.88	3789.81	23337.65	3818.50	814.21	3462.19	627.84
45-3	34-44	2Auh	25649.83	3470.07	23205.16	3744.91	850.23	3383.86	599.30
45-3	44-54	2Auh	24815.40	3257.99	21567.27	3522.91	742.51	3049.23	622.67
45-3	54-66	Ahb	26144.83	3985.65	23594.19	3324.91	815.82	3758.30	605.09
45-3	66-76	Bwb	27675.38	4255.83	25203.12	4268.87	1126.40	3832.22	664.86
45-3	76-86	Bwb	30529.50	4231.76	27973.30	2310.48	802.05	3737.86	382.15
45-3	86-96	Bwb	30544.56	6370.97	28180.65	3036.50	1015.10	5381.04	411.92
46-1	0-8	Auh	26348.55	3496.63	18364.01	5219.74	920.13	2264.59	420.15
46-1	8-16	Auh	27537.72	4044.77	21340.01	5500.02	801.15	3716.61	492.51
46-1	16-26	Auh	28569.39	4068.84	21311.43	5153.36	752.90	2415.95	433.59
46-1	26-36	Bwb	38537.75	5069.60	28923.46	5394.08	1106.28	3089.02	395.59
46-2	0-8	Auh	26002.69	3617.36	20573.24	7245.82	824.23	2853.15	1045.68

RCH no.	Depth [cm]	Horizon	Fe	Mg	Al	Ca	Na	K	Mn
mg kg <sup>-1</sup>									
46-2	8-16	Auh	25997.51	3967.77	21142.00	9968.22	763.72	3234.76	740.54
46-2	16-26	Auh	24177.78	3863.46	18653.23	10260.69	701.76	2505.79	689.17
46-2	26-36	Auh	26987.05	4313.55	20900.73	9758.99	887.02	3186.03	624.28
46-2	36-43	Bwb	28770.31	4134.50	24865.89	4221.91	886.57	3234.34	283.65
46-3	0-12	Auh	25416.28	3414.15	19354.30	4684.19	797.30	2524.23	486.08
46-3	12-22	Auh	26174.59	3780.16	20098.36	4877.14	791.00	2611.62	521.21
46-3	22-32	Auh	28906.88	3917.95	20704.54	5402.63	816.96	2709.47	518.61
46-3	32-40	Ahb	29950.04	4545.27	21695.17	3774.09	692.80	3117.47	279.14
46-3	40-50	Bwb	29873.20	5083.07	21745.39	4210.86	720.72	3545.37	299.04
46-3	50-60	Bwb	30000.21	5634.28	19636.99	4837.20	717.57	3883.56	323.24
56-1	0-10	Auh	23854.85	4477.98	21731.85	3113.78	865.08	3687.08	433.23
56-1	10-20	Bwb	27038.40	4962.68	23631.11	2557.01	803.17	3777.01	397.75
56-2	0-9	Auh	22273.44	3805.80	19668.78	3032.77	745.66	3241.44	551.12
56-2	9-18	Auh	23773.46	4481.15	21045.33	3393.65	799.27	3620.47	558.71
56-2	18-27	Auh	23740.26	4380.81	20817.07	3407.90	758.90	3344.86	575.20
56-2	27-40	Bwb	26751.09	5440.98	23178.42	3206.92	831.50	3811.55	388.63
56-3	0-10	Auh	21458.16	3834.55	18734.59	3122.39	724.71	3015.31	499.14
56-3	10-18	Cu	23374.98	4822.79	19612.74	3589.11	731.42	3520.91	505.76
56-3	18-27	2Auh	21330.71	3980.94	18629.67	3481.90	732.55	2979.76	435.12
56-3	27-32	2Cu	23142.02	4456.60	21087.19	3584.49	743.46	3408.84	572.33
56-3	32-42	2Cu	23373.40	4493.79	21425.86	4400.43	828.47	3627.14	537.73
56-3	42-52	2Cu	23779.47	5004.95	21505.97	4585.22	921.13	4190.79	482.19
56-3	52-62	2Cu	24051.36	5392.06	20930.89	4094.87	809.45	3825.32	469.33
56-3	62-65	2Cu	25092.63	5124.53	23251.19	4156.51	951.40	4214.70	862.80
56-3	65-72	Ahb	23434.77	4433.08	21579.45	2952.26	757.13	3285.20	465.28
56-3	72-85	Bwb	25513.57	4236.12	25326.40	3356.50	977.83	3946.32	404.73

**Table A12.** Total element concentrations for reference soils

RCH no.	Depth [cm]	Horizon	Fe	Mg	Al	Ca	Na	K	Mn
mg kg <sup>-1</sup>									
28-4	0-9	Ah	42595,74	6583,31	26262,40	4607,25	1054,65	2035,70	1204,04
28-4	17-25	Ah	39988,56	6329,38	24780,66	3858,96	871,56	1870,00	653,07
28-4	25-37	Bw	43343,45	8473,09	24200,99	4247,53	938,10	2468,56	541,37
28-4	37-49	Bw	42057,90	8148,78	25651,91	7529,84	1053,03	3425,97	714,41
29-4	0-5	Ah	28962,50	4570,64	23616,35	3845,54	1076,71	2201,11	1041,73
29-4	5-15	Bw	41199,59	6354,95	27169,96	4338,15	1288,30	2952,56	586,99
29-4	15-22	Bw	37804,49	7349,38	29337,15	4168,30	1332,74	2747,26	568,57
29-4	22-32	Bw	44214,26	7845,93	26830,81	4494,98	1362,79	3198,16	581,16
29-4	32-42	C	44477,00	9337,77	27867,24	4855,25	1408,18	3437,43	653,00
30-4	0-4	Ah	41559,98	6885,97	24509,36	5498,46	1157,97	2885,31	667,37
30-4	4-14	Bw	46121,17	7764,45	27338,59	6688,36	1405,10	3140,92	1034,32
30-4	14-21	Bw	44987,03	8148,98	29009,41	6618,64	1455,81	3273,26	1041,19
32-4	0-3	Ah	32630,31	6955,07	22653,52	7502,54	1151,60	2691,77	1036,58
32-4	3-11	Ah	40756,20	8776,70	29774,51	10468,66	1569,79	3869,67	1073,53
32-4	11-20	Ah	41783,65	8848,09	29982,43	10284,93	1594,88	3601,55	856,13
32-4	20-34	Bw	37623,16	8312,27	27664,30	9929,25	1525,09	3428,02	738,40
33-4	0-5	Ah	39077,27	4348,04	19959,11	3998,98	633,99	2036,76	651,11
33-4	5-10	Ah	42583,76	4404,95	20146,28	4253,90	745,87	1975,00	1092,11
33-4	10-15	Bw	41739,29	5021,82	22268,39	4918,26	902,49	2363,02	785,53
33-4	15-20	Bw	42651,77	6471,19	23647,66	4879,75	835,14	2734,36	562,22
33-4	20-25	Bw	49480,60	6122,80	24055,17	5068,94	736,40	2557,28	665,01
33-4	25-30	Bw	44823,33	6219,03	22369,10	5357,88	903,16	2829,25	558,35
33-4	30-35	Bw	42776,09	5874,02	20699,32	4866,46	870,75	2703,97	524,23
33-4	35-40	Bw	41775,91	6116,97	22282,09	5168,14	925,55	2963,03	521,15
39-4	0-12	Ah	31291,30	4194,86	26079,91	3614,04	1147,21	4523,33	769,37
39-4	12-20	Bw	33625,79	5167,39	26879,92	3354,26	1023,15	4188,33	509,13
39-4	20-35	Bw	32570,75	6359,05	25831,86	3113,46	991,29	4832,45	484,90

RCH no.	Depth [cm]	Horizon	Fe	Mg	Al	Ca	Na	K	Mn
			<b>mg kg<sup>-1</sup></b>						
39-4	35-50	Bw	30389,33	8287,61	25853,25	4015,85	1044,94	6255,31	530,64
39-4	50-65	C	43537,55	10855,91	30616,27	12338,60	1301,74	9444,72	617,83
39-4	65-80	C	29665,57	7012,92	23818,14	3632,10	915,21	4402,98	466,72
41-4	0-10	Ah	29675,98	3202,26	28837,45	2751,24	774,90	2647,83	854,18
41-4	10-20	Bw	33824,90	5051,62	32824,30	3058,12	904,67	3724,19	568,17
41-4	20-30	Bw	33882,00	5731,52	31513,53	3127,38	900,78	3684,37	498,66
41-4	30-40	Bw	33523,31	5430,17	29636,22	3503,33	889,74	3509,45	486,31
45-4	0-10	Ah	26759,56	2639,12	22036,23	2919,89	793,18	2898,36	273,29
45-4	10-20	Ah	30368,59	3449,02	29524,01	2810,92	866,05	3224,04	335,47
45-4	20-30	Bw	31690,91	5270,35	27898,40	2007,38	722,30	3345,99	349,84
45-4	30-40	Bw	31008,66	6413,57	26545,03	2996,01	857,36	3927,82	401,99
45-4	40-50	C	31870,47	8180,31	25598,49	3760,43	855,99	3852,62	443,42
45-4	50-60	C	32463,65	7997,84	26318,12	3450,74	871,32	4181,82	444,51
46-4	0-10	Ah	21354,15	1314,66	17895,69	2094,71	642,62	2005,03	155,16
46-4	10-20	Bw	24573,08	2163,48	23006,66	1747,38	638,11	2093,43	184,80
46-4	20-30	Bw	30448,05	3776,37	26558,92	1591,95	629,59	2613,46	234,10
46-4	30-38	Bw	29306,40	4895,13	21718,43	2284,34	686,39	3048,95	288,58
46-4	38-50	C	28870,12	5739,01	20377,65	1829,00	664,80	3538,31	316,68
59-4O	0-12	Ah	27152,02	4150,21	22581,13	3548,45	704,45	2534,81	325,86
59-4O	12-20	Bw	31054,37	5443,82	26204,78	4149,71	756,17	2927,03	395,89
59-4O	20-30	Bw	32499,99	6060,98	26861,88	4260,03	741,71	3247,01	393,75
59-4O	30-40	Bw	34350,81	7355,79	28063,38	4967,71	802,84	3824,70	375,36
59-4O	40-50	C	36259,52	8617,14	29537,24	5959,14	813,51	5371,35	402,86
59-4O	50-70	C	40629,31	9742,98	30632,49	8037,28	869,06	6790,62	457,34
59-4O	70-75	C	28839,35	7527,45	22669,42	2578,19	677,67	4579,74	449,80
59-4W	0-10	Ah	25321,30	3435,46	18539,70	4093,80	860,92	2772,47	396,66
59-4W	10-20	Bw	29241,22	4363,01	25559,63	3952,88	993,90	3515,55	3515,55
59-4W	20-30	Bw	29980,48	5282,03	23604,68	3512,11	780,34	3595,82	329,84
59-4W	30-40	Bw	29641,11	6277,20	22924,81	4289,92	734,72	4226,48	347,20
59-4W	40-50	Bw	27777,94	6374,81	20526,38	4607,19	729,26	4299,96	357,41
59-4W	50-60	C	28317,10	6509,21	21109,85	4902,69	933,49	4748,22	374,03
59-4W	60-70	C	28564,56	6387,63	21099,31	4680,96	772,47	4350,61	368,93



**Table A13.** Pedogenic (hydr)oxide concentrations in RCH soils

RCH no.	Depth [cm]	Horizon	Fep	Feo	Fed	Alp	Alo	Ald	Mnp	Mno	Mnd
$\text{mg kg}^{-1}$											
39-1	10-21	Auh	1545,75	2845,33	6568,51	3839,29	2288,90	2087,32	0,00	309,06	41,71
39-1	21-31	Bwb	448,52	1702,38	7501,36	1269,29	1696,02	2252,59	253,40	159,43	24,97
39-3	9-14	Cu	2025,76	2517,94	5924,56	3137,07	1908,00	1809,57	0,00	136,06	0,00
39-3	14-22	2Auh	1500,41	2712,74	6083,06	4221,29	2151,87	1861,77	0,00	357,49	0,00
39-3	22-32	2Cu	937,21	2746,02	7552,95	2018,74	2462,04	2565,14	0,00	268,51	74,79
39-3	41-51	2Cu	750,45	3369,50	8205,75	1547,12	2719,51	3136,43	0,00	380,65	58,27
39-3	61-71	3Auh	1356,73	2608,65	5355,77	3235,58	2066,35	1984,62	0,00	382,12	0,00
39-3	77-81	Ahb	664,38	2570,78	6814,31	1605,02	2034,25	2648,40	0,00	309,44	37,52
41-1	0-8	Auh	1808,59	2953,89	5417,07	2425,70	2024,75	2199,08	170,84	270,20	151,66
41-1	18-35	Bwb	392,77	3087,77	9463,40	1554,49	3095,15	3799,56	127,24	49,79	263,69
41-2	31-40	Bwb	702,43	3909,69	10714,01	1940,37	6456,97	4307,22	66,58	59,82	140,87
41-3	0-10	Auh	1196,06	2976,17	8893,30	2083,41	1864,05	3037,55	129,08	86,66	99,30
41-3	10-20	Cu	880,76	3678,01	9079,44	2143,46	2374,66	3178,35	80,45	134,65	181,23
41-3	42-50	Bwb	525,27	3826,56	12199,21	1379,58	2915,76	5229,93	100,10	108,03	234,89
45-1	0-15	Auh	1940,14	3451,94	6447,28	3254,94	2854,09	2793,77	145,83	308,47	0,00
45-1	15-20	Auh	1464,70	3404,71	8267,65	2983,85	3041,07	3217,35	0,00	305,49	0,00
45-1	25-35	Bwb	354,93	1904,76	9743,32	654,10	1661,36	6592,32	163,75	92,05	0,00
45-2	10-20	Auh	1999,43	3845,56	7337,61	2811,84	2869,32	2790,76	187,78	341,06	0,00
45-2	20-26	Cu	1465,37	3724,84	7750,69	2360,11	2767,31	2944,60	186,52	368,42	0,00
45-2	33-40	Bwb	533,36	2610,77	11060,86	685,50	1909,38	6789,83	0,00	116,20	0,00

RCH no.	Depth [cm]	Horizon	Fep	Feo	Fed	Alp	Alo	Ald	Mnp	Mno	Mnd
			$\text{mg kg}^{-1}$								
45-3	0-13	Auh	2291,04	3615,93	7367,65	3345,26	2715,85	3674,65	201,85	342,23	0,00
45-3	23-33	Cu	2011,05	3671,03	7408,89	2529,63	2200,84	3090,08	113,16	237,90	0,00
45-3	34-44	2Auh	1969,68	4259,81	6999,90	2964,60	2560,68	2914,71	143,91	292,62	0,00
45-3	54-66	Ahb	1598,68	3819,24	8185,36	2322,54	2696,46	2196,56	121,98	267,95	0,00
45-3	66-76	Bwb	1037,27	3976,53	9931,97	1059,95	2080,46	4391,64	0,00	282,98	0,00
46-1	8-16	Auh	1911,11	3553,82	8210,72	2300,37	2222,33	3018,94	0,00	132,29	0,00
46-1	26-36	Bwb	539,79	3431,24	14314,35	1002,18	2975,79	5401,87	0,00	0,00	0,00
46-2	0-8	Auh	2344,15	4008,17	5750,85	2938,66	3096,00	1707,83	128,46	381,40	0,00
46-2	16-26	Auh	1202,32	2780,11	6465,95	1429,00	2507,49	2121,03	107,85	282,60	0,00
46-3	0-12	Auh	2379,86	3668,29	6545,62	2612,68	2105,26	2237,59	0,00	100,49	0,00
46-3	32-40	Ahb	507,05	2288,57	7988,45	881,95	2065,39	3484,73	0,00	85,16	0,00
46-3	40-50	Bwb	247,93	1513,60	5574,96	677,21	1444,14	2265,10	0,00	0,00	0,00
56-1	0-10	Auh	1678,06	3837,27	5997,41	2500,92	1807,35	2173,07	0,00	0,00	65,57
56-1	10-20	Bwb	397,51	2518,81	9395,37	624,13	1570,54	3711,34	0,00	0,00	76,16
56-2	0-9	Auh	2429,67	3583,82	5212,91	2532,76	1953,76	1491,33	170,52	109,83	58,77
56-2	27-40	Bwb	247,57	2803,15	8117,42	601,25	1808,81	3750,00	156,63	0,00	0,00
56-3	0-10	Auh	3259,90	3580,27	5393,66	3547,79	2552,44	1892,39	156,24	132,54	56,17
56-3	10-18	Cu	1988,34	3186,05	5421,91	2623,50	1520,92	1926,97	84,89	154,44	102,28
56-3	18-27	2Auh	3537,69	3629,21	4867,15	3900,81	1984,85	1798,86	132,85	73,80	0,00
56-3	27-32	2Cu	1956,03	3691,30	4997,19	2972,87	1962,58	1739,01	91,67	166,51	121,61
56-3	65-72	Ahb	831,26	4045,84	5619,07	1715,00	2173,43	2621,74	90,21	124,28	0,00
56-3	72-85	Bwb	282,34	6007,24	5833,57	1553,82	5015,32	2448,22	158,82	94,73	104,02

**Table A14.** Pedogenic (hydr)oxide concentrations in reference soils

RCH no.	Depth [cm]	Horizon	Fep	Feo	Fed	Alp	Alo	Ald	Mnp	Mno	Mnd
mg kg <sup>-1</sup>											
39-4	0-12	Ah	2830,72	4837,37	4450,79	4212,82	1969,24	1392,50	0,00	240,15	37,62
39-4	12-20	Bw	568,34	2345,70	7215,59	2157,82	2493,19	2342,88	0,00	0,00	17,66
39-4	35-50	Bw	0,00	1362,62	4946,44	1367,24	1552,22	1264,74	0,00	0,00	38,00
39-4	50-65	C	353,19	1050,88	5810,68	860,46	966,34	990,83	0,00	0,00	63,05
41-4	0-10	Ah	2229,46	5918,37	7024,52	4764,19	3304,75	3603,16	204,94	258,96	14,58
41-4	10-20	Bw	805,31	4005,59	8477,20	2296,18	3277,12	4257,06	196,59	0,00	102,78
45-4	0-10	Ah	3120,98	4689,51	9318,73	3766,08	2299,04	4886,45	137,66	17,08	12,06
45-4	20-30	Bw	383,22	1938,76	10401,34	1050,92	1600,83	4371,26	0,00	0,00	60,70
45-4	40-50	C	281,48	1968,54	6499,86	1475,49	2861,74	2737,56	181,22	23,00	32,20
46-4	0-10	Ah	3530,17	3320,47	6050,45	3505,44	1205,74	2084,08	0,00	0,00	0,00
46-4	10-20	Bw	910,07	1271,95	10877,82	1404,51	1699,21	4541,38	0,00	0,00	146,01
46-4	38-50	C	0,00	1106,44	5336,33	336,33	969,81	1578,44	0,00	0,00	43,00
59-4O	0-12	Ah	3416,22	4721,39	4563,61	3900,54	1945,28	1850,41	0,00	71,90	57,92
59-4O	12-20	Bw	911,96	4197,31	6758,77	2047,70	3208,66	2905,02	0,00	80,90	78,80
59-4O	40-50	C	320,12	1747,97	4815,04	1378,05	2439,02	1673,78	0,00	73,17	65,04
59-4W	0-10	Ah	4338,56	4118,25	4316,02	3275,95	1348,50	1422,28	0,00	158,83	59,43
59-4W	10-20	Bw	635,88	2966,20	8994,51	1416,07	2326,60	2984,82	0,00	129,41	43,76
59-4W	30-40	Bw	360,90	1628,00	4932,58	1100,54	1920,48	1453,50	0,00	93,20	17,85
59-4W	50-60	C	237,04	1314,06	4455,59	1023,90	1587,49	684,57	0,00	43,28	141,63



- Vol. 01** Raab, T., Raab, A., Gerwin, W., Schopper, F., Dähnert, D. (Hrsg., 2013): **Land-schaftswandel – Landscape Change.**

<https://opus4.kobv.de/opus4-btu/frontdoor/index/index/docId/4047>

- Vol. 02** Raab, T., Hirsch, F., Raab, A., Schopper, F., Freytag, K. (Hrsg., 2013): **Arbeits-kreis Geoarchäologie – Jahrestagung 2013, 2. – 4.5. 2013, BTU Cottbus. Tagungsband und Exkursionsführer.**

<https://opus4.kobv.de/opus4-btu/frontdoor/index/index/docId/4061>

- Vol. 03** Schneider, A. (2014): **Spatial and temporal development of sediment mass balances during the initial phase of landform evolution in a small catchment.**

<https://opus4.kobv.de/opus4-btu/frontdoor/index/index/docId/4062>

- Vol. 04** Sut, M. (2014): **Detection and behaviour of iron-cyanide complexes in soils of a former Manufactured Gas Plant site.**

<https://opus4.kobv.de/opus4-btu/frontdoor/index/index/docId/4063>

- Vol. 05** Hirsch, F. (2016): **Post-LGM-zeitliche Pedogenese und Geomorphodynamik in den spanischen Zentralpyrenäen.**

<https://opus4.kobv.de/opus4-btu/frontdoor/index/index/docId/4376>

- Vol. 06** Müller, F. (2017): **Der Wandel der Kulturlandschaft im Raum Peitz infolge des mehrhundertjährigen Betriebes des dortigen Eisenhüttenwerkes (Mitte 16. bis 19. Jahrhundert).**

<https://opus4.kobv.de/opus4-btu/frontdoor/index/index/docId/4144>

- Vol. 07** Knoop, C. (2019): **Anaerobic treatment of municipal organic waste from separate collection: digestate properties and substance flows during two-stage digestion and subsequent aerobic treatment.**

<https://doi.org/10.26127/BTUOpen-4820>

**Vol. 08** Raab, T., Raab, A., Schopper, F. (Hrsg., 2019): **Erfassung und Bewertung von vorindustriellen Meilerstandorten – Workshop 19. Februar 2019.**

<https://doi.org/10.26127/BTUOpen-4817>

**Vol. 09** Raab, T., Gerwin, W., Hinz, C. (Hrsg., 2020): **Anthropogenetische Geomorphologie - Geomorphologie im Anthropozän. Virtuelle Jahrestagung des Arbeitskreises für Geomorphologie 2020. 28./29. September 2020, BTU Cottbus-Senftenberg.**

<https://doi.org/10.26127/BTUOpen-5363>

**Vol. 10** Hirsch, F., Raab, A., Raab, T. (Hrsg., 2021): **Beiträge zur Landnutzungsgeschichte in der Niederlausitz und im Erzgebirge**

<https://doi.org/10.26127/BTUOpen-5388>

**Vol. 11** Raab, A., Raab, T., Bonhage, A., Schneider, A., Hirsch, F., Agthe, M., Pommerenke, A. (Hrsg., 2021): **Historische Köhlerei in Südbrandenburg - Begleitband zum Köhlerpfad Waldschule Kleinsee**

**Vol. 12** Nils Dietrich (2021): **Einflüsse unterschiedlich aufbereiteter Bioabfallgärreste auf die bodenphysikalischen Kennwerte von Ackerböden**

<https://doi.org/10.26127/BTUOpen-5653>

ISSN 2196 - 4122